Colección de Estudios de Física 70

A new insight into the interpretation of the T K-edge and $L_{2,3}$-edges XMCD spectra in R-T intermetallics

María Ángeles Laguna Marco

A new insight into the interpretation of the T K-edge and $L_{2,3}$-edges XMCD spectra in R-T intermetallics

Colección de Estudios de Física
Vol. 70

Esta colección recoge las tesis presentadas en el Departamento de Física de la Materia Condensada de la Universidad de Zaragoza desde su constitución en 1987.

Colección de Estudios de Física Vol. 70

A new insight into the interpretation of the T K-edge and $L_{2,3}$-edges XMCD spectra in R-T intermetallics

María Ángeles Laguna Marco

Prensas Universitarias de Zaragoza

FICHA CATALOGRÁFICA

LAGUNA MARCO, María Ángeles
A new insight into the interpretation of the T K-edge and $L_{2,3}$-edges XMCD spectra in R-T intermetallics / María Ángeles Laguna Marco. — Zaragoza : Prensas Universitarias de Zaragoza, 2007
X, 247 p. ; 24 cm. —(Colección de Estudios de Física ; 70)
Tesis-Universidad de Zaragoza
ISBN 978-84-7733-952-6
1. Materia condensada–Tesis doctorales. I. Universidad de Zaragoza. II. Título. III. Serie: Colección de Estudios de Física (Prensas Universitarias de Zaragoza) ; 70
538.9(043.2)

1.ª edición, 2007

Prensas Universitarias de Zaragoza. Edificio de Ciencias Geológicas, c/ Pedro Cerbuna, 12, 50009 Zaragoza, España. Tel.: 976 761 330. Fax: 976 761 063
puz@unizar.es http://puz.unizar.es

Impreso en España
Imprime: Servicio de Publicaciones. Universidad de Zaragoza
D.L.: Z-3587/2007

Contents

Introduction **1**

1 Basic Theoretical Concepts **5**
1.1 Magnetic interactions in R-T intermetallic materials. 5
1.2 X-ray absorption spectroscopy, XAS 10
1.2.1 XAS: basic principles 10
1.2.2 XAS spectrum: structural and electronic information . . 12
1.3 X-ray magnetic circular dichroism XMCD 14
1.3.1 XMCD: basic principles 14
1.3.2 Magneto-optical sum rules 18
1.4 Mössbauer spectroscopy 20
1.4.1 Mössbauer effect 20
1.4.2 Mössbauer spectroscopy: Hyperfine interactions 21
1.4.3 Local model for the magnetic hyperfine field. 29

2 XMCD in R-T intermetallics **33**
2.1 Background 33
2.1.1 Interpretation of the $L_{2,3}$-edge XMCD spectra of the rare-earths: a brief review of the available models. . . . 34
2.1.2 T K-edge XMCD spectra: an alternative approach to the magnetic characterization of the R-T conduction band 37
2.2 Scope of this thesis 38

3 Experimental Techniques and procedures **41**
3.1 Sample preparation 41
3.2 Basic sample characterization 43
3.2.1 X-ray powder diffraction (XRD) 43
3.2.2 Magnetic Characterization: M(T) and M(H) 44
3.3 Mössbauer spectroscopy 45
3.3.1 Experimental setup 45
3.4 XAS and XMCD spectroscopies 47
3.4.1 Synchrotron radiation facilities 47

3.4.2 Experimental Station: BL39XU, SPring-8 49
3.4.3 XAS and XMCD Experimental procedure 53
3.4.4 Analysis of experimental XAS and XMCD data. 55

4 XMCD in the $RFe_{11}Ti$ series and its hydride derivatives. 59
4.1 Introduction 59
4.2 Synthesis and structural characterization of the $RFe_{11}Ti$ series 62
4.3 Macroscopic characterization : Two sub-lattice model 64
4.4 XMCD results and discussion 67
4.5 Conclusions 75

5 Thermal XMCD study in the R_6Fe_{23} compounds. 77
5.1 Introduction 77
5.2 Macroscopic characterization : Two sub-lattice model. 79
5.3 XMCD Results and Discussion 81
5.4 Conclusions 94

6 XMCD in $R(Al_{1-x}T_x)_2$ Laves phases compounds 97
6.1 Introduction 97
6.2 Sample preparation 99
6.3 Crystallographic structure 102
6.4 Macroscopic magnetic characterization 110
6.5 Mössbauer measurements 124
6.5.1 Pure RFe_2 compounds 124
6.5.2 Diluted $R(Al_{1-x}Fe_x)_2$ compounds 133
6.6 XAS at the Fe and Co K-edges 154
6.7 XMCD at the Fe and Co K-edges 156
6.8 XMCD at the R-L_2 edge 167
6.9 XMCD at the R-L_3 edge 186
6.10 Conclusions 189

7 Application of the XMCD technique to specific problems 193
7.1 Introduction 193
7.2 $Er_{1-x}Y_xCo_2$ systems. 195
7.2.1 Introduction 195
7.2.2 Synthesis and structural characterization. 197
7.2.3 Macroscopic Magnetic Measurements 197
7.2.4 XMCD results and discussion 201
7.2.5 Summary and Conclusions 212
7.3 $(Y_tLu_{1-t})(Co_{1-x}Al_x)_2$ systems 213
7.3.1 Introduction 213
7.3.2 Synthesis and structural characterization 214
7.3.3 Macroscopic Magnetic Measurements 215

7.3.4 XMCD results and discussion 219
7.3.5 Summary and Conclusions 228

Concluding Remarks **231**

Bibliography **234**

Introduction

In the last years, the advent of new synchrotron radiation sources has stimulated wide-reaching interest in the development of magnetic studies by using X-ray core-level spectroscopies, such as X-ray circular magnetic dichroism (XMCD). The element and shell selectivity properties of XMCD together with the possibility of obtaining a quantitative determination of spin and orbital magnetic moments through sum-rule analysis of experimental spectra, have revealed XMCD as a unique element-selective magnetic probe.

The *nominal* capabilities of the XMCD are of special significance in the case of intermetallic compounds based on rare-earth (R) and transition metal (T) elements. The study of R-T compounds has attracted considerable attention during the last decades owing to their industrial interest as, for example, hard permanent magnets. However, the understanding of the magnetic properties of the R-T intermetallic is still incomplete due to the lack of a detailed magnetic characterization of the conduction band. In particular, the magnetic characterization of the rare-earth 5d states is essential to get a complete understanding of the magnetic properties of R-T intermetallics as they mediate the R(4f)-T(3d) exchange interaction between the rare-earth and the transition metal atoms so that However, this information is still unattained because their magnetic response to macroscopic magnetic probes is hidden by that of the 4f electrons.

Within this scenario the use of XMCD was a very promising tool to study the magnetism of the rare-earth 5d-electrons in R-T intermetallics by tuning the R-$L_{2,3}$ absorption edges. Nevertheless, while XMCD has demonstrated its feasibility through the application of the sum rules at the transition metal $L_{2,3}$-edges in a wide variety of systems, the expectations regarding the rare-earth 5d magnetism have not been fulfilled. The experimental magnetic characterization of the R(5d) states has not been achieved up to now due to the difficult interpretation of the XMCD spectra recorded at the R $L_{2,3}$-edges. Consequently, the probe of the magnetic state of the R(5d) conduction electrons is still missing.

This thesis was aimed to solve this shortage by providing a deeper insight

into the understanding of the exact nature of the XMCD spectra corresponding to the conduction band states of the R-T systems. To this end we have performed a systematic XAS and XMCD study in different R-T series regarding the modification of the R $L_{2,3}$-edges and T K-edge XMCD spectra with different parameters, namely temperature, specific transition metal (T) and rare-earth (R) elements, R:T ratio and pressure.

The work developed in this thesis was planned within the framework of the coordinated research projects MAT2002-04178-C04 and MAT2005-06806-C04 devoted to the magnetic study of R-T intermetallic systems and comprises not only the XAS and XMCD study but an extensive research including sample preparation, structural characterization, macroscopic magnetic description and Mössbauer spectroscopy measurements. In particular, the correlation of Mössbauer spectroscopy with the XMCD results obtained at the Fe K-edge, has been of special significance to the study of the magnetic properties of the $R(Al_{1-x}Fe_x)_2$ series.

Dissertation overview

The first chapter of this thesis is devoted to the basic theoretical background related to both the magnetism of R-T intermetallic materials and the main techniques employed in this work: XAS, XMCD and Mössbauer spectroscopies.

In chapter 2 a summary of the state of the art regarding the interpretation of the XMCD spectra at the R $L_{2,3}$ and T K edges is given. This chapter includes a brief review of the available models for the R $L_{2,3}$ and T K edges XMCD spectra and presents the open questions which motivated this dissertation and its main objectives.

Chapter 3 comprises the technical information about the different experimental techniques and procedures implicated in the development of this thesis.

The results obtained from XAS, XMCD and Mössbauer measurements along with details about the basic structural and magnetic characterization are presented in chapters 4-6. In chapter 4 we present a systematic XMCD investigation at the Fe K-edge in the case of $RFe_{11}Ti$ compounds and their hydride derivatives. Chapter 5 deals with the temperature dependence of the dichroic signals at both T K-edge and R $L_{2,3}$-edges in the Ho_6Fe_{23} compound. The results obtained from these two systems constitute the basis of a more comprehensive study of the XMCD spectra performed at both the T K-edge and R $L_{2,3}$ edges in R-T intermetallics, that is presented in chapter 6. In this chapter, the modification of the XMCD spectra recorded on the $R(Al_{1-x}Fe_x)_2$ and $R(Al_{1-x}Co_x)_2$ Laves phases series as a function of different parameters and the comparison with other R-T series is shown.

In chapter 7 we present two examples of the usefulness of XMCD to study specific questions in R-T intermetallic compounds: *"The study of the decoupling of the magnetic ordering of the Er and Co sublattices in* $Er_{1-x}Y_xCo_2$ *systems"* and *"The relationship between the Lu magnetic moment and the magnetic behavior of* $(Y_tLu_{1-t})(Co_{1-x}Al_x)_2$ *systems"*. Both subjects are at the present a matter of controversy. What we present in this thesis is the XMCD investigations we have carried out trying to get a deeper insight into each of them.

Lastly, the main conclusions (applicable to any R-T system) and some general comments on this work will be drawn.

Chapter 1

Basic Theoretical Concepts

1.1 Magnetic interactions in R-T intermetallic materials.

Intermetallic compounds based on rare-earth (R) and transition metal (T) elements have attracted considerable attention for the last decades owing to their industrial interest as permanent magnets. The combination of these two classes of elements in one compound may lead to materials with a high magnetic ordering temperature (associated to the presence of Fe) and large magnetization, as well as large magnetocrystalline anisotropy (owing to the R) [1, 2, 3, 4].

In R-T intermetallic compounds the spins of the magnetic atoms in the compound (from T(3d) and R(4f) unpaired electrons) are interacting with each other via an exchange interaction which is supposed to be of the Heisenberg type:

$$\mathcal{H} = -\sum_{i,j} J_{ij} S_i . S_j \tag{1.1}$$

where S_i and S_j are the spin corresponding to the i and j sites and J_{ij} is the exchange parameter of the exchange interaction between these two spins and gives information about the type of interaction (ferro or antiferromagnetic) and its magnitude.

Since three different kinds of spin pairs can be distinguished in the R-T compounds, the exchange interactions are usually classified as: **T-T**, **R-T** and **R-R**. The intensity of each kind of interaction and the way it is described strongly depends on the specific atoms taking part as their electronic configu-

rations are very different:

$$\text{Transition metal} = \text{T} :: [Ar]3d^n 4s^2$$
$$\text{Rare-earth} = \text{R} :: [Xe]4f^n(5d)6s^2$$

In general, in compounds where the transition metal carry a well established moment (Fe *vs.* Co) the **T-T** interaction dominates. Regarding those interactions involving the rare-earth (**R-T** and **R-R**), the **R-T** is the most important and essentially determines the magnetic behaviour of the rare-earth sublattice. In the following we provide a brief outline of the nature of these magnetic interactions, which determine the magnetic properties of the R-T compounds.

R-R interaction

The rare-earth magnetic moment arises from unpaired electrons in the well-localized 4f shell. Since these electrons are situated deep inside the atom, the spin-orbit coupling is much larger than the crystal field interaction so that the total angular momentum is a good quantum number and they can be dealt as localized magnetic moments. The magnetism of these electrons is "basically the same as in the free atom". Moreover, owing to the spatial extent of the 4f wave function being rather small compared to atomic distances, there is not overlap between 4f wave functions, so the interaction has to take place in an **indirect** way. Thus, it is assumed that the R-R interaction is mediated by polarization of the conduction electrons, leading to a long-range spin interaction. Usually, this interaction is supposed to be a long-range oscillatory RKKY (Ruderman, Kittel, Kasuya, Yoshida) type, which is also observed in pure rare-earth systems [5]. This model states that the interaction is mediated by the s electrons of the conduction band. [1]

Because of the highly localized character of the 4f magnetic moments, the **R-R** interaction is about one order of magnitude weaker than the **T-T** and **R-T** ones. For this reason the **R-R** interaction is usually neglected in the study of R-T systems.

T-T interaction

The magnetic moment of a T atom originates from unpaired spins of the 3d shell. The 3d electrons are at the edge of the atom and the interaction with the neighboring charges is very large. The crystal field is therefore much stronger

[1] Alternatively, Campbell's model suppose the interaction to be mediated by the intra-atomic R(4f)-R(5d) interaction and the hybridization of the 5d states within the conduction band.

than the the $L-S$ interaction, the orbital moment L is quenched (partly or completely) due to the strong crystal field and J is not longer a good quantum number. More important, the 3d wave functions have a large spatial extent and, thus, a strong overlap with those of neighboring atoms. Owing to this overlap of the wave functions, the 3d electrons are not longer localized and no longer accommodated into atomic energy levels. These energy levels have broadened into energy bands whose width depends on the interatomic separation. As a consequence, the 3d electrons do not have a well defined quantum spin S and their magnetic behaviour is best described by an **itinerant band-type model**[6]. On the other hand, the width of the 3d band is small and this implies that the 3d electrons are still rather strongly localized at the 3d atoms [7]. To some extent, this justifies the use of local moments in molecular field approximations for describing the magnetic coupling between 3d moments (T-T interaction).[2]

The interaction between the 3d electrons is the strongest exchange interaction in the R-T compounds.

R-T interaction

The R-T exchange interaction is larger than the R-R exchange but smaller, although of the same order of magnitude, than the T-T one. Experimental data indicate that for all the R-T intermetallics without exception, the coupling between the rare-earth and the transition metal moments is always ferrimagnetic for heavy rare-earths (R with more than half-filled 4f shell, $J = L + S$), and ferromagnetic for compounds with light R element (with a less than half-filled 4f shell, $J = L - S$) [1, 2, 3, 4].

In contrast to the R-R and T-T interactions, R-T interaction is not well modelized by any theoretical model in the sense that no theoretical formalism can quantitatively account for this interaction. The main reason is the difficulty into treating the interaction between highly localized R(4f) and itinerant-like T(3d) magnetic moments on an equal footing. Based on the universal coupling scheme experimentally observed, Campbell proposed a phenomenological description for the R-T coupling in which the 5d spins of the rare-earth play a critical role [8]. Due to the localized character of R(4f) moments, the R-T exchange is thought to be an indirect interaction involving an intra-atomic exchange between the R(4f) and R(5d) electrons, and an inter-atomic interaction between the spin polarized R(5d) and the T(3d) electrons [9]. According to Campbell's model the R(4f) spins are parallel coupled to the R(5d) spins, while the coupling between the rare-earth spin and the transition metal spin

[2] Further explanation about the molecular field approximation is giver later on.

is always antiparallel. If, in addition, we take into account the $L - S$ coupling of the R(4f) electrons and the quenching of the orbital moment of T(3d) electrons, this coupling scheme leads to the experimentally observed magnetic couplings, as illustrated in Figure 1.1.

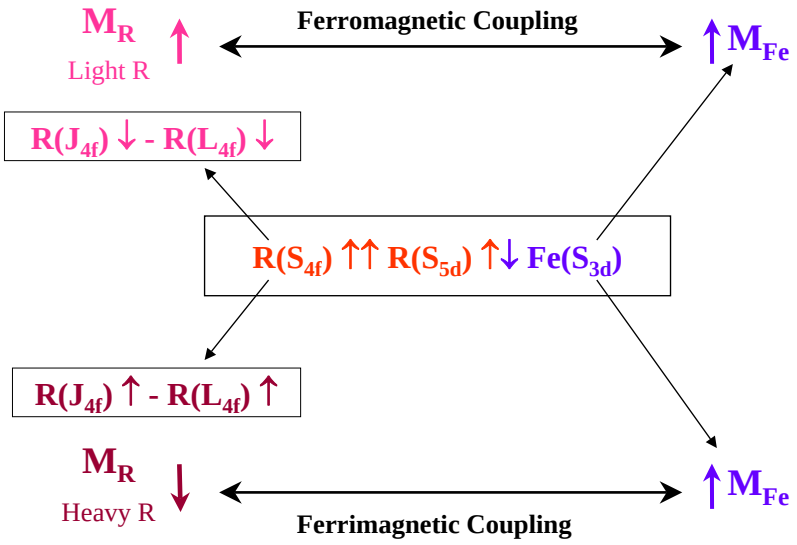

Figure 1.1: Schematic layout of the arrangement of the couplings that take place between the different magnetic moments in the R-T intermetallic compounds. See details in the text.

Later, Yamada *et al.* and Brooks *et al.* proposed a simple approach, taking into account the hybridization between 5d and 3d bands, to account for this universal coupling picture. [10, 11, 12, 13, 14, 15, 16, 17]. However, the exact nature of the R-T interaction is still undefined and no quantitative property can be a priori formulated. As a matter of fact, estimates of the R-T interaction are commonly derived from the experimental data by using a **mean-field two-sublattice model**. Within this framework the system can be divided into two magnetic sublattices: the R sublattice and the T sublattice. Then, the magnetic behaviour of the system can be described by the three types of interactions previously described: *i)* the R-R interaction between the magnetic moments within the R sublattice, *ii)* the T-T interaction between the magnetic moments of the T sublattice and *iii)* the R-T intersublattice interaction. This model does not describe the nature of the interactions themselves, but it was developed to provide a simple way to quantitatively deal with them. Therefore, the interactions are described via the mean fields experienced by the R, H_R, and T, H_T, atoms:

$$H_R = H_0 + n_{RR}M_R + n_{RT}M_T$$
$$H_T = H_0 + n_{RT}M_R + n_{TT}M_T, \tag{1.2}$$

where H_0 is the external applied magnetic field, M_R and M_T represent the magnetization of the R and T sublattices, respectively, and n_{AB} are the macroscopic molecular field coefficients. These coefficients n_{AB} are related to the J_{AB} ones [3] through:

$$n_{RR} = 2Z_{RR}J_{RR}(g_J - 1)^2/g_J^2\mu_B^2N_R, \quad n_{TT} = Z_{TT}J_{TT}/2\mu_B^2N_T,$$
$$n_{RT} = Z_{RT}J_{RT}(g_J - 1)/g_J\mu_B^2N_T, \quad n_{TR} = Z_{TR}J_{TR}(g_J - 1)/g_J\mu_B^2N_R \tag{1.3}$$

where Z_{RR}, Z_{RT} are the number of the R and T nearest neighbours of a R atom, respectively, and Z_{TR} and Z_{TT} those of the R and T nearest neighbours of a T atom. N_R (N_T) are the number of R (T) atoms per formula unit and g_J is the Landé factor. J_{ij} parameters are more appropriate to compare the intensity of the interactions. However, very often J_{ij} cannot be directly determined from experimental data, whereas this is possible for n_{ij}. It can be shown that this approach leads to the following expression:

$$T_c = \frac{1}{2}\left(T_T + T_R + \sqrt{(T_T - T_R)^2 + 4T_{RT}^2}\right) \tag{1.4}$$

where

$$T_T = n_{TT}C_T, \qquad T_R = n_{RR}C_R \qquad and \qquad T_{RT} = n_{RT}\sqrt{C_RC_T}$$
$$C_R = N_Rg_J^2J(J+1)\mu_B^2/3k_B \qquad and \qquad C_T = N_Tg_T^2S(S+1)\mu_B^2/3k_B$$

Once the Curie temperatures have been experimentally determined, the values of n_{TT}, n_{RT} and n_{TR} are straightforwardly obtained from these expressions. For a given R-Fe series, n_{TT} is calculated from the value of T_T, which is usually obtained as the Curie temperature of the isostructural compound with R = Y or Lu. n_{RR} is determined from T_R, whose value can be obtained as the order temperature of the isostructural compound based on T = Ni. On the other hand, it is also customary to neglect T_R in the expression (1.4) since it is one order of magnitude smaller than T_T and T_{RT}. This latter simplification allows us to obtain the values of n_{RT} from the expression (1.4) for all the compounds through the R-T series:

[3] J_{AB} are the coefficients of the exchange interaction between spins. Notice that in Eq.1.1 the i and j subscripts are related to the i and j sites respectively. Within a mean-field model, however, A and B subscripts are related to the type of atom, R or T, ignoring the exact position in the lattice and distances between atoms.

$$n_{RT} = \frac{\sqrt{T_c(T_c - T_{Fe})}}{\sqrt{C_R C_T}} \tag{1.5}$$

The value of n_{RT} is found to decrease as the atomic number of the rare-earth increases (from Pr to Tm). Additionally, in the case of light R, n_{RT} is about twice larger than for heavy R. According to *Belorizky et al.* this diminution of n_{RT} is related to the fact that the R(4f)-R(5d) interaction decreases as the atomic number of R increases. In turn, this decrease is associated with the spatial reduction of the R(4f) shell, which is about 10 times larger than the spatial reduction of the 5d shell. [18]

1.2 X-ray absorption spectroscopy, XAS

1.2.1 XAS: basic principles

X-ray absorption spectroscopy is based on the interaction between electromagnetic radiation and matter. Photons passing through matter will interact by means of three different kinds of processes: scattering, photoelectron absorption and pair production. In the X-ray energy region of our interest (actually up to $\sim$ 100 keV) the photoabsorption is the dominating process.

The physical process of X-ray absorption is the excitation of electrons from deep core levels of an atom by the absorption of an X-ray photon when the photon has enough energy. The phenomenon is schematized in Fig. 1.2.

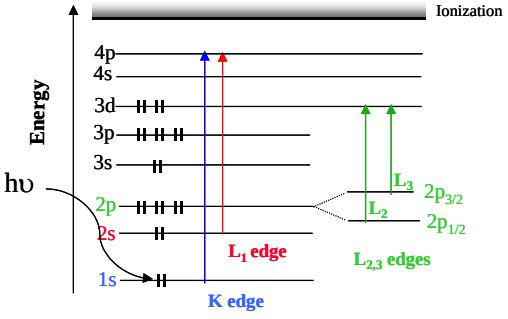

Core state	Spectroscopic name
1s	K
2s, 2p	L_1, $L_{2,3}$
3s, 3p, 3d	M_1, $M_{2,3}$, $M_{4,5}$
4s, 4p, 4d, 4f	N_1, $N_{2,3}$, $N_{4,5}$, $N_{6,7}$

Figure 1.2: Scheme of the excitation of an electron by the absorption of a X-ray photon. Each transition is characterized by the initial and final states of the excited electron and is usually labeled by the spectroscopic name.

According to Fermi's Golden Rule the transition probability per unit of time from a core state to a final state can be written as:

$$W = \frac{2\pi}{\hbar} | < f|H_{int}|i > |^2 \rho_f(\hbar\omega - E_c), \tag{1.6}$$

where $| < f|H_{int}|i > |$ is the matrix element of the electromagnetic field operator, H_{int}, between the initial core-electron state $|i >$ and the final valence state $|f >$, $\rho_f(E)$ is the density of empty states at the energy E above the Fermi level and E_c is the core-electron binding energy. The evaluation of this transition probability requires several approximations concerning both the description of the initial and final states and the interaction operator.

In relation to the description of initial and final states, the simplest approach to the description of X-ray absorption spectra employs the single-electron model as a starting point. In this picture, all the electrons of the system remain passive during the absorption process except the photo-excited core electron, which is excited to the unoccupied states of the system. This picture allows an easy description of both the core initial states and the delocalized final states (bands, continuum states), as only the excited electron is taken into account.

Regarding the interaction operator, when the energy of the incident photon is within the X-ray region it is customary, and usually valid, to make the electric dipolar approximation,[4]

$$| < i|H_{int}|f > | \propto | < i|\varepsilon \mathbf{r}|f > | \tag{1.7}$$

where ε is the polarization vector.

Since the electric dipole operator, $\varepsilon\mathbf{r}$, is odd and acts only on the radial part of the electronic wave-function (the x-ray photon carries angular momentum one and no spin), transitions can be made only between states which have opposite parity and differ in angular momentum by one: $\mathbf{\Delta l = \pm 1}$ **and** $\mathbf{\Delta s = 0}$**, the dipole selection rules.**

It is important to highlight that the use of X-rays to excite the electrons along with the the dipole selection rules offers unique capabilities in comparison with typical laser light ($\sim$ 1-4 eV):

- X-rays are energetic enough to excite electrons from core shells. As the inner-shell absorption occurs at characteristic energies (there is a

[4]This approximation is correct if the wavelength is larger than the atomic size. If $\lambda \approx 1$, this approximation becomes invalid, except for $r << 1$ which is generally the case for core electrons. In the soft X-ray range ($\lambda \geq 5$) all the electrons can be treated in this approximation. In the hard X-ray range ($0.5 \leq \lambda \leq 5$), this approximation remains only valid if we consider interactions with very localized core electrons.

clear energy separation between the different core shells) this method is **element-selective**.

- Moreover, by tuning the X-ray energy one can not only select the specific elements in the sample but also select the different shells within the same atom, i.e., select the final-state symmetry. The core states are highly localized with defined quantum numbers. Consequently, by tuning the X-ray energy and due to the dipole selection rules it is possible to select the character of the final states (p-, d-, f-like states). In the frame of the single electron approximation and considering dipolar transitions only, the selection rules mean that, for instance, an excited $1s$ core electron can be only sent to a empty level with p symmetry. Hence, XAS spectra contain intrinsically **shell selective** information.

1.2.2 XAS spectrum: structural and electronic information

As a result of this interaction between electromagnetic radiation and matter, an incident beam passing through any sort of material, will be attenuated. The expression relating the intensity of the incident beam, I_0, and the intensity of the beam after crossing a sample of thickness x, I, is the so-called Lambert equation:

$$I = I_0 e^{-\mu x} \tag{1.8}$$

where μ is the absorption coefficient, which depends on the specific atom and the density of the sample (the particular compound it is embedded). From what we have seen in section 1.2.1 it can be easily deduced that the absorption coefficient, μ, is also dependent on the photon energy. Indeed, μ is smoothly varying with photon energy except at some discrete energies where the abrupt increases occur, called absorption edges. These jumps correspond to the electron having enough energy to excite from a core state to an empty state. This is shown in Fig. 1.3, where an absorption spectrum is schematically illustrated. In this example three different absorption edges are observed: the electrons excited from the $2p_{3/2}$ level give rise to the Lu L_3 edge. As one increases the energy of the incident photons, the electrons from the $2p_{1/2}$ (Lu L_2 edge) and $2s$ (Lu L_1 edge) levels are also excited.

Depending on the energy of the incoming photons, the X-ray absorption spectrum is divided into several regions: the pre-edge, the edge, the near-edge (XANES) region, which extends to 30-100 beyond the edge, and the EXAFS region, which extends from 30-100 eV to 600-1000 eV beyond the edge.

The physical origin of the absorption features in the pre-edge and edge

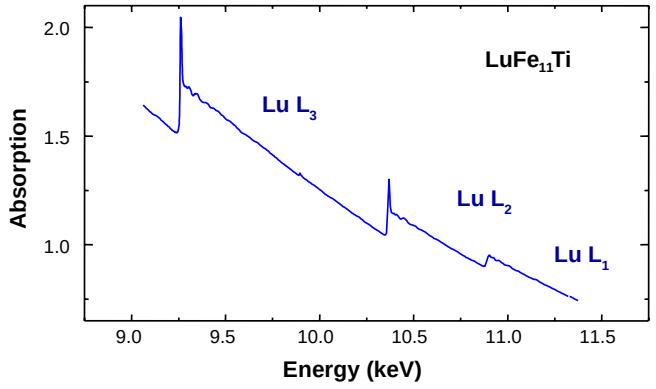

Figure 1.3: XAS spectrum measured at the Lu L_1, L_2 and L_3 edges in a sample of $LuFe_{11}Ti$.

regions depends on the material, i.e., Rydberg states in free atoms, bound valence states or bound multiple scattering resonances in molecules, unoccupied local electronic states in metals and insulators. Thus, analysis of these edge features in the spectrum of a particular sample can provide information about vacant orbitals, electronic configuration and the site symmetry of the absorbing atom.

For more energetic X-rays, the absorption will vary monotonically if isolated atoms are considered (namely, in gas state). However, in condensed matter it has a complicated behavior which extends past the edge by an amount typically of the order of 1 keV. The absorption coefficient presents small oscillations superimposed on the edge step that gradually die away as the X-ray energy increases. The oscillations are known as EXAFS (Extended X-ray Absorption Fine Structure) and are due to the interaction of the photoelectron with the surrounding atoms. The physical processes giving the XANES and EXAFS structures in the X-ray absorption spectra can be understand as follows: the photon is completely absorbed and kicks out a core photoelectron from the absorbing atom leaving behind a core hole. This photoelectron will be ejected with an energy equal to energy of the incoming photon less its binding energy, when in the core, and will interact with the surrounding atoms. Regarding the emitted photoelectron as a wave and the surrounding atoms as point scatterers, a simple picture can be seen in which the backscattered waves interfere with the forward wave to produce either peaks or troughs. This is an interference effect on the final state. Since the transition probability is given by a matrix element between the final and initial states and the absorption coefficient is related to the transition probability, this interference affects the

absorption coefficient which is the quantity that is measured in a XAS experiment. The wavelength of the photoelectron is dependent on its energy and thus the phase of the back scattered wave at the central atom will change with the energy of the incoming photon. This leads to the oscillatory nature of the interference effect with the X-rays energy. In addition, backscattering amplitude and phase are dependent on the type of neighbouring atom doing the backscattering and on the distance the neighbour atoms are from the central atom. Therefore, from the analysis of the XANES and EXAFS regions information regarding the coordination environment of the absorbing atom can be obtained.[19]

1.3 X-ray magnetic circular dichroism XMCD

1.3.1 XMCD: basic principles

XMCD can be defined as the difference of the X-ray absorption coefficient $\mu_c = (\mu^- - \mu^+)$ for antiparallel, μ^-, and parallel, μ^+, orientation of the incident photon helicity and sample magnetization.[5]

Thus, XMCD consists basically on recording XAS spectra under two particular conditions: i) the incident light is circular polarized and ii) the sample under study has a net magnetization. Therefore, XMCD exhibits the same **element and shell selectivity** properties as the standard XAS, i.e. by tuning the appropriate energy one can choose the electron (transition) to excite, i.e., the precise final state to explore.

In addition, when XAS is performed with polarized X-rays, some extra selection rules have to be taken into account, thus extending the range of information available from this technique. Right circularly polarized light (RCP)[6] carries helicity, i.e. angular momentum along the direction of propagation, +1 (-1 for LCP). Therefore, within the electric dipolar approximation approach, $| < i|\mathrm{H}_{int}|f > | \propto | < i|\varepsilon\ \mathbf{r}|f > |$, and taking into account conservation of angular momentum, [7] absorption of RCP light gives rise to transitions with $\Delta \mathrm{m}_j = +1$ ($\Delta \mathrm{m}_j =$ -1 for LCP). That is, the dipole selection rules for RCP

[5] Some authors define XMCD as the difference for antiparallel and parallel orientation of the incident photon helicity and the direction of the majority spins. This definition needs the knowledge of the relationship between $\vec{M}$ and $\vec{S}$ of the selected shell of the selected atom, which is not evident in some cases.

[6] **sign convention**: In this thesis we are using the physics definition for right and left polarization of the light: right corresponds to $+\hbar$ (positive helicity) and left corresponds to $-\hbar$ (negative helicity) (In the optical definition the signs are just the opposite).

[7] We are considering the quantification axis is parallel to the photon propagation direction.

(LCP) light are:

$$\Delta j = 0, \pm 1 \quad \Delta l = \pm 1 \quad \Delta s = 0 \quad and \quad \Delta m_j = +1 \quad (\Delta m_j = -1)$$

$\Delta m_j = \pm 1$ is at the origin of XMCD. As we will see below this extra selection rule allows us to scan the difference in the density of empty states with different spin moment supplying **magnetic information** of the material under study.

One can qualitatively understand the basic principle of XMCD by using the one-electron model along with the **two-step approach** formulated by G. Schütz and coworkers[20, 21]. According to this model, in a first step, partially spin-polarized core electrons are excited from an unpolarized initial core state [22] by a circularly-polarized photon. Due to the conservation of angular momentum in the absorption process, the angular momentum of the photon is entirely transferred to the photoelectron. As there is no explicit spin dependence, electronic spins remain unaltered unless they are coupled to the orbital momenta by strong spin-orbit interaction. Thus, in the absence of a connection between the spin and orbital part of the electron angular momentum, both LCP and RCP light will excite 50% electrons with spin-up and 50% with spin down. However, when spin-orbit is present, the angular moment of the photon can be partially transferred to the spin through the spin-orbit coupling. The photoelectrons are therefore ejected with a spin polarization [23] (i.e. there is an imbalance between spin-up and spin-down excited electrons). In the second step the spin-polarized photoelectrons will probe, taking into account the Pauli exclusion principle, the spin polarization of the final empty states. Consequently, the XMCD spectrum reflects the difference in the density of empty states with different spin moment. (The magnetic properties of the sample are probed in the second step because the spin-split valence shell acts as a detector for the spin of the excited photoelectron). The transition probability is proportional to both the electron polarization, P_e also called Fano parameter [22, 24], and the spin-density differences $\Delta\rho = \rho\uparrow$ - $\rho\downarrow$, $\rho\uparrow$ and $\rho\downarrow$ being the majority- and minority-like final state densities, in the form:

$$\frac{\mu^-(E) - \mu^+(E)}{\mu^-(E) + \mu^+(E)} = P_e \frac{\Delta\rho}{\rho} \tag{1.9}$$

In order to understand more clearly this picture, we present below the application of this model to the particular case of the T $L_{2,3}$-edges XMCD spectra ($2p \rightarrow 3d$ transitions):

In a first step the core electrons are excited by a circularly-polarized photon from the initial states L_3 ($2p_{3/2}$) and L_2 ($2p_{1/2}$) that can be characterized by

the quantum numbers j and m_j with $j = l + s$ and $j = l - s$, respectively. For the final $3d$ states we shall assume a Stoner model: there is not spin-orbit splitting and the exchange interaction splits the band into a spin-up and spin-down components. Therefore we will have five degenerate spin-up states with density of states, DOS, $\rho\uparrow$ and five degenerate spin-down states with DOS $\rho\downarrow$.

For evaluation of the matrix elements it is useful to express the dipole operator in terms of spherical harmonics:

$$\varepsilon\mathbf{r} = \sqrt{\frac{4\pi}{3}} Y_1^1 \cdot r \qquad for\ RCP\ light \tag{1.10}$$

$$\varepsilon\mathbf{r} = \sqrt{\frac{4\pi}{3}} Y_1^{-1} \cdot r \quad for\ LCP\ light \tag{1.11}$$

Since the dipole operator does not act on the spin-state, the matrix elements can be written with regard to a $|l, m_l, s, m_s\rangle$ basis (the product of spherical harmonics and a spin dependent function). According to the dipole selection rules the transitions occur from $2p$ states $|l, m_l\rangle$ into the 3d states with $|l + 1, m_l \pm 1\rangle$ and the possible matrix elements are obtained from:

$$\sqrt{\frac{4\pi}{3}} \langle l+1, m_l \pm 1 | Y_1^{\pm 1} | l, m_l \rangle \mathcal{R} = -\sqrt{\frac{(l \pm m_l + 2)(l \pm m_l + 1)}{2(21+3)(2l+1)}} \mathcal{R} \tag{1.12}$$

where the radial part is given by:

$$\mathcal{R} = \langle n', l+1 | r | n, l \rangle \tag{1.13}$$

and can be assumed as constant for the considered transitions.

The angular part of the matrix elements

$$I_{jm}^{\pm} = \left| \sqrt{\frac{4\pi}{3}} \langle j', m \pm 1 | Y_1^{\pm 1} | j, m \rangle \right|^2 \tag{1.14}$$

is listed in Table 1.1 for the $|jm_j\rangle$ sublevels with respect to the the spin and circular polarization of the X-rays. It shows that at the L_3 edge right circular polarized light prefers excitation of spin-up electrons, while the situation is the opposite at the L_2 edge.

In the second step, taking into account the Pauli exclusion principle and the different DOS for spin-up, $\rho\uparrow$, and spin-down, $\rho\downarrow$, (in a material with

j, m_j	m_l, m_s	I^+	I^-
$\frac{3}{2}$, + $\frac{3}{2}$	$\|+1\uparrow\rangle$	$(\frac{2}{5})\uparrow$	$(\frac{1}{15})\uparrow$
$\frac{3}{2}$, + $\frac{1}{2}$	$\sqrt{\frac{1}{3}}\|+1\downarrow\rangle + \sqrt{\frac{2}{3}}\|0\uparrow\rangle$	$(\frac{2}{15})\downarrow + (\frac{2}{15})\uparrow$	$(\frac{1}{45})\downarrow + (\frac{2}{15})\uparrow$
$\frac{3}{2}$, - $\frac{1}{2}$	$\sqrt{\frac{2}{3}}\|0\downarrow\rangle + \sqrt{\frac{1}{3}}\|-1\uparrow\rangle$	$(\frac{2}{15})\downarrow + (\frac{1}{45})\uparrow$	$(\frac{2}{15})\downarrow + (\frac{2}{15})\uparrow$
$\frac{3}{2}$, - $\frac{3}{2}$	$\|-1\downarrow\rangle$	$(\frac{1}{15})\downarrow$	$(\frac{2}{5})\downarrow$
$\frac{1}{2}$, + $\frac{1}{2}$	$\sqrt{\frac{2}{3}}\|+1\downarrow\rangle$ - $\sqrt{\frac{1}{3}}\|0\uparrow\rangle$	$(\frac{4}{15})\downarrow + (\frac{1}{15})\uparrow$	$(\frac{2}{45})\downarrow + (\frac{1}{15})\uparrow$
$\frac{1}{2}$, - $\frac{1}{2}$	$\sqrt{\frac{1}{3}}\|0\downarrow\rangle$ - $\sqrt{\frac{1}{3}}\|-1\uparrow\rangle$	$(\frac{1}{15})\downarrow + (\frac{2}{45})\uparrow$	$(\frac{1}{15})\downarrow + (\frac{4}{15})\uparrow$

Table 1.1: The angular part of the matrix elements for excitations from 2p core levels $|jm_j\rangle$ decomposed into $|l = 1, m_l, s = 1/2, m_s\rangle$ and catalogued with respect to spin and circular polarization of light.

net magnetization) we obtain a different transition probability, i.e., a different absorption for left and right circular polarized light as shown in Table 1.2.

	I^+	I^-	ΔI ($\propto$ XMCD)
L_2	$\frac{1}{3}\ \rho\downarrow + \frac{1}{9}\ \rho\uparrow$	$\frac{1}{9}\ \rho\downarrow + \frac{1}{3}\ \rho\uparrow$	$\frac{2}{9}(\rho\downarrow$ - $\rho\uparrow)$
L_3	$\frac{1}{3}\ \rho\downarrow + \frac{5}{9}\ \rho\uparrow$	$\frac{5}{9}\ \rho\downarrow + \frac{1}{3}\ \rho\uparrow$	$\frac{2}{9}(-\ \rho\downarrow + \rho\uparrow)$

Table 1.2: The X-ray absorption for RCP (LCP) light involves preferentially spin up (spin down) electron on the $2p_{3/2}$ core level (L_3 edge). The opposite situation is observed for the $2p_{1/2}$ core level (L_2 edge).

Thus, from this picture it is easy to see both, why the absorption is different for left and right circular polarized light and why the XMCD is related to the magnetism of the band we are probing.

In the explanation given above we have used a band (Stoner) model to describe the final 3d states. Alternatively, one can consider an atomic picture with spin-orbit splitting in both initial and final states. In this case, dichroic intensity can be obtained following the procedure described above if the degeneracy of final states is assumed lifted and the different m_j final states have different occupation.[25]

The one-electron picture can be also used to explain the XMCD signal at the K-edge of the transition metals. In these cases, however, due to the spherical symmetry of the initial state (no spin-orbit coupling in the initial state), a small spin-orbit coupling of the final p states is invoked to account

for spin-dependent X-ray absorption.[22]. In addition, the XMCD signal at the K-edge of the 3d transition metal element is much weaker than at the $L_{2,3}$ edges since we are not probing the 3d band, responsible for magnetism in 3d metals, but the extended 4p band. In fact, K-edge signals are typically of the order of 10^{-3} (or less) in saturation conditions.

1.3.2 Magneto-optical sum rules

Magneto optical sum rules were derived within a localized picture i.e., single ions in a crystal field with a partially filled valence shell, by Thole, Carra and coworkers.[26, 27] Later, these sum rules were reformulated within an independent particle approximation.[28, 29] These sum rules are of great significance because they interrelate, under certain approximations, in a **quantitative manner** the integrated XMCD of a specific shell to the ground state orbital and spin magnetic moment. In this way, for an excitation of a photoelectron from the core state $j^{\pm} = c \pm 1/2$ into the valence shell $l = c \pm 1$ with n electrons (where c and l are the orbital angular momenta of the core and valence states, respectively), the orbital sum rule states that the integral over both spin-orbit-splitted absorption edges $j^{\pm}$ is proportional to the orbital magnetic moment μ_l = - $\langle L_z \rangle$:

$$\frac{\int_{j^+ + j^-}(\mu^- - \mu^+)d\omega}{\int_{j^+ + j^-}(\mu^- + \mu^+ + \mu^0)d\omega} = -\frac{1}{2}\frac{l(l+1) + 2 - c(c+1)}{l(l+1)(4l + 2 - n)}\langle L_z \rangle \qquad (1.15)$$

The spin sum rule yields that the spin moment μ_s = - $2\langle S_z \rangle$ is proportional to the expresion:

$$\frac{\int_{j^+}(\mu^- - \mu^+)d\omega - c(c+1)\int_{j^-}(\mu^- - \mu^+)d\omega}{\int_{j^+ + j^-}(\mu^+ + \mu^- + \mu^0)d\omega} = -\frac{l(l+1) - 2 - c(c+1)}{3c(4l + 2 - n)}\langle S_z \rangle$$
$$-\frac{l(l+1)[l(l+1) + 2c(c+1) + 4] - 3(c-1)^2(c+2)^2}{6lc(l+1)(4l + 2 - n)}\langle T_z \rangle \qquad (1.16)$$

where $\langle T_z \rangle$ is the magnetic dipole operator that corresponds to the asphericity of the charge density of the l valence shell.

For the $2p \rightarrow nd$ transitions, ($L_{2,3}$, c = 1, l = 2) this yields to:

$$\langle L_z \rangle = -2 \times \frac{\int_{L_3}(\mu^- - \mu^+)dE + \int_{L_2}(\mu^- - \mu^+)dE}{\int_{L_3 + L_2}\mu\, dE} \times n_h \qquad (1.17)$$

$$\frac{2}{3}\langle S_z\rangle + \frac{7}{3}\langle T_z\rangle = -\frac{\int_{L_3}(\mu^- - \mu^+)dE - 2\int_{L_2}(\mu^- - \mu^+)dE}{\int_{L_3+L_2}\mu\, dE} \times n_h \qquad (1.18)$$

In the case of the $1s \rightarrow np$ (K -edge, c = 0, l = 1) transition, the initial state is not spin-orbit split. Therefore, only the orbital contribution can be evaluated:

$$\langle L_z\rangle = -\frac{\int_K(\mu^- - \mu^+)\, dE}{\int_K \mu\, dE} \times n_h \qquad (1.19)$$

where n_h is the number of holes states per atom, μ_0 is $\frac{1}{2}(\mu^- + \mu^+)$, and μ corresponds to the unpolarized cross-section and is approximated by $\frac{3}{2}(\mu^- + \mu^+)$.

We have adopted the same convention for the sign of the circular dichroism as in Ref.[26] i.e., with the quantization axis determined by the direction of the Fe majority spins.

For the sake of clarity it should be noted that these sum rules have been derived under several assumptions:

- The $2p \rightarrow ns$ dipole allowed transitions are ignored. The shallow s band has a very small density of states and its contribution to the spectra can be neglected.
- The sum rules are based on the assumption that transition between pure electronic configuration occurs. Apart from free atoms the initial and final states cannot in principle be described by pure electronic configurations but one would need to account for configuration interactions.
- The radial matrix element is taken constant.
- There is an ambiguity in the choice of the integration range and the definition of the number of holes.
- Another important assumption is that the two transition channels $j^{\pm}$ (i.e. $L_{2,3}$) do not interfere. In other words, the core hole must be denoted by well defined quantum numbers jm. This assumption is only satisfied when the spin-orbit coupling in the core hole is large compared to other interactions.
- In the case of the $L_{2,3}$ edges $\langle T_z\rangle$ is usually neglected.

It is important to bear in mind that all these approximations will affect to the obtained values of the spin and orbital magnetic moments.

1.4 Mössbauer spectroscopy

Mössbauer spectroscopy, as XMCD, is an element-selective technique. In this work the ^{57}Fe Mössbauer spectroscopy will be used to obtain complementary information about the Fe sublattice in R$(Al_{1-x}Fe_x)_2$ series. In addition, the site selectivity of the Mössbauer spectroscopy will allow us to obtain valuable information about the influence of the number of nearest-neighbour Al atoms on the magnetic moment of Fe.

1.4.1 Mössbauer effect

A radioactive nucleus in an excited state that decays to its ground state will emit a γ ray, which, in turn, can be absorbed by another stable nucleus of the same isotope. This process is known as resonant absorption of γ rays or Mössbauer effect. Usually, when a γ photon is absorbed or emitted part of its energy is lost as recoil energy due to linear moment conservation. Hence, the resonant absorption cannot take place. However, when this atom is bonded to other atoms (say, in a crystal) it is possible to achieve resonant absorption provided that the recoil energy is smaller than the lower vibrational mode (phonon) of the solid.

The probability of recoil-free events (and hence the strength of the signal) is strongly dependent upon the γ ray energy. Consequently, the Mössbauer effect is only detected in isotopes with very low lying excited states. Moreover, the ease to observe Mössbauer effect in a particular isotope strongly depends on the lifetime of the excited state which determine the linewidth (the energy dispersion) of the emitted γ ray. These two factors strongly limit the number of isotopes that can be successfully used for Mössbauer spectroscopy. One of the most suitable nucleus and the most widely used one is ^{57}Fe, which fulfils both requirements: a very low energy γ ray and long-lived excited state. In the case of ^{57}Fe spectroscopy, the usual source is radioactive ^{57}Co, which undergoes a spontaneous electron capture transition and decays to a metastable state of ^{57}Fe. In turn, ^{57}Fe decays to its fundamental state by emitting, among others, the Mössbauer γ ray of 14.4 keV.

1.4.2 Mössbauer spectroscopy: Hyperfine interactions

In Fig. 1.4 the schematic layout used in Mössbauer spectroscopy is presented. γ rays are emitted by a radioactive source and go over the specimen under study, the absorber. The energy levels of a Mössbauer nucleus in a crystal are slightly modified due to interaction with its environment so that the energy levels in the absorber will not be exactly the same as in the emitting atom. By oscillating the γ ray source the energy of the γ ray beam can be modulated due to first order Doppler shift. When the energy-modulated beam matches the difference in energy between the ground and first excited state of the absorber, the gamma rays are resonantly absorbed as is schematically shown in Fig. 1.4.

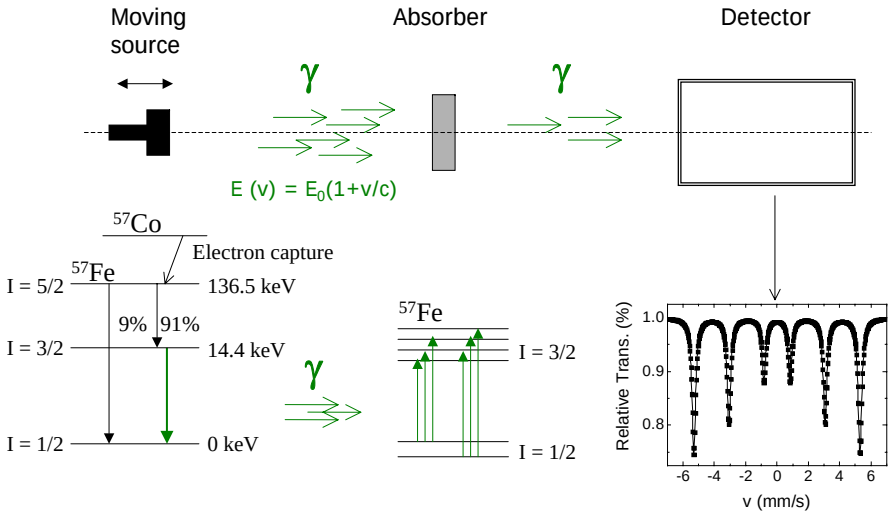

Figure 1.4: Schematic layout of the Mössbauer experiment. The decay process undergone by the ^{57}Co nucleus in the source and the transition giving rise to the Mössbauer γ ray are also shown.

Therefore, the recorded Mössbauer spectrum, obtained by measuring the absorption as a function of the energy of the incident gamma ray, gives information about the position of the energy levels and so it informs indirectly about the interactions between the nucleus and the electrons surrounding it. That is, Mössbauer technique allows to use the nucleus as a probe of its electronic environment. More precisely, the particular spectrum profile is determined by the specific hyperfine interactions: electric monopole interaction, electric quadrupole interaction and magnetic dipole interaction. It is worth noticing that these interactions are much weaker that those responsible of the nucleus structure so that they can be handled as a perturbation. In what follows we will briefly describe these hyperfine interactions and how they determine the

Mössbauer spectra.

Electric monopole interaction - the nuclear isomer shift

The Coulomb interaction between the nuclear charge distribution and the s electron charge density at the nucleus changes the energy of both ground and excited states (relative to the energy in the isolated nucleus) without lifting the degeneracy, as shown in Fig. 1.5 (a). As the volume of the nucleus is dissimilar for ground and excited states, the electric monopole interaction will be also different for each state. Consequently, the energy variation will be different for ground and excited states. If, in addition, the electron densities in the emitting and absorbing atoms are not equal, the energy jump between ground and excited states will also be different. This difference in the energies of the ground and excited states is defined as the isomer shift,

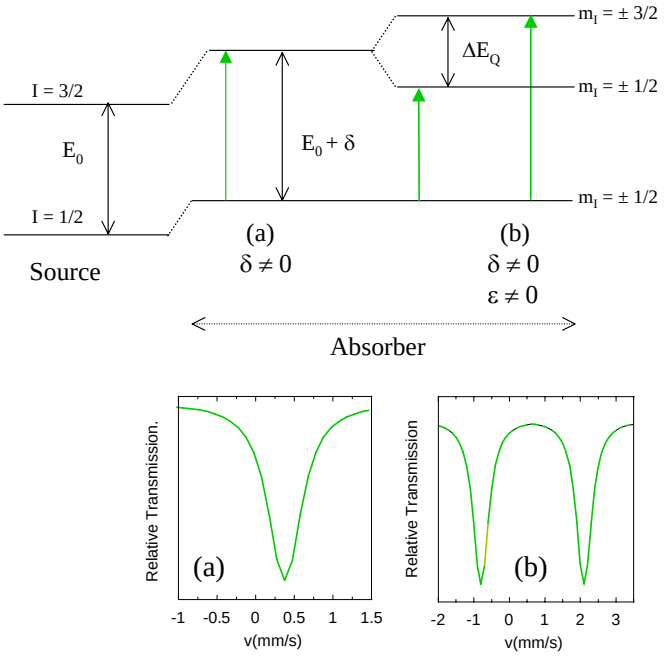

Figure 1.5: (top) Effect of the isomer shift (a) and quadrupole splitting (b) in the energy levels of a ^{57}Fe nucleus. Green arrows represent the different possible transition between ground and excite states. (bottom) Mössbauer spectra produced by the transitions in cases (a) and (b).

$$\delta = \frac{2}{3}\pi[R_e^2 - R_g^2][|\psi(0)|_A^2 - |\psi(0)|_S^2] \tag{1.20}$$

where R_e and R_g are the average nuclear radius for excited and ground state respectively (nuclear factor, R_e^2 - R_g^2 <0) and $|\psi(0)|_A^2$ and $|\psi(0)|_S^2$ are the total density of s electrons in the absorber and source atoms (electronic factor). The isomer shift depends on both nucleus and electron environment. As the nuclear factor is constant for a given nucleus, the isomer shift is directly linked to the electron environment. It has to be noticed that the electronic density at the nucleus is mainly contributed by the s orbitals, which have a non zero density (probability) at the nucleus. The "$no-s$" orbitals do not directly affect the isomer shift as they have zero probability of being at the nucleus. However, they can partially shield the s electrons and hence effectively change the s electron density at the nucleus.

The shift produced by the electric monopole interaction can be calculated by fitting the experimental Mössbauer spectra, yielding information about the electron densities around the absorber. This provides a way of distinguishing between, for example, different ion charge states.

In general, more than a single absorption line will be present in the spectrum due to other interactions affecting the energy scheme. The isomer shift will always indicate the center of gravity of the spectrum. It is important to notice that the isomer shift is not an absolute value, but give us the difference in the energy jump between source and absorber. Therefore, its value for a given absorber is given in relation to a reference value, typically the α-Fe at room temperature, which defines both the zero energy and the velocity scale.

One more effect to take into account is the thermal vibrations in the nucleus, which can also change the energy of the γ ray due to relativistic second order Doppler effect. This makes δ to linearly decrease with temperature (with a slope of 4×10^{-4} - 6×10^{-4} mm/sK in the case of R-T intermetallics.[30])

Electric quadrupole interaction - The nuclear quadrupole splitting

If the nucleus under investigation does not have a spherically symmetric charge distribution, i.e. if I > 1/2, the nucleus will possess a nuclear quadrupole moment, Q, given by:

$$Q = \int_V \rho(r) r^3 (cos^2\theta - 1) d\tau \tag{1.21}$$

where ρ(r) is the charge density in a volume element dτ at a distance r from the center of the nucleus and making an angle θ to the nuclear spin quantization axis.

If, in addition, the electric charges around the nucleus have an asymmetric

distribution, they produce an Electronic Field Gradient (EFG) at the nucleus that will interact with the nuclear quadrupole moment giving rise to a splitting, ΔE_Q, of the nuclear energy levels (see 1.5 b). In an electrostatic potential, V, the EFG is defined as: $V_{ij} = \partial^2 V/\partial x_i x_j$ (x_i, x_j = x, y, z). The principal component of the diagonalized EFG tensor (usually called V_{zz}) is defined as the direction for which V_{ij} is maximum and the EFG asymmetric parameter is defined as $\eta = (V_{xx}\text{-}V_{yy})/V_{zz}$. The interaction between Q and the EFG can be described by the following hamiltonian: [31]

$$\mathcal{H}_{quadrup} = \frac{eQ}{2I(2I-1)}[V_{zz}I_z^2 + V_{xx}I_x^2 + V_{yy}I_y^2] = \frac{eQV_{zz}}{4I(2I-1)}[3I_z^2 - I(I+1) + \eta(I_x^2 - I_y^2)] \tag{1.22}$$

where e is the electron charge and I is the nuclear spin quantum number. If the EFG possesses axial symmetry, ($V_{xx} = V_{yy} \Rightarrow \eta = 0$), this expression converts into:

$$\mathcal{H}_{quadrup} = \frac{eQV_{zz}}{4I(2I-1)}[3I_z^2 - I(I+1)] \tag{1.23}$$

And the energy levels will be given by:

$$E_Q = \frac{eQV_{zz}}{4I(2I-1)}[3m_I^2 - I(I+1)] \tag{1.24}$$

where I and m_I are the nuclear spin and nuclear magnetic quantum number, respectively.

Therefore, the quadupolar interaction splits the nuclear energy levels giving rise to the energy level scheme shown in Figure 1.5.(b). In this case, the Mössbauer spectrum is a symmetric doublet, with an energy difference between the lines, ΔE_Q:

$$\Delta E_Q = (1/2)eQV_{zz}, \tag{1.25}$$

The quadrupolar splitting measures the asymmetry of the electron charge distribution around the Fe nucleus. If the lattice has a cubic symmetry, as in α-Fe, the shift will be zero. The more asymmetric the charge distribution, the largest the quadrupole shift.

Magnetic dipole interaction - Magnetic Splitting

When a magnetic field B is present on the sample, a new interaction has to be taken into account to describe the Mössbauer spectra: the nuclear Zeeman interaction between the nuclear magnetic dipole moment and the magnetic field. The Hamiltonian describing this interaction is given by:

$$\mathcal{H}_{dipmag} = -\mu.B = -g\mu_N I.B \tag{1.26}$$

where μ is the nuclear magnetic moment, g is the gyromagnetic ratio and μ_N is the nuclear Bohr magneton. The field experienced by the system, B, is a combination of the applied, B_0, and the hyperfine, B_{hf}, fields. Hyperfine field is due to the interactions between nuclear and atomic spins:

$$B = B_0 + B_{hf} = B_0 + B_c + B_{dip} + B_{orb}, \tag{1.27}$$

where B_c is the so-called Fermi contact term, which accounts for the interaction of the nucleus with an imbalance in the s-electron spin density at the nucleus. As only s electrons may have non zero density at the nucleus, B_c is originated either from non-full s shells in the atom or from the spin polarization of the valence and core s states due to exchange interaction with other unpair (3d) electrons.[31, 32]

The second term, B_{dip}, corresponds to the dipolar field induced by the atomic spin moment and the last term, B_{orb}, is the magnetic field that stems from the orbital movement of electrons in the non-full shell[31, 32].

Therefore, there are three main components to the hyperfine field, B_{hf}. Among them, B_c is isotropic, while B_{dip} and B_{orb} are anisotropic, i.e., will depend on the direction of the magnetization. [33, 32, 34]. These two contribution are usually much smaller than B_c and so they are typically neglected. For the sake of simplicity, in the following we will write: $B_{anis} = B_{orb} + B_{dip}$. The hyperfine magnetic field is one of the most important magnitudes obtained from Mössbauer spectroscopy. As we will see in the following section, it can provide site selective information about the magnetic moment of Fe.

The interaction between the nuclear magnetic moment and any magnetic field raises the degeneracy of nuclear states with quantum number $I > 0$ to $2I+1$. For example, the ^{57}Fe ground state $I=1/2$ splits into two energy levels, and the excited state $I=3/2$ splits into four energy levels as shown in Fig. 1.6 . The corresponding nuclear energies are given by:

$$E_{m_I} = -g_I \mu_N m_I B \tag{1.28}$$

where $g_{I=1/2} = g_g = 0.1806$ and $g_{I=3/2} = g_e = -0.1033$ are the gyromagnetic ratio for ground and excited state respectively.

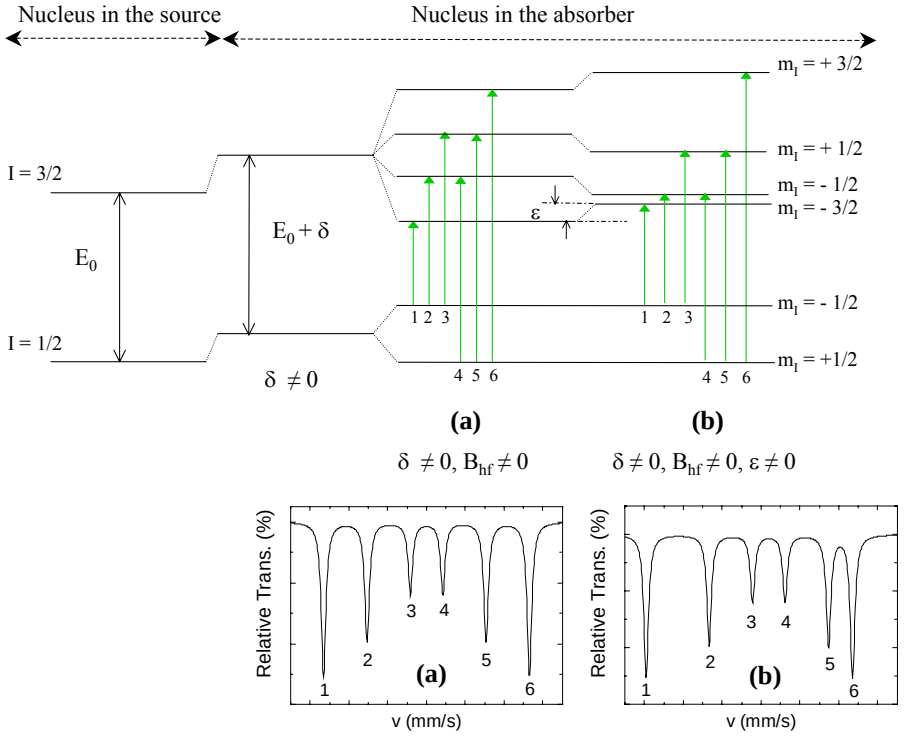

Figure 1.6: (a) Combined effect of the electric monopole and the magnetic dipole interactions into the the energy levels of a ^{57}Fe nucleus. (b) Combined effect of the electric monopole, the electric quadrupole and the magnetic dipole interactions into the the energy levels of a ^{57}Fe nucleus. Green arrows represent the different possible transition between ground and excite states.

The magnetic dipole selection rule, Δm_I=0, ±1 yields six possible transitions as shown in Figure 1.6 . The energy difference between the more external absorption lines is directly proportional to the magnetic field experienced by the nucleus and so Mössbauer spectroscopy provides a way of measuring it.

The intensity of the absorption lines in the spectrum are determined by the transition probability between the nuclear states. In the particular case of Fe, the relative size of the lines ($l1 : l2 : l3 : l4 : l5 : l6$) is given by the following formula:

$$3 : \frac{4sen^2\alpha}{1 + cos^2\alpha} : 1 : 1 : \frac{4sen^2\alpha}{1 + cos^2\alpha} : 3, \tag{1.29}$$

The angle α being the angle between the gamma ray beam and the axis of quantization of the nuclear spins. In the case of a powdered sample without preferred orientation, and with zero net magnetization, the directions of B_{hf} are randomly oriented and the relative intensity of lines 2 and 5 becomes 2.

The relation between the measured intensities can vary due to the finite size of the grains. In addition, when there is a preferred orientation in the sample or and external magnetic field is applied, this relation gives information about the relative orientation between the magnetic moment in the nucleus and the propagation direction of γ rays.

Combined Magnetic and Quadrupole Hyperfine Interactions.

Typically, the analysis of Mössbauer spectra requires to take into account the three interactions described above. Both electric quadrupole and magnetic dipole interactions lift the degeneracy of the nuclear energy levels so that it is very important to correctly combine the effect of these two interactions.

When the EFG tensor has axial symmetry and its principal axis, V_{zz}, deviates an angle θ from the quantum magnetic axis, a simple solution can be found if $eQV_{zz} \ll \mu$B. In this case, the quadrupolar term can be considered as a perturbation to the magnetic interaction and the energy corresponding to a state (I, m_I) turns out:

$$E_{m_I} = -g_I\mu_N m_I B_{hf} + (-1)^{|m_I|+1/2}\frac{eQV_{zz}}{4}\left(\frac{3cos^2\theta - 1 + \eta sin^2\theta cos2\phi}{2}\right)$$
$$= -g_I\mu_N m_I B_{hf} + (-1)^{|m_I|+1/2}\varepsilon \qquad (1.30)$$

The quadrupole shift, ε, is defined as the absolute value of the energy shift of the nuclear excited levels when the quadrupole interaction is treated as a first-order perturbation to the magnetic interaction (see Fig. 1.6 (b)):[31, 35]

$$\varepsilon = \frac{eQV_{zz}}{4}(\frac{3cos^2\theta - 1 + \eta sin^2\theta cos2\phi}{2}) \qquad (1.31)$$

where e is the electron charge, Q the iron nuclear quadrupole moment, V_{zz} the principal component of the EFG, η the asymmetry parameter, and θ and ϕ the polar and azimutal angles of the hyperfine field direction (magnetic axis) with respect to the principal axis, V_{zz}, of the EFG tensor. In an axial system where $V_{xx} = V_{yy}$ the asymmetry parameter, η, of the EFG tensor is zero.

The energy level scheme is illustrated in Fig. 1.6(b). As a result of the quadrupolar interaction, the energy separation between two, (I, m_I) and (I,

$m_I + 1/2$), levels will not be a constant anymore and the absorption lines of the corresponding spectrum will not be equally spaced as shown in the figure. The energy shift due to the quadrular interaction, ε parameter, can be easily obtained from the spectrum fit and will give information about the quadrupolar interaction. The angular dependence of the quadrupole shift can be also used to obtain information about the orientation of the spins in the absorber.

Bearing in mind the energy level scheme presented in Fig. 1.6(b) it is quite easy to work out the energy of the allowed transitions between the nuclear states:

$$E_1 = (E_0 + \delta) + (-\frac{3}{2}|g_e| - \frac{1}{2}|g_g|)\mu_N B_{ef} + \varepsilon \tag{1.32}$$

$$E_2 = (E_0 + \delta) + (-\frac{1}{2}|g_e| - \frac{1}{2}|g_g|)\mu_N B_{ef} - \varepsilon \tag{1.33}$$

$$E_3 = (E_0 + \delta) + (\frac{1}{2}|g_e| - \frac{1}{2}|g_g|)\mu_N B_{ef} - \varepsilon \tag{1.34}$$

$$E_4 = (E_0 + \delta) + (-\frac{1}{2}|g_e| + \frac{1}{2}|g_g|)\mu_N B_{ef} - \varepsilon \tag{1.35}$$

$$E_5 = (E_0 + \delta) + (\frac{1}{2}|g_e| + \frac{1}{2}|g_g|)\mu_N B_{ef} - \varepsilon \tag{1.36}$$

$$E_6 = (E_0 + \delta) + (\frac{3}{2}|g_e| + \frac{1}{2}|g_g|)\mu_N B_{ef} + \varepsilon \tag{1.37}$$

where $g_{I=1/2} = g_g = 0.1806$ and $g_{I=3/2} = g_e =$ -0.1033 are the gyromagnetic ratio for ground and excited state respectively. Each energy corresponds to one of the six lines in the Mössbauer spectrum depicted in Fig. 1.6. Typically, Mössbauer spectrum is not recorded as a function of energy but velocity. The conversion factors for magnetic field and energy are: $C_B = 3.1079$ T.s/mm y $C_E = 4.8067\times10^{-8}$ eV.s/mm.

Finally, it is worth noticing that if there is not hyperfine magnetic interaction, the Fe atom contributes only with two absorption lines (two allowed possible transitions) of equal intensity to the Mössbauer spectrum. In addition, in a general case, there are different environments for the Fe atom in a given compound. These Fe atoms will undergo different interactions and, therefore, their contribution to the total Mössbauer spectra will be also different. The Mössbauer analysis, i.e., the determination of the hyperfine parameters described above, B_{hf}, ε and δ, is based on the adjustment of the experimental spectrum to an addition of sextets by means of a least-squares fit programme. Each sextet will we characterized by a maximum of 7 parameters: the three hyperfine parameters (δ , B_{hf} and ε), the linewidth (Γ), and the intensities of the six absorption lines (modelized with Lorentzians). Due to the relation between the intensities of the six lines, only three parameters are necessary:

the total intensity and the I_2/I_1 and I_3/I_1 relative intensities.

1.4.3 Local model for the magnetic hyperfine field.

The main aim of the Mössbauer experiments in the $R(Al_{1-x}Fe_x)_2$ compounds is to obtain information about the modification of the Fe magnetic moment, μ_{Fe}, with Al substitution. This information can be obtained from the analysis of the hyperfine fields if one knows the relationship between B_{hf} and μ_{Fe}. In the previous section we have presented just a brief description of B_{hf}. Here, we present a simple local model for B_{hf} in R - Fe intermetallic compounds, which offer us an accurate description of the relationship between B_{hf} and μ_{Fe}.

The most common expression for the hyperfine magnetic field experienced by the nucleus of an iron atom is:[31, 32]

$$B_{hf}(k) = B_c(k) + B_{orb}(k) + B_{dip}(k) = \\ B_{cp}(k) + B_{4s}(k) + B_t(k) + B_{orb}(k) + B_{dip}(k) \quad (1.38)$$

where k represents the different crystallographic iron sites.

The Fermi contact field, B_c, is isotropic and for transition metals is usually the main contribution to the total hyperfine field.[31, 32] It is usually divided into three terms. The core polarization term, B_{cp}, represents the contribution from the spin density of the 1s, 2s and 3s core electrons polarized by the 3d electrons of the parent atom. In a local model, this term can be written as $B_{cp}(k) = \alpha\mu_{Fe}(k)$,[36, 37, 38, 39, 40, 41] where $\mu_{Fe}(k)$ is the iron local magnetic moment at the k site, and α is the field at the nucleus produced by a 3d local iron moment of one μ_B. The 4s electrons, much more delocalized than the core electrons, can be polarized by the on-site 3d magnetic moment and by the magnetic moments of the atoms in the first neighbor shell. The contribution coming from the 4s spin density polarized by the 3d electrons of the atom itself is the term B_{4s}, which is usually modeled as $B_{4s}(k) = \beta\mu_{Fe}(k)$,[38, 39] where β mainly depends on the number of 4s spins contributing to the polarization and the intensity of the 4s-3d intratomic exchange interaction.[36, 37, 38, 39, 40, 41] The field due to the 4s spin density polarized by the magnetic moments of the atoms in the first neighbor shell is the transferred hyperfine field, $B_t(k)$. This field possesses contributions from both nearest-neighbors, nn, the iron and the rare earth atoms:

$$B_t(k) = B_{tFe}(k) + B_{tR}(k). \quad (1.39)$$

where the iron sublattice transferred field, B_{tFe}, can be taken as:

$$B_{tFe}(k) = \sum_{l} \zeta_{Fe}(l,k)\mu_{Fe}(l) \tag{1.40}$$

B_{tFe} will depend on the magnetic moment of the iron atoms in the first neighbor shell, $\mu_{Fe}(l)$. A proportionality factor, $\zeta_{Fe}(l,k)$, different for each crystallographic site, should be included. This parameter depends on the number of 4s spins contributing to the polarization, the intensity of the inter-atomic exchange interactions 3d-4s, and also on the particular magnetic and crystallographic environment of the involved atom.[39, 40, 41] In a mean field approximation, the iron sublattice transferred field, B_{tFe}, can be taken as proportional to the average magnetic moment of the iron atoms in the first neighbor shell, $\langle\mu_{Fe}\rangle_{1nn}(k)$.[38, 39, 40, 41] Consequently, this term can be written as:

$$B_{tFe}(k) = \zeta_{Fe}(k)Z_{Fe}(k)\langle\mu_{Fe}\rangle_{1nn}(k), \tag{1.41}$$

where $Z_{Fe}(k)$ is the number of nearest neighbours (nn) iron atoms.

The rare earth transferred field, B_{tR}, stems from the polarization of the iron 4s spin density by the R magnetic moments. On the one hand, it has been proposed that this term could be due to direct polarization of the conduction band, via the RKKY mechanism.[40] However, in a recent study it has been shown that, in R-Fe intermetallics, the B_{tR} term is mainly due to the Campbell mechanism, rather than by the RKKY mechanism.[41] According to this model, B_{tR} should be in the form:

$$B_{tR}(k) = \zeta_{R}(k)\tilde{n}_{RFe}Z_{R}(k)\gamma_{R}\mu_{R} = \tilde{\zeta}_{R}(k)Z_{R}(k)\gamma_{R}\mu_{R}, \tag{1.42}$$

where $\zeta_R(k)$ is a proportionality factor which depends on the number of 4s spins contributing to the polarization and, also, on the particular magnetic and crystallographic environment of the probe atom, $\tilde{n}_{RFe}$ is the R-Fe exchange coefficient, i.e. the coefficient reflecting the interaction between R and Fe spin magnetic moments, $Z_R(k)$ is the number of rare earth nn, γ_R *is* $2(g_J\text{-}1)/g_J$ and μ_R is the rare earth magnetic moment.

The remaining terms are the anisotropic contributions to the hyperfine field. The term B_{dip} is due to the dipolar interaction of the nuclear spin with the magnetic moments. It is usually described as:[31, 32]

$$B_{dip} = -2\mu_B\langle 3\mathbf{r}(\mathbf{S}.\mathbf{r})r^{-5} - \mathbf{S}r^{-3}\rangle \tag{1.43}$$

for axial symmetry systems, it turns out:

$$B_{dip} = -2\mu_B < S >< r^{-3} >< 3cos^2\theta - 1 > \tag{1.44}$$

where θ is the angle between the magnetic axis and the principal axis of the EFG tensor.

B_{orb} is the magnetic field at the nucleus caused by the orbital motion of the unpaired electrons:[31, 32]

$$\mathbf{B}_{orb} = -2\mu_B < r^{-3} >< \mathbf{L} > \tag{1.45}$$

In the case of transition metals this component is small due to the crystal field producing an almost zero orbital angular moment. The small orbital angular moment is due to the spin-orbit interaccion giving a component <L> = $(g-2)$<S>, turning out a B_{orb} term:

$$B_{orb} = -2\mu_B < r^{-3} > (g-2) < \mathbf{S} > \tag{1.46}$$

where g is the Landé electronic factor.

Both terms, B_{orb} and B_{dip}, are much smaller than the isotropic contribution,[40, 36, 37, 42] and they are usually neglected. Grouping the anisotropic contributions in a single contribution, B_{anis}, the final expression for the hyperfine field at a given iron site, k, is:

$$\begin{aligned} B_{hf}(k) &= \alpha\mu_{Fe}(k) + \beta\mu_{Fe}(k) + \sum_l \zeta_{Fe}(l,k)\mu_{Fe}(l) \\ &\quad + \tilde{\zeta}_R(k)Z_R(k)\gamma_R\mu_R + B_{anis}(k) \\ &= \alpha\mu_{Fe}(k) + \beta\mu_{Fe}(k) + \zeta_{Fe}(k)Z_{Fe}(k)\langle\mu_{Fe}\rangle_{1nn}(k) \\ &\quad + \tilde{\zeta}_R(k)Z_R(k)\gamma_R\mu_R + B_{anis}(k) \end{aligned} \tag{1.47}$$

Chapter 2

XMCD in R-T intermetallics

2.1 Background

As we have seen in section 1.1, the intrinsic magnetic properties of R-T materials are determined by the exchange interaction between the R(4f) and Fe(3d) electrons. This interaction takes place through the 5d states of the rare-earth [8]. Consequently, the study of the R(5d) states is of great significance to the search of new advanced magnetic materials within the R-Fe series. Indeed, the detailed knowledge of the mechanism which couples the magnetic properties of both R and Fe atoms depends on the complete magnetic characterization of these R(5d) states. As a consequence, many efforts have been done for a long time, from both theoretical and experimental points of view, focused to get the magnetic description of the R(5d) states. However, as the magnetic response of the R(5d) states is hidden to macroscopic magnetic probes by the presence of the 4f electrons, its magnetic characterization is still unattained.

Being this task rather slippery to standard macroscopic tools, the application of X-ray absorption spectroscopy to address magnetic aspects in the electronic structure and magnetism of condensed matter on the microscopic level entailed an important advance in the field. Specially, X-ray magnetic circular dichroism (XMCD) technique has involved great interest in the last years because of its capability to study the magnetic properties of materials from the atomic level.

The main characteristic of XMCD resides in its element and shell selectivity that combined with the so called sum-rules[26, 27], makes it an unique element-selective magnetic probe. In this way, by tuning **the $L_{2,3}$- edges of the rare earth (2p $\rightarrow$ 5d electric dipole transitions)** one can obtain, in principle, the magnetic description of the R(5d) states. Therefore, XMCD early evoked a far-reaching interest in the field of R-T intermetallics as a promising tool to

(finally) characterize the magnetism of the 5d states of the rare-earths. Thus, numerous XMCD experiments have been performed at the $L_{2,3}$-edges of the rare-earth in several R-Fe compounds aimed to provide direct information on the magnetism of the rare-earth 5d states [43, 44, 45, 46, 47, 48, 49, 50, 51, 52, 53, 54].

However, while XMCD has demonstrated its feasibility at the transition metal $L_{2,3}$- edges in a wide variety of systems, the possibility of disentangling the magnetic contribution of the 5d and 4f states by means of XMCD through an adequate choice of the absorption edge has not been fulfilled yet. This shortage is due to the difficult interpretation of the XMCD spectra recorded at the R $L_{2,3}$- edges, which is still a matter of controversy. Thus, it is found that while XMCD data can be satisfactorily accounted for cases in which the final states are localized (T(3d), R(4f)) by using an atomic approach, the mechanism governing the XMCD for cases in which the final state is delocalized (Fe(4p), R(5d)) is still unclear. In addition, it has been shown that the approximations used for the sum-rules derivation are not valid in the case of the rare-earth $L_{2,3}$-edge spectra [55].

2.1.1 Interpretation of the $L_{2,3}$-edge XMCD spectra of the rare-earths: a brief review of the available models.

The two-step model formulated by G. Schütz and coworkers [20, 21], was successfully applied to the $L_{2,3}$-edges of 5d (Os, Ir, Pt and Au) impurities in iron [21, 56]. However, the same does not hold for the $L_{2,3}$-edges XMCD spectra of the rare-earths. Indeed, the analysis of the XMCD signals of Gd and Tb metal according to the Schütz's model yields that there is a large density of unoccupied spin-up states at and above the Fermi energy. Consequently, the derived 5d spin would be antiparallel to the 4f spin, which is in contradiction with the current knowledge, both experimental and theoretical, of the coupling between the 4f and 5d spin moments in the Lanthanides[8, 11].

This contradiction was explained by Wang et al.[55] by taking into account the previously neglected spin-dependence of the radial part of the matrix elements. These calculations show that there are more unoccupied spin-down states above the Fermi level. However, despite there are fewer spin-up states above the Fermi level, the matrix elements for transitions to spin-up bands are larger and cause the spectra to be dominated by spin-up transitions. The reason for this significant spin dependence of the matrix elements can be found in the radial part of the wave functions for the 5d conduction electrons [57]. The spin-up 5d radial functions are "pulled-in" relative to the spin down functions because their stronger exchange interaction with the localized 4f orbitals. This

"pulling in" causes the 5d radial functions to have a significantly larger amplitude in the region of the 2p radial function. This correction can be "ad-hoc" added to the expression (1.9) in the form:

$$\frac{\mu^-(E) - \mu^+(E)}{\mu^-(E) + \mu^+(E)} = P_e \frac{(M\Delta\rho + \rho\Delta M)}{M\rho} \tag{2.1}$$

where Δ M = M$\uparrow$ - M$\downarrow$, is the difference between the spin-dependent radial part of the transition matrix elements [58].

In addition to this problem, the understanding of the $L_{2,3}$ spectra is further complicated since the addition of quadrupolar 2p$\rightarrow$4f transitions (E_2) to the dipolar main 2p$\rightarrow$5d transitions (E_1) is not negligible [59]. E_2 transitions have been experimentally identified in the XMCD spectra at both L_3 [45, 46, 47, 48] and L_2 [52] absorption edges, being in agreement with resonant inelastic x-ray scattering (RIXS) experiments [60, 61, 62].

The combination of both the spin dependence of the radial part of the matrix elements and the presence of quadrupolar transitions modify both the sign and magnitude of the XMCD signals. This prevents the determination of the 5d magnetic moments by the simple application of the sum-rules.

Moreover, there is as further major problem into the understanding of the XMCD at the $L_{2,3}$-edges of the Lanthanides as it is the observed nonstatistical XMCD branching ratio, i.e. a nonstatistical L_3/L_2 ratio. According to the model of Schütz, the ratio of the XMCD at the L_2- and the L_3- edges would correspond to the statistical one and thus to the ratio between the Fano factors at both edges, being -2 according to calculations [24]. This stems from the fact that the model does not consider orbital polarization of the 5d states and, consequently, there is no difference in the transition probability towards both $5d_{3/2}$ and $5d_{5/2}$ sub-bands other than the different (statistical) number of allowed transitions. Similar result was obtained by Brouder and Hikam by using a multiple scattering approach [63]:

$$\frac{\mu^-(E) - \mu^+(E)}{\mu^-(E) + \mu^+(E)}|L_2 \simeq -2(\frac{\mu^-(E) - \mu^+(E)}{\mu^-(E) + \mu^+(E)})|L_3 \tag{2.2}$$

However, the experimentally observed XMCD branching ratios are far from the statistical value [64, 65] if the rare-earth shows unfilled and localized 4f states (La, Ce, Yb and Lu are the exceptions), which indicates the presence of an orbital momentum in the probed band. However, this interpretation is not free of controversy. Indeed, different models have been proposed for account

for such effects in order to get the whole understanding of the XMCD at the $L_{2,3}$ spectra of the rare-earths.

In this way, Jo and Imada early pointed the need of including the full 5d-4f exchange interaction [66] to account for the rare-earths $L_{2,3}$ XMCD. Then, by inclusion of not only the spin-spin interactions but also the strong orbital polarization due to the exchange interaction with the 4f shell, the variation of the branching ratio is well reproduced. However, the sign of the calculated L_2- and the L_3- XMCD signals is the opposite to the experimentally observed. Posteriorly, this model was improved by Harada's group [67, 68], by considering the enhancement of the transition dipole matrix elements due to the contraction of the radial part of the 5d orbit occurring in an incomplete 4f shell system. In this way, the sign and the intensity of the XMCD signals are well accounted as well as the variation of the branching ratio through the rare-earth series. One common point of both Jo and Harada's models is that the 5d band is partly occupied ($5d^1$) in the ground state.

By contrast, van Veenedal et al. [69] propose that the $L_{2,3}$-XMCD of the rare-earths can be accounted in terms of a $5d^0$ configuration in the ground state. In brief, this means that the 5d states are non magnetic and do not carry magnetic (either spin or orbital) moment. The resulting non-zero XMCD signals would be due to the contraction of the 5d radial wave function by the complete exchange 4f-5d interaction. A characteristic result of this model is that the XMCD signals have a dispersive-like shape in insulating materials and, in the case of metals, they are transformed into one peak due to the breathing effect of 5d orbitals.

Thus, we stand in front of a debate of great importance regarding the magnetism of the 5d states. According van Veenedal et al. the dominant effect is the interaction of the photoelectron with the open 4f shell being the presence of a 5d electron in the ground state not important. On the contrary, Harada's model suggests that the intensity of the XMCD is dominated also by the Pauli exclusion effect due to the inclusion of the 5d electron in the ground state. In this way, by contrast to the van Veenedal's model in which the XMCD lineshape is always dispersion like, the Pauli exclusion effect introduces not only a variety of intensity diagrams for the entire series of rare-earth elements but also a variety of spectral shapes, specially if one considers that the 5d occupation number changes for different environments around the rare-earth in solids.

Recently, the performance of the different available models has been carefully examined by Giorgetti et al. [54]. They show that the fact that XMCD spectra are more derivative-like when they are small cannot be predicted by the theory of van Veenendaal et al., whereas it is explained by the presence of

the 5d electron in the initial state by Harada's. For the metallic spectra, for which the van Veenedal's model is devoted, the spectra cannot be reproduced either at the L_3 or at the L_2 edges. Indeed, it should be noted that the van Veenedal's model was tentatively validated with the measurements on ionic systems reported by Neuman et al. [70]. However, while the L_2-XMCD displays a derivative shape in agreement with the model, the L_3-XMCD is found to deviate, having a more complicated shape. The authors invoked CEF effects to justify the worse agreement at the L_3 edge as compared to the L_2-edge. This argumentation can be maybe held for ionic compounds but not for the metallic ones. As shown by Giorgetti et al., this is one of the major drawbacks of the van Veenedal's model.

Finally, the Harada's model has been further developed aimed to provide a proper description of the XMCD at the $L_{2,3}$-edges of the rare-earths in the case of R-Fe intermetallics. Recent theoretical works suggest the need of including the hybridization between the R(5d) and Fe(3d) bands to account for the R-$L_{2,3}$ XMCD [71, 72] in such a class of materials. However, the way in which these models incorporate the role of the 3d-5d hybridization (ad-hoc like) is not free of controversy and, consequently, further work is still needed to get the complete understanding of the $L_{2,3}$-XMCD in R-T intermetallic materials.

2.1.2 T K-edge XMCD spectra: an alternative approach to the magnetic characterization of the R-T conduction band

Trying to overcome the limitation derived from the unclear interpretation of the R $L_{2,3}$-edges XMCD spectra, alternative edges have been chosen to get a deeper insight into the characterization of the conduction band in R-T intermetallic compounds. To this respect, special attention has been paid to the Fe K-edge. X-ray absorption at the K edge of 3d transition metals involves electronic transitions from 1s to 4p final states. As in the case of the R $L_{2,3}$-edges, the exact nature of the features at the T K-edge XMCD is not completely understood. Thus, different theories have been proposed to interpret the results. Igarashi and Hirai[73, 74] suggest that the XMCD signal is generated by the 3d orbital moment on the neighboring sites through the p-d hybridization, while Guo[75, 76, 77] indicates that the K edge XMCD spectrum probes the p-projected orbital magnetization density of unoccupied states.

In relation to the interpretation of T K-edge XMCD, a further matter to be considered is related to the determination of the ferromagnetic character of the sample in terms of the specific profile of the XMCD spectrum. Thus, the XMCD spectrum of pure Fe, a weak ferromagnetic system for which neither majority nor minority spin bands are full, exhibits both a positive and a

negative peak, while Co and Ni, strong ferromagnets for which majority-spin band is full, present only a negative peak. It is commonly accepted that the positive peak is related with the density of unoccupied spin-up d states close to the Fermi level, while the negative peak observed at higher energies is related to the density of unoccupied spin-down d states. [78, 79] In the light of the comparison between Fe and Co spectra, Fdez-Gubieda *et al.* proposed a method to distinguish the ferromagnetic character (weak *vs.* strong) of Fe [80] by taking advantage of the distinct features in the recorded spectra.

Despite the relationship between the Fe K-edge XMCD spectra and the local magnetic moments is not well defined, [73, 74, 75, 76, 77, 81, 82, 83] in recent works, Chaboy *et al.* have explored the feasibility offered by the study of the Fe K-edge XMCD in R-T intermetallic compounds to characterize the rare-earth conduction band [84, 85, 86]. Their results indicated that there is a rare-earth contribution to the Fe K-edge XMCD and that this contribution reflects the magnetic state of the R atoms. So, these findings led to an alternative approach of characterizing the R(5d) states. However, by the beginning of this thesis they were limited to the systematic study of the $R_2Fe_{14}B$ series and their hydride derivatives. Hence, it is necessary to extend previous research to different R-Fe intermetallic series to establish if the observed behavior constitutes a general characteristic of the Fe K-edge XMCD in R-Fe intermetallic compounds.

2.2 Scope of this thesis

The above presented scenario reveals the need of an exhaustive study of the XMCD signals at both T K-edge and R $L_{2,3}$ edges in order to attain the complete understating of these signals, that will lead to the R(5d) magnetic characterization.

Both, the experimental results obtained at the Fe K edge for the $R_2Fe_{14}B$ series and the last theoretical models to account for the R $L_{2,3}$ XMCD spectra, point out the role of the Fe(3d)-R(5d) hybridization into determining these XMCD signals in R-T intermetallic compounds.

Within this framework we have planned a systematic XMCD study at both T K edge and R $L_{2,3}$ edges for several R-T systems. For each R-T series, we present a systematic study regarding the modification of the XMCD spectra with different parameters such us temperature, specific transition metal or rare-earth element, R:T ratio, etc. The study of the modification of the dichroic signals as a function of the different parameters is expected to provide essential information about the magnetic description of the conduction band

and the understanding of the role of the R(5d)-T(3d) hybridization in the magnetic behavior of the R-T intermetallic compounds. More in particular, our specific purpose is to determine if there is any spectral feature at the T K-edge XMCD spectrum that can be undoubtedly addressed to the magnetic moment of the rare-earth and *vice versa*, i.e., if the transition metal magnetic moment contributes to the XMCD spectra at the R-$L_{2,3}$ absorption edges.

Chapter 3

Experimental Techniques and procedures

In this chapter we present a description of the different experimental setups and procedures involved in this thesis. Some of the employed techniques, such as X-ray diffraction (XRD) and magnetization measurements (M(T) and M(H)) are of standard use in the study of intermetallic compounds. They are well known and only a brief review will be given. On the other hand, X-ray absorption spectroscopy (XAS) and X-ray magnetic circular dichroism (XMCD) techniques are not so commonly utilized to face magnetic problems. In addition, the results obtained from these techniques constitute the main part of this thesis. So, they will be described in a more detailed way.

3.1 Sample preparation

Three different series of R-T intermetallic compounds have been studied in this thesis, namely $R(Al_{1-x}T_x)_2$ Laves phases, $RFe_{11}Ti$ and R_6Fe_{23} compounds.

Polycrystalline Laves phases samples were synthesized by either arc-melting or induction-melting technique. The arc-melted samples were prepared in the arc furnace model Mini Arc Melting System MAM-1 (from Edmund Bühler GmbH) placed on the Magnetism laboratory of the CITIMAC department of the University of Cantabria. A photograph of this arc furnace is shown in Figure 3.1. The induction-melted samples were synthesized in the high frequency induction furnace (model I-12 from G. H. Electrotermia S.A.) located at the Instituto de Ciencia de Materiales de Aragon (ICMA, DEI V Laboratory).

Starting elements have been purchased from commercial companies (Alfa Aesar, Strem Chemicals and Goodfellow). The rare earths present a nominal

purity of 99.9 wt.%. The purity in the case of the transition metal elements is 99.97 wt. % for Fe pieces and 99.9+ wt.% purity for Co pieces. It is worth noting that the purity of the commercial rare earths is referred only to other rare-earth elements.

Figure 3.1: Photograph of the Mini Arc Melting System MAM-1 arc furnace

Both, arc melting and induction-melting, methods are based on the direct melting of the constituent metal elements in an argon atmosphere. The arc-melting operating sequence can be summarized as follows: the appropriate amounts of the several elements, previously weighed and properly cleaned, are placed in Cu base plate of the furnace. Once the furnace is closed, the chamber is purged with 3 or 4 cycles of Ar gas and vacuum. After that, the chamber is filled again with argon gas at a value slightly bellow ambient pressure (0.7-1.0 bar). Then, the tungsten electrode tip is moved towards the anode (tungsten tip on the crucible plate) by means of the knob handle and the arc is ignited. In order to avoid the oxidation of the metals, the gas in the chamber is first tested by melting a Ti getter. If the Ti getter does not whiten, the arc is approached to the pieces of metal, which are instantly melted. After melting, the power supply is switched off to ensure a fast quenching and the resulting button is weighed to check that the mass loss is negligible. This process should be carried out several times to ensure homogeneity. However, the compounds we have synthesized (Laves phases) blow up upon approaching the arc once the compound is synthesized. This is likely due to the cooling process producing many strains and cracks in the inner part of the sample. We have sort this inconvenience out by melting the pieces only twice for a longer time.

The synthesis procedure in the case of induction melting is very similar. The main disadvantages are that (i) there is not possibility of checking the air in the chamber and (ii) the mass loss may not be negligible because of the design of the crucible. On the other hand, as an advantage, we have not observed blowing up problems operating with this furnace.

Some of the as-cast samples were wrapped in Ta foil and thermally treated in quartz tubes with argon atmosphere for about 3-7 days at a temperature of 800^{o}C - 850^{o}C in a Carbolite 1400^{o}C-1600^{o}C chamber furnace, model RHF 14/3. After annealing, samples where quenched to room temperature in cool water in order to avoid appearance of secondary phases.

More detailed information about the specific synthesis and annealing procedures of each sample will be given in the corresponding chapters.

The series studied in chapters 4, i.e. $RFe_{11}Ti$, were also prepared following the arc-melting procedure. $RFe_{11}Ti$ samples were alloyed by Dr. L. Bozukov in Sofia University. Melting of pure $RFe_{11}Ti$ compounds was followed by vacuum annealed at 1273 K for one week and hydrogenation by means of an automated experimental setup based on the volumetric method [87]. The detailed experimental set up and operation are reported in Refs.[87, 88]. The arc-melting synthesis and XRD analysis of R_6Fe_{23} compounds, studied in chapter 5, were carried out by Dr. A. S. Markosayan in the Laboratory of Problems of Magnetism at the Moscow State University.

3.2 Basic sample characterization

The quality of the samples has been checked by a number of complementary techniques. This experiments help us to certify the crystallographic and magnetic properties of the newly synthesized alloys.

3.2.1 X-ray powder diffraction (XRD)

X-ray diffraction (XRD) patterns were recorded in order to control phase homogeneity in all the synthesized samples. Structural characterization was performed at room temperature on powdered specimens. Measurements have been performed on a Rigaku RTO 500RC diffractometer with Bragg-Brentano geometry and Cu Kα radiation in the EXAFS National Service of the University of Zaragoza. Data have been collected between $2\Theta = 20^o$ and 80^o with an step scan mode of $\Delta\Theta = 0.03^o$.

Typically, the diffraction patterns were Rietveld refined using the FULLPROF code. [89] Analysis of X-ray patterns gives us information about the

crystallinity and homogeneity of the sample, value of cell parameters and presence of impurities. This is an essential first step in order to correctly interpret the data from other experiments. Indeed, most of the samples were catalogued as "suitable", but some of them were not considered good enough and were discarded. Details of the specific crystal structure and existence of secondary phases on each prepared sample will be given in the following chapters.

3.2.2 Magnetic Characterization: M(T) and M(H)

Basic magnetic characterization, M(H) and M(T), was performed in the commercial superconducting quantum interference device (SQUID) magnetometers (Quantum Design MPMS-5S and MPMS-XL models) in the Magnetic Measurements Service of the University of Zaragoza. A number of different magnetic measurements can be performed such us dc magnetization and ac magnetic susceptibility in a temperature range of 1.8 - 350 K. Continuous magnetic fields up to 50 kOe can be generated by a superconducting magnet and ac measurements can be performed on a frequency range from 0.01 Hz to 1 KHz. Magnetization measurements as a function of temperature and applied magnetic field were performed systematically on all the samples that were not rejected after XRD analysis.

Occasionally, the magnetic field operating range of the SQUID magnetometer was not high enough for our purposes. For that reason, some additional magnetic measurements were carried out using a commercial PPMS (Physical Property Measurement System) magnetometer (Quantum Design model) also in the Magnetic Measurements Service of the University of Zaragoza. The PPMS magnetometer is a multipurpose equipment designed to perform several kinds of measurements such us heat capacity, resistivity, etc. It allows to perform magnetization measurements under continuous magnetic fields up to 90 kOe. In the same way, some of the studied samples have a very high order temperature, T_C, so that this temperature cannot be reached in a SQUID. For these cases, a Faraday balance designed and manufactured in the ICMA (DEI V Laboratory) by Prof. Juan Bartolomé has been used.

These measurements provide basic magnetic information, such as order temperature, spontaneous magnetization and magnetization of saturation. In some cases, separated magnetic information about each element sublattice in the compound can be obtained by application of a simple two-sublattices method. In addition, they constitute an alternative method to check the correct crystallization of the sample (an abrupt decreases at T_c indicates an homogeneous sample) and to identify impurity phases (a magnetic impurity will give rise to an additional sudden drop of the M (T) signal at the corresponding T_c).

3.3 Mössbauer spectroscopy

Mössbauer experiments were performed in the transmission mode, as schematically shown in Fig. 3.2. Gamma rays are emitted by a radioactive source containing a Mössbauer isotope in a excited state. γ rays go over the specimen under study, the absorber, which has got the same isotope but in its fundamental state. Beam intensity after crossing sample is measured in a detector. The analysis of the recorded spectra will provide information about the magnetic moment of the absorbing atoms. Therefore, this technique constitutes an atom-selective magnetometry. In addition, the site selectivity of Mössbauer spectroscopy along with the simplicity and availability of the experimental setup (compared to synchrotron and neutron facilities) make this technique a valuable tool into the study of R-Fe intermetallic compounds.

3.3.1 Experimental setup

Room temperature measurements were performed by Dr. C. Piquer in the Mössbauer spectrometer of the Instituto de Ciencia de Materiales de Aragón (ICMA, DEI V Laboratory). Low temperature experiments were carried out in the Laboratory of nuclear techniques of the University of the Basque Country by Dr. F. Plazaola and Dr. J. J. S. Garitaonandia. The main components of both equipments are schematized in Figure 3.2 and their task is briefly explained below:

- **Radioactive source.** In the case of ^{57}Fe spectroscopy, the usual source is radioactive ^{57}Co, which undergoes a spontaneous electron capture transition and decays to a metastable state of ^{57}Fe. In turn, ^{57}Fe decays to its fundamental state by emitting, among others, a γ ray of 14.4 keV. (The decay scheme was already shown in Figure 1.4). Typically, ^{57}Co isotopes are embedded in a Rh matrix with cubic symmetry (the environment has to be as much symmetric as possible to obtain a single and sharp emission).

- **Waveform generator and transducer**. They move the source with constant amplitude and acceleration so that each oscillation records a complete spectrum. As explained in the previous chapter, the energy levels of a Mössbauer nucleus in a crystal are slightly modified due to interaction with its environment so that energy levels in the absorber will not be exactly the same as in the emitting atom. In order the resonant absorption to take place, the γ-ray energy is varied by moving the source with a linear motor while keeping fixed the position of the

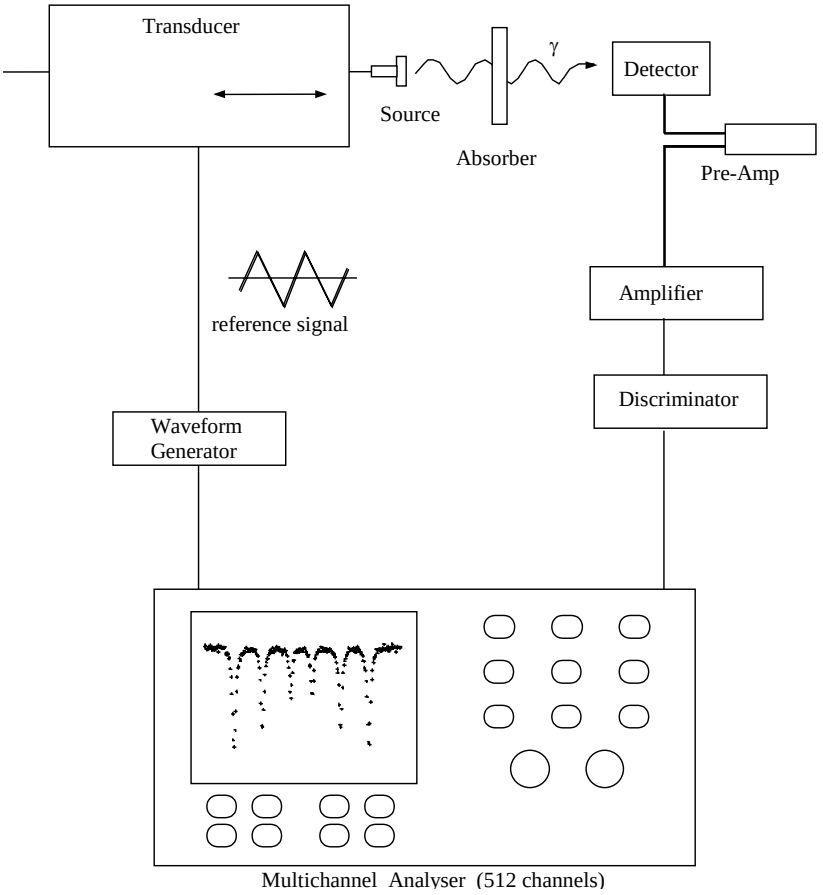

Figure 3.2: Layout of the different elements in a Mössbauer experimental set-up.

absorber. The relative motion between the source and sample results in an energy shift due to the relativistic Doppler effect ($E(v) = E_0(1 + v/c)$). The necessary speed providing the required energy variation is not a very big one, about 1 cm/s. The so-obtained Mössbauer spectrum is a plot with the number of detected gamma rays (relative transmission) *vs.* source velocity, usually measured on mm/s. Negative (positive) velocity corresponds to a source moving away from (coming near to) the absorber. The velocity-energy conversion factor is $C_E = 4.8067 \times 10^{-8}$ eVs/mm.

- **Detector**. A proportional detector of 2 at. of Xe.

- **Preamplifier and amplifier**. The basic functions of preamplifier are to amplify weak signals from the detector and present the correct impedances to the detector and the electronics. Amplifier also shapes the output pulses to a convenient form for further processing.

- **Discriminator**. Its use is for blocking out pulses with a different origin than the 14.4 KeV Mössbauer γ ray.

- **Multichannel analyzer.** This device records the relative transmission as a function of its energy (velocity of the source).

In addition, for the 15-20 K measurements a Gifford-McMahon closed cycle He cryostat from Janis Inc.(model CCS-850) has been used. This cryostat is widely used for measurements down to T = 15 K. One of its main advantages is that no liquid He is required as it works with He gas. Measurements at the temperature range 70 K < T < 250 K were done with a LN_2 cryostat. The coupling system between the elements of the spectrometer and the cooling system has been designed in order to avoid vibrations being transferred to the spectrometer, to obtain a perfect alignment of source and absorber with the mylar window of the cryostat and to optimize the accessibility to the absorber. Mössbauer spectrometer contains a radioactive source, so the equipment is covered with the required Pb shields.

Some equipments also include the possibility of applying an external magnetic field. In the case of the spectra showed on this thesis no magnetic field has been applied.

3.4 XAS and XMCD spectroscopies

3.4.1 Synchrotron radiation facilities

The advent of intense, tuneable, polarized synchrotron radiation sources has stimulated world-wide interest in using X-rays to address electronic and magnetic aspects of condensed matter. Very schematically, synchrotron radiation is obtained as follows: electrons emitted from a thermionic electron gun are first bunched and accelerated in a linear accelerator (LINAC). Then, electrons are injected into a circular accelerator (the booster synchrotron) where they are accelerated by electrical fields in radio frequency (rf) cavities. In the case of SPring8, electron are accelerated to reach an energy level of 8 GeV. The 8-GeV electrons are injected into the storage ring, where they travel round the ring passing through different types of magnets (bending magnets, wigglers, undulators). In these magnets, they are deflected from their straight path by several degrees, which causes them to emit synchrotron radiation, which will be used in the beamlines to perform different kinds of experiments.

Synchrotron radiation [90] is superior to conventional radiation sources like X-ray tubes, with respect to several properties. Among them:

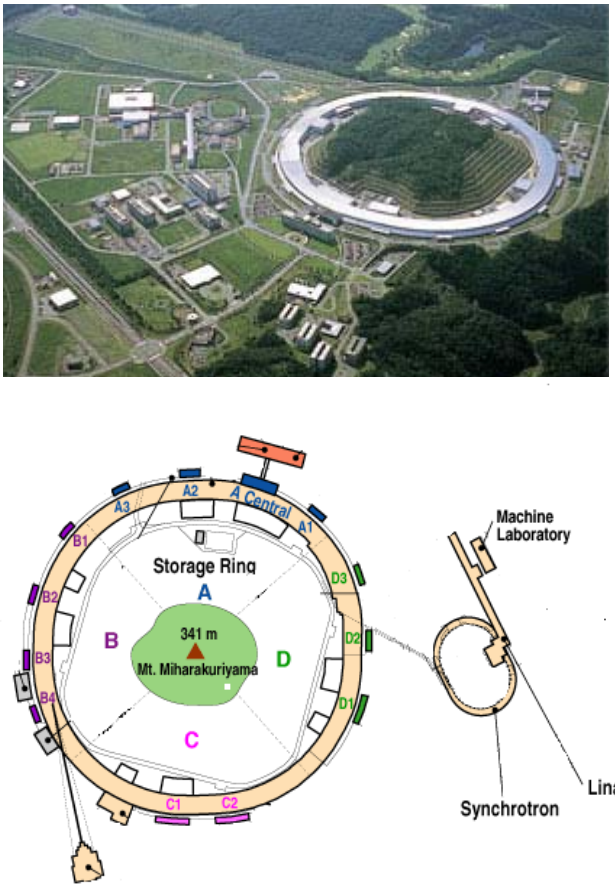

Figure 3.3: Photography of Spring-8 and schematic layout of the campus showing the linac, the booster synchrotron and the storage ring.

- **Its high intensity**. This is of tremendous importance for the experimentalist. To this respect it is important to note that XMCD is about 1000 times smaller than the XAS signal so that a very intensive source of radiation is necessary in order to get an acceptable signal to noise ratio.

- **It is a continuously tuneable radiation source**. The emitted radiation has a high intensity which is available over a broad region of the spectrum from the ultraviolet up to hard X-rays. A monochromatic source can be achieved with the aid of monochromators, which are adjusted to the required wavelength; and can be varied throughout the course of the experiments as needed.

- **Synchrotron radiation is highly polarized**. In the orbital plane the electric field vector of the emitted radiation is in the direction of the instantaneous acceleration. Thus radiation from bending magnets

is linearly polarized in the plane of the orbit. Out of the orbit plane the polarization becomes elliptical and eventually circular, with opposite helicity above and below the plane. However, to get some circularly polarized intensity, the observer has to move out of the orbital plane at the price of a weak flux. This disadvantage can be overcome by using special insertion devices such as asymmetric wigglers or helical undulators, which provide either high intensity circularly polarized radiation in the orbital plane or a extremely intense linearly polarized radiation that becomes circularly polarized by using phase retarders. In this latter case, despite the flux lost at the phase retarder, the intensity impinging on the sample is still very high.

3.4.2 Experimental Station: BL39XU, SPring-8

The whole XAS and XMCD spectra presented in this thesis were performed at the BL39XU beamline of the SPring-8 Facility. [91, 92] BL39XU is an undulator beamline that is dedicated to hard X-ray spectroscopy and diffractometry requiring control of the X-ray polarization state. One of the major applications of this beamline is X-ray magnetic circular dichroism (XMCD) spectroscopy in 3d transition metals, rare-earth elements, and 5d metals. An schematic illustration of the beamline set up is displayed in Figure 3.4.

Optics hutch

Typically, the optics setup required to obtain a focused, monochromatic and circularly polarized beam in a synchrotron station is very complex and in this thesis only the main components will be described.

The light source is an **in-vacuum undulator** of the SPring8 standard type. It provides extremely high brilliance X-rays linearly polarized in the horizontal plane. The fundamental, third and fifth harmonics cover the photon energy range between 5 and 70 keV. The undulator gap is changed at each energy point so that one can obtain a very smooth I_0 spectrum as if using a "white source". BL39XU is also equipped with a **rotated-inclined double-crystal monochromator**. The monochromator angle tuning is combined with undulator gap tuning to maximize the photon flux onto a sample and to keep it almost constant. The combination of fundamental/third harmonics of undulator radiation with the Si (111) reflection of the monochromator enables an energy range from 5 to 37 keV.

Once monochromatic linear polarized radiation is obtained, the right/left circular tunability of X-ray polarization states is available by using a **diamond**

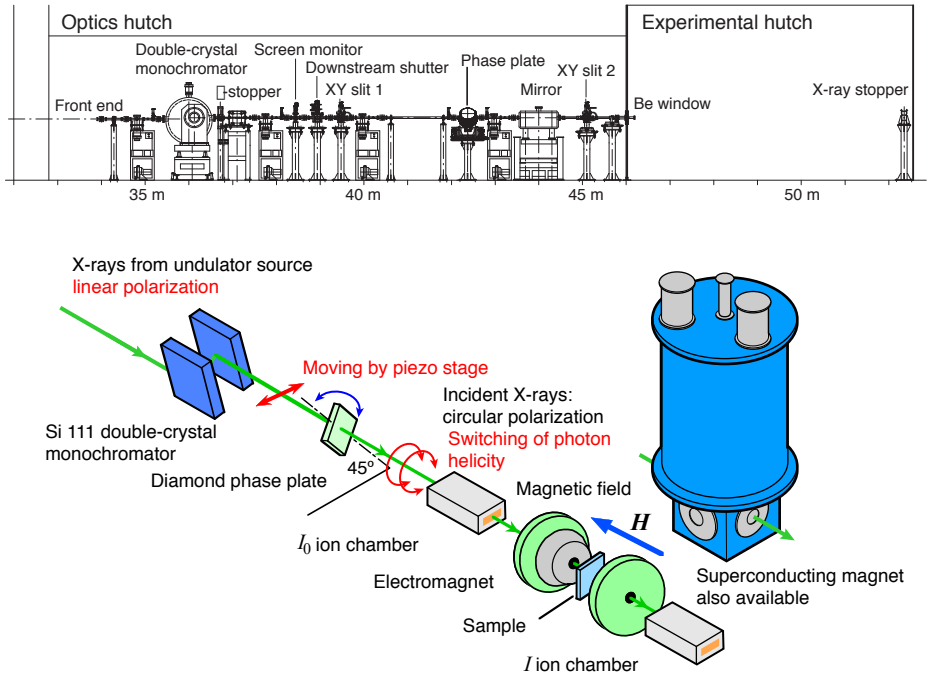

Figure 3.4: (top) Layout of beamline BL39XU. (bottom) Layout of the XMCD spectrometer.

X-ray phase retarder (XPR) that functions as a quarter wave plate.[93] The XPR, which is used in the off-Bragg transmission geometry, exploits the birefringence of crystals for σ and π electric field components (where σ and π represent perpendicular and parallel to the scattering plane, respectively) for geometries on or close to diffraction conditions. This birefringence leads to a phase shift between σ and π components of the transmitted X-rays. For a polarization transformation from linear to circular, the phase plate is arranged to satisfy the following two conditions: both σ and π electric field components must have an equal amplitude and a phase shift of $(n+1/2)\pi$ rad must be produced. The former condition is satisfy by tilting the diffraction lattice plane by 45^o with respect to the polarization plane of the incident beam, and the latter by tuning the offset angle from the diffraction condition. thicknesses (0.34, 0.45, 0.73, and 2.7 mm) are available to optimize both polarization purity and X-ray intensity after the phase plate at the X-ray energy of interest. They are used either in the (220) Laue or (111) Bragg transmission geometry (see Table 3.1).

After the XPR, a **horizontal-focusing mirror** is placed. It also serves

Thickness (mm)	Orientation	Geometry	Energy range (keV)	Transmittance (%)
0.34	(111)	111 Bragg	5 - 5.8	3 - 7
		220 Laue	5.8 - 7.5	7 - 41
0.45	(111)	220 Laue	6 - 9	5 - 53
0.73	(111)	220 Laue	8 - 12	22 - 65
2.7	(001)	220 Laue	11 - 16	13 - 47

Table 3.1: X-ray energy available with the four diamond crystals of the X-ray phase plate.

for the reduction of the amount of higher harmonics to less than 10^{-4}.

Experimental hutch

The experimental station is equipped with two **ionization chambers** to measure the intensity of the beam before and after the sample. Three different lengths, 4, 14 and 30 cm, of the electrodes are available and suitable absorbing gas (N_2 or Ar) is selectable depending on X-ray energy range.

In addition, there are two available sample environments: i) an **0-2 T electromagnet** with a 20-300 K closed-cycle helium refrigerator and ii) a 10 T **superconducting magnet (SCM)** system for further high-field and low-temperature environments. The SCM is designed to perform XMCD experiments under a magnetic field up to 10 T. Moreover, the assembly of a variable temperature insert (VTI) allows measurements between 1.7 and 300 K. A maximum of 6 samples can be placed in the sample holder which, in turn, is placed inside a 25 mm-diameter cylinder in the VTI. The split-type superconducting coils design includes also an horizontal magnet clear bore so that the sample can be placed in the middle of the magnet and the X-ray beam, moving parallel to the field in the horizontal direction, is incident on a cold, magnetized sample. The SCM has X-ray transparent Be windows at both front and back (on the field axis) and on both sides (perpendicular to the field). The opening size of the front and back windows is 10 mm diameter, while the sides are 20 mm diameter. This design of the coils and the windows allows XMCD measurements in either transmission or fluorescence mode as well as non-resonant magnetic diffraction experiments with a 90^o scattering angle. The SCM is equipped with a liquid helium recondensing cooler which enables continuous operation of the SCM for more than 7 days with no additional coolant needed. Figure 3.5 shows a schematic drawing of the SCM system.

The electromagnet system was used to perform the first measurements

on the R_6Fe_{23} compounds. Further development of the experimental hutch allowed us to carry out the rest of the experiments under lower temperatures and higher applied magnetic fields by using the 10 T superconducting magnet. We have observed that the signals recorded using the former experimental equipment are slightly noisier than those measured with the SCM.

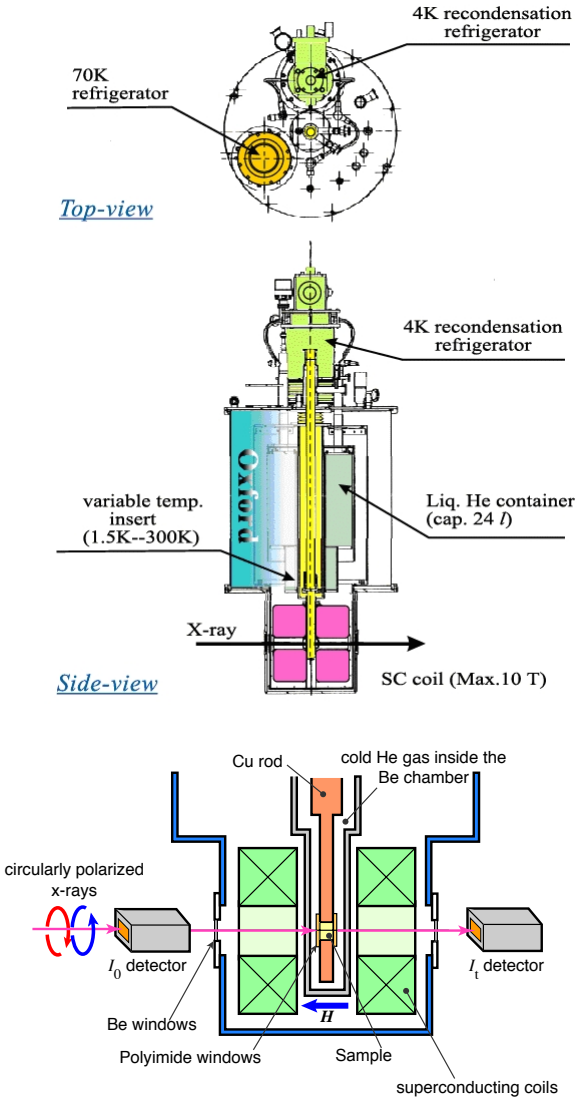

Figure 3.5: Drawing of the 10 T superconducting magnet.

Additionally, the installation of a diamond-anvil-cell (DAC) allows performance of XMCD experiments under pressure up to 20 GPa. The DAC part is designed to be insertable between the coils of the superconducting magnet,

allowing XMCD experiments under multiple extreme conditions of high magnetic field, high pressure and low temperature. The design is based on that reported by Ishimatsu et al. [94]. This type of DAC is equipped with thin diamond crystals so as to extend the usable X-ray energy to low energy region (< 7 KeV).

3.4.3 XAS and XMCD Experimental procedure

For the measurements, homogeneous layers of the powdered samples are made by spreading of fine powders of the material on an adhesive tape. Thickness and homogeneity of the samples are optimized to obtain the best signal-to-noise ratio, giving a total absorption edge jump ~ 1. Once the samples are inside the SCM, the temperature and applied magnetic field conditions are settled. To this respect, it is important to indicate that samples must be inserted or removed at T = 300K and H = 0 T.

Our spectra were all recorded in the **transmission geometry**. An schematic layout of this geometry is included in Figure 3.6. In the transmission mode, the intensity of the X-ray beam before and after the sample is directly measured using radiation detectors (ionization chambers in our case) and the absorption coefficient, i.e. the XAS espectrum, can be directly obtained from application of the Lambert law (eq. (1.8)).

As we have already explained, XMCD is the difference of the X-ray absorption coefficient $\mu_c = (\mu^- - \mu^+)$ for antiparallel, μ^-, and parallel, μ^+, orientation of the incident photon helicity and sample magnetization. Therefore, XMCD experiments can be performed in two equivalent ways: either by changing the helicity while keeping constant the applied magnetic field, or alternatively, by changing the direction of the magnetic field while the photon helicity remains invariable.[1]

Typically, the XMCD spectra are obtained following a "static procedure", i.e., after acquisition, normalization and substraction of XAS^- (i.e. μ^-) and XAS^+ (i.e., μ^+) spectra. However, at BL39XU a new recording method, **the helicity-modulation technique (HMT)**, has been developed. [95]. With this method both, unpolarized XAS and XMCD signals, are directly recorded. Moreover, this technique allows extremely high quality XMCD spectra obtained in a shorter acquisition time than if the static method is used. A dichroic signal in the order of 10^{-4} is obtainable with a good signal-to-noise ratio for 10 s-integration time at each energy point. Helicity-modulation technique has been developed by combining fast polarization switching in XPR

[1] In order to record correct XMCD signals, special attention has to be paid to hysteresis effects when magnetic field is reversed.

with a phase-sensitive (lock-in) detection system. Figure 3.6 illustrates the set up and the basic principle of HMT.

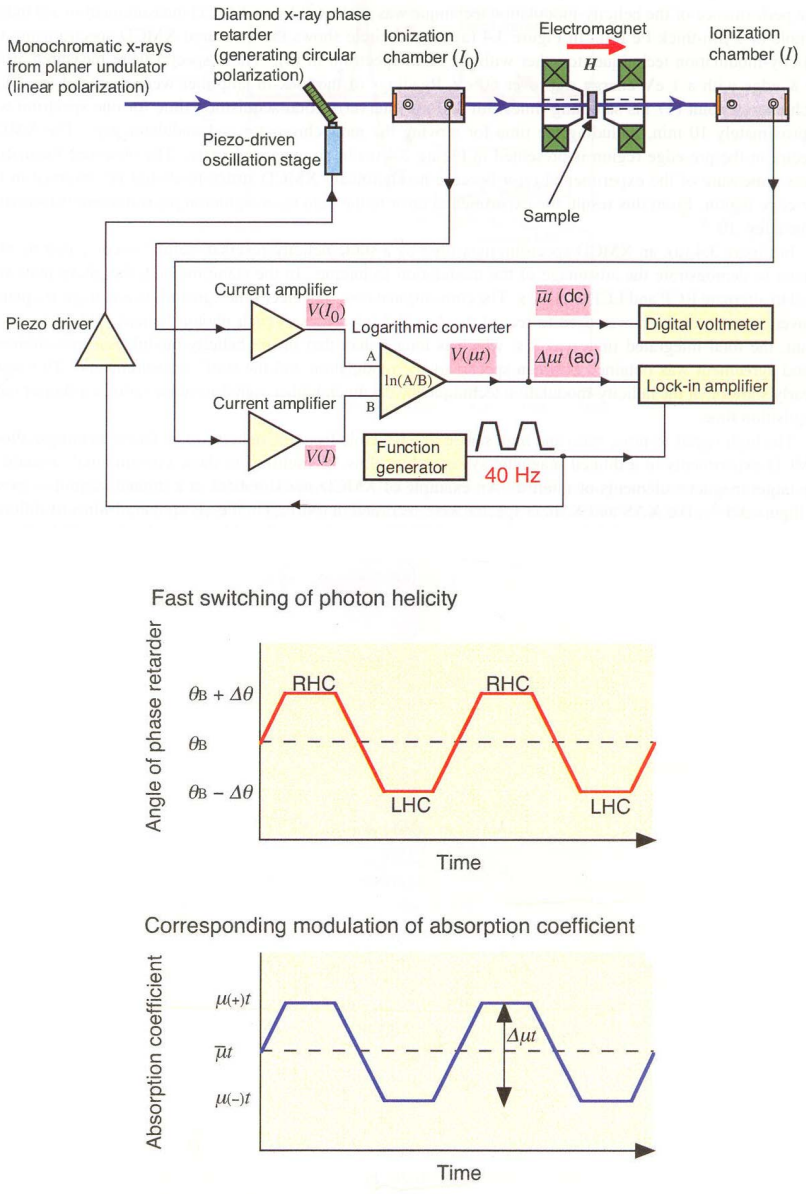

Figure 3.6: a) The setup scheme of XMCD measuremetns in HM technique. b) Principle of the HM technique: angular oscillation of the XPR causes helicity alternation. Consequently, the absorption coefficient will show an oscillation whose amplitude will correspond to the XMCD signal and whose average value will give the unpolarized XAS signal.

The magnetic field reminds fixed through the measurement. The XPR is mounted on a piezo-driven stage, which oscillates the retarder crystal at 40 Hz around the Bragg angle Θ_B with an amplitude $\pm\Delta\Theta$. As a result, an X-ray beam whose helicity alternates from right (RCP) to left circular polarization (LCP) is incident on the sample. Consequently, the absorption coefficient also changes as a function of time with a 40 Hz frequency as illustrated in Figure 3.6. The intensities of the incident and transmitted beam are measured with ionization chambers and converted into voltage signals, $V(I_0)$ and $V(I)$, by current amplifiers. A logarithmic converter gives a voltage signal $V(\mu t)$ which corresponds to the absorption coefficient $\ln(I/I_0)$. The ac component is proportional to XMCD and is directly measured using an amplifier locked to the helicity modulation frequency. The dc component corresponds to the average absorption coefficient and is measured with a digital voltmeter.

Consequently, with this technique the XMCD values are directly recorded at each energy point, thus minimizing possible errors coming from data treatment of the XAS^+ and XAS^- spectra. This XMCD recording procedure has been carried out for both directions of the applied magnetic field, which gives the same signal but with opposite sign. The final XMCD signal is then obtained as $\Delta XMCD/2$. This modus operandi allows to improve the statistics (reduce the noise) and remove any spurious contribution to the signal (usually our signals are affected by an small offset).

3.4.4 Analysis of experimental XAS and XMCD data.

Once the XAS spectra have been experientially recorded, it is necessary to follow a simple normalization procedure before making direct comparisons between spectra. To understand why this normalization is necessary, Fig. 3.7(a) exemplifies an XAS spectrum as obtained from the measurement process. The spectrum is superimposed over a curve (called Victoreen curve) whose origin are all the possible absorptions in the compound corresponding to less energetic edges. Victoreen curve is determined in a empirical way assuming a dependence on energy:

$$\mu_V = A - C/E^3 + D/E^2 \tag{3.1}$$

Usually, considering Victoreen curve as a straight line at each edge is a good approximation. This line is obtained by fitting the values of an energy range at the pre-edge region to a linear function and the extra contribution is removed by simple substraction of this line. The intensity of the post-edge region varies from one sample to other due to the difference of thickness between the samples. To remove this dependence, the spectra are normalized

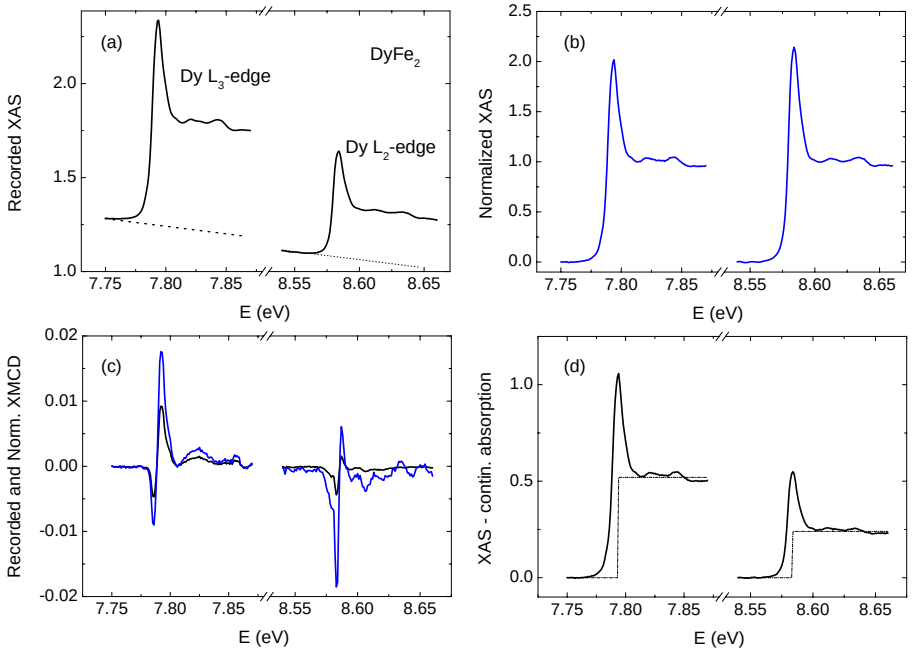

Figure 3.7: (a) recorded XAS signal (b) XAS signal after background substraction and normalization to 1. (c) Comparison recorded XMCD *vs.* Normalized XMCD. (d) XAS signal after background substration. Dotted line corresponds to the step function used to subtract the continuum absorption. No normalization is done in order to preserve direct application of the sum-rules.

to the average absorption coefficient at high energy so that in this energy region the averaged intensity is always one no matter the thickness of the sample (Fig. 3.7(b)).

In order to do a systematic analysis, the same normalization energy ranges should be chosen for all the spectra measured at the same edge (Fe K-edge or R $L_{2,3}$-edges), whenever it is possible. Unfortunately, through the analysis of our signals we have found some cases where different normalization ranges had to be chosen to obtain the optimal normalization for every spectra (for example, the Dy L_3 edge (7790 eV) in $DyCo_2$ is strongly affected by the EXAFS oscillations at the Co K-edge (7709 eV)).

Usually, the origin of the energy scale is chosen at the inflection point of the absorption edge. This energy "re-definition" avoids errors in the energy scale coming from an incorrect calibration of the experimental device or step loss of the motor and allows a direct comparison between, for example, the R L_2-edge and the R L_3-edge spectra of a compound.

The XMCD spectra are obtained as the difference of the absorption coef-

ficient $\mu_c = (\mu^- - \mu^+)$ for antiparallel, μ^-, and parallel, μ^+, orientation of the photon helicity and sample magnetization. If the substraction is made after both XAS spectra (μ^- and μ^+) have been normalized, no extra normalization is required. Within the Modulation Technique Method, however, this difference is performed automatically by the recording system at each energy point. The output we get is the XMCD signal (difference of the absorption coefficient $\mu_c = (\mu^- - \mu^+)$) and the unpolarized absorption spectrum, obtained as the $(\mu^- - \mu^+)/2$ average value also computed at each energy point. In this case, the normalization procedure of the XAS spectrum is the same but the normalized XMCD is obtained via simple division by the XAS normalization factor. This recording method is highly desirable as the profile (relative intensity of the features) of the XMCD signal is not affected by the normalization procedure.(Fig. 3.7 (c))

Finally, a further data treatment is necessary before applying XMCD sumrules to the experimental spectra: since the recorded XAS signals are due to the superposition of the considered absorption line and the continuous absorption, the latter contribution is typically removed by using a step function as shown in Fig. 3.7(d).

Chapter 4

XMCD in the $RFe_{11}Ti$ series and its hydride derivatives.

4.1 Introduction

As mentioned in the general introduction, the interpretation of the XMCD spectra corresponding to the $L_{2,3}$-edges of the rare-earth is still a matter of controversy. This situation prevents from obtaining the magnetic description of the R(5d) states in R-T intermetallics. Within this framework, Chaboy *et al* have proposed in recent works an alternative method to overcome this hindrance. They have explored the feasibility offered by the study of the Fe K-edge XMCD in $R_2Fe_{14}B$ intermetallic compounds to characterize the rare-earth conduction band [84, 85, 86]. Despite the relationship between the Fe K-edge XMCD spectra and the local magnetic moments is not well defined, [73, 74, 81, 82, 83, 75, 76, 77] their results indicate that there is a rare-earth contribution to the Fe K-edge XMCD and that this contribution reflects the magnetic state of the R atoms (see figure 4.1). The finding of the rare-earth contribution to the Fe K-edge spectrum on the $R_2Fe_{14}B$ series gives rise to an alternative approach to characterize the R(5d) states.

In addition, in the light of the observed results, Chaboy *et al* extended the XMCD study on the $R_2Fe_{14}B$ series to the $R_2Fe_{14}BH_x$ hydrides as an attempt of getting a deeper insight into the mechanism which tunes the impact of hydrogen into the magnetism of the system. The case of the R-T compounds with interstitial doping with light elements such as hydrogen or nitrogen is a clear example of the interest of getting the magnetic characterization of the rare-earth 5d states. In such a class of compounds the interstitial doping leads to interesting changes in the magnetic properties respect to their "undoped" compounds. These modifications, namely increase of both magnetization and

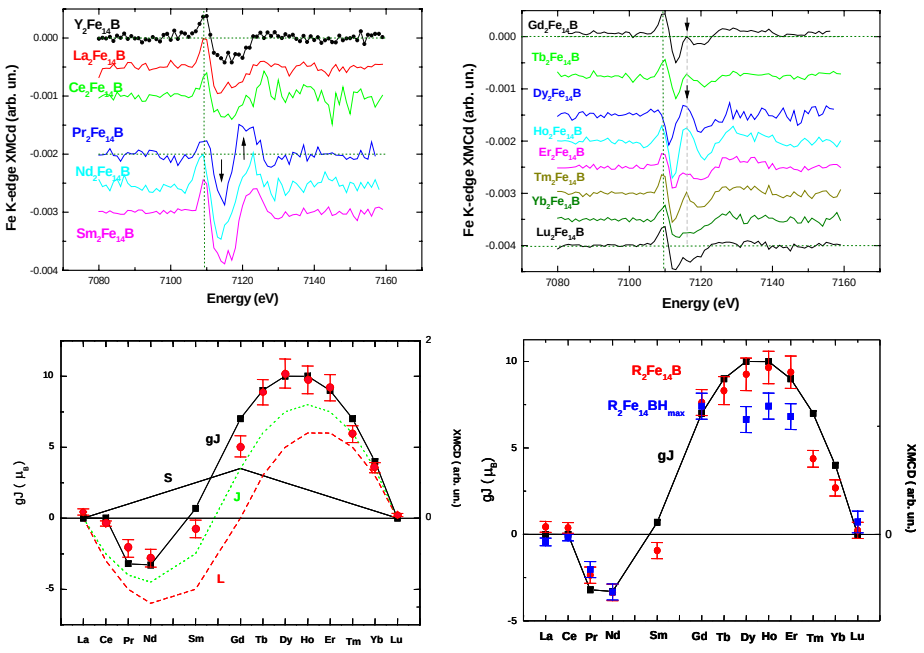

Figure 4.1: Comparison of the normalized Fe K-edge XMCD signal of the $R_2Fe_{14}B$ systems for R =light (top left panel) and heavy (top right panel) rare-earth. The vertical scale corresponds to the $Y_2Fe_{14}B$ (left) and $Gd_2Fe_{14}B$ (right) compounds. All the signals have been plotted by using the same scale and vertically shifted for the sake of clarity. Bottom left panel: comparison between the free-ion rare-earth 4f magnetic moments, gJ, (■) and the integrated Fe K-edge XMCD signal for the $R_2Fe_{14}B$ (●), after subtracting the XMCD signal of the Y-based compound. The values of **S** (solid line), **L** (red dashed line) and **J** (green dotted line) for the ground state of rare-earth ions along the lanthanide series are also shown. Bottom right panel: comparison between the free-ion rare-earth 4f magnetic moments, gJ, (■) and the integrated Fe K-edge XMCD signal for the $R_2Fe_{14}B$ (●) and their hydride derivatives (■), after subtracting the XMCD signal of the Y-based compound. (results from Refs.[84, 85])

T_C, are in connection with the improvement of their technological performance as hard-magnets. As a consequence, the study of the impact of hydriding on the magnetic properties of intermetallics compounds, such us $R_2Fe_{14}B$, R_2T_{17} and $RFe_{11}Ti$, has received special attention in the last two decades. [96, 97, 98, 103, 102, 99, 100, 107, 106, 101, 108, 109, 110, 111, 112, 113, 114, 105, 115, 116, 104] However, notwithstanding the great body of research performed to date, several aspects regarding the relationship between hydrogen absorption and the modification of the magnetic properties of R-Fe compounds have not been clarified yet. As a consequence, a detailed explanation about

the origin of the modifications driven by hydrogen uptake is still missing.

In the hydride R-Fe compounds is commonly considered that the enhancement of the Fe magnetic moments is due to either the lattice expansion strengthening the Fe-Fe exchange [96, 97, 98], or to the electron transfer from hydrogen to the iron sublatttice.[99, 100, 101] The rare-earth moments are often considered less sensitive to the hydrogen uptake. In this way, the μ_{Fe} enhancement is commonly deduced from the analysis of macroscopic magnetization based on the assumption that μ_R does not change after the hydrogen loading. [102, 99] However, this conjecture is not supported by any experimental evidence. On the contrary, the behaviour of the magnetocrystalline anisotropy upon hydrogen uptake poses serious doubts regarding the validity of the naive scheme above. Indeed, a dramatic loss in the magnetocrystalline anisotropy is observed upon hydrogenation.[103, 104] By considering that hydrogen atoms are located in the vicinity of the R atoms and that the magnetocrystalline anisotropy of the systems is dominated by the rare-earth contribution, it seems reasonable to consider that the rare-earth sublattice should also be affected by the absorption process.

To this respect, several works based on neutron diffraction and Mössbauer spectroscopy experiments on $R_2Fe_{14}B$ and $RFe_{11}Ti$ compounds have shown that the magnetic properties of the rare-earth sublattice are affected by hydrogen absorption. The modification of the magnetocrystalline anisotropy and of the hyperfine field at the rare-earth sites suggests the decrease of μ_R upon hydrogen loading.[103, 96] Moreover, X-ray absorption spectroscopy results indicate the modification of the R(5d)-Fe(3d) hybridization upon hydrogen uptake.[105] Therefore, the modification of this R(5d)-M(3d) hybridization upon hydrogenation can be considered to play a major role into determining the change of the electronic and magnetic properties of undoped intermetallics materials.

In the light of these Mössbauer and XAS results, Chaboy *et al.* performed an XMCD study on the $R_2Fe_{14}BH_x$ hydrides. Taking benefit of the recently observed capability of Fe K-edge XMCD to monitor the magnetic state of the rare-earth in the case of $R_2Fe_{14}B$ compounds, they have determined both the influence of hydrogen on the magnetic state of R and the decrease of μ_R after hydrogen loading.[85, 86]

Thus, we stand in from of a problem in which studies based on macroscopic tools, such as magnetization, are strongly limited by the inherent unfeasibility of discriminating between the contributions of the transition metal and the rare-earth sublattices to the total magnetization. Consequently, the impact of the interstitial doping on each magnetic sublattice cannot be separately accounted. By contrast, XMCD can offer an valuable tool to disentangle the

different effect induced by hydrogen on both the transition metal and the rare-earth sublattices and, consequently, of providing a complete understanding of the hydrogenation impact in intermettalic materials.

However, XMCD studies on R-T intermetallics extracting information about the R(5d) magnetism from the transition-metal edges, as proposed by Chaboy *et al.* are limited to the systematic study of the $R_2Fe_{14}B$ series and its $R_2Fe_{14}BH_x$ hydrides. Therefore, it is necessary to extend previous research to different R-Fe intermetallic series to establish if the observed result is just a particularity on the $R_2Fe_{14}B$ compounds or, on the contrary, it constitutes a general characteristic of the Fe K-edge XMCD in R-Fe intermetallic compounds. To this end, we have performed a systematic XMCD investigation at the Fe K edge in the case of $RFe_{11}Ti$ compounds and their hydride derivatives. Our main goal was to verify the results obtained on the $R_2Fe_{14}B$ series (namely, presence of a rare-earth contribution, $XMCD_R$, at the Fe K-edge XMCD and reduction of μ_R upon hydrogenation). If the previous relationship between the iron K-edge XMCD signal and the rare-earth magnetic moment also holds true for this series, it would be possible to determine the influence of hydrogen on the magnetic properties of both Fe and rare-earth sublattices separately.

4.2 Synthesis and structural characterization of the $RFe_{11}Ti$ series

The $RFe_{11}Ti$ compounds have been extensively studied in the last years, specially those in which R is a heavy rare-earth ion. In addition, detailed studies have been performed on both polycrystalline [99, 100, 107, 106, 101, 108] and single-crystal specimens [109, 110, 111, 112, 113] to determine the way in which the hydrogen modifies the magnetic properties of the parent $RFe_{11}Ti$ compounds. The knowledge of their basic magnetic properties turn them into appropriate candidates for investigating the fundamental relationship between Fe K-edge XMCD and rare-earth magnetism in R-M intermetallics as well as the influence of hydrogen on the magnetic properties of both Fe and rare-earth sublattices separately.

The synthesis, thermal treatment and hydrogenation of the $RFe_{11}Ti$ samples used in this study were carried out by Dr. Bozukov in Sofia University. The X-ray diffraction (DRX) patterns have been recorded in the EXAFS National Service of the University of Zaragoza. The XRD analysis shows that all the $RFe_{11}Ti$ samples crystalize in the tetragonal $ThMn_{12}$ structure, having I4/mmm space group. For all the studied samples, the $ThMn_{12}$ structure is retained upon hydrogen absorption in agreement with previous results. The

crystallographic structure of these compounds is represented in Fig. 4.2 (top panel). In the bottom panel, the diffraction pattern of $DyFe_{11}Ti$ is shown as an illustrative example.

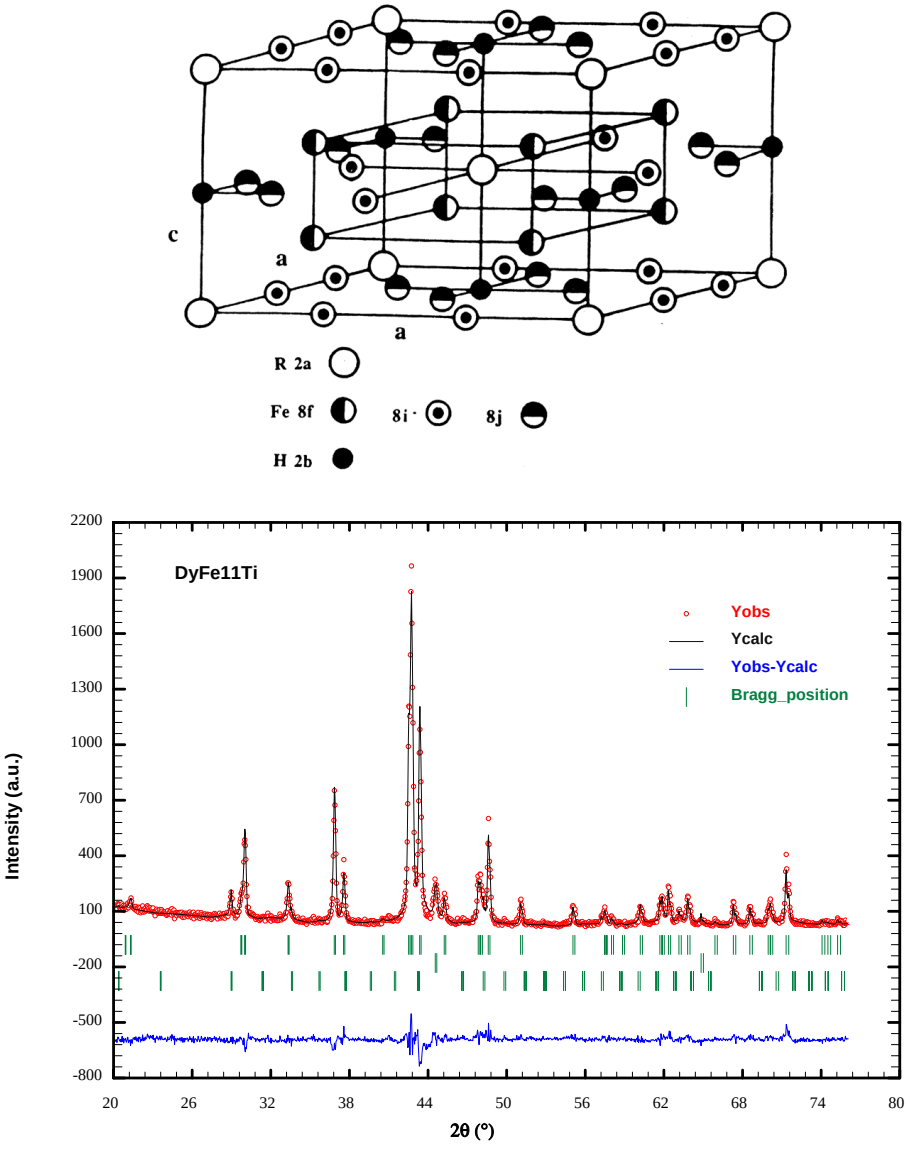

Figure 4.2: Top panel: Schematic representation of the crystal structure. Different symbols are used to identify the ion sites. Bottom panel: Rietveld refinement of the $DyFe_{11}Ti$ X-ray diffraction pattern collected at room temperature. The first row of vertical bars corresponds to the Bragg reflections of the $RFe_{11}Ti$ main phase, while the second and third rows correspond to the α-Fe and R_2O_3 impurities, respectively.

Table 4.1: Structural parameters of the $RFe_{11}Ti(H_x)$ compounds (R = Ce, Tb, Dy, Ho, Er and Lu): a and c: lattice constants, V: unit-cell volume, secondary phases (%) and reliability Bragg factor (defined in Ref. [117]) associated to the main phase.

Compound	a(Å)	c(Å)	V(Å^3)	c/a	α-Fe (%)	R_2O_3 (%)	R_{Bragg}
$CeFe_{11}Ti$	8.529	4.774	347.329	0.5597	1.3	<1	38.9*
$CeFe_{11}TiH_{0.8}$	8.559	4.797	351.396	0.5605	1.2	<1	19.9*
$TbFe_{11}Ti$	8.508	4.785	346.332	0.5624	5.6	1.5	7.7
$TbFe_{11}TiH_{0.6}$	8.522	4.791	347.946	0.5622	5.8	1.9	8.1
$DyFe_{11}Ti$	8.498	4.786	345.629	0.5633	4.0	2.1	9.3
$DyFe_{11}TiH_{0.5}$	8.509	4.789	346.750	0.5628	3.2	1.4	10.0
$HoFe_{11}Ti$	8.484	4.781	344.136	0.5636	6.4	3.0	10.0
$HoFe_{11}TiH_{0.5}$	8.500	4.789	346.001	0.5634	6.4	3.1	8.6
$ErFe_{11}Ti$	8.479	4.783	343.828	0.5641	1.7	3.0	13.2
$ErFe_{11}TiH_{0.65}$	8.493	4.784	345.109	0.5633	1.3	3.5	12.1
$LuFe_{11}Ti$	8.446	4.771	340.322	0.5648	8.6	2.6	12.2

*Pref. orientation

The cell parameters of the $RFe_{11}Ti$ and their hydride derivatives, determined from the XRD patterns, are summarized in Table 4.1. Our results are in agreement with previous published data.[100, 114] As shown in the table, all the $RFe_{11}Ti$ compounds undergo an expansion upon hydrogen absorption. In addition, the c/a ratio of the alloys is slightly reduced, with the exception of $CeFe_{11}Ti$, after the hydrogenation process. The peculiar behavior of $CeFe_{11}Ti$ hydride is linked to the modification of the Ce mixed-valence state previously observed [107]. From the Rietveld refinement also the presence of secondary phases and their content (in %) is obtained. Two kind of impurities have been found in our samples: α-Fe and R_2O_3. The percentage of secondary phases depends on the specific sample and is shown in Table 4.1.

4.3 Macroscopic characterization : Two sub-lattice model

The behavior of the magnetization *vs* applied magnetic field, for the pure $RFe_{11}Ti$ compounds and their hydride derivatives is shown in Fig. 4.3. The maximum magnetization is found for both $CeFe_{11}Ti$ and $LuFe_{11}Ti$ compounds, while it is reduced for compounds in which the rare-earth is magnetic as a consequence of the ferrimagnetic coupling between the iron and the heavy rare-earth sublattices (as explained in section 1.1). The same holds in the case of their hydrogen derivatives.

Both, room temperature magnetization measured in an applied magnetic

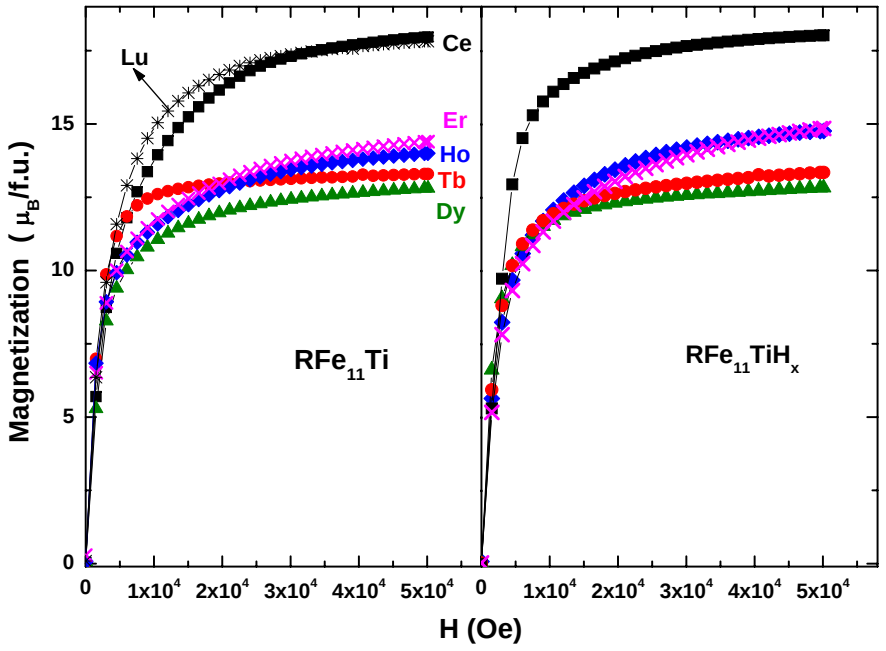

Figure 4.3: Magnetic isotherms, T = 300 K, were measured on loose powders in applied magnetic fields up to H $\leq$ 50 kOe.

field H = 50 kOe, M_{50kOe}, and saturation magnetization (M_s), determined from Honda (M *vs* $1/H$) plots are reported in Table 4.2. Our results are in agreement with previous published data [106].

In table 4.2 the separate values of the magnetic moment of the rare-earth, μ_R, are also included. In order to derive μ_R from $RFe_{11}Ti$ ($RFe_{11}TiH_x$) compounds we have performed several approximations. We have considered that: i) the total magnetization of the $RFe_{11}Ti$ ($RFe_{11}TiH_x$) compounds, M_T, corresponds to the simple $\overrightarrow{M}_{Fe} + \overrightarrow{M}_R$ addition, M_R and M_{Fe} being, respectively, the magnetization of the rare-earth and iron sublattices; and ii) M_{Fe} is assumed to be the magnetization of one $RFe_{11}Ti$ ($RFe_{11}TiH_x$) compound in which R is non magnetic, i.e. Ce or Lu, and that it remains unaltered through the whole $RFe_{11}Ti$ ($RFe_{11}TiH_x$) series. The latter assumption is supported by the fact that both Ce and Lu compounds shows a very similar magnetization, corresponding to an average magnetic moment μ_{Fe} of 1.63 and 1.62 μ_B, respectively.

The application of this simple two sublattice approach to separate the magnetic moment of R and Fe, supplies a way to study the modification of the magnetization of both sublattices induced by hydrogen. As indicated in Ta-

Table 4.2: Magnetic parameters of the $RFe_{11}TiH_x$ compounds (R = Ce, Tb, Dy, Ho, Er and Lu): M_s is the saturation magnetization determined from Honda plots (see details in the text) and M_{50kOe} is the magnetization measured at 50 kOe. $\mu_R|_{Ce}$ and $\mu_R|_{Lu}$ are the rare-earth magnetic moments derived from M_{50kOe} by applying the two-sublattice model and by assuming that the Fe magnetization of the $RFe_{11}TiH_x$ compounds corresponds to the Ce- and Lu-based compounds, respectively (see details in the text).

Compound	M_{50kOe} (μ_B/f.u.)	$\mu_R\|_{Ce}$ (μ_B/f.u.)	$\mu_R\|_{Lu}$ (μ_B/f.u.)	M_s (μ_B/f.u.)
$CeFe_{11}Ti$	17.97	0	0.15	18.24
$CeFe_{11}TiH_{0.8}$	18.02	0		18.51
$TbFe_{11}Ti$	13.29	-4.68	-4.53	13.67
$TbFe_{11}TiH_{0.6}$	13.35	-4.67		14.20
$DyFe_{11}Ti$	12.81	-5.16	-5.01	13.45
$DyFe_{11}TiH_{0.5}$	12.83	-5.19		13.38
$HoFe_{11}Ti$	14.00	-3.97	-3.82	14.86
$HoFe_{11}TiH_{0.5}$	14.76	-3.26		15.56
$ErFe_{11}Ti$	14.40	-3.57	-3.42	15.48
$ErFe_{11}TiH_{0.65}$	14.85	-3.17		16.70
$LuFe_{11}Ti$	17.82	-0.15	0	18.28

ble 4.2, the introduction of hydrogen within the metallic host leads to a slight increase of the magnetization for all the studied compounds. In the case of compounds with non-magnetic rare-earth, the increase of magnetization is usually explained as due to the lattice expansion which strengthens the exchange interaction by reducing the negative exchange interactions between Fe ions. In addition, several authors have argued that the increase of the magnetization, and therefore of μ_{Fe}, may be accounted for by considering the effect of electron transfer from hydrogen to the iron sublattice [99, 100, 101]. This simple scheme becomes involved in the case of the $RFe_{11}Ti$ compounds with R being a magnetic rare-earth, as the magnetic properties of both Fe and R sublattices can be affected by hydrogen. No information regarding the effect of hydrogen on the magnetic properties of both sublattices can be directly inferred from magnetization. However, after applying a two sub-lattice model, the obtained values are consistent with a slight decrease of μ_R upon hydriding. In particular, whereas for Tb and Dy compounds the decrease is near negligible (for the Dy case even a slight $\sim 0.6\%$ increase is obtained), a significant depletion of μ_R is found in the case of Ho ($\sim$ 18 %) and Er ($\sim$ 11 %) systems. To this respect it should be noted that several authors have reported that the magnetization of $ErFe_{11}Ti$ at room temperature decreases upon hydriding [108]. This result has been interpreted as reflecting the increase of the Er sublattice magnetization upon hydriding. However, the proposed increase of μ_{Er} is in contradiction with reported results on single-crystal samples [113] and, on the other hand, it does

not agree with the general trend observed for the whole $RFe_{11}TiH_x$ series. Our magnetization data, obtained on polycrystalline samples, are consistent with the reduction of the rare-earth magnetic moment upon hydriding.

By comparing the hydrogen-induced modification of μ_{Fe}, as derived from magnetization of the Ce-based compounds, and that of μ_R, derived from the two-sublattice model above, it seems that hydrogen mainly influences the rare-earth magnetic sublattice. This result is in contrast with the proposed charge transfer model from hydrogen to the iron bands to account for the modification of the magnetic properties of the $RFe_{11}Ti$ hydrides with respect to those of the pure parents [99, 100, 101].

As discussed in the introduction, the exact knowledge of the influence of hydrogen on the conduction states is fundamental to get a deeper insight into the underlying mechanism driving the change of the magnetic properties of these materials upon hydrogen uptake. However, the results obtained from magnetization are not direct but based on several approximations so they may be called into question. Hence, trying to get this essential information by means of a more direct method, we have monitored the modification of the electronic structure induced by hydrogen uptake by performing a detailed Fe K-edge XAS and XMCD study in both pure and hydride $RFe_{11}Ti$ compounds.

4.4 XMCD results and discussion

The normalized Fe K-edge XMCD signals of $CeFe_{11}Ti$ and $LuFe_{11}Ti$ are shown in Fig. 4.4 and compared to that of $TbFe_{11}Ti$.

For the samples in which the rare-earth is non-magnetic, i.e. Ce and Lu, the shape of the XMCD signal is similar to that of Fe metal[81], as previously observed for other intermetallic compounds [84, 85, 86]. In these cases the spectrum is characterized by a prominent peak at the absorption edge followed by a broad dip. However, in the case of $TbFe_{11}Ti$, the Fe K-edge XMCD profile is markedly different. Indeed, while the first narrow peak is still present and nearly unaltered, there is a second positive peak growing on the corresponding negative dip observed on the spectrum of both Ce and Lu compounds. Besides, the low energy part of the negative dip, ~ 4 eV, is more pronounced for $TbFe_{11}Ti$.

As shown in Fig. 4.5, **the existence of a positive peak (A) at the absorption edge, resembling that of Fe metal, is a common feature of the XMCD spectra of the $RFe_{11}Ti$ compounds. By contrast, the XMCD spectra at higher energies is different for compounds in which R is magnetic or not**. Indeed, the spectra of R-magnetic compounds show

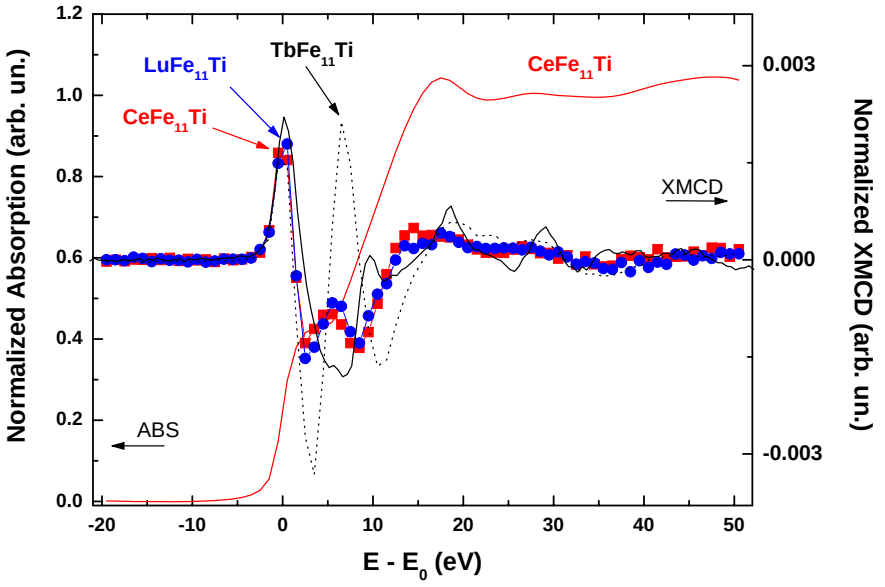

Figure 4.4: Comparison of the Fe K-edge XMCD signal for $CeFe_{11}Ti$ (■), $LuFe_{11}Ti$ (●) and $TbFe_{11}Ti$ (dotted line). The black solid line corresponds to the XMCD spectrum of pure iron. For the sake of completeness, the normalized Fe K-edge absorption spectrum of $CeFe_{11}Ti$ is also shown (red solid line). All the XMCD spectra were recorded at room temperature and under the action of an applied magnetic field of 50 kOe.

an extra peak (B) at $\sim$ 7 eV above the absorption threshold. Moreover, while the intensity of peak A remains practically invariable throughout the $RFe_{11}Ti$ series, peak B is strongly dependent on the specific rare-earth. The same behavior is also found in the case of the hydride derivatives (bottom panel of Fig. 4.5). Indeed, it is worth noting that, for a given R, the comparison between the XMCD signals of pure $RFe_{11}Ti$ and its hydride derivative shows small differences in both shape and amplitude.

Such a kind of modification of the Fe XMCD profile induced by the presence of a magnetic rare-earth neighbor, was already addressed through the study of both the $R_2Fe_{14}B$ compounds and their hydrides derivatives [84, 85]. In those previous works it was suggested that while feature A is exclusively due to Fe, feature B is due to the hybridization of the outermost states of the absorbing Fe with the 5d states of the rare-earth neighbors. **Therefore, by isolating this contribution from the total Fe XMCD signal it would be possible to get some insight on the magnetic state of the rare-earth even when the Fe atoms are probed.** To verify this hypothesis we have compared the intensity of the maxima of features A and B, to the values of the rare-

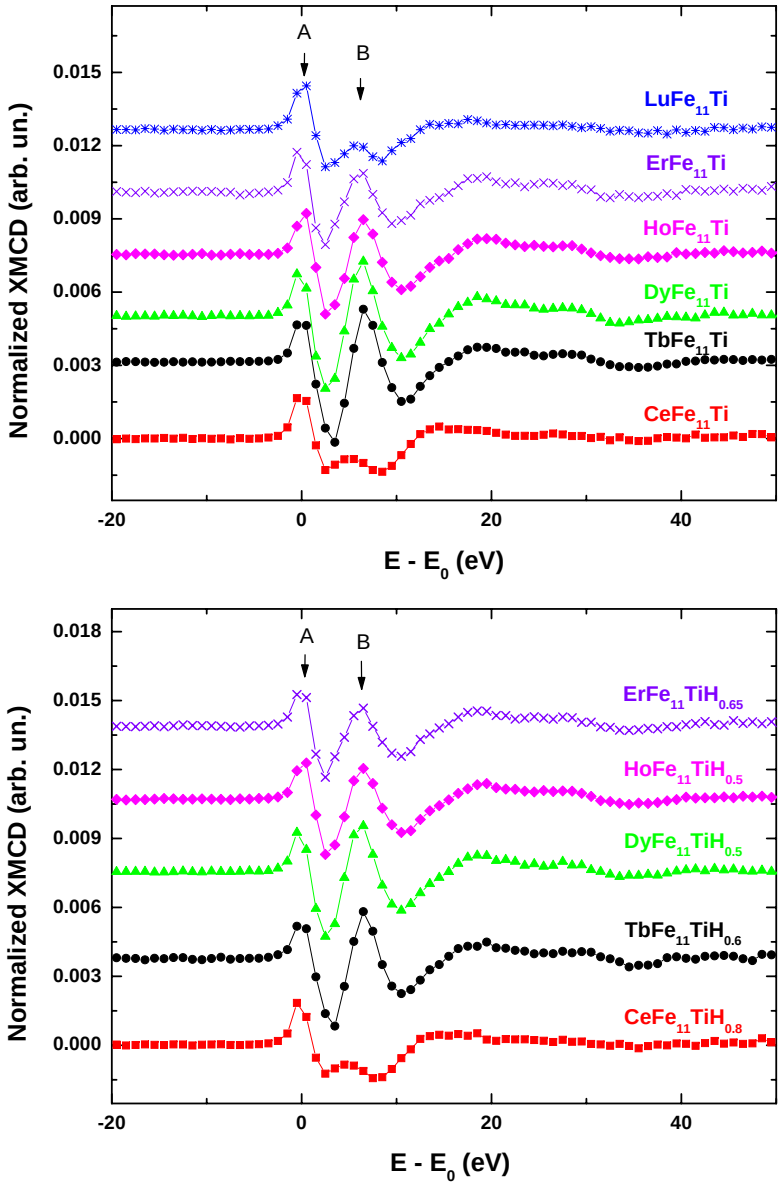

Figure 4.5: Comparison of the Fe K-edge XMCD signal of the $RFe_{11}Ti$ (top panel) and $RFe_{11}TiH_x$(bottom panel) systems. The vertical scale corresponds to the $CeFe_{11}Ti$ (top) and $CeFe_{11}Ti_{0.8}$ (bottom) compounds. All the signals have been plotted by using the same scale and vertically shifted for the sake of clarity.

earth moment, μ_R, obtained from both free-ion values and those derived from the two-sublattice model analysis of the magnetization data. As shown in Fig. 4.6, the intensity of the first peak (A) remains nearly constant through the whole $RFe_{11}Ti$ series, including both $CeFe_{11}Ti$ and $LuFe_{11}Ti$ compounds. This result support on the one hand our previous hypothesis that only Fe is contributing to this XMCD feature. On the other hand, this constant behavior indicates that the magnetization of the Fe sublattice remains, at least in a first approximation, near unaltered through the series, a need for the validity of the two sublattice model to estimate μ_R from magnetization data. The absence of feature B in the case of the non-magnetic rare-earth compounds $CeFe_{11}Ti$ and $LuFe_{11}Ti$ suggests that it is due to the magnetic contribution of the rare-earth. The intensity of feature B shows a maximum for Dy and a pronounced decay for heavier Ho and Er-based compounds. This trend is in agreement with the variation of μ_R obtained from the magnetization analysis, i.e., it is reflecting the magnetic contribution of the rare-earth sublattice.

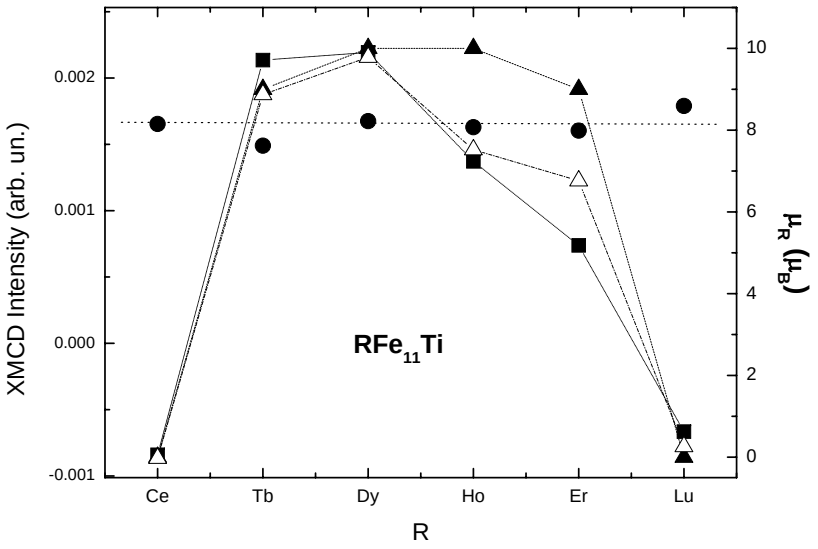

Figure 4.6: Comparison of the intensity of the main spectral features in the XMCD spectra of the $RFe_{11}Ti$ compounds (A (●) and B (■)) and the modulus of the rare-earth magnetic moment obtained from the free-ion values (▲) and from the magnetization data (△). The magnetization data of Table II have been scaled to the free-ion values to be displayed in the same frame. The dotted lines are guides for the eye.

Further confirmation of the above result can be obtained by considering the integral of the XMCD signals. We have applied a similar two-sublattice method as used for the magnetization analysis. We have considered that the Fe K-edge XMCD signal of the $RFe_{11}Ti$ corresponds to the addition of two components:

$XMCD_{RFe_{11}Ti}$ = $XMCD_R$ + $XMCD_{Fe}$, being $XMCD_R$ and $XMCD_{Fe}$ the magnetic contributions of the rare-earth and Fe magnetic sublattices, respectively [86]. Then, we have assumed that the contribution of the Fe sublattice, $XMCD_{Fe}$, corresponds to the XMCD signal of either $CeFe_{11}Ti$ or $LuFe_{11}Ti$, i.e. the compounds in which the rare-earth is non magnetic. Fig. 4.7 reports the results of applying this procedure: the integral of the extracted $XMCD_R$ signal, obtained after subtracting $XMCD_{Fe}$ to the total XMCD signal for each $RFe_{11}Ti$ compound, is compared to the rare-earth magnetic moment obtained from magnetization data. The results shown in this figure correspond to the use of the integral of $XMCD_{CeFe_{11}Ti}$ as $XMCD_{Fe}$. The same result is obtained if the Lu compound is considered.

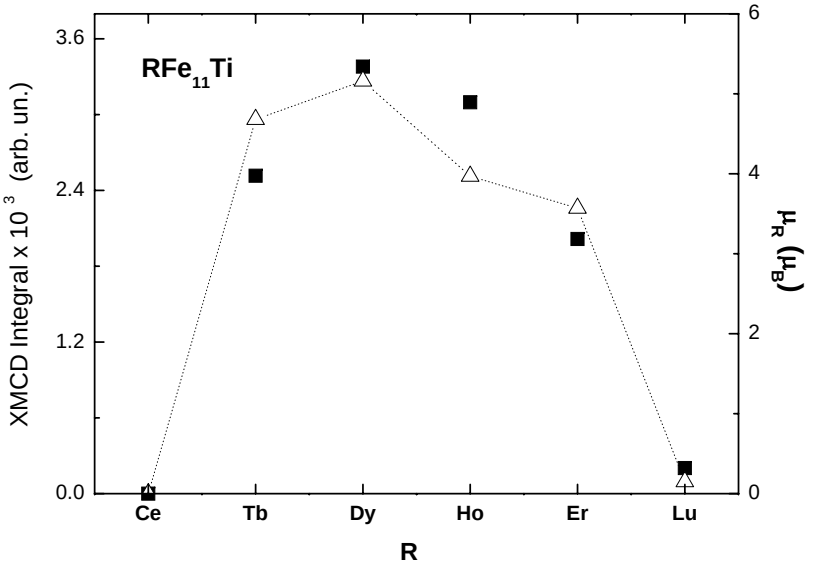

Figure 4.7: Comparison of the integral of the Fe K-edge XMCD spectra of $RFe_{11}Ti$ compound after subtracting the integral of the $CeFe_{11}Ti$ compound(■)) and the modulus of the rare-earth magnetic moment obtained from magnetization data (△).

These results confirm the previous trend found on the $R_2Fe_{14}B$ series: **there is a contribution to the Fe K-edge XMCD spectra of R-Fe intermetallic compounds whose origin is due to the rare-earth magnetic moment even when one is looking at the Fe sites.**

Additional support to our hypothesis can be found in the sum-rule analysis. It is well known that application of sum-rules to the R $L_{2,3}$-edges XMCD spectra gives the wrong signs for the R-Fe magnetic coupling, but what about the coupling scheme derived from this Fe K edge?

According to the K-edge sum-rule proposed by Igarashi and Hirai [73, 74],

the integral of the Fe K-edge XMCD signal is proportional to the orbital magnetic moment of the Fe p-states, $<L_z>|_p$, through the relation:

$$\frac{\int^{E_c}(\mu^-(E)-\mu^+(E))\,dE}{\int^{E_c}\mu(E)\,dE} = -\frac{<L_z>|_p}{n_h} \tag{4.1}$$

where μ is the unpolarized absorption and n_h is the number of 4p holes per absorbing Fe atom. We have applied this expression to both $RFe_{11}Ti$ and $RFe_{11}TiH_x$ series by assuming [26] $\mu = \frac{3}{2}(\mu^- + \mu^+)$, $n_h = 5$ and a cutoff energy $E_c = 20$ eV. The obtained ground-state expectation values of $<L_z>|_p$ per hole are plotted in Fig. 4.8.

We have adopted the same convention for the sign of the circular dichroism as in Ref.[?], i.e., with the quantization axis determined by the direction of the Fe majority spins. Therefore, the orbital angular moment L_p is positive, i.e. parallel to both S_{3d} and L_{3d}. This result is in agreement with theoretical calculations [73] and neutron magnetic scattering reports [118, 119]. In addition, we find that $<L_z>|_p = 0.00043\ \mu_B$ and $0.00045\ \mu_B$ for $CeFe_{11}Ti$ and $LuFe_{11}Ti$ compounds, respectively. This value is in agreement with theoretical calculations reporting an orbital contribution of the Fe 4p states of the same order of magnitude for iron metal [73].

In the case of the $RFe_{11}Ti$ compounds in which R is magnetic, the orbital contribution of the Fe 4p states is twice as much as that of $CeFe_{11}Ti$ or $LuFe_{11}Ti$. This result confirms the influence of the rare-earth magnetism on the XMCD signal at the Fe K-edge. The orbital moment of the 4p states is thought to be mainly induced by that of the 3d states through the p-d hybridization [73, 74]. Because of the existing Fe(3d)-R(5d) hybridization it seems reasonable to think that the rare-earth contribution to the XMCD is related to the 5d states.

Once the existence of an extra contribution of R origin, $XMCD_R$, has been verified also for the $RFe_{11}Ti$ series, we will attempt to take benefit of this capability of discerning between R and Fe contributions offered by the XMCD technique to monitor the impact of hydrogen on both Fe and rare-earth magnetic sublattices separately. For each rare-earth element, the comparison of the XMCD spectrum of the pure $RFe_{11}Ti$ compound and that of its hydride derivative shows small differences in both shape and amplitude (see Fig. 4.5). This result is in agreement with the slight modification of the magnetization found upon hydriding.

More precise information can be inferred if we compare the integrated values of peaks A and B between $RFe_{11}Ti$ and the corresponding hydride derivative. The modification of the area of the first peak A can be used as a direct

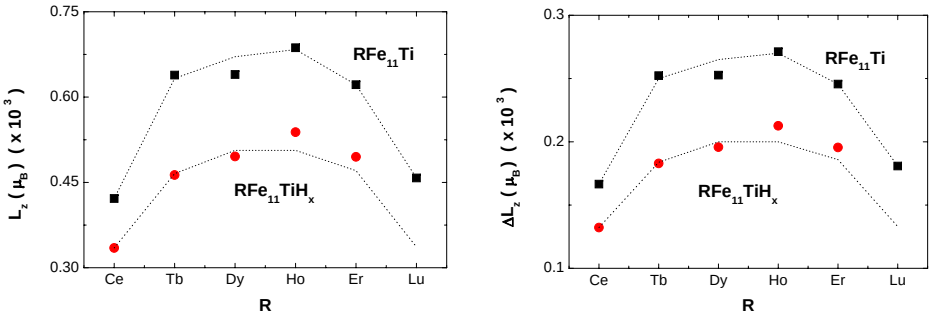

Figure 4.8: Left: Values of $<L_z>$ for the Fe p-states obtained after applying the sum rule to the Fe K-edge XMCD of both the $RFe_{11}Ti$ compounds (■) and their hydide derivatives (●). The dotted lines are guides for the eyes. Right: $<L_z>$ after substracting the values found for the compounds in which the rare-earth is not magnetic. The dotted lines are guides for the eyes and have been scaled to the gJ values of the rare-earth 4f moment.

measure of the influence of H on magnetization the Fe sublattice. The influence of hydrogen on the R sublattice (in the case of compounds with magnetic R) can be obtained by comparing the area of peak B after subtracting the Fe contribution, i.e., after subtracting the XMCD signal of $CeFe_{11}Ti$ in the case of $RFe_{11}Ti$ compounds and $CeFe_{11}TiH_{0.8}$ for their hydrides. The comparison of the integrated signals of both peak A (with no substraction) and peak B (calculated after substraction) for $RFe_{11}Ti$ and $RFe_{11}TiH_x$ are shown in Fig. 4.9. In all the cases, the integrals have been performed from -5 to 10 eV (-5 to 2.5 eV for A peak and from 2.5 to 10 eV for peak B).

The magnitude of the effect induced by hydrogen is different for both the A and B features, i.e., for the Fe and R contributions to the XMCD signal. As shown in Fig. 4.9, the area of the first peak A undergoes a slight, $\sim$ 3% - 6%, modification by hydrogen absorption, while differences in the peak B area between pure and hydride compounds are more significant (10% - 15%). According to our hypothesis, peak A is exclusively due to iron while the isolated feature B arises from the contribution of the magnetic rare-earth. Within this framework, the results reported in Fig. 4.9 can be interpreted as the influence of hydrogen on the rare-earth magnetic contribution to the XMCD being larger than on Fe. These results suggest that hydrogen exerts larger influence on the R magnetic sublattice than in the Fe one, in agreement with the observed modification of the magnetic anisotropy [113]. Indeed, as discussed by Nikitin *et al.* [113], the modification of the magnetic anisotropy constant upon hydrogenation cannot be accounted in terms of the increase in the atomic volume. On the contrary, this effect seems to be mainly due to the change in the crystal field at the R site upon hydrogen uptake. The analysis of the rare-earth

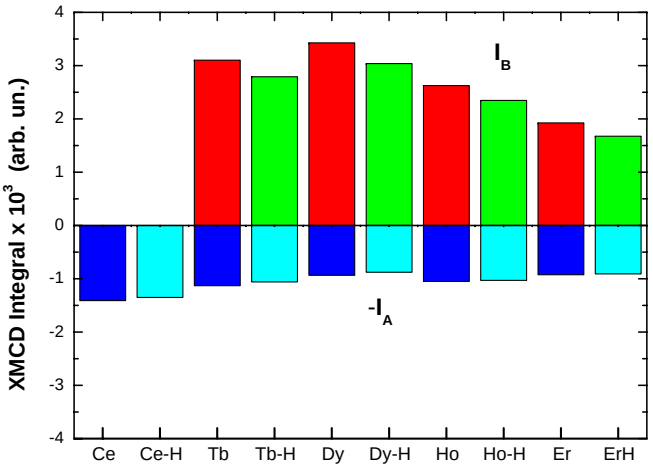

Figure 4.9: Integral of the A (I_A) and B (I_B) features on Fe K-edge XMCD spectra of $RFe_{11}Ti$ compounds and their hydride derivatives. In the case of B feature, the values correspond to the integral after substracting respectively the $CeFe_{11}Ti$ and $CeFe_{11}TiH_{0.8}$ XMCD signals. Pure compounds: blue (I_A) and red (I_B) bars; hydrides: cyan(I_A) and green (I_B) bars. The A integrals are multiply by -1 for the sake of clarity.

contribution to the Fe K-edge XMCD supports the above picture.

The influence of hydrogen absorption on the R contribution to the XMCD signal can be also inferred from Fig. 4.8 (right panel), where the values of $<L_z>|_p$ for $RFe_{11}Ti$ and their hydride derivatives are compared after substracting the values obtained for $CeFe_{11}Ti$ and $CeFe_{11}TiH_{0.8}$, respectively. Also in this case, the result of the comparison agrees with the proposed reduction of the rare-earth magnetic moment upon hydrogen absorption.

XAS: electronic modification

For the sake of completeness, we have tried to get additional information on the modification of the electronic structure induced by hydrogen from XAS spectra. Indeed, the study of the near-edge region of the XAS spectrum offers a unique opportunity to infer the electronic perturbation induced by hydrogen as it is directly linked to the dipolar allowed angular-momentum density of states projected on the absorbing atom.

By contrast to previous studies on the $R_2Fe_{14}BH_x$ series [120], no significant variation of the Fe K-edge XAS profile is found between the pure $RFe_{11}Ti$ compounds and their hydride derivatives. This can be seen in Figure 4.10 (left panel) where the comparison between the XAS spectra for $DyFe_{11}Ti$ and

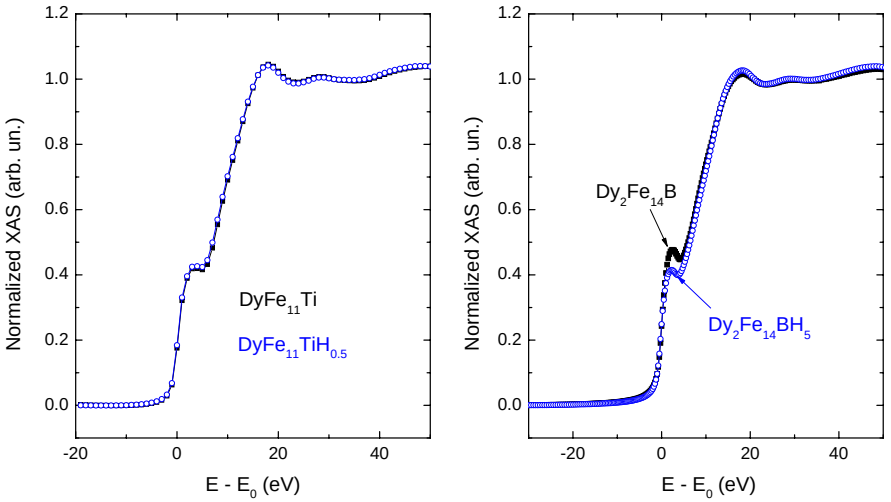

Figure 4.10: Left panel: Normalized absorption spectra measured at the Fe K edge for $DyFe_{11}Ti$ and $DyFe_{11}TiH_{0.5}$. Right panel: Normalized absorption spectra measured at the Fe K edge for $Dy_2Fe_{14}B$ and $Dy_2Fe_{14}BH_5$.

$DyFe_{11}TiH_{0.5}$ has been plotted as an illustrative example. This result indicates that the electronic perturbation at the Fe sites induced by hydrogen absorption is very weak, thus disregarding the main role of electron transfer effects into driving the observed magnetic modifications. The diversity in behavior of the Fe K-edge for both $R_2Fe_{14}BH_x$ and $RFe_{11}TiH_x$ series can be ascribed to the different maximum hydrogen content observed in both series ($\sim$ 5 and 1 H atom/f.u., respectively).

4.5 Conclusions

1. Our results confirm that the Fe K-edge XMCD signal in R-Fe intermetallic compounds is due to the addition of magnetic contributions from both the iron and the rare-earth sublattices.

2. The comparison of the isolated R-sublattice magnetic contribution to the Fe K-edge XMCD and magnetization data indicates that these signals resemble the magnetic state of the rare-earth. That is, this technique allows to monitor the rare-earth moment even when one is looking at the Fe K-edge absorption!!

3. The comparison of the XMCD signals between the pure $RFe_{11}Ti$ compounds and their hydrides shows that hydrogen effects are more impor-

tant for the rare-earth sublattice than for the iron one. Moreover, no evidence of charge transfer from hydrogen to the iron bands has been found. The contribution of the R-sublattice to the XMCD signal has been extracted yielding to a correlation with the rare-earth magnetic moment, that is determined to decrease upon hydrogen absorption, in agreement with magnetization data.

These results show that the previous findings on the $R_2Fe_{14}B$ series are not a particular case but seems to be a general result of the R-Fe intermetallics and constitute the background of a more comprehensive study, that will be presented in chapter 6, aimed to get as much insight as possible on the interpretation of the XMCD spectra at the Fe K edge.

Chapter 5

Thermal XMCD study in the R_6Fe_{23} compounds.

5.1 Introduction

In the preceding chapter we have studied the presence of a R contribution to the Fe K-edge XMCD spectrum of the $RFe_{11}Ti$ compounds to check previous results on the $R_2Fe_{14}B$ compounds. In both $R_2Fe_{14}B$ and $RFe_{11}Ti$ series the experimental results point out the presence of a non-negligible contribution of the rare-earth added to that of Fe at the Fe K-edge XMCD spectrum. Moreover, the analysis performed indicates that this R contribution is related to the magnetic moment of the rare-earth. These studies have been carried out by varying the specific R element in the compound while keeping constant the crystal structure (stoichiometry) and the external parameters such as applied magnetic field and temperature. In this chapter we propose an alternative approach to the study of the XMCD spectra. According to the obtained results, the Fe and R contributions to the Fe K-edge XMCD signal are related to the magnetic moment of Fe and R respectively. Consequently, we expect this spectrum to be also sensitive to the temperature dependence of the magnetic moments, i.e., to μ_{Fe}(T) and μ_R(T). Therefore, the systematic monitoring of the spectra as a function of temperature will help us to determine if there is any spectral feature at the Fe K-edge XMCD spectrum that can be undoubtedly addressed either to the iron or to the rare-earth sublattice.

The best suited compound to verify this hypothesis would be one with a clearly different thermal variation of the magnetization of Fe and R sublattices. With this idea in mind, we have carried out a XMCD study on the Ho_6Fe_{23} compound between room temperature and T = 80 K. The R_6Fe_{23} systems (with R = Dy, Ho, Er and Tm) present a magnetic compensation phenomenon

as the temperature varies from T = 300 K towards lower temperature.[121] The corresponding temperature is called temperature of compensation, T_{comp} and in the particular case of Ho_6Fe_{23} is $\sim$ 192 K. The total magnetization of this compound results from the ferrimagnetic coupling of Fe and Ho magnetic moments. At temperatures near ambient, the magnetization of the Fe sublattice predominates over the Ho one. However, as the temperature decreases the increase of μ_{Ho} is clearly more noticeable (about 6 times, as we will see later on) than that of μ_{Fe} so that the Ho sublattice magnetization becomes dominant for temperatures below $T_{comp} \simeq 192$ K. This is illustrated in Figure 5.1, where the magnetic scheme is displayed for $T < T_{comp}$ and $T > T_{comp}$.

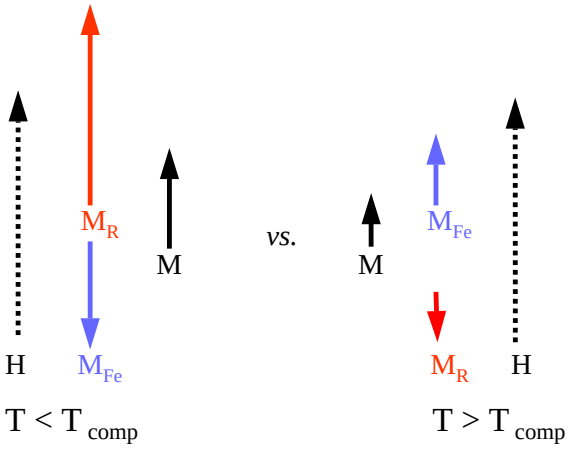

Figure 5.1: Scheme of the magnetization in Ho_6Fe_{23} for temperatures above and below the compensation.

In this chapter, we try to take benefit of this peculiarity of the Ho_6Fe_{23} system to get a deeper insight into the understanding of the XMCD signals in the case of lanthanides-iron intermetallic compounds. Thus, the dichroic spectra at the Fe K-edge have been recorded in Ho_6Fe_{23} and Y_6Fe_{23} compounds for different temperatures from T = 80 K up to 300 K. The great difference between the thermal dependence of both μ_{Fe} and μ_{Ho} throughout the whole temperature range studied is expected to be clearly reflected on these XMCD spectra, allowing the disentanglement of both Fe and Ho contributions, if any, to the XMCD signals.

The study of the Fe K-edge XMCD spectra as a function of temperature has been also extended to the Ho $L_{2,3}$-edges in Ho_6Fe_{23}. As we have already explained, the interpretation of these signals is not clear. Here, we will explore the possibility of having an iron influence at the Ho $L_{2,3}$-edges in analogy with the findings at the Fe K-edge. The corresponding results are presented and

discussed in the last part of this chapter.

Polycrystalline R_6Fe_{23} samples (with R =Y and Ho) were prepared following standard arc-melting procedures. Both phase and structural analysis were performed by using a standard x-ray diffractometer. X-ray analysis showed that all the samples are single phase. As mentioned in section 3.1, both synthesis and DRX analysis of these compounds were performed at the Laboratory of Problems for Magnetism, of the M.V. Lomonossov Moscow State University. This work is not considered as a part of this thesis. For this reason, no detailed further information will be given in this chapter regarding structural details.[122]

5.2 Macroscopic characterization : Two sub-lattice model.

The thermal dependence of the magnetization of both Y_6Fe_{23} and Ho_6Fe_{23} compounds is reported in Fig. 5.2. In the case of Y_6Fe_{23}, the magnetization increases continuously as the temperature decreases from ambient to T = 4.2 K. This increase corresponds to the enhancement of the Fe magnetic moment from room temperature, μ_{Fe}= 1.61 μ_B, to μ_{Fe}= 1.87 μ_B at T = 5 K, as derived (μ_{Fe} = $M_{Y_6Fe_{23}}/23$) from the magnetization *vs* applied magnetic field behavior (see Fig. 5.2.b). On the other hand, the magnetization of Ho_6Fe_{23} decreases when cooling from room temperature down to reach a minimum at $T_{Comp} \sim$ 192 K and then shows a continuous increase to the lowest measured temperature. This behavior reflects the compensation phenomenon due to the different enhancement of both iron and holmium magnetic sublattice magnetization. In a first approach, the total magnetization can be written as: $\overrightarrow{M}_{Ho_6Fe_{23}}(T) = \overrightarrow{M}_{Ho}(T) + \overrightarrow{M}_{Fe}(T) = 6\overrightarrow{\mu}_{Ho}(T) + 23\overrightarrow{\mu}_{Fe}(T)$. Due to the ferrimagnetic coupling between Fe and Ho magnetic sublattices, the modulus of the overall magnetization corresponds to: $|M_{Ho_6Fe_{23}}(T)| = |6\mu_{Ho}(T) - 23\ \mu_{Fe}(T)|$. At room temperature the Fe sublattice dominates the overall magnetization of the system as 6 μ_{Ho} (300 K) < 23 μ_{Fe} (300 K). However, the Ho magnetic moment, μ_{Ho}, increases more than μ_{Fe} does as the temperature decreases. Therefore, the total magnetization decreases until it vanishes at the compensation temperature $T_{Comp} \sim$ 192 K. Below T_{Comp} the magnetization of the Ho sublattice prevails (6 $\mu_{Ho} >$ 23 μ_{Fe}) and the total magnetization of the system continuously increases on further cooling. The existence of this antiparallel coupling can be easily concluded from the M(H) behaviour reported in Fig. 5.2.b, showing the reduction of the Ho_6Fe_{23} magnetization as compared to that of Y_6Fe_{23}.

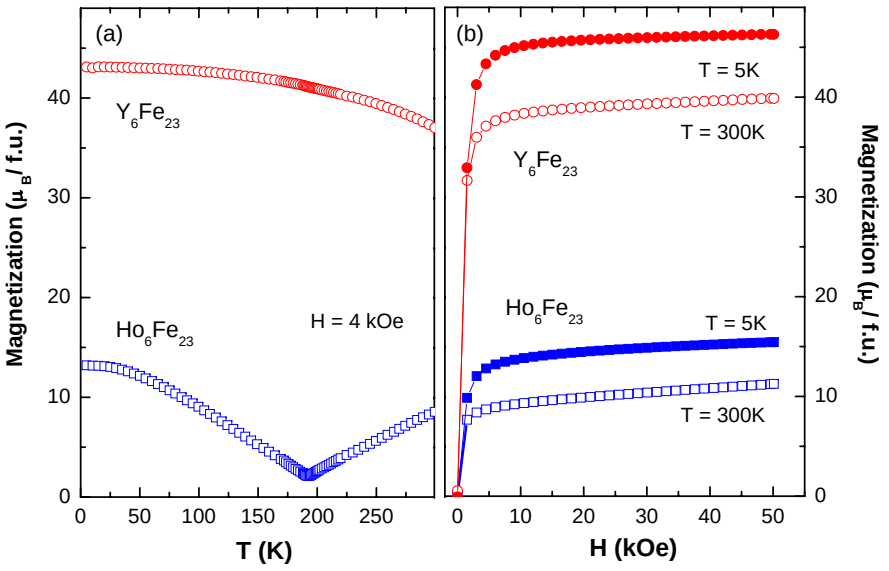

Figure 5.2: Left panel: Thermal dependence of the magnetization of Y_6Fe_{23} and Ho_6Fe_{23} compounds at an applied magnetic field of 4 kOe. Right panel: Behavior of the magnetization *vs* applied magnetic field of Y_6Fe_{23} and Ho_6Fe_{23} at T = 5 K (solid symbols) and at room temperature (open symbols).

The thermal dependence of the magnetization of both Fe and Ho sublattices in Ho_6Fe_{23} can be disentangled, in a first approximation, by applying a two sublattices model. In this way, the total magnetization of Ho_6Fe_{23} is assumed to correspond to the simple addition of the magnetization of each magnetic sublattice: $\overrightarrow{M}_{Ho_6Fe_{23}}$(T)= $\overrightarrow{M}_{Ho}$(T) + $\overrightarrow{M}_{Fe}$(T). In addition, M_{Fe}(T), is assumed to be identical to that of Y_6Fe_{23} through the whole temperature range. This latter assumption is supported by Mössbauer and neutron diffraction data reporting a similar value of the iron magnetic moment in both compounds.[123, 124, 125, 126]. Applying this two sublattices procedure the Ho magnetic moment, μ_{Ho}, can be extracted from both M(H) and M(T) data by subtracting the corresponding values of Y_6Fe_{23} (shown in Fig. 5.2.a and Fig. 5.2.b). It turns out that μ_{Ho} increases from 4.70 μ_B, at room temperature, to 9.26 μ_B at T = 5 K[1]. The relative modification of μ_{Ho} between ambient and low temperature is 97 %, i.e. about six times stronger than that of the Fe sublattice (17 %), which clearly accounts for the change of the dominant magnetic sublattice, Fe *vs* Ho, at both sides of the compensation temperature.

Regarding the temperature region very close to T_{comp}, it has to be noted

[1]The given values for μ_{Ho} and μ_{Fe} have been evaluated at H = 0.4 k Oe in order to reproduce the magnetic conditions of the XMCD experiments. M(H) curves show that this field is high enough to obtain magnetization values close to saturation.

that the total magnetization of Ho_6Fe_{23} is not exactly zero at T_{comp}. This result has been accounted for in terms of both the canting of the magnetic moments and the polycrystalline nature of the specimen. [121, 127]. A more thorough comment about the behavior of μ_{Ho} and μ_{Fe} in this temperature range will be given when discussing the XMCD data.

5.3 XMCD Results and Discussion

The spectra presented in this chapter were recorded by using a 0-2 T electromagnet and a 20-300 K closed-cycle helium refrigerator. The XMCD spectra were recorded under the action of a 0.6 T magnetic field applied at 45^o away from the incident-beam direction and at different fixed temperatures from room temperature down to 80 K. The maximum value of the magnetic field projection on the beam direction is $\sim$ 0.4 T. Although it may seem a low field, we have verified that for such an applied field, the system is near saturation and, consequently, no effects due to an incomplete reversal of the magnetization when reversing the sense of the applied field appear.

XMCD at the Fe K-edge

The comparison of the Fe K-edge XMCD spectra recorded at room temperature in both Y_6Fe_{23} and Ho_6Fe_{23} is shown in Fig. 5.3. The XMCD spectrum of Y_6Fe_{23} closely resembles that of Fe metal [81], in agreement with the spectra of $CeFe_{11}Ti$ and $LuFe_{11}Ti$ in chapter 4. It shows a narrow positive peak at the absorption threshold (A), a negative dip ($\sim$12 eV wide) showing a small superimposed peak (B), and a broad positive resonance at higher energies (C). Despite the magnetic properties of the Fe sublattice in both Y_6Fe_{23} and Ho_6Fe_{23} compounds are though to be similar [121, 123, 124, 125, 126], their XMCD spectra present noticeable differences. Indeed, as shown in Fig. 5.3, the Fe K-edge XMCD spectrum of Ho_6Fe_{23} also exhibits the narrow ($\sim$4 eV wide) peak at the edge (A). However, the former negative dip in Y_6Fe_{23} splits into two intense peaks of negative (B_1) and positive (B_2) sign. This strong modification of the Fe K-edge XMCD spectral shape cannot be easily assigned to differences of the Fe sublattice magnetic properties between Y_6Fe_{23} and Ho_6Fe_{23} compounds [121]. On the contrary, it points out the possibility of an additional contribution to the Fe K-edge XMCD spectrum coming from the Ho magnetic sublattice, in agreement with the conclusions of previous works on the $R_2Fe_{14}B$ and $RFe_{11}Ti$ series. **Consequently, the appearance of peaks B_1 and B_2 in the Fe K-edge XMCD spectrum of Ho_6Fe_{23} can be addressed to the influence of the rare-earth magnetic state on the**

Fe XMCD signal. [84, 85, 86, 128]

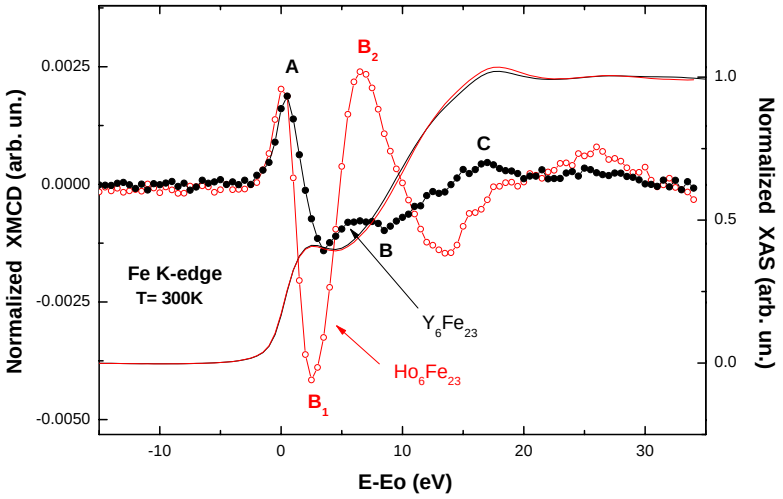

Figure 5.3: Room temperature normalized Fe K-edge XMCD spectra of Y_6Fe_{23} (•) and Ho_6Fe_{23} (○) compounds. For sake of clarity, the normalized Fe K-edge XAS spectrum of Y_6Fe_{23} and Ho_6Fe_{23} are also shown (solid line).

Further confirmation about the origin of the additional spectral features found in the Fe K-edge XMCD spectrum of Ho_6Fe_{23} as compared to that of Y_6Fe_{23} can be obtained from the thermal dependence of the dichroic signals. At room temperature, both Y_6Fe_{23} and Ho_6Fe_{23} XMCD spectra show the same sign (see Figure 5.3), which confirms that the magnetization of the Fe sublattice determines the sign of the overall magnetization in both compounds. In the case of Y_6Fe_{23} both the sign and the spectral profile of the XMCD spectra remain unchanged throughout the whole temperature range (Figure 5.4). By contrast, the sign of the XMCD signal of Ho_6Fe_{23} is reversed between T = 195 K and 190 K as it can be seen in Figure 5.5. As the direction of the total magnetization of the system remains fixed during the XMCD measurements by the action of the external applied field, this result reflects the reversing of the magnetization of each, Fe and Ho, sublattice relative to the total magnetization below T_{Comp}.

In the right panel of Figure 5.5, the same Ho_6Fe_{23} spectra are plotted but in this case the signals corresponding to $T<T_{comp}$ have been reversed in order to see more clearly the thermal evolution of the amplitude of the different peaks. As it can be observed, the differences between the Fe K-edge XMCD signals of both Y_6Fe_{23} and Ho_6Fe_{23} compounds are retained through the whole temperature range. Furthermore, in relation to the thermal modification of the intensity of peaks A, B_1 and B_2 two different behaviours can be distinguished:

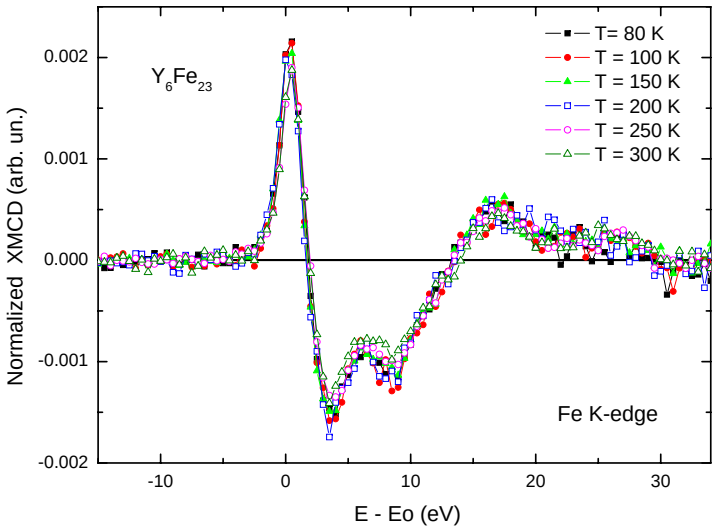

Figure 5.4: Fe K-edge XMCD signals of Y_6Fe_{23} compound recorded at different temperatures.

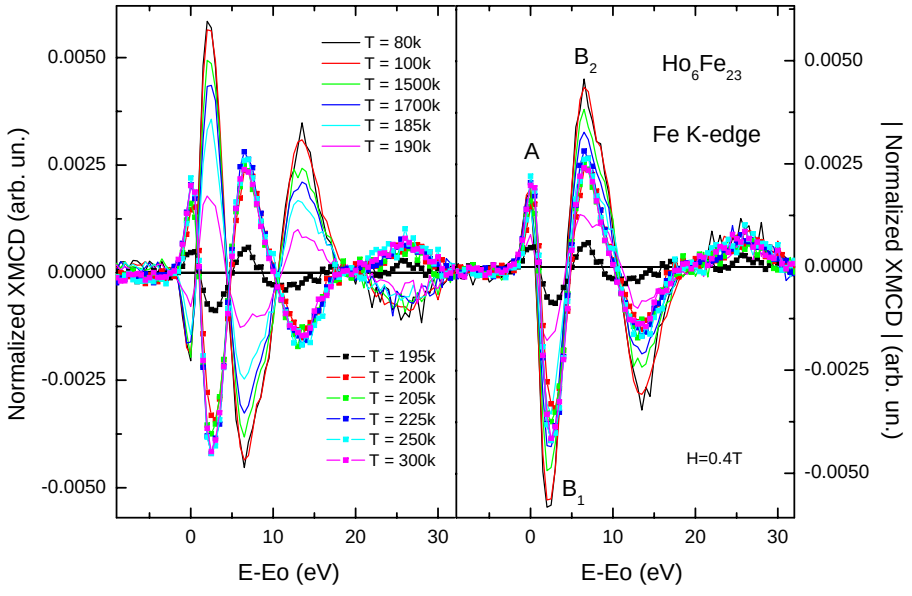

Figure 5.5: Left: Fe K-edge XMCD signals of Ho_6Fe_{23} for different temperatures. Right: The spectra recorded at $T < T_{comp}$ have been reversed for the sake of clarity.

i) Far enough from T_{comp} (i.e. T = 80 K, 100 K, 150 K, 170 K, 225 K,

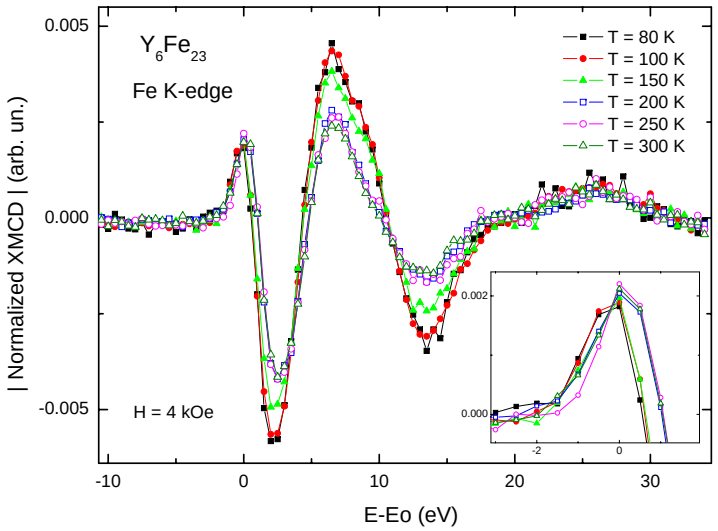

Figure 5.6: Fe K-edge XMCD signals of Ho_6Fe_{23} recorded at temperatures = 80K, 100K, 150K, 170K, 225K, 250K and 300K. Inset: Detail of the spectra in the region from -3 eV to 2 eV.

250 K and 300 K) the intensity of peak A in Ho_6Fe_{23} remains almost the same through the whole temperature range. By contrast, the intensity of peaks B_1 and B_2 varies in a more abrupt way: there is a tendency to increase the intensity as the temperature decreases, in agreement with the different origin (Ho sublattice) of these features.

ii) The spectra recorded at temperature close to T_{Comp} (i.e. T=185 K, 190 K, 195 K, 200 K and 205 K) do not follow the above described evolution, but there is a general diminution of the intensity that affects to all the features.

The behaviour observed in the temperature region close to compensation can be understood as due to the fact that the reversal of the magnetic moments at T_{Comp} is not instantaneous, but is a gradual process due to the polycrystalline nature of the material. As a consequence, the rotation of the magnetization for the different crystallites does not take place simultaneously and within the temperature range close to T_{Comp} (170 K -205 K) the magnetic moments will not be parallel (antiparallel) to the applied magnetic field but canted away from the H_{appl} direction. As XMCD measures the average magnetic moment in the direction of the applied magnetic field, the overall decrease of the spectra around the compensation point simply reflects the gradual rotation process.

Excluding the region around the compensation point, the thermal dependence of the main spectral features can be quantitatively evaluated. The intensity of the positive peak A in both Y and Ho compounds, and the corresponding to peak B_2 in the case of Ho_6Fe_{23} have been compared in Fig. 5.7 to the thermal dependence of both μ_{Fe} and μ_{Ho} obtained from the magnetization data. **The variation of the intensity of peak A, for both Y and Ho compounds, agrees in a first approximation with the thermal dependence of** μ_{Fe}. By contrast, the intensity of peak B_2, that is absent in the case of Y_6Fe_{23}, increases by a 90 % in the same temperature range. Both, the appearance and the thermal dependence of the B_2 spectral feature, cannot be accounted for in terms of the μ_{Fe}(T) dependence. On the contrary, **the variation with temperature of the intensity of peak B follows that of** μ_{Ho}**(T)**. These results demonstrate that the magnetic moment of the neighboring Ho atoms contributes to the K-edge XMCD spectrum of the absorbing Fe atom. Finally, it should be noted that the thermal dependence of the A-peak XMCD intensity of Ho_6Fe_{23} slightly deviates from both that of the Y_6Fe_{23} XMCD and μ_{Fe}(T). This result indicates that, although to a much lesser extent than at higher energies (B_1 and B_2 peaks), the Ho contribution also influences the edge (peak A) region. Indeed, a more careful inspection of peak A in the case of the spectra recorded at Ho_6Fe_{23} (see inset of Figure 5.6) shows two significant trends: i) the intensity slightly decreases when cooling down and ii) also the width of the peak narrows. The effect of the R sublattice on peak A will be detailed discussed in chapter 6, where a comprehensive study will be presented.

For the sake of completeness, the two components have been disentangled by applying a two sublattice model. Thus, the Ho contribution has been worked out as $XMCD_{Diff}$ (T) = $XMCD_{Ho_6Fe_{23}}$(T) - $XMCD_{Y_6Fe_{23}}$(T) for T > T_{comp} and $XMCD_{Diff}$ (T) = - $XMCD_{Ho_6Fe_{23}}$(T) - $XMCD_{Y_6Fe_{23}}$(T) for T<T_{comp}. The thermal dependence of the difference (Ho contribution) signal is shown in Figure 5.8. It can be observed that while the shape of the $XMCD_{Diff}$ signal remains unaltered, its magnitude is enhanced by a factor two as temperature decreases from ambient down to 80 K. This increase resembles that of the Ho magnetic moment in the same temperature range, pointing out that the extracted signal is due to the contribution of the Ho magnetic state to the XMCD even when Fe is probed. It should be also noted that the $XMCD_{Diff}$ signals are not exactly canceled at the threshold, i.e., at the A-peak region.

The existence of a magnetic contribution of the Ho atoms to the Fe K-edge XMCD spectrum of Ho_6Fe_{23} is of particular significance in order to get a correct determination of the orbital moment of the Fe p-states. Indeed, according to Igarashi and Hirai [**?**, **?**], the integral of the Fe K-edge XMCD signal is related to the orbital moment of the Fe p-states, $<L_z>_p$, through the sum-rule relationship:

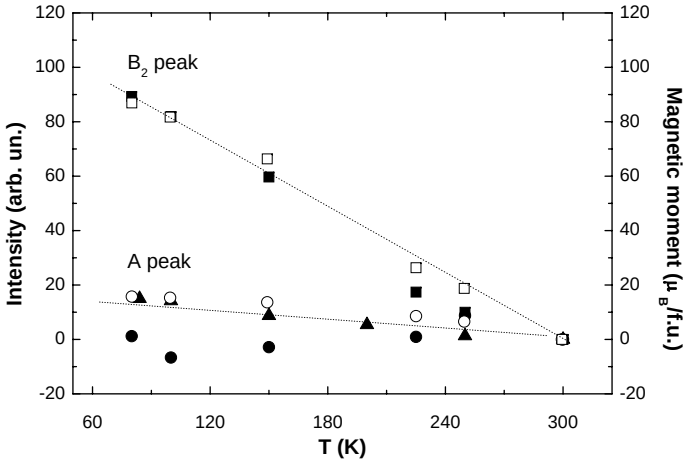

Figure 5.7: Comparison of the modification, with respect to the room-temperature values, of the intensity of the main spectral features in the XMCD spectra of Y_6Fe_{23} (A,(▲)) and Ho_6Fe_{23} (A,(•); B_2, (■)) and that of the magnetic moments of Ho (□) and Fe (○) obtained from magnetization data.

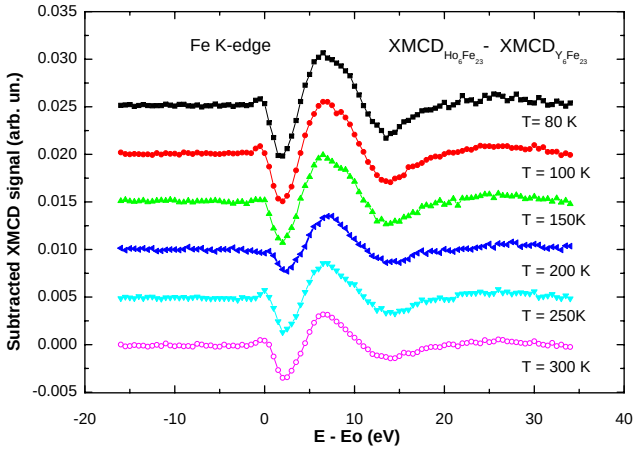

Figure 5.8: Thermal dependence of the difference signal XMCD_{Diff} between the Fe K-edge XMCD spectra of Ho_6Fe_{23} and Y_6Fe_{23} (see text for details). The scale is referred to the room temperature case. For sake of clarity, the XMCD_{Diff} signals obtained at different temperatures have been vertically shifted.

$$\frac{\int^{E_c}(\mu^-(E)-\mu^+(E))\,dE}{\int^{E_c}\mu(E)\,dE} = -\frac{<L_z>|_p}{n_h} \tag{5.1}$$

where n_h is the number of Fe 4p holes states per atom and μ, the unpolarized absorption, is approximated by $\mu = \frac{3}{2}(\mu^- + \mu^+)$. By selecting a cutoff energy E_c = 22.5 eV and $n_h = 5$, the obtained ground-state expectation value of $<L_z>_p$ per hole at room temperature is 0.00040 μ_B for Y_6Fe_{23}. However, in the case of Ho_6Fe_{23} the same integration procedure yields $<L_z>_p$ = 0.00081 at the same temperature as for Y_6Fe_{23}. In addition, while the $<L_z>_p(T)/<L_z>_p(T=300\ K)$ ratio remains nearly constant for Y_6Fe_{23}, it increases by a $\sim 50\%$ for Ho_6Fe_{23}. These results indicate that the orbital contribution of the Fe p-states in Ho_6Fe_{23} is twice as much as that of Y_6Fe_{23}.[2] However, as we have previously said, such a significant modification of the Fe magnetism in both Y_6Fe_{23} and Ho_6Fe_{23} compounds has been never reported. As in the case of the $RFe_{11}Ti$ series, these differences can be related to the contribution of the Ho ions to the Fe K-edge XMCD spectrum (stemming from the hybridization of the Fe states with the Ho(5d) states). Thus, the present data demonstrate the need of extracting the Ho contribution prior to obtain reliable estimates for the orbital moment of the Fe p-states.

To this respect it should be noted that the K-edge ($1s \rightarrow \epsilon p$ transition) XAS absorption of transition metals is strongly influenced by the p-d hybridization. In fact, the characteristic double-step feature at the threshold is due to the overlapping of the p-states with the outer s- and d-symmetry orbitals [129, 19]. In the case of R-M intermetallic materials the 3d states of the transition metal are also strongly hybridized with the 5d states of the lanthanides, in such a way that the R(5d)-M(3d) hybridization plays a major role into determining the magnetic properties of the system. Consequently, Fe K-edge absorption in these materials can be sensitive also to the lanthanide 5d states through the hybridization of the outermost states of the absorbing Fe with the 5d states of the rare-earth neighbors. Within this framework it is instructive to compare the differences of both XAS and XMCD Fe K-edge spectra recorded in both Y_6Fe_{23} and Ho_6Fe_{23} compounds. As shown in Fig. 5.9 differences between the unpolarized absorption spectra of both compounds are found in the near-edge region, i.e., in the region of the absorption spectrum which carries information about the electronic state of the system. As the electronic structure of Fe is though to be similar in both Y_6Fe_{23} and Ho_6Fe_{23} compounds, these differences can be addressed to the additional contribution of the holmium 5d states hybridized with the Fe d-states. In a similar way, the main differences between Ho_6Fe_{23} and Y_6Fe_{23} XMCD spectra extend in the same region as for the unpolarized case. The comparison of the XAS signals offers further support, at least in a first approximation, to the interpretation given above for the peculiar shape of the Fe K-edge XMCD signal of Ho_6Fe_{23}.

[2] It has to be noted that the choice of n_h does not affect to the relative values of $<L_z>_p$

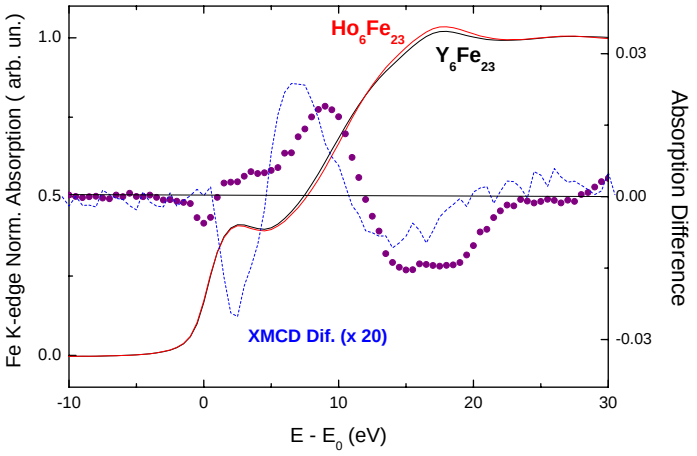

Figure 5.9: Comparison of the difference (•) between the normalized Fe K-edge XAS spectra of Y_6Fe_{23} (solid black line) and Ho_6Fe_{23} (red line) and the difference of the corresponding XMCD spectra (dashed blue line).

XMCD at the Ho $L_{2,3}$-edges

According to our hypothesis, the influence of the Ho magnetic sublattice to the XMCD at the Fe absorbing sites comes from the strong Fe(3d)-Ho(5d) hybridization. Then, it could be also expected that Fe atoms contribute to the XMCD spectra recorded at the rare-earth sites. Hence, we have extended our investigation to the XMCD spectra at the Ho $L_{2,3}$-edges in Ho_6Fe_{23} aimed to determine if Fe is at the origin of well defined spectral features at these absorption edges. The Ho $L_{2,3}$ are the best suited absorption edges to do it because the excited photoelectron directly probes the local density of empty d-states projected on the Ho sites. The contribution of Fe, through the Fe(3d)-Ho(5d) hybridization, should be directly reflected at the Ho $L_{2,3}$-edges XMCD spectra.

The Ho $L_{2,3}$-edge XMCD spectra show a sign reversal below the compensation temperature (see Figure 5.10). As in the case of the Fe K-edge, this effect reflects the change of the magnetic sublattice governing the sign of the total magnetization above (Fe) and below (Ho) T_{Comp}. Additionally, in analogy with the Fe K-edge case, the reduction of the signal at temperatures close to compensation, i.e. 190 K, 195 K and 200 K, also affects these signals. The most immediate finding reported in Figure 5.10 is that the sign of the L_2-edge signal is opposite to that of the L_3-edge signal through the whole temperature range. Moreover, the L_2 signal is also much smaller. The analysis of the XMCD spectra at the Ho L_2 and L_3 edges shows that the L_3/L_2 ratio is kept

constant through all the temperature range. The peak intensity ratio between the main dichroic peaks of the XMCD signals at the L_3 (B) and L_2 (E) absorption edges, B/E, is ~ 5, being the integral of the L_3 signal about twenty times larger than that of the L_2 signal.

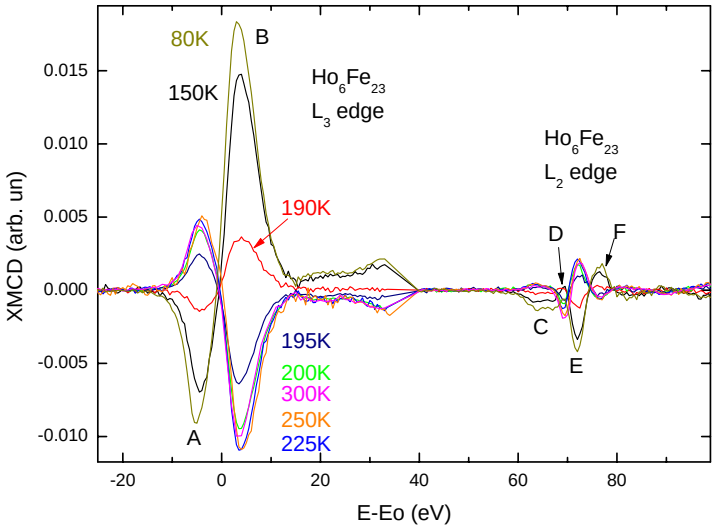

Figure 5.10: Comparison of the Ho $L_{2,3}$-edges XMCD spectra recorded for Ho_6Fe_{23} at different temperatures. For the sake of clarity the L_2 spectra have been horizontally shifted (70 eV).

As we made in the case of the Fe K-edge spectra, we have excluded the temperature range near T_{comp} from the thermal study. Thus, the temperature dependence of the Ho L_3 and L_2 XMCD signals is reported in Fig. 5.11. For the sake of clarity all the spectra are displayed with the same sign as the low temperature ones, i.e., when Ho dominates the overall magnetization of the system. The L_3-edge spectra exhibit an small structure (A) at energies below the edge ($\sim$ -5 eV) and a prominent peak of contrary sign (B) at $\sim$ 3 eV above the edge. The main structure, B, is of dipolar origin, while the low-energy feature (A) is due to a quadrupolar transition [**?**]. By contrast, up to four different structures are clearly identified at the L_2-edge XMCD spectra, whose overall amplitude is about five times smaller than the L_3 one. The L_2 XMCD spectrum is made up of a positive peak at the absorption threshold (D), a negative one at $\sim$ 4 eV above the edge (E) and a positive structure (F) at higher energies ($\sim$ 8.5 eV). Moreover, an additional feature (C) of negative intensity appears at energies below the edge ($\sim$ -5 eV) as temperature decreases.

The shape of the L_2 spectrum is strongly modified as temperature varies, specially regarding the intensity of both the positive peak D at the edge and

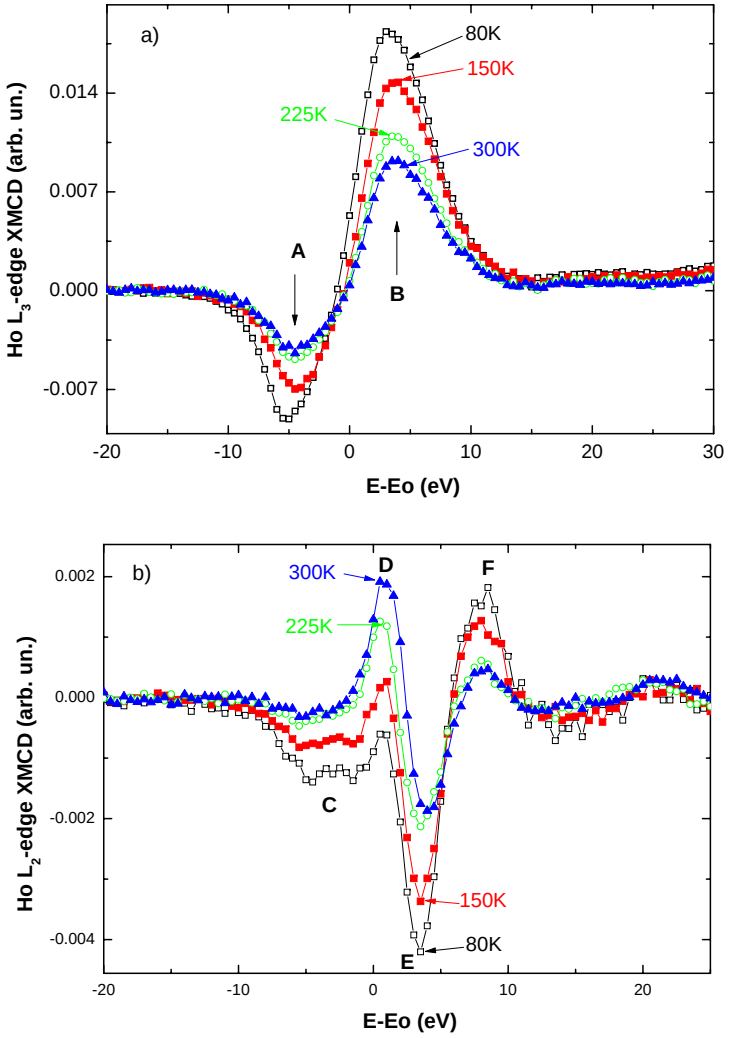

Figure 5.11: Thermal dependence of the XMCD spectra recorded at the Ho L_3-edge (panel a) and L_2-edge (panel b) in Ho_6Fe_{23}. The spectra corresponding to $T > T_{comp}$ have been reversed.

the low energy feature C. Furthermore, the evolution of peak D is not envisaged on the basis of the expected modification of the electronic structure of Ho with the temperature. In principle, one expects that the amplitude of the Ho $L_{2,3}$ XMCD signals continuously decreases as temperature increases, reflecting the diminution of μ_{Ho} at high temperatures. This behaviour is fulfilled by C, E and F features but not by the D one whose intensity surprisingly enhances! This is also shown in Fig. 5.12 where the temperature dependence of the intensity of the different XMCD peaks is compared.

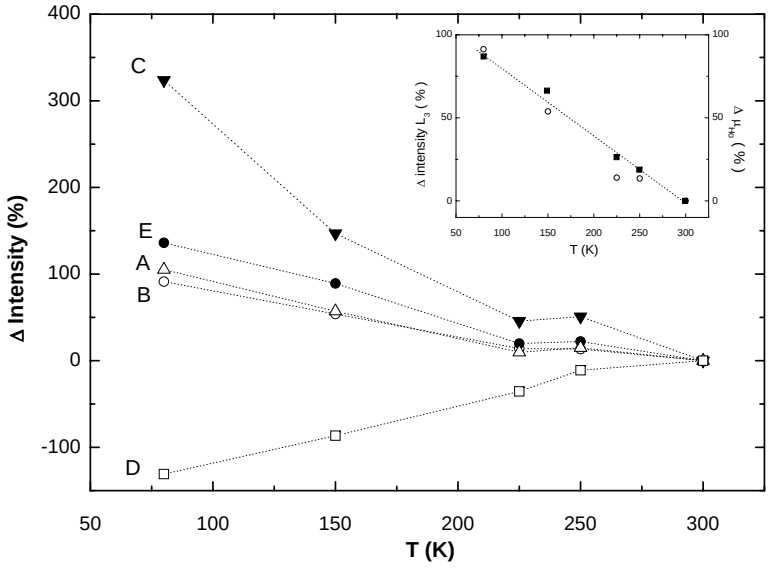

Figure 5.12: Temperature dependence of the intensity of the main spectral features of the Ho $L_{2,3}$-edges XMCD spectra (see Fig. 5.11) relative to the room temperature values. In the inset, the thermal dependence of μ_{Ho} (■) and the Ho L_3-XMCD intensity (○), relative to their room temperature values, are compared.

The intensity of the main dichroic peaks for both L_3 (B) and L_2 (E) absorption edges present a similar thermal dependence. Also the intensity of the quadrupolar (A) structure of the L_3 XMCD spectra, directly related to the Ho 4f states, exhibits the same trend. The increase under cooling of the intensities of these three XMCD peaks relative to the room temperature values shows a remarkable agreement with that of μ_{Ho} derived from the magnetization data (see inset of Fig. 5.12). By contrast, the temperature dependence of the intensity of features C and D bears little relation with that of the Ho magnetic moment. **Therefore, the thermal evolution of the Ho L_2-edge XMCD spectrum cannot be understood if we assume that it is purely due to the magnetism of Ho sublattice. On the other hand, this anomalous behavior can be easily understood if an additional feature of Fe origin is included.**

Making a parallel to the Fe K-edge case, one can suspect that there is a contribution of the Fe sublattice to the rare-earth XMCD spectra being the counterpart of the detected lanthanide contribution to the Fe K-edge. **According to our hypothesis, the Fe contribution is located at $\sim$ 0 eV so that features C and D are strongly influenced by the Fe magnetic moment**. Thus, the measured XMCD at the threshold region results from

the addition of both Fe and Ho contributions. The sign of these contributions is opposite at the edge being positive for Fe and negative for Ho. Therefore, there is a competition between the negative contribution of Ho, corresponding to μ_{Ho}, and the contribution from the surrounding Fe atoms. As we have seen in section 5.2, at low temperature the magnetization of the Ho sublattice is larger than the magnetization of the Fe sublattice. This turns out in a negative value of the intensity at the threshold. As temperature increases μ_{Ho} decreases faster than μ_{Fe} and the total XMCD signal at the edge is progressively dominated by the positive Fe contribution. This effect is maximum at room temperature, i.e., when the negative Ho contribution is the minimum through the whole temperature range studied. As a consequence, the XMCD spectrum of Ho_6Fe_{23} recorded at room temperature exhibits a strong positive (D) peak at the threshold region.

In relation to the influence of Fe on the XMCD signals recorded at the L_3, it is worth noticing that neither peak A nor peak B seem to be affected by Fe as both peaks follow the thermal dependence of μ_{Ho}.

The existence of a magnetic contribution of the Fe ions to the Ho $L_{2,3}$ XMCD spectra is of special significance concerning the sum-rule analysis. Despite the application of these sum-rules at the rare-earth L-edges is not free of controversy, it is interesting to show the importance of extracting the Fe contribution from the Ho XMCD signals in order to get reliable information about the orbital and spin contribution to μ_{Ho}. In a similar way as for the Fe K-edge, two sum-rules have been derived connecting the integrated XMCD spectra at the $L_{2,3}$-edges of Ho with the ground-state expectation value of both $\langle$ Lz $\rangle$ and $\langle$ Sz $\rangle$ of the 5d states [26, 27]:

$$\langle L_z \rangle = \ 2 \times (A_{L_3} + A_{L_2}) \times \frac{n_h}{\mu} \tag{5.2a}$$

$$\langle S_z \rangle + \frac{7}{2}\langle T_z \rangle = \frac{3}{2} \times (A_{L_3} - 2 \times A_{L_2}) \times \frac{n_h}{\mu}, \tag{5.2b}$$

where A_{L_3} and A_{L_2} are the integrals over the dichroic signal at the L_3 and L_2 edges, respectively. n_h is the number of holes in the Ho $5d$ band and μ is the unpolarized $L_{2,3}$-edge cross-section after subtraction of a double step function that ideally models the contribution of the continuum states. No normalization to the absorption jumps has been done neither in the L_3-edge, nor in the L_2-edge spectra in order to preserve the direct applicability of the sum rules.

The analysis of the XMCD signals has been performed under the following assumptions: i) μ is approximated by $\frac{3}{2}(\mu^+ + \mu^-)$; ii) $\langle T_z \rangle$ is assumed to be

negligible in the spin sum rule; iii) estimates of both the orbital, $\langle L_z \rangle$, and spin, $\langle S_z \rangle$, moments have been derived from the sum-rule by considering $n_h = 9$. Both the orbital and spin moments derived from the sum-rules are strongly affected by the different used approximations, specially regarding estimates of n_h. In order to minimize the uncertainty of the n_h values we have focussed the analysis on both the $\langle L_z \rangle / \langle S_z \rangle$ ratio and the relative modification of $\langle$ Lz $\rangle$ and $\langle$ Sz $\rangle$ moments with respect to the room temperature values.

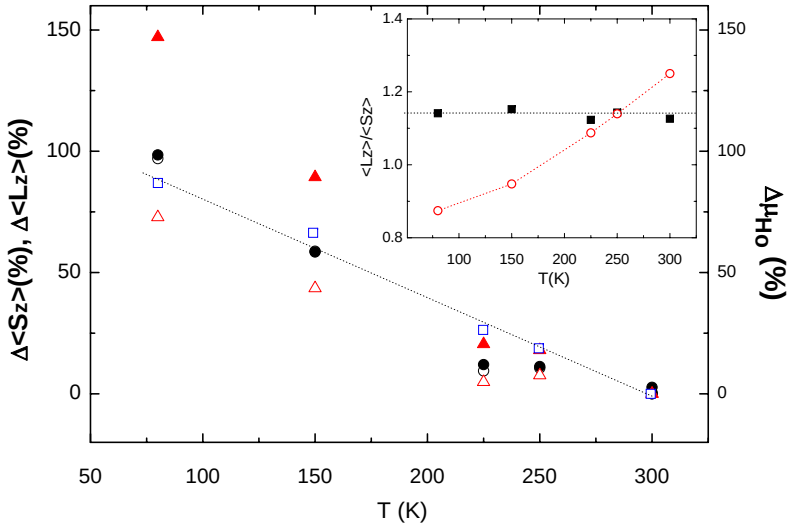

Figure 5.13: Comparison between the thermal variation, relative to the room temperature values, of μ_{Ho} (□) and the L_z (▲) and S_z (△) values derived from the Ho $L_{2,3}$-edges XMCD spectra. The same comparison is shown after the Fe contribution to the Ho $L_{2,3}$-edges spectra has been removed: L_z (●) and S_z (○). The inset reports the thermal dependence of the L_z/S_z with (■) and without (○) correcting by the Fe contribution.

Estimates of both the orbital, $\langle L_z \rangle$ and spin, $\langle S_z \rangle$, moments are respectively 0.063 (0.121) and 0.056 (0.106) μ_B at room (T = 80 K) temperature. It should be noted that both $\langle L_z \rangle$ and $\langle S_z \rangle \mu_B$ are parallel, i.e., contrary to what is expected for a $5d^1$ configuration. This result stems from the spin dependence of the dipolar matrix elements [55, 57] and has been previously discussed in chapter 2. As a consequence, the difference in the 5d radial functions is proportional to the net spin moment of the 4f states and the XMCD at the $L_{2,3}$ is related to μ_{4f} rather than to μ_{5d}. Indeed, as shown in Fig. 5.13, the modification of the obtained $\langle$Lz$\rangle$ and $\langle$Sz$\rangle$ moments with respect to the room temperature values agrees well with that of μ_{Ho} derived from magnetization

data.

The values above have been obtained by removing not only the quadrupolar contribution but also the Fe contribution in L_2 at the integration procedure. However, if the additional iron contributions are not considered, the thermal dependence is quite different. This effect results more evident from the analysis of the $\langle$ Lz $\rangle/\langle$ Sz $\rangle$ ratio. As shown in the inset of Fig. 5.13, the ratio remains constant $\langle$ Lz $\rangle/\langle$ Sz $\rangle$ = 1.14 through the whole temperature range if the extra Fe contributions are removed. However, if the integration procedure is performed without considering the presence of the Fe contribution R should decrease from $\langle$ Lz $\rangle/\langle$ Sz $\rangle$ = 1.3 at room temperature to $\langle$ Lz $\rangle/\langle$ Sz $\rangle$ = 0.86 at low temperature, suggesting erroneously a considerable ($\sim$ 35 %) reduction of the orbital component.

5.4 Conclusions

1. The thermal dependence analysis performed on both Fe K-edge and Ho $L_{2,3}$-edges XMCD spectra recorded through the magnetic compensation transition has allowed us to identify the Fe and Ho magnetic contributions to the signals.

2. The results at the Fe K-edge indicate that in the case of Ho_6Fe_{23} there is a contribution to the XMCD signals coming from the rare-earth sublattice. This contribution has been extracted and shown to be proportional through the whole temperature range to the μ_{Ho} obtained from magnetization data. The contribution of the Ho magnetic sublattice to the Fe K-edge XMCD spectra stems from the strong Fe(3d)-Ho(5d) hybridization.

3. Analogously, the thermal study of the XMCD spectra at the rare-earth $L_{2,3}$-edges points out the presence of a extra contribution of Fe origin. In order to properly account for the thermal dependence of the different features in the Ho L_2 dichroic signal a non-negligible contribution of the transition metal has to be considered. Our results indicate that this contribution is "localized" at $\sim$ 0 eV. However, the presented thermal analysis did not allow us to isolate it. The study of the XMCD signals at the $L_{2,3}$-edges will be completed in chapter 6, where a more comprehensive study of the signals at the rare-earth $L_{2,3}$-edges will let us to isolate the Fe signal by applying a two sub-lattice model.

4. Our results indicate that, by correctly accounting these mixed effects it is possible to reveal the transition-metal magnetism by tuning the

rare-earth absorption edges and, conversely, the rare-earth magnetism by looking at the transition metal.

5. The influence of these contributions to the values of the orbital and spin moments derived by using sum rules analysis has been also shown.

6. These results point out the need of including contributions from rare-earth ions to the Fe K-edge XMCD signals and, conversely, from Fe ions to the R $L_{2,3}$-edge XMCD spectra prior to account for the XMCD at the rare-earth $L_{2,3}$-edges in R-Fe intermetallic materials and, consequently, of getting the characterization of the lanthanides 5d states by means of XMCD.

Chapter 6

XMCD in $R(Al_{1-x}T_x)_2$ Laves phases compounds

6.1 Introduction

In chapters 4 and 5 we have analyzed the modification of the Fe K-edge and R $L_{2,3}$- edges dichroic spectra as a function of both the specific lanthanide element and the temperature. In this chapter we present a comprehensive and systematic XMCD study performed at both the Fe K-edge and the R $L_{2,3}$-edges in $R(Al_{1-x}Fe_x)_2$ Laves phases trying to further verify the conclusions suggested in the previous chapters. To this end, the modification of these spectra with different rare-earth, temperature and pressure have been monitorized. In addition, in this study the XMCD spectra have been compared for different R:Fe concentration ratios by gradually substituting Fe by non magnetic Al atoms while keeping fixed the crystal structure. Finally, the effect of the specific transition metal on the XMCD signals has been explored by performing an analogous study the $R(Al_{1-x}Co_x)_2$ compounds.

In addition to the XMCD study, the work presented in this chapter also includes the synthesis of the $R(Al_{1-x}T_x)_2$ compounds as well as their crystallographic (DRX) and magnetic (SQUID magnetometry and Mössbauer spectroscopy) characterization.

Our final aim is to perform an XMCD study as much complete as possible to determine if we are able to unambiguosly identify, and thus disentangle, both Fe and R contributions to the XMCD signals. This is of fundamental importance in order to correctly extract element and shell-selective magnetic information from the XMCD spectra. The verification of the existence of a contribution of R origin, $XMCD_R$, to the T K-edge signal and, conversely, a contribution of T origin, $XMCD_T$, to the R $L_{2,3}$-edges signals is expected to be

achieved by consistently explaining all the observed variations within the same two-sublattice model (XMCD = $XMCD_T$ + $XMCD_R$) frame. In addition, from the results provided by XMCD, we shall try to evaluate to what extent the analysis of these XMCD spectra is a valid method to: *i)* monitor both Fe and R magnetic state and *ii)* study the R-T interaction (particularly the role played by the R(5d)-T(3d) hybridization).

In order to accomplish these objectives, we have selected the $R(Al_{1-x}Fe_x)_2$ Laves phases compounds with x = 0, 0.25, 0.50, 0.75 and 1. The main reasons motivating this choice were:

1. The magnetic properties of the RFe_2 compounds are determined by the competition between the localized 4f magnetism of the R sublattice and the itinerant 3d magnetism of the Fe sublattice.

   This competition shows an evolution through the $R(Al_{1-x}Fe_x)_2$ series and, for pure RAl_2 compounds, RKKY-like magnetism is obtained. R(5d) states are thought to play an essential role in the RFe_2 compounds, while they are ignored in the case of RAl_2. This competition shows an evolution through the $R(Al_{1-x}Fe_x)_2$ series. The R(5d) states are thought to play an essential role in the RFe_2 compounds, while they are ignored in the case of RAl_2 compounds, where the magnetic behaviour is explained in terms of the RKKY theory. Monitoring the changes of the XMCD signal along the $R(Al_{1-x}Fe_x)_2$ series seems to be a excellent approach to study the evolution of the R(5d) band and how the R(5d)-Fe(3d) hybridization is modified by the introduction of Al.

2. RAl_2 and RFe_2 Laves phases compounds present the same crystal structure independently on R. Moreover, as we will see in the following section, the crystal structure is kept the same for the selected $R(Al_{1-x}Fe_x)_2$ pseudo-binary compounds. This simplifies the analysis of the XMCD signals as we can assert that the observed changes will not depend on structural modifications.

3. In addition, binary Laves phases have just one crystallographic site for R atoms and one site for Fe or Al atoms. Therefore, all the Fe atoms will be equivalent, which simplifies the analysis of Mössbauer spectra. This simple scheme becomes more complicated for compounds with partial Al-Fe substitution. In this case, the Fe atoms may present different possible environments depending on the number of Al atoms surrounding the Fe one. This influence will be determined through the Mössbauer spectroscopy study of the $R(Al_{1-x}Fe_x)_2$ series.

4. The magnetic properties of the $R(Al_{1-x}Fe_x)_2$ compounds have been widely studied, especially regarding both RFe_2 and RAl_2 series. There-

fore, the initial idea was to take benefit of the previous knowledge to correctly interpret the XMCD signals. Unfortunately, despite the great deal of research performed, no satisfactory explanation has been achieved yet for the magnetic properties of the $R(Al_{1-x}Fe_x)_2$ dilutions. In particular, the way in which both the rare-earth and iron magnetic moments change by the effect of Al substitution is still an open question. Indeed, macroscopic magnetic measurements have given place to very diverse and sometimes contradictory results for the dependence of both μ_R and μ_{Fe} on the Al concentration. In addition, just occasional and insufficient Neutron Diffraction and ^{161}Dy Mössbauer spectroscopy experiments have been published so that they are not complete enough to solve this shortage. As a result, the precise characterization of the modification of μ_{Fe} and μ_R as Fe is substituted by Al through the $R(Al_{1-x}Fe_x)_2$ series remains still unsolved.

The main objective of this thesis is, however, not directly related to this topic itself but providing a full understanding of the XMCD of R-T intermetallics. This is the reason why we focus on the study of XMCD at H = 50 kOe and T = 5 K (As we will see throughout the next sections the magnetic description of $R(Al_{1-x}Fe_x)_2$ becomes clearer under these conditions). However, we shall also provide a brief summary of what it is possible to contribute to the above problem by the combined analysis of Magnetization, XMCD and Mössbauer measurements.

5. Furthermore, RFe_2 and RCo_2 Laves phases compounds present the same crystal structure. Taking benefit of this fact, we have extended our study to the $R(Al_{1-x}Co_x)_2$ series in order to determine the effect of the specific transition metal in the XMCD signals of intermetallic materials.

6.2 Sample preparation

Polycrystalline $R(Al_{1-x}\ Fe_x)_2$ and $R(Al_{1-x}\ Co_x)_2$ Laves phases samples were synthesized by either induction-melting or arc-melting technique as detailed in Tables 6.1 and 6.2. In order to have single-phase samples, the melted elements need to be slightly out of stoichiometry. In the case of the R-Fe-Al series an excess of 1.5 %wt of R (1 %wt in the case of R = Gd, Tb and Lu) and 1 %wt of Al has been used. The excesses added on the R-Co-Al compounds were 3%wt R and 1%wt Al.

With the purpose of studying the evolution from RFe_2 to RAl_2, we have synthesized $R(Al_{1-x}Fe_x)_2$ compounds with different iron content. The x = 0, 0.25, 0.50 , 0.75 and 1 iron concentrations have been chosen trying to include

the whole series and, at the same time, to avoid the concentration regions in which both C15 and C14 structures may coexist. (As we will see in the next section regions of C15-C14 multiphase mixture exists around 30% and 70% of Al). The precise extent of these single-phase regions depends on both specific R and T in the compound. As a result, when we extended our study to $R(Al_{1-x}Co_x)_2$, different x concentrations (x = 0, 0.3, 0.50 , 0.7 and 1) had to be synthesized.

Most of the samples were successfully synthesized. However, in the case of the $R(Al_{1-x}\ Fe_x)_2$ series with Nd or Pr, only the compounds with low Fe content (25% and 0% of Fe) could be prepared. According to previous studies,[130] the synthesis of $NdFe_2$ and $PrFe_2$ samples is only possible under high pressure conditions. With the aim of preparing a complete (from Fe = 0% to 100%) series with a light rare-earth, we tried several combinations of light and heavy rare-earths in the form $(R_{0.5}R'_{0.5})(Al_{1-x}\ Fe_x)_2$. In these cases, the expected Laves structure has been found only for compounds with 50%, 25% and 0% of Fe. In the same way, the low boiling point of Sm (1794 ^{o}C) very close to the melting point of Fe (1538 ^{o}C) makes difficult the synthesis of the $Sm(Al_{1-x}\ Fe_x)_2$ compounds owing to Sm loss. In tables 6.1 and 6.2 only the $R(Al_{1-x}Fe_x)_2$ compounds that have been considered for the XMCD study are shown.

Sample	Excess		Furnace	H. T.	
	R	Al		T (^{o}C)	Days
YFe_2	1.5	1	ind.	800	3
$Y(Al_{0.25}Fe_{0.75})_2$	1.5	1	ind.	800	3
$Y(Al_{0.50}Fe_{0.50})_2$	1.5	1	ind.	800	3
$Y(Al_{0.75}Fe_{0.25})_2$	1.5	1	arc.		
$Nd(Al_{0.75}Fe_{0.25})_2$	1.5	1	arc		
$NdAl_2$	-	-	ind.*	800	4
$Pr(Al_{0.75}Fe_{0.25})_2$	1.5	1	arc		
$PrAl_2$	-	-	ind.*	800	4
$GdFe_2$	1	1	ind.	800	3
$Gd(Al_{0.25}Fe_{0.75})_2$	1	1	ind.	800	3
$Gd(Al_{0.50}Fe_{0.50})_2$	1	1	ind.	800	3
$Gd(Al_{0.75}Fe_{0.25})_2$	1	1	ind.	800	3
$GdAl_2$	-	-	ind.*	800	4
$TbFe_2$	1	1	ind	800	3
$Tb(Al_{0.25}Fe_{0.75})_2$	1	1	ind.	800	3
$Tb(Al_{0.50}Fe_{0.50})_2$	1	1	ind.	800	3
$Tb(Al_{0.75}Fe_{0.25})_2$	1	1	ind.	800	3
$TbAl_2$	-	-	ind.*	800	4
$DyFe_2$	1.5	1	arc		
$Dy(Al_{0.25}Fe_{0.75})_2$	1.5	1	arc		
$Dy(Al_{0.50}Fe_{0.50})_2$	1.5	1	arc		
$Dy(Al_{0.75}Fe_{0.25})_2$	1.5	1	arc		
$DyAl_2$	-	-	ind.*	800	4
$HoFe_2$	1.5	1	arc		
$Ho(Al_{0.25}Fe_{0.75})_2$	1.5	1	arc		
$Ho(Al_{0.50}Fe_{0.50})_2$	1.5	1	arc		
$Ho(Al_{0.75}Fe_{0.25})_2$	1.5	1	arc		
$HoAl_2$	-	-	ind.*	800	4
$ErFe_2$	1.5	1	arc		
$Er(Al_{0.25}Fe_{0.75})_2$	1.5	1	arc		
$Er(Al_{0.50}Fe_{0.50})_2$	1.5	1	arc		
$Er(Al_{0.75}Fe_{0.25})_2$	1.5	1	arc		
$ErAl_2$	-	-	ind.*	800	4
$LuFe_2$	1	1	arc		
$Lu(Al_{0.25}Fe_{0.75})_2$	1	1	arc		
$Lu(Al_{0.50}Fe_{0.50})_2$	1	1	arc		

Table 6.1: Synthesis details of $R(Al_{1-x}Fe_x)_2$: excess added to the stoichiometric amounts (in % wt.), kind of furnace (induction,ind., or arc) and heat treatment (H.T.). *Synthesis by Dr. N. Plugaru.

Sample	Excess		Furnace	H. T.	
	R	Al		T (^{o}C)	Days
$NdCo_2$	3		arc	850	7
$PrCo_2$	3		arc	850	7
$GdCo_2$	3		arc	850	7
$Gd(Al_{0.5}Co_{0.5})_2$	3	1	arc		
$Gd(Al_{0.8}Co_{0.2})_2$	3	1	arc		
$GdAl_2$	-	-	ind.*	800	4
$TbCo_2$	3		arc		
$DyCo_2$	3		arc	850	7
$HoCo_2$ (x 2)	3 (3)		arc (arc)	850 (0)	7 (0)
$Ho(Al_{0.2}Co_{0.8})_2$	3	1	arc		
$Ho(Al_{0.50}Co_{0.50})_2$	3	1	arc		
$Ho(Al_{0.7}Co_{0.3})_2$	3	1	arc		
$HoAl_2$	-	-	ind.*	800	4
$ErCo_2$ (x 2)	3 (3)		arc (arc)	850 (0)	7 (0)
$Lu(Al_{0.1}Co_{0.9})_2$	3	0	arc	850	7

Table 6.2: Synthesis details of $R(Al_{1-x}Co_x)_2$: excess added to the stoichiometric amounts (in % wt.), kind of furnace and heat treatment. *Synthesis was carried out by Dr. N. Plugaru in collaboration with Dr. J. Chaboy prior starting this thesis. (x 2) as-cast and annealed compounds.

Some of the samples were thermally treated in quartz tubes with argon atmosphere for about 3-7 days at a temperature of 800^{o}C- 850^{o}C (see tables 6.1 and 6.2 for details). Heat treatment is usually carried out with the purpose of ensuring phase homegeneity. In our case, as-cast *vs.* annealed comparisons indicate that the effect of heat treatment is negligible as no significative differences have been observed neither in the crystallographic nor in the magnetic properties.

6.3 Crystallographic structure

Binary RFe_2, RCo_2 and RAl_2 Laves phases crystallize in the $MgCu_2$-type structure (C15 structure having space group Fd3m), where the R atoms form a diamond lattice and the remaining space inside the cell is occupied by regular tetrahedra consisting of the Fe (or Co or Al) atoms.[131, 132] ($PrFe_2$ and $NdFe_2$ do not form at normal conditions although a pressure synthesis has been successfully in stabilizing the C15 structure[130]). In this structure, the R and Fe (Co, Al) atoms each occupy one crystallographic site, namely the 8a and 16d sites, respectively. Interestingly, the C15 structure is not stable in the course

of the whole pseudobinary $R(Al_{1-x}Fe_x)_2$ and $R(Al_{1-x}Co_x)_2$ series. In the concentration regions close to binary compounds, RT_2 and RAl_2, the $R(Al_{1-x}T_x)_2$ Laves phases present a cubic crystal structure (C15), whereas in an intermediate concentration range near equiatomic composition ($\sim$ 50% of T), compounds crystallize in a hexagonal $MgZn_2$-type structure (C14, space group: P63/mmc).[133, 134] The crystallographic structure of these compounds is presented in Fig. 6.1. In addition, regions of multiphase mixture (C14 and C15) exist between concentration regions of C15 and C14 structure as schematized in the bottom bar of Fig. 6.1. Generally speaking, the concentration regions corresponding to C14-C15 phase boundaries can be established around 30% and 70% T. However, the extent of the single and mixed-phase regions clearly depends on both the specific R and T in the compound and, in some cases, these phase boundaries have been just roughly determined. [133, 134, 135]

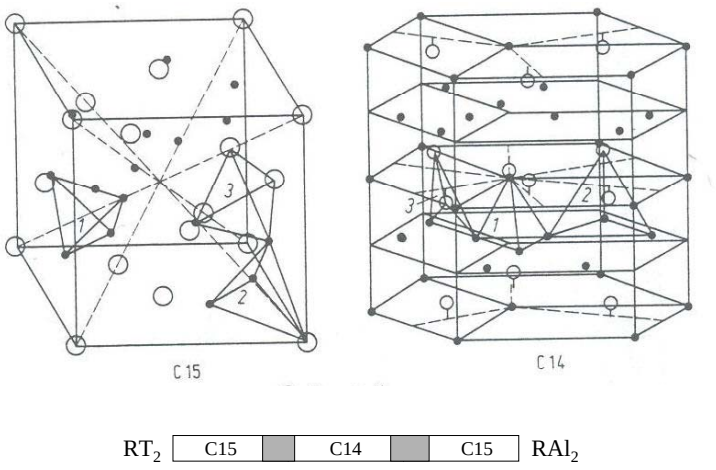

Figure 6.1: Schematic drawings of cubic (C15) and hexagonal (C14) Laves phases in which RT_2 compounds crystallize (from Ref.[122]). The R atoms are plotted as open circles and T atoms as solid circles. The three kinds of interstices are also shown (1, 2, 3). The ideal C14 and C15 structures are in fact very similar, the only difference being a slight different stacking arrangement [137, 138]. The bottom bar is a schematic layout presenting the regions of C14 and C15 structure. Gray areas are regions of C14-C15 coexistence.

As in the case of binary Laves phases, in $R(Al_{1-x}T_x)_2$ compounds crystallizing in the C15 structure. The R atoms occupy the 8a sites and the Fe (Co) and Al atoms are randomly distributed on the 16d sites. In the C14 structure, the R atoms occupy the 4f sites, while the Fe (Co) and Al atoms are distributed on both the 2a and 6h sites without exhibiting any preferential oc-

cupancy. Some authors report on ordering tendencies between T and Al in relative poor-Al ($\sim$ 40% Al) and rich-Al ($\sim$ 60% Al) concentrations. However no deviation from statistical distribution is found at equiatomic composition.[136] Details about the kind of site and nearest-neighbours for the different crystallographic sites are given in Table 6.3.

C15	kind of neighbour		C14	kind of neighbour		
site	8a	16d	site	4f	2a	6h
8a	4	12	4f	4	3	9
16d	6	6	2a	6	0	6
			6h	6	2	4

Table 6.3: Kind of site and number of nearest neighbours for the different crystallographic sites in both C14 and C15 structures of $R(Al_{1-x}T_x)_2$.[131, 132]

As discussed by Berry et al. and by Kitano et al.[137, 138], the C15 and C14 structures are in fact very similar. This can be also easily derived from XAS spectra at both T K edge and R $L_{2,3}$ edges, where the comparison of the spectral profiles indicates a very similar local environment around the absorbing (T or R) atomic specie.

The diffraction patterns were Rietveld refined using the FULLPROF code.[89][1] In all the cases the XRD pattern analysis shows that compounds with x = 0, 0.25, 0.75 and 1 crystallize in a cubic C15 ($MgCu_2$-type) structure, whereas compounds with 50% of Fe present a hexagonal C14 ($MgZn_2$-type) structure. In Fig. 6.2, the diffraction pattern of $HoFe_2$ (C15) and $Ho(Al_{0.50}Fe_{0.50})_2$ (C14) are shown as an illustrative example. For the sake of completeness the modification of the XRD patterns with the Fe concentration in a complete $R(Al_{1-x}Fe_x)_2$ series for a fixed R, and in the RFe_2 series as R varies, are presented in Figure 6.3. As expected, the profile is the same along the series, with the exception of x = 0.50, and only slight modifications on the relative intensities and a small shift of the pattern can be observed. Moreover, it is clearly seen that for x = 0.50 the crystal structure has changed, as expected for a compound in the intermediate concentration range.

[1] In some samples (see Tables 6.4 and 6.5) a complete Rietveld refinement could not be successfully accomplished. For those cases a simple pattern matching, which is enough for our purposes, was performed.

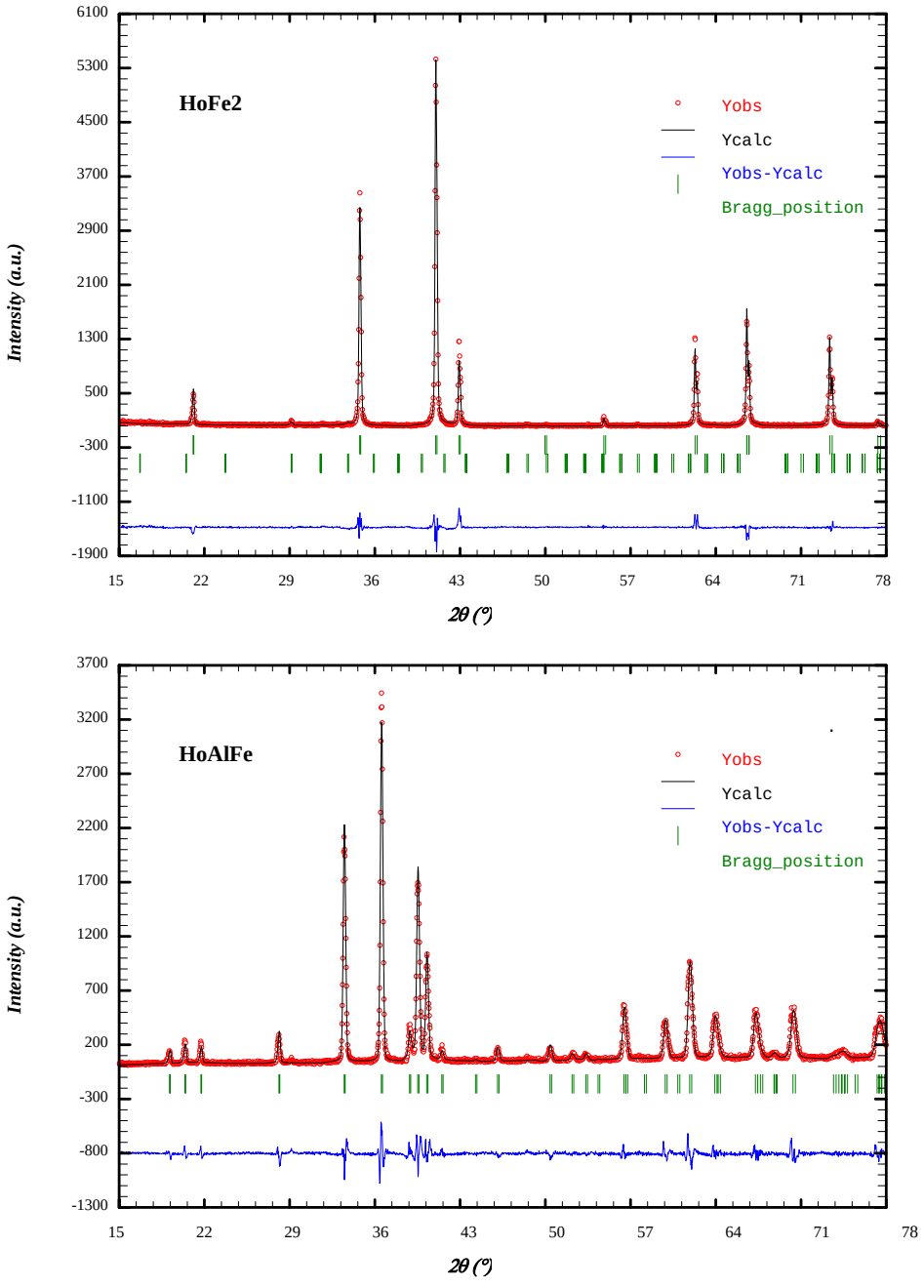

Figure 6.2: Rietveld refinement of the X-ray diffraction pattern collected at room temperature for $HoFe_2$ (top panel) and $Ho(Al_{0.50}Fe_{0.50})_2$ (bottom panel). The first row of vertical bars corresponds to the Bragg reflections of the 1:2 main phase, while the second row corresponds to the Ho_2O_3 impurity in $HoFe_2$.

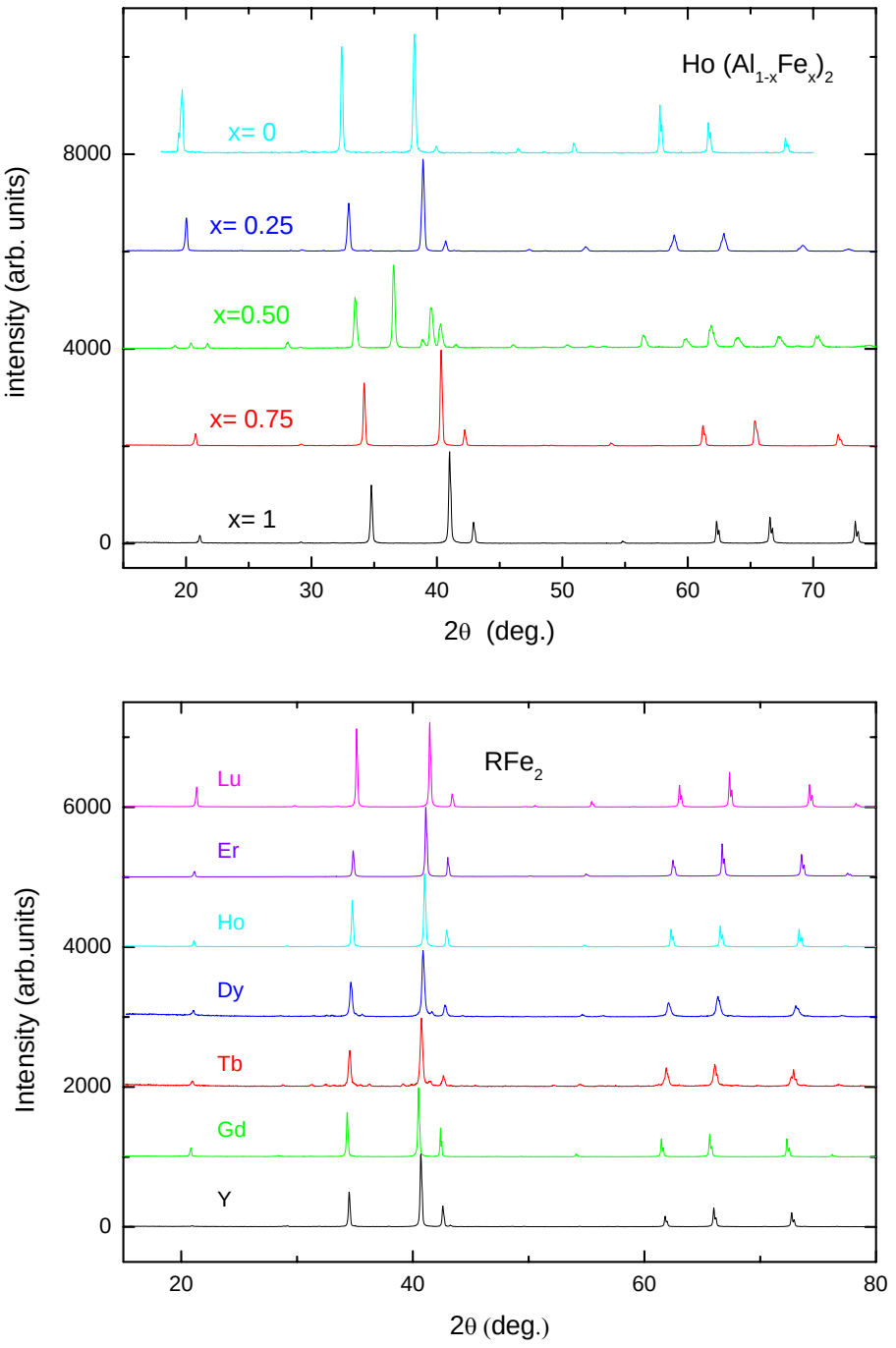

Figure 6.3: X-ray diffraction patterns collected at room temperature for $Ho(Al_{1-x}Fe_x)_2$ (top panel) and RFe_2 compounds (bottom panel).

Sample		a(Å)	c(Å)	R_{Bragg}	R_2O_3 (%)	Comment
YFe_2	C15	7.350		3.56	<2	
$Y(Al_{0.25}Fe_{0.75})_2$	C15	7.497		5.55	<2	
$Y(Al_{0.50}Fe_{0.50})_2$	C14	5.401	8.768	2.07	<2	pattern matching
$Y(Al_{0.75}Fe_{0.25})_2$	C15	7.736		5.29	<2	
$Pr(Al_{0.75}Fe_{0.25})_2$	C15	7.949		12.68		
$PrAl_2$	C15	8.028		11.87		
$Nd(Al_{0.75}Fe_{0.25})_2$	C15	7.887		11.64		
$NdAl_2$	C15	8.001		14.88		preferred orientation
$GdFe_2$	C15	7.386		8.95	<2	
$Gd(Al_{0.25}Fe_{0.75})_2$	C15	7.513		6.37	<2	
$Gd(Al_{0.50}Fe_{0.50})_2$	C14	5.422	8.793	4.67	<2	pattern matching
$Gd(Al_{0.75}Fe_{0.25})_2$	C15	7.784		5.08	<2	
$GdAl_2$	C15	7.898		32.02	<2	preferred orientation
$TbFe_2$	C15	7.343		10.5	<2	
$Tb(Al_{0.25}Fe_{0.75})_2$	C15	7.469		8.78	<2	
$Tb(Al_{0.50}Fe_{0.50})_2$	C14	5.399	8.754	3.78	7	pattern matching
$Tb(Al_{0.75}Fe_{0.25})_2$	C15	7.746		6.51	<2	
$TbAl_2$	C15	7.863		14.80	<2	preferred orientation
$DyFe_2$	C15	7.318		7.55		
$Dy(Al_{0.25}Fe_{0.75})_2$	C15	7.441		14.1		
$Dy(Al_{0.50}Fe_{0.50})_2$	C14	5.383	8.715	2.3		pattern matching
$Dy(Al_{0.75}Fe_{0.25})_2$	C15	7.736		-		
$DyAl_2$	C15	7.837		12.86		
$HoFe_2$	C15	7.295		4.94	<2	
$Ho(Al_{0.25}Fe_{0.75})_2$	C15	7.413		6.58	3	
$Ho(Al_{0.50}Fe_{0.50})_2$	C14	5.349	8.697	1.55	<2	pattern matching
$Ho(Al_{0.75}Fe_{0.25})_2$	C15	7.682		18.5	<2	preferred orientation
$HoAl_2$	C15	7.812		14.54		preferred orientation
$ErFe_2$	C15	7.278		16.96		preferred orientation
$Er(Al_{0.25}Fe_{0.75})_2$	C15	7.380		16.87		preferred orientation
$Er(Al_{0.50}Fe_{0.50})_2$	C14	5.336	8.676	2.07		pattern matching
$Er(Al_{0.75}Fe_{0.25})_2$	C15	7.666		6.51		
$ErAl_2$	C15	7.791		9.78	<2	
$LuFe_2$	C15	7.219		10.5	<2	
$Lu(Al_{0.25}Fe_{0.75})_2$	C15	7.337		22.8	5	preferred orientation
$Lu(Al_{0.50}Fe_{0.50})_2$	C14	5.289	8.616	2.88	4	

Table 6.4: Kind of structure, lattice constants (a and c), percentage of R_2O_3 impurity and reliability Bragg factor (defined in Ref.[117]) associated to the main phase.

Sample		a(Å)	c(Å)	R_{Bragg}	R_2O_3 (%)	Comment
$NdCo_2$	C15	7.300	-	7.01		
$PrCo_2$	C15	7.306	-	7.22		
$GdCo_2$	C15	7.252	-	9.39		
$Gd(Al_{0.5}Co_{0.5})_2$	C15	5.395	8.581	14.24		
$Gd(Al_{0.8}Co_{0.2})_2$	C14	7.797	-	12.21		
$GdAl_2$	C15	7.898		32.02		preferred orientation
$TbCo_2$	C15	7.208	-	0.00	<2	
$DyCo_2$	C15	7.198	-	4.86	<2	
$HoCo_2$ (as-cast)	C15	7.172	-	6.58		
$HoCo_2$ (annealed)	C15	7.173	-	6.69		
$Ho(Al_{0.2}Co_{0.8})_2$	C15	7.267	-	10.56		
$Ho(Al_{0.50}Co_{0.50})_2$	C14	5.320	8.497	9.53		
$Ho(Al_{0.7}Co_{0.3})_2$	C15	7.607		14.60	3	phase coexistence:
	C14	5.371	8.571	15.92		C14 + C15
$HoAl_2$	C15	7.810	-	14.54		preferred orientation
$Lu(Al_{0.1}Co_{0.9})_2$	C15	7.168	-	5.80	<2	
$ErCo_2$ (as-cast)	C15	7.154	-	6.16		
$ErCo_2$ (annealed)	C15	7.157	-	6.79		

Table 6.5: Kind of structure, lattice constants (a and c), percentage of R_2O_3 impurity and reliability Bragg factor (defined in Ref.[117]) associated to the main phase.

The structural information of the synthesized samples is largely summarized in Tables 6.4 and 6.5, where the kind of structure, lattice parameters and the reliability Bragg factor[117] associated to the main phase are shown. The cell parameters of the $R(Al_{1-x}Fe_x)_2$ determined from the XRD patterns, are in agreement with previous published data. [139] The $R(Al_{1-x}T_x)_2$ compounds undergo a contraction with both increasing atomic number of R and increasing T concentration. This is illustrated in Figure 6.4, where the comparison of the lattice constant,a, is shown as a function of both T concentration and R element.

Good crystallinity of the samples is indicated by the low Bragg factor obtained. In some cases (indicated in tables 6.4 and 6.5) the pattern are affected by preferred orientation giving rise to higher values of R_{Bragg}. This is, for example, the case of $Ho(Al_{0.75}Fe_{0.25})_2$, which despite its high R_{Bragg} factor (18.5) presents very narrow peaks (see Fig.6.2). The effect of preferred orientation has been checked in $HoCo_2$: the R_{Bragg} factor reduces from 21.5 to 6.6 after mixing the sample powder with SiO_2 (Cab-osil ® M5). On the other hand, the high R_{Bragg} values in the pseudobinary samples of the $R(Al_{1-x}Co_x)_2$ series are due to wide linewidths. Moreover, as $R(Al_{1-x}Co_x)_2$ present broad and ambiguously determined C14-C15 multiphase boundaries, no single-phase

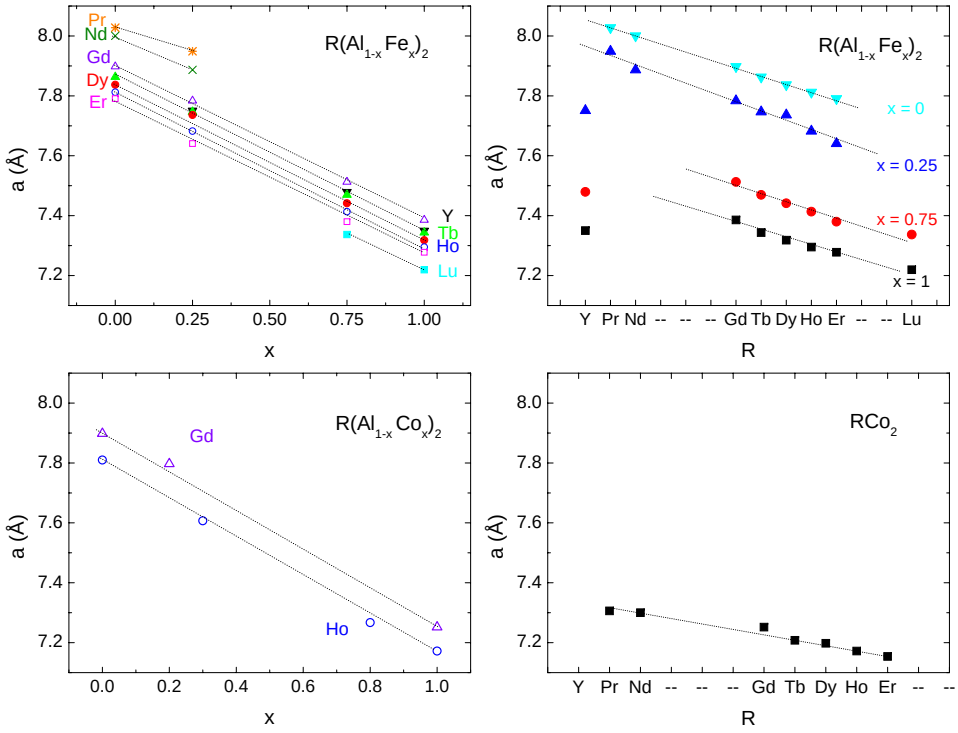

Figure 6.4: Modification of the cell parameter a collected at room temperature in cubic $R(Al_{1-x}T_x)_2$ compounds as a function of the T content, x (left), and the rare-earth, R (right).

sample could be synthesized in the $0.2 < x < 0.3$ region. For this reason we have included in our study the $Ho(Al_{0.70}\ Co_{0.30})_2$ compound, although it presents C14-C15 phase coexistence.

Pattern comparison of as-cast *vs.* annealed compounds does not indicate any evident structural modification or improvement after the annealing procedure.

From the Rietveld refinement also the presence of secondary phases and their content (in %) has been obtained. A small amount of R_2O_3 has been commonly found in our samples as indicated in Tables 6.4 and 6.5. In addition, the presence of R-T (1:3 phase mainly) and R-Al secondary phases, less than 10% overall, has been occasionally identified in our samples, being undistinguishable in most of the compounds.

Finally, it is to be noted that some RT_2 Laves phases exhibit huge magnetostrictive effects bellow T_c. Indeed, $TbFe_2$ possesses the largest known room

temperature magnetostriction, λ = 2600 x 10^{-6} (λ(0K) = 0.0045).[140] Thus, in compounds where the easy magnetization axis is [111], such as $TbFe_2$ and $ErFe_2$, an elongation along the [111] direction leads to rhombohedral distortion, whereas $DyFe_2$ and $HoFe_2$ (easy magnetization axis [100]) present tetragonal distortion.[140, 141, 142] The effect of such a distortion, however, is less significative than the volume differences due to T-Al substitution, where the lattice constant shows a modification of $\sim$ 1.7 % between x = 0 and x = 0.25. Even for $TbFe_2$, the refinement of the room temperature XRD pattern can be successfully (as indicate the reliability Bragg factor) performed considering a cubic C15-type structure. Therefore, in a first approximation, all the compounds will be considered as possessing a C14 or C15 crystallographic structure. As we will discuss later, the magnetostrictive effect is not detected in the XAS and XMCD signals.

6.4 Macroscopic magnetic characterization

The dependence of the magnetization *vs* applied magnetic field for the binary RFe_2, RCo_2 and RAl_2 compounds is shown in Figure 6.5. All the RAl_2 compounds show ferromagnetic ordering. In RFe_2 and RCo_2 compounds the magnetic moments of the transition metal and rare-earth sublattices exhibit ferromagnetic coupling for compounds with light rare-earth and ferrimagnetic coupling if the rare-earth is a heavy one. For all the compounds with a magnetic rare-earth the magnetization of the R sublattice governs the total magnetization of the sample ($|M_R|>|M_T|$). As a result, RAl_2 presents a larger magnetization than RFe_2 and RCo_2 for heavy rare-earths ($|M_{TOT}|=|M_R| - |M_T|$), while the opposite case occurs for light R ($|M_{TOT}|=|M_R| + |M_T|$), as it can be clearly seen in Fig. 6.5.

In the case of the M(H) curves of the RCo_2 series, shown in the middle panel of Fig. 6.5, the magnetization of $Lu(Al_{0.10}Co_{0.90})_2$ has been included instead of those of $LuCo_2$ and YCo_2. The reason motivating this substitution is the fact that both $LuCo_2$ and YCo_2 compounds are enhanced Pauli paramagnets, whereas a small substitution of Co by Al renders these compounds itinerant ferromagnets.[2]

To this respect, it has to be noted that while Fe exhibits an intrinsic magnetic moment, $\mu_{Fe} \sim 1.4\ \mu_B$, that remains roughly constant through the RFe_2 series,[143, 145] the Co moment is induced by the effective field due to the R atoms and, consequently, it is strongly dependent on the specific R through the RCo_2 series. [133] The different magnetic behaviour of the transition metal

[2]The effect of Al on $LuCo_2$ and YCo_2 will be seen in detail in chapter 7.

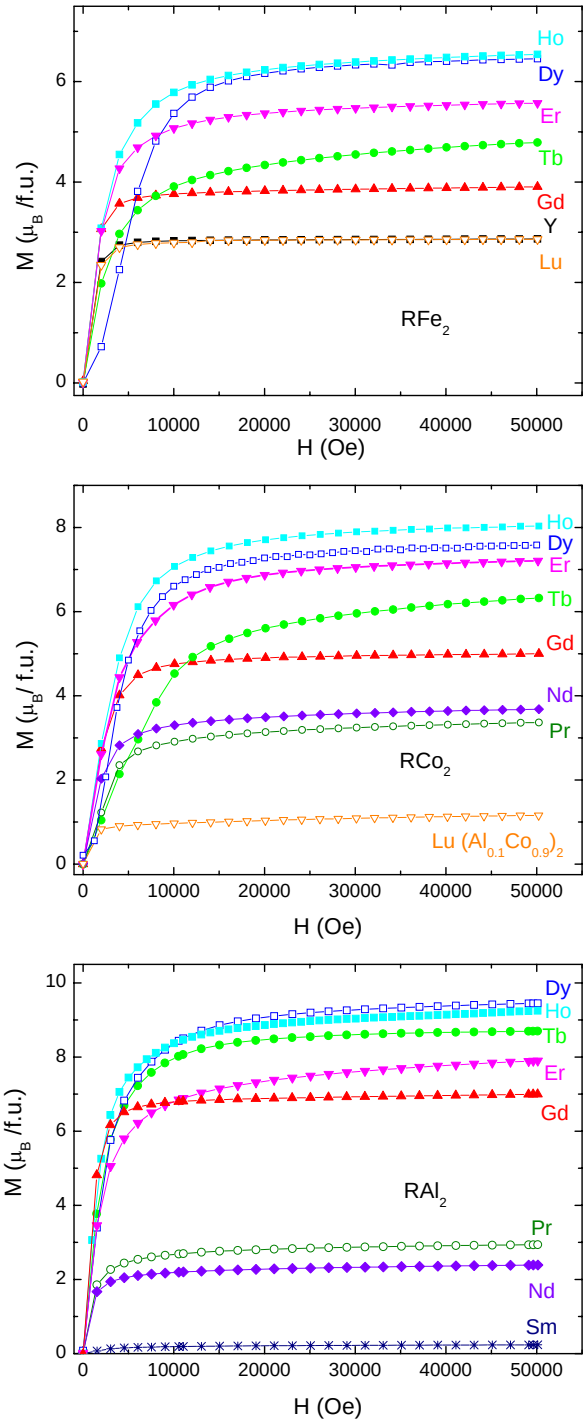

Figure 6.5: M(H) curves for RFe_2 (top), RCo_2 (middle) and RAl_2 (bottom) compounds measured at T = 5 K.

atoms, Fe *vs.* Co, in the Laves phase compounds is usually accounted in terms of the peculiarity of the DOS and the Stoner criterion for the onset of magnetism (DOS(E_F)$\cdot$ I $>$ 1).[146, 12] As shown in Fig. 6.6, the DOS of the YT_2 compounds is similar no matter the specific T involved. However, for each different transition metal the Fermi level lies in a different position of the DOS and, consequently, the magnetic behaviour is markedly different for the four compounds.

In the case of YFe_2 and $LuFe_2$ the DOS at the Fermi energy, DOS(E_F), is high enough to fulfil the Stoner criterion, DOS(E_F)$\cdot$ I $>$ 1, and these compounds exhibit ferromagnetic behaviour. By contrast, for YCo_2 and $LuCo_2$ DOS(E_F)$\cdot$ I $<$ 1 and these compounds show Pauli paramagnetism behaviour. Besides, despite the Fermi level lies in a low DOS region, it is not so far from a sharp peak in the DOS, so the magnetic behaviour of these compounds strongly depends on external parameters and they show metamagnetism. Consequently, YCo_2 and $LuCo_2$ are not good "references" for Co moment if one wants to apply a two sublattice procedure in a similar manner to that followed so far for the $RFe_{11}Ti$ and R_6Fe_{23} series. On the other hand, as it will be discussed in detail in chapter 7, a small substitution of Co by Al renders these compounds itinerant ferromagnets. $Lu(Al_{0.10}Co_{0.90})_2$ is the compound within the $(Lu_t,Y_{1-t})(Al_{1-x}Co_x)_2$ series showing the highest Co magnetic moment, $\mu_{Co} \sim 0.6\ \mu_B$, being the most similar to that found in RCo_2 compounds with magnetic R (see, for example, Ref.[147]). This is the reason why we have chosen $Lu(Al_{0.10}Co_{0.90})_2$ as the reference of the Co sublattice magnetization in the RCo_2 series.

The comparison of the M(H) behaviour as a function of the transition metal content for the different $R(Al_{1-x}T_x)_2$ compounds is shown in Figures. 6.7 and 6.8. Three different kinds of behaviour can be observed:

R = Y and Lu. Compounds with a non-magnetic R, i.e. Lu and Y Laves phases, present a rapid nonlinear diminution of the magnetic moment of Fe. Thus, YFe_2 and $LuFe_2$ are ferromagnets with $\mu_{Fe} \sim 1.43\ \mu_B$, while long-range order disappears for x $\leq$ 0.75.

R = Gd. For diluted $Gd(Al_{1-x}Fe_x)_2$ compounds the Gd-Fe coupling is ferrimagnetic. The observed reduction of the M(H) curves with increasing Fe content can be explained by simple Al-Fe replacement with basically constant Gd and Fe magnetic moments. For $Gd(Al_{1-x}Co_x)_2$ compounds, assuming a constant Gd moment, the M(H) curves indicate an abrupt decrease of the Co magnetic moment.

R = Tb, Dy, Ho and Er. For diluted $R(Al_{1-x}Fe_x)_2$ compounds with a heavy rare-earth different from Gd the coupling is also ferrimagnetic as indicates the reduction of the magnetization with respect to RAl_2. As a general

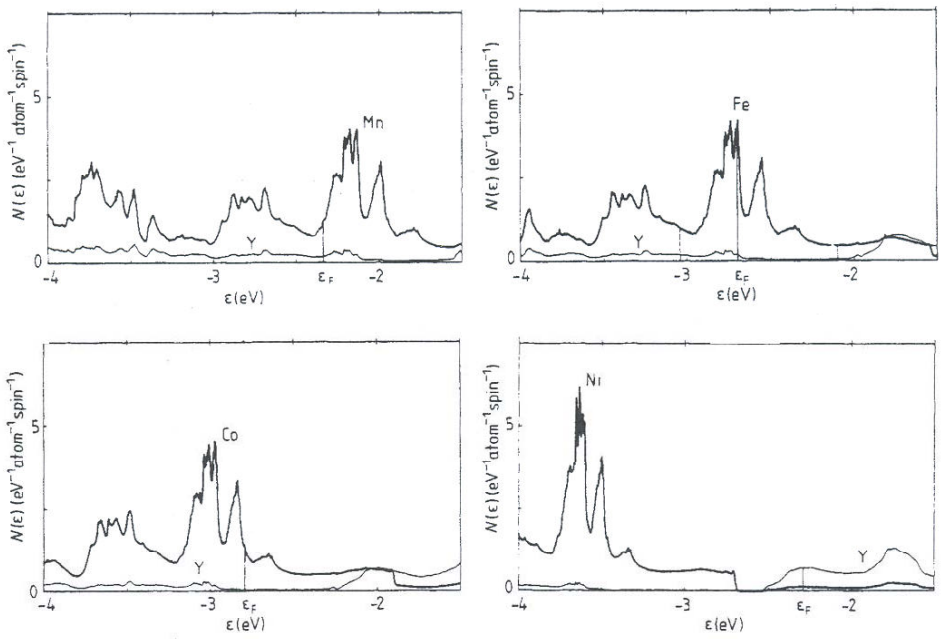

Figure 6.6: Calculated local DOS curves for YMn_2, YFe_2, YCo_2 and YNi_2. ε_F denotes the Fermi level at 0 K (From Ref.[12]).

trend there is a decrease of the magnetization in all likelihood caused by Al-Fe replacement. However, the M(H) curves do not show a gradual evolution with increasing Fe content as in the Gd series. The decrease of the magnetization with increasing Fe content is more pronounced than it would be expected from a simple dilution effect if both μ_{Fe} and μ_R remain unaltered. Moreover, it can be observed that the compounds showing this irregular modification of the magnetization present also a considerable increase of the magnetization (considerable slope in the M(H) curve) even at high fields and they develop S-type saturation behaviour, i.e. discontinuous increases of magnetization with applied magnetic field. This S-type behaviour does not occur in the case of Ho compounds.

The diluted $R(Al_{1-x}Fe_x)_2$ compounds with light rare-earth, should show the lowest magnetization for RAl_2 accordingly to the parallel coupling between R and Fe, but this is not the observed situation. As in the case of heavy compounds, it has to be noted that the high field magnetization is still far from saturation.

All the above described M(H) curves are in agreement with those found for diluted $R(Al_{1-x}T_x)_2$ compounds in previous works.[148, 149, 150, 151, 156,

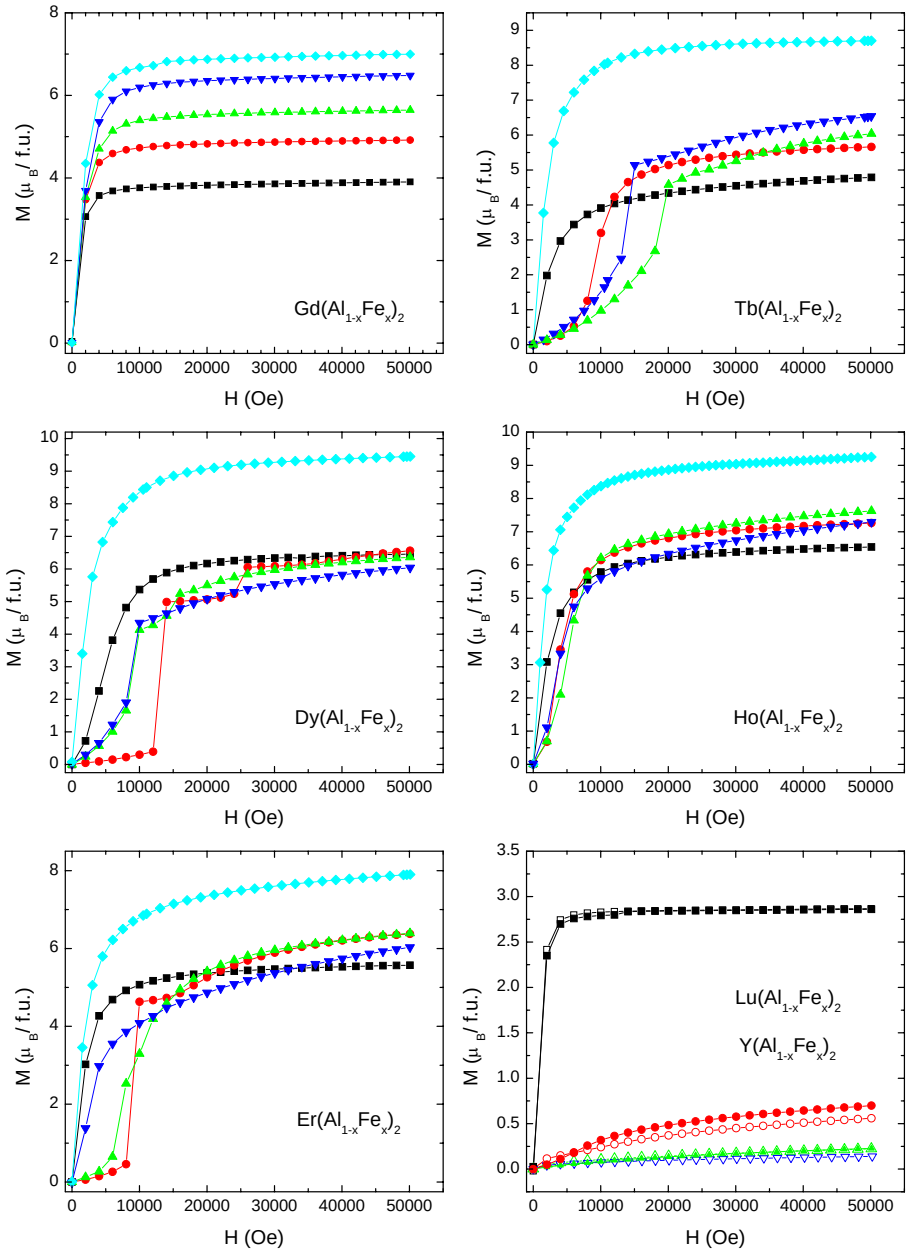

Figure 6.7: Magnetic isotherms, T = 5 K, measured on $R(Al_{1-x}Fe_x)_2$ powdered samples in applied magnetic fields up to H = 50 kOe: x=0 (♦), x = 0.25 (▼), x = 0.50 (▲), x = 0.75 (●) and x = 1(■). In the bottom right panel open symbols correspond to Y samples.

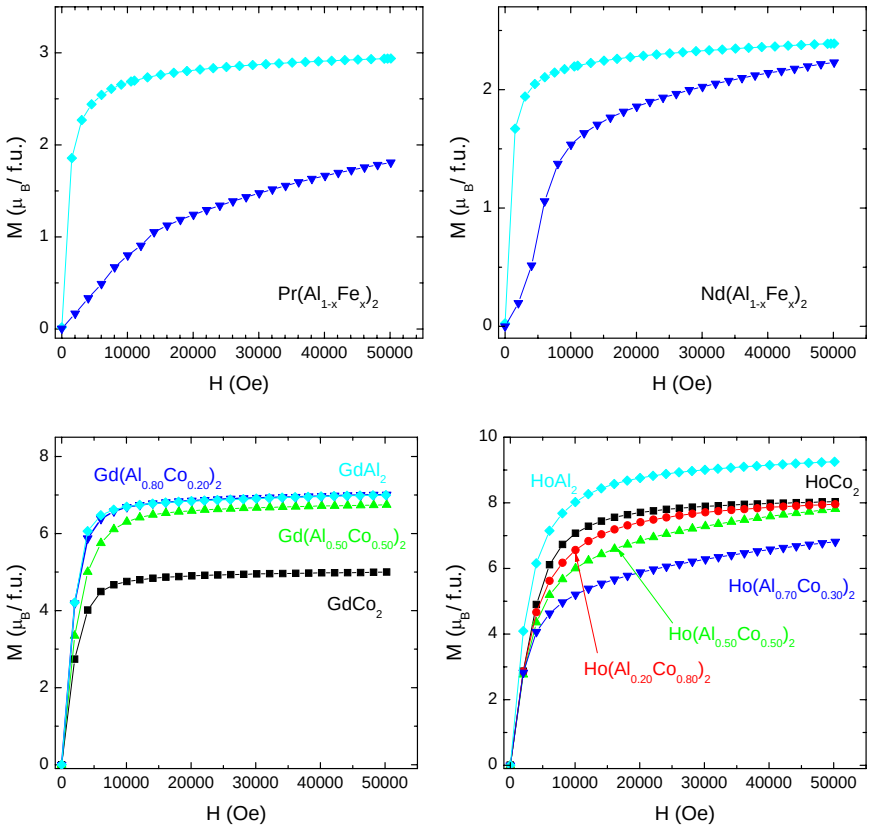

Figure 6.8: Top panels: magnetic isotherms, T = 5 K, measured on $R(Al_{1-x}Fe_x)_2$ powdered samples in applied magnetic fields up to H = 50 kOe: x = 0 (♦) and x = 0.25 (▼). Bottom panels: magnetic isotherms, T = 5 K, measured on $R(Al_{1-x}Co_x)_2$ powdered samples in applied magnetic fields up to H = 50 kOe: x=0 (♦), x = 0.20 (for R = Gd, x = 0.30 for R = Ho) (▼), x = 0.50 (▲), x = 0.80 (●) and x = 1(■).

155, 153, 136, 152, 157, 158, 159, 160, 161, 162, 135, 154] In the case of Y and Lu samples, the rapid decrease of magnetization with Al content has been explained in terms of a local environment model.[148] According to this model, the Fe atoms carry an ordered moment if surrounded by at least 15 nearest and next-nearest iron neighbours. For $LuFe_2$ and YFe_2 all the atoms fulfil this condition showing ferromagnetic order. In the case of $Lu(Al_{0.25}Fe_{0.75})_2$ and $Y(Al_{0.25}Fe_{0.75})_2$ compounds some of the Fe atoms will exhibit ferromagnetic order, whereas in compounds with 50% and 25% of Fe, all the Fe sublattice will have paramagnetic character. This model seems to explain our M(H) curves measured on the Y and Lu series. Alternatively, Pösinger *et al.* proposed a model in which magnetic clusters are formed stochastically to explain the

Mössbauer spectra recorded in $Y_{1.1}(Fe_{0.75}Al_{0.25})_2$.[163]

The M(H) behaviour of $Gd(Al_{1-x}Fe_x)_2$ series is consistent with a constant magnetic moment of Gd and a slightly decreasing Fe magnetic moment in agreement with previous works[150, 151]. Comparison between the magnetic behaviour of Fe for Lu (Y) and Gd pseudobinary compounds seems to indicate that the Gd atoms act as magnetising elements of the diluted Al-Fe matrix.

The peculiar behaviour observed for R = Tb, Dy, Ho and Er at low temperatures involves a strong decrease of the magnetization between pure RAl_2 and compounds with low Fe content (x<0.25), marked magnetic hardness and a considerable increase of magnetization with applied magnetic field even at high applied magnetic fields. This behaviour of the diluted $R(Al_{1-x}Fe_x)_2$ compounds has been previously reported[156, 155, 153, 136, 152, 157, 158, 159, 160, 161, 162, 135, 154]. However, the detailed description of this behaviour is still not clear. In particular, a quantitative description of μ_{Fe} though the $R(Al_{1-x}Fe_x)_2$ series is still missing.

In relation to the saturation mechanism of the magnetization, Grössinger *et al.* have suggested that the step-like increases on the M(H) curves may be explained in terms of lattice distortions.[135] On the other hand, Oesterreicher regards the S-type behaviour as the result of either metamagnetism or, more likely, magnetic hardness arising from domain wall effects.[152] To this respect, several neutron diffraction experiments (ND)[135, 152, 153, 154] report a low-ordered rare-earth sublattice moments and reveal the "lost part" as a disordered component, i.e. the magnetic moments are not totally collinear. This "partial quenching" of M_R has been reported to be connected either with changes of the free electron concentration or with crystallographic disorder. In relation to the latter possibility, the partial quenching of M_R can be explained as follows: in systems where an anisotropic R is placed into a randomized environment, crystal field effects on R dictate a partially randomized magnetic structure. Moreover, combination of magnetic disorder and large anisotropy fields can combine to be responsible for very thin domain walls. As a result, these domain walls are pinned at obstacles of atomic dimension giving rise to the development of strong magnetic hardness.[136] The combination of these two effects can be also at the origin of the noticeable increase of magnetization even at high applied fields as, within this framework of disorder and strong magnetocrystalline anisotropy, the saturation is then hardly obtained.[135, 152, 155] This would also explain why Gd compounds saturates more straightforwardly and shows practically no hardness, as Gd has not angular contribution to the magnetic moment. Moreover, Grossinger *et al.* have suggested that Dy Laves phases show a change of the easy magnetization direction (EMD) from [001] for x = 1 to [111] for x = 0.9. This implies that Tb, Dy, and Er diluted

compounds would exhibit the same [111] EMD. This may explain why diluted Ho compounds show a slightly different behaviour, as the detailed magnetic behaviour of each sample will depend on the specific R and its interaction with the CEF.

To this respect, it is interesting to know that a similar magnetic behaviour has been also observed for (R,R')Al_2 compounds.[164, 165, 166, 167] In these compounds the partial quenching of M_R is explained in terms of Random Magnetic Anisotropy (RAM) and Spin Glass behaviour.

As we can see from the above scenario, the precise characterization of the behaviour of μ_{Fe} and μ_R as Fe is substituted by Al throughout the $R(Al_{1-x}Fe_x)_2$ series is still an open problem. This interesting study is, however, beyond the objectives of this thesis. Indeed, in this thesis we are mainly involved into providing a full understanding of the XMCD of R-T intermetallics. This is the reason why we will focus on the combined study of M(H,T) and XMCD at H = 5 kOe and T = 5 K. Although M(H) curves show that these conditions are not enough to completely reach saturation, the existing state is expected to be close to the ideal situation with saturated moments, both μ_{Fe} and μ_R, and ferrimagnetic coupling between R and Fe sublattices.

The values of the magnetization measured at T = 5 K in an applied magnetic field H = 50 kOe are reported in Table 6.6. From the total magnetization values we have derived μ_R and μ_{Fe} by applying a simple two sublattice model. We have assumed that the total magnetization of the $R(Al_{1-x}Fe_x)_2$ compounds, M_{Tot}, corresponds to the simple $\vec{M}_{Fe} + \vec{M}_R$ addition, where M_R and M_{Fe} are respectively the magnetization of the rare-earth and iron sublattices. In addition, several alternative approximations have been considered to derive the values of μ_R and μ_{Fe}:

(*a*) M_{Fe} is assumed to correspond to the magnetization of one $R(Al_{1-x}Fe_x)_2$ compound in which R is non magnetic, i.e. Y or Lu, and that it remains independent on R. Thus, for example, M_{Fe} in $Er(Al_{0.25}Fe_{0.75})_2$ is assumed to be equal to M_{Fe} in $Lu(Al_{0.25}Fe_{0.75})_2$.

(*b*) Alternatively, μ_{Fe} can be assumed to be the iron magnetic moment of one RFe_2 compound in which R is non magnetic, i.e. Y or Lu. That is, the magnetic moment of Fe remains the same independently on both R and x. Thus, for example in $Er(Al_{0.75}Fe_{0.25})_2$, μ_{Fe} is assumed to be the same as in $LuFe_2$.

Otherwise, we can apply different approximations for the magnetization of the R sublattice and derive the values of μ_{Fe}:

Sample	M ($\mu_B/f.u.$)	T_C (K)	Sample	M ($\mu_B/f.u.$)	T_C (K)
YFe_2	2.87	541			
$Y(Al_{0.25}Fe_{0.75})_2$	0.60	50			
$Y(Al_{0.50}Fe_{0.50})_2$	0.22	PM			
$Y(Al_{0.75}Fe_{0.25})_2$	0.14	PM			
$Pr(Al_{0.75}Fe_{0.25})_2$	1.81	35	$PrCo_2$	3.37	40
$PrAl_2$	2.94	33			
$Nd(Al_{0.75}Fe_{0.25})_2$	2.23	65	$NdCo_2$	3.68	100
$NdAl_2$	2.39	79			
$GdFe_2$	3.91	793	$GdCo_2$	5.00	400
$Gd(Al_{0.25}Fe_{0.75})_2$	4.92	420	$Gd(Al_{0.5}Co_{0.5})_2$	6.86	100
$Gd(Al_{0.50}Fe_{0.50})_2$	5.64	265	$Gd(Al_{0.8}Co_{0.2})_2$	7.13	75
$Gd(Al_{0.75}Fe_{0.25})_2$	6.48	135			
$GdAl_2$	7.00	164			
$TbFe_2$	4.79	653	$TbCo_2$	6.32	235
$Tb(Al_{0.25}Fe_{0.75})_2$	6.09	354			
$Tb(Al_{0.50}Fe_{0.50})_2$	6.04	190			
$Tb(Al_{0.75}Fe_{0.25})_2$	6.54	90			
$TbAl_2$	8.70	109			
$DyFe_2$	6.45	628	$DyCo_2$	7.46	150
$Dy(Al_{0.25}Fe_{0.75})_2$	6.56	280			
$Dy(Al_{0.50}Fe_{0.50})_2$	6.36	130			
$Dy(Al_{0.75}Fe_{0.25})_2$	6.04	60			
$DyAl_2$	9.45	58			
$HoFe_2$	6.54	606	$HoCo_2$	7.98	78
$Ho(Al_{0.25}Fe_{0.75})_2$	7.26	214	$Ho(Al_{0.2}Co_{0.8})_2$	7.96	
$Ho(Al_{0.50}Fe_{0.50})_2$	7.63	85	$Ho(Al_{0.50}Co_{0.50})_2$	7.81	20
$Ho(Al_{0.75}Fe_{0.25})_2$	7.29	40	$Ho(Al_{0.7}Co_{0.3})_2$	6.81	17
$HoAl_2$	9.25	28			
$ErFe_2$	5.57	582	$ErCo_2$	7.15	32
$Er(Al_{0.25}Fe_{0.75})_2$	6.38	140			
$Er(Al_{0.50}Fe_{0.50})_2$	6.39	60			
$Er(Al_{0.75}Fe_{0.25})_2$	6.03	26			
$ErAl_2$	7.90	13			
$LuFe_2$	2.86	582	$Lu(Al_{0.1}Co_{0.9})_2$	1.16	90
$Lu(Al_{0.25}Fe_{0.75})_2$	0.70	60			
$Lu(Al_{0.50}Fe_{0.50})_2$	0.23	PM			

Table 6.6: II. Magnetic parameters of the $R(Al_{1-x}Fe_x)_2$ compounds: M is the magnetization measured at T = 5 K and H = 5 kOe and T_C is the Curie temperature obtained as the inflection point of the M(T) curves recorded at H = 1 kOe.

(c) We assume free ion moment for each R independently on x.

(d) μ_R is assumed to be that obtained for the RAl_2 compounds, independently on x.

The results of applying these procedures are displayed in Figure 6.9.

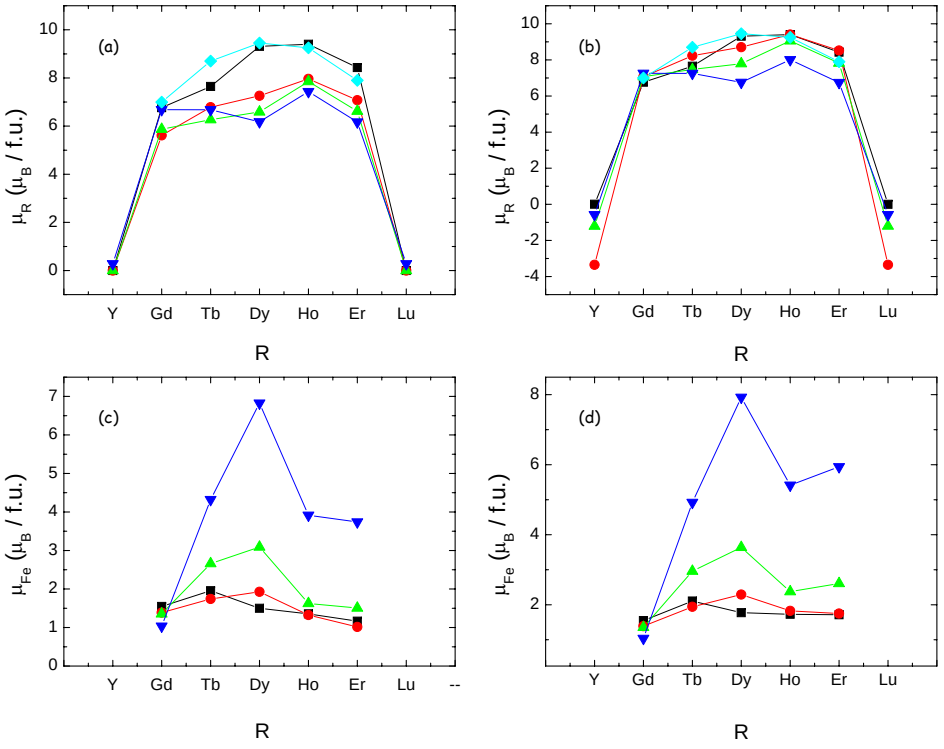

Figure 6.9: μ_R and μ_{Fe} are the rare-earth and iron magnetic moments derived from M(50 kOe, 5 K) by applying the two-sublattice model and by assuming different approximations either for μ_R or for μ_{Fe} (see details in the text).x=0 (♦), x = 0.25 (▼), x = 0.50 (▲), x = 0.75 (●) and x = 1(■).

In the case of Gd compounds, our results can be explained with the simplest model, i.e., a constant μ_R, a slightly decreasing μ_{Fe} (from 1.55 μ_B in $GdFe_2$ to 1.04μ_B in $Gd(Al_{0.75}Fe_{0.25})_2$) and all the magnetic moments being collinearly ordered (ferrimagnetic coupling between the Fe and R sublattices). These results are in agreement with previous results on the $Gd(Al_{1-x}Fe_x)_2$ series[150, 151] indicating an almost constant magnetic moment of iron upon dilution even at high Al contents. The small decrease of the iron magnetic moment has been ascribed to the reduced exchange splitting of Fe 3d states as the iron is substituted by aluminium.

A more complex situation is found for the rest of the compounds. According to Fig. 6.9 (*a*), if the behaviour of μ_{Fe} upon Al substitution is the same no matter the R (i.e., if μ_{Fe} behaves as in the $Lu(Al_{1-x}Fe_x)_2$) series), then the magnetic moment of the rare-earth clearly decreases in the diluted compounds. For instance, μ_{Ho} decreases ~21% (from 9.40 μ_B in $HoFe_2$ to 7.43μ_B in $Ho(Al_{0.75}Fe_{0.25})_2$). If, on the other hand, a constant, $\sim$ 1.4 μ_B, magnetic moment is assumed for the Fe atoms (case *b*), μ_R also decreases but much slightly than in the previous case. Thus, the decrease of μ_{Ho} is in this case $\sim$ 15% (from 9.40 in $HoFe_2$ μ_B to 8.01μ_B in $Ho(Al_{0.75}Fe_{0.25})_2$).

Conversely, when μ_R is approximated to a constant value (either the moment found for RAl_2 or the free ion value), then an almost constant μ_{Fe} is obtained for compounds with 100% and 75% of Fe. ($\mu_{Fe} \approx 1.4$ μ_B in case c and $\mu_{Fe} \approx 1.7$ μ_B in case d). By contrast, μ_{Fe} strongly increases for higher Al contents. This strong increase of μ_{Fe} makes no sense at all and clearly indicates a reduction of M_R, which would be in agreement with the "lost disordered component" reported by Neutron Diffraction data. [135, 152, 153, 154]

Therefore, our results indicate that the magnetic moments in the diluted compounds are partially disordered (i.e. they are non-collinear and the orientation and angle of deviation from the magnetic axis varies locally). Consequently, a precise description of μ_{Fe} and μ_R through $R(Al_{1-x}Fe_x)_2$ is unattained due to the difficulty of separating unambiguously the magnetic moment of the iron and the rare-earth. The value of the R moment is uncertain due to quenching effect of the crystal field and an accurate contribution of the transition metals to the total magnetization cannot be derived. In addition, Oesterreicher has proposed that there is an electron transfer from R and Al to Fe giving rise to decrease of μ_{Fe} with Al increase. This transfer will occur to the extent that Fe(Co) becomes nonmagnetic. Investigations of the L_3 emission spectra show that the increase of Al causes larger spread of the iron 3d wavefunction and the corresponding delocalization makes charge transfer between Fe(3d) and Dy(5d) bands possible.[168].

On the other hand, Gd compounds are free from the quenching effect of the crystal field and therefore, the magnetic moments of both μ_{Fe} and μ_R have been easily disentangled. Despite the role of electron transfer giving rise to the decrease of μ_{Fe} cannot be completely rejected, the results on the $Gd(Al_{1-x}Fe_x)_2$ series[150, 151] indicate an almost constant magnetic moment of iron upon Al dilution even at high Al contents (a gradual reduction from $\mu_{Fe} = 1.55$ μ_B in $GdFe_2$ to 1.04μ_B in $Gd(Al_{0.75}Fe_{0.25})_2$).

In addition, taking into account that the reported magnetization values correspond to low temperatures (T = 5 K) and high magnetic fields (H = 5 kOe), it seems reasonable to consider that, among the possible situations,

the most feasible one is that where *i)* the magnetic moments are close to collinearity, *ii)* M_R is slightly reduced due to small deviations from collinearity and *iii)* M_{Fe} also exhibits a minor decrease, similar to that found for Gd series. Indeed, in $R(Al_{0.25}Fe_{0.75})_2$ compounds the magnetization values reasonable fit with a model where the only effect is the dilution one, i.e. if we assume that μ_{Fe} and μ_R are kept constant.

Finally, it should be noted that the determination of the saturation magnetization (M_{sat}) by Honda (M *vs* $1/H$) plots is not a good method to overcome this difficulty. Indeed, in those cases in which the observed linear increase of M(H) is not minor at high fields, the saturation magnetization (M_{sat}) determined from Honda (M *vs* $1/H$) plots bears little reliability as the M(H) curves are far from saturation.

The thermal dependence of the magnetization has been summarized in figure 6.10, where the zero field cool (ZFC) curves recorded under an applied magnetic field of 1000 Oe are shown. From the M(T) curves the Curie temperature, T_C, has been obtained as the inflection point. The T_C values, included in table 6.6, will give us information about the strength of the T-T, R-T and R-R couplings.

For the sake of completeness, M(T) curves have been also measured at a higher magnetic field, H = 35 kOe, for some $R(Al_{1-x}Fe_x)_2$ systems. As it can be seen in Fig. 6.11 the modification of the thermal behaviour is the expected one: the magnetic transition spreads and the onset of magnetic ordering shifts towards higher temperature.

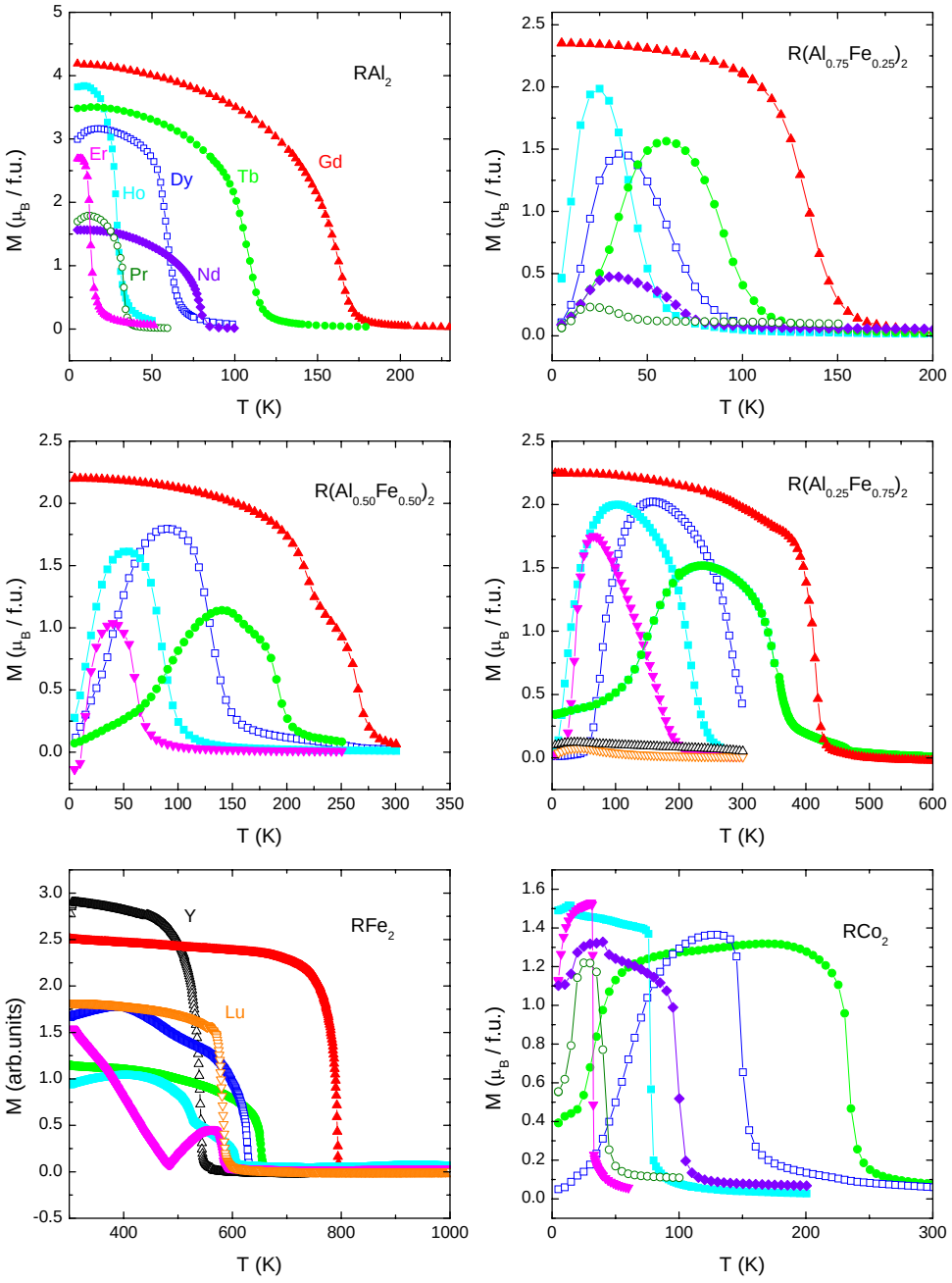

Figure 6.10: Magnetization of the $R(Al_{1-x}Fe_x)_2$ systems as a function of the temperature. Those compounds whose T_C is lower than room temperature were measured in a SQUID magnetometer under an applied magnetic field H = 1 kOe, whereas those compounds whose T_C is higher than room temperature where measured in a Faraday balance.

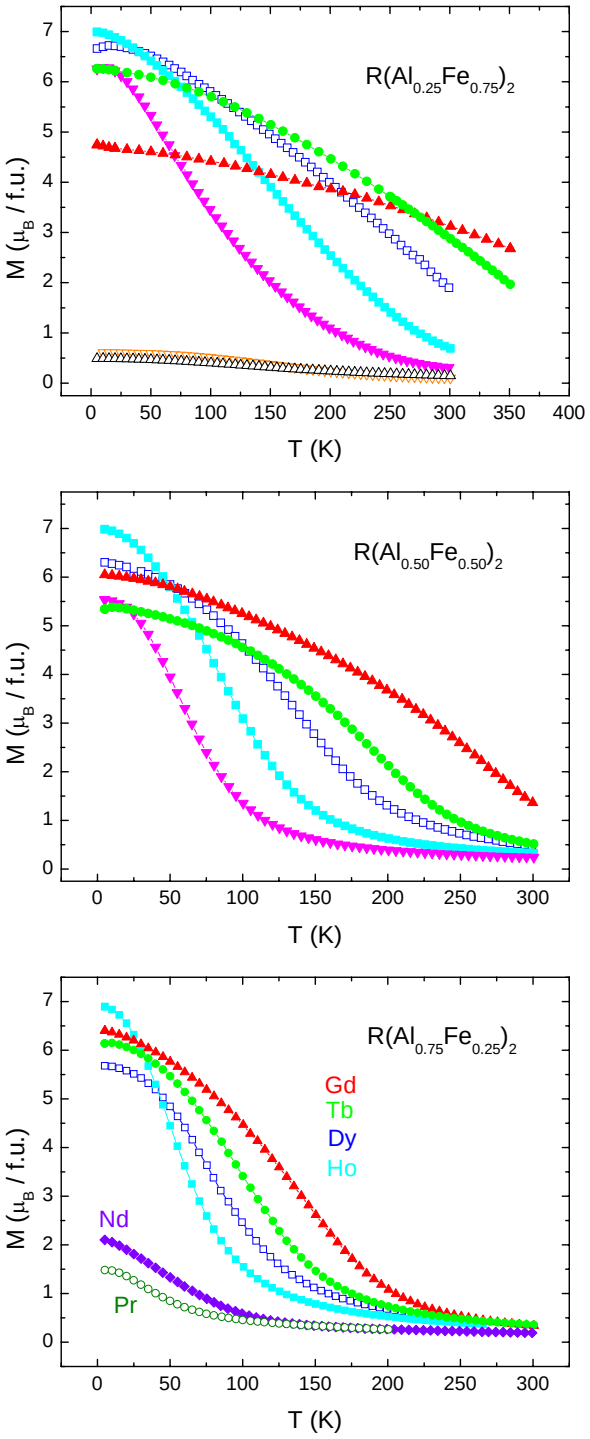

Figure 6.11: Magnetization of the $R(Al_{0.25}Fe_{0.75})_2$ (top), $R(Al_{0.50}Fe_{0.50})_2$ (middle) and $R(Al_{0.75}Fe_{0.25})_2$ (bottom) systems as a function of the temperature, measured under an applied magnetic field H = 35 kOe.

6.5 Mössbauer measurements

As we have seen, magnetization measurements, M(H,T), do not allow us to clearly discern between Fe and R contributions in all the cases. Consequently, the detailed magnetic behaviour of the iron sublattice as a function of its concentration in the compound is still missing. Within this framework we have carried out a Mössbauer study through the $R(Al_{1-x}Fe_x)_2$ series. Mössbauer spectroscopy is a element-selective magnetometry. Therefore, we expect this technique will provide the required additional information about the magnetic moment of iron atoms in $R(Al_{1-x}Fe_x)_2$. The site selectivity of Mössbauer spectroscopy will allow us to obtain valuable information about the magnetic moment of Fe as a function of the number of Al (Fe) atoms around the absorbing Fe atom. In addition, from the analysis of the variation of the hyperfine parameters, specially the hyperfine magnetic field, B_{hf}, across the binary RFe_2 series, we expect to obtain further information about the R-Fe interaction.

The Mössbauer study has been divided into two parts. In the first part room temperature spectra have been recorded in the binary compounds to study the behaviour of the Fe sublattice in the parent compounds and the effect of the specific rare earth. In the second part, the spectra of $Gd(Al_{1-x}Fe_x)_2$, $Tb(Al_{1-x}Fe_x)_2$ and $Ho(Al_{1-x}Fe_x)_2$ compounds have been analyzed at room temperature and T = 15 K trying to disentangle the effect of Al replacement in the Fe sublattice.

6.5.1 Pure RFe_2 compounds

Mössbauer spectral measurements and analysis

In RFe_2 compounds the iron atoms occupy just one inequivalent, 16d, crystallographic site. As a consequence, the iron atoms have just one near neighbour, nn, environment and the Mössbauer spectrum should consist in just one sextet. However, further subdivision of this sextet assigned to the 16d iron site may be necessary if multiple relative orientations of V_{zz} (the principal axis of the electric field gradient tensor, EFG) and B_{hf} (or, equivalently, the easy magnetization direction, EMD) are possible at this iron site. Depending on the point symmetry of the iron site, V_{zz} can be along different crystallographic directions. As a consequence, a crystallographic site may become different sites from the point of view of the hyperfine interactions as they depend on the relative angle, θ, between the direction of B_{hf} and V_{zz}. In particular, the different orientations of both magnitudes can lead to different quadrupole shifts (Eqs. 1.30 and 1.31) and also may affect the hyperfine field through the anisotropic component of B_{hf} (Eq. (1.44)).

In order to know the correct Mössbauer spectral distribution for each compound it is necessary to know the possible V_{zz} directions at each iron site and the EMD. In the case of RFe_2, the point symmetry of each iron atom is $\bar{3}$m with the threefold axis lying along one of the [111] directions.[169] The EMD can be [111], [001] or [101] depending on the R lanthanide in the RFe_2 compound. This leads to three different situations summarized in table 6.7:

EMD	θ	site %	ε(I)/ε(II) ($\varepsilon \propto (3cos^2\theta - 1)$)	R
[111]	θ (I) = 70°32'	75	-0.33	Y, Gd, Tb, Er, Lu
	θ (II) = 0	25		
[001]	θ (I) = 54.7°	100		Dy, Ho
[101]	θ (I) = 35 °16'	50	-1	Sm
	θ (II) = 90 °	50		

Table 6.7: EMD, relative angle between V_{zz} and B_{hf} (θ), percentage of the site corresponding to each θ and ε(I)/ε(II) ratio for the different RFe_2 compounds.[169, 170]

1. EMD = [111]. In the 75% of the sites θ is 70°32', whereas 25% of the sites have θ = 0°. Therefore, the Mössbauer spectrum will be made up of two sextets with relative intensities 3:1. They will be called sites I and II respectively. As the value of θ is known in each case, we can calculate the value of the ε(I)/ε(II) ratio (-0.33).

2. EMD = [001]. All the sites will be equivalent and the Mössbauer spectrum will consist on just one sextet. Besides, the relative angle between B_{hf} and V_{zz} is the so-called magic angle, θ = 54.7°, and so the quadrupole shift, ε, is zero.

3. EMD = [101]. θ can be 35 °16' (in the 50% of the sites) or 90 ° (also in 50% of the sites). In this case, the Mössbauer spectrum consists on two sextets with relative intensities 1:1. As in case 1, they will be called sites I and II respectively. The value of θ is known in each case, so we can calculate the value of the ε(I)/ε(II) ratio (-1).

Therefore, three different fitting models are proposed for the Mössbauer spectra of RFe_2. When the EDM lies along the [001] direction, the Mössbauer should be fitted with just one sextet. In such a case, three hyperfine parameters, B_{hf}, δ and ε, one linewidth and the total absorption area are involved in the fit. In the same way, when two sextets are used to fit the spectrum, five

hyperfine parameters, one linewidth and the total absorption area are involved in the fit. In this case it has been considered that since the magnetically inequivalent pairs are crystallographically equivalent, their isomer shifts should be identical.[171]

The validity of these models will be checked from the goodness of the fit and by the requirement of physically reasonable hyperfine parameters. In some cases, the choice of the best suited model to fit a spectrum was not straightforward. In these cases, the following criteria have been regarded:

The linewidths were allowed to vary in the fit from 0.27 mm/s, the linewidth obtained for the iron foil used in the calibration procedure, to $\approx$ 0.40 mm/s. Whenever the fit yielded widths larger than these, it was discarded as non-physical.

In a general case, the goodness of a fit can be estimated from the value of χ^2 that is calculated as:[172]

$$\chi^2 = \sum_{i=1}^{N} \left(\frac{y_i - y(x_i; a_1 ... a_M)}{\sigma_I} \right)^2, \tag{6.1}$$

were (x_i, y_i) (i = 1,...N) are the experimental data, $y(x_i; a_1 ... a_M)$ is the function describing the model we are using to fit the experimental data and a_j (j = 1,...M) are the parameters to fit. This χ^2 parameter has been designed in such a way that the lower its value is, the better the agreement between both calculated and experimental points. Indeed, the program used to perform the fit determine the value of the parameters by minimizing this χ^2 function.

In all cases the estimated errors of the obtained hyperfine parameters are at most $\pm$ 0.3 T for the hyperfine fields, $\pm$ 0.020 mm/s for the isomer shifts and $\pm$ 0.050 mm/s for the quadrupole shifts. The values of the isomer shifts are relative to the α-iron at 295 K. The observed linewidths were typically of 0.28 $\pm$ 0.02 mm/s for RFe_2 compounds. Below, the different tested models are discussed.

R = Y, Tb, Gd, Er and Lu, (EMD = [111])

In the case of R = Y, Tb and Er a [111] EMD has been proposed (see Table 6.7). The Mössbauer spectrum is clearly made up of two contributions with relative intensities 3:1, in agreement with a [111] EMD, as it can be seen in figure 6.12. For this fit, the relative intensities of each contribution have been kept fixed and we have considered δ(I) = δ(I) and LW(I) = LW(II). The observed linewidths are $\sim$ 0.28 mm/s, i. e. close to the calibration linewidth, for all the compounds. The corresponding hyperfine parameters are given in

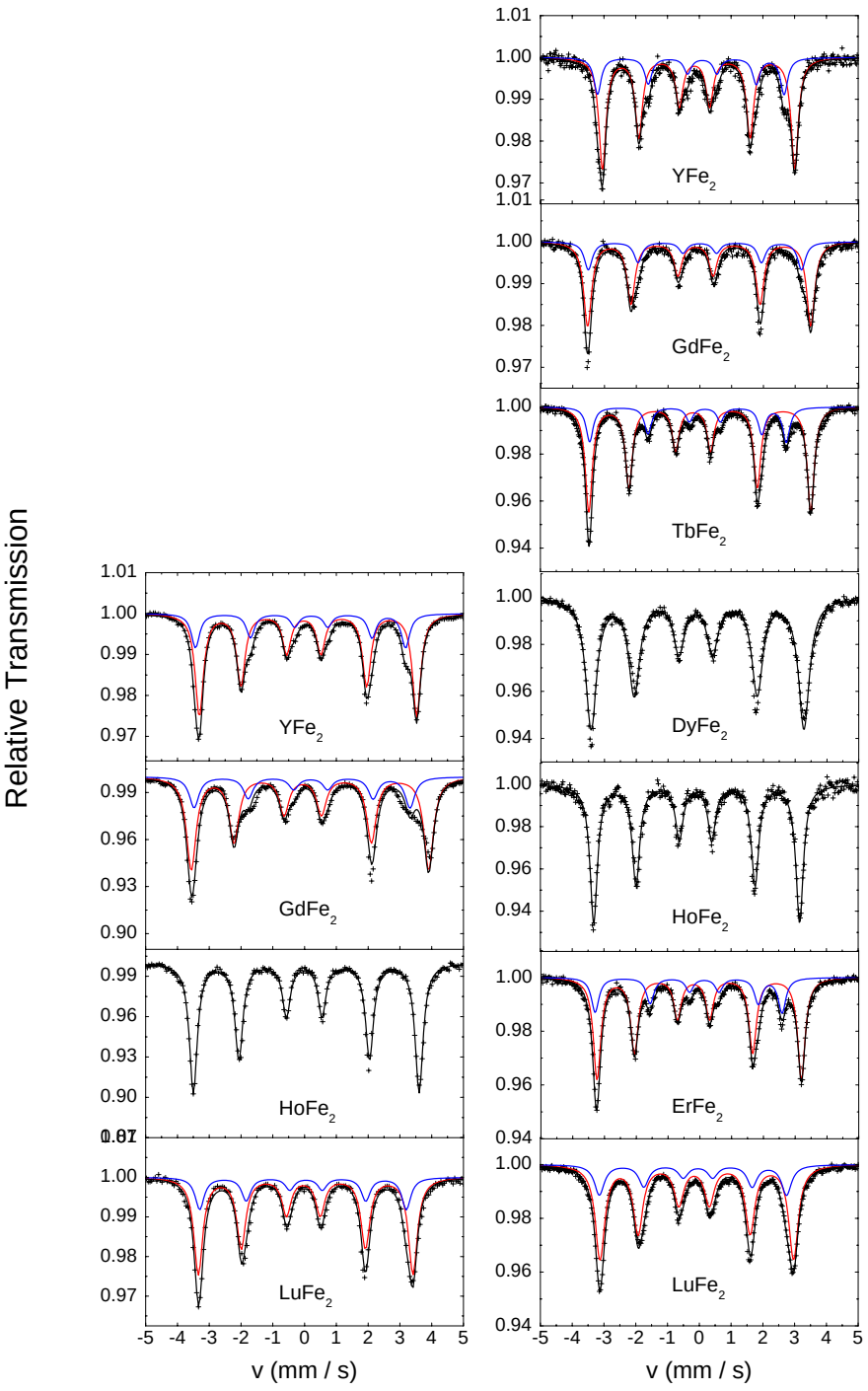

Figure 6.12: The Mössbauer spectra of RFe_2 recorded at T = 15 K (left) and T = 295 K (Right)

table 6.8. As we can see, the ε(I)/ε(II) ratio is close to the theoretical value (-0.33). This shows the adequacy of the model for the fitting of these spectra.

In the case of $GdFe_2$ and $LuFe_2$ the presence of two sextets is not so straightforward as for R = Y, Tb and Er. As it can be seen in Fig.6.12 one cannot distinguish two different sextets in a first sight. However, it becomes clear when one compares the results of fitting the spectra to one sextet or to two sextets with relative intensities 3:1. For both compounds, the linewidths are slightly smaller in the latter case. In addition, in $GdFe_2$ $\chi^2 = 1198$ if the fitting is done with one sextet and $\chi^2 = 778$ if we consider two sextets (For $LuFe_2$: $\chi^2 = 1661$ in the one sextet fitting and 1133 in the two sextets fitting). Consequently, both the linewidth and the value of χ^2 indicate that the Mössbauer spectra should be fitted with two sextets with relative intensities 3:1. As one can see in Table 6.8, the values obtained for ε in $LuFe_2$ are much smaller than those found in the case of R = Y, Tb and Er. As a consequence, the two sextets I and II strongly overlap making difficult to disentangle the two contributions in the fitting procedure. Moreover, since the values of ε(I) are within the experiential error, the ε(I)/ε(II) ratio can be strongly affected by this error. This would explain why for $LuFe_2$ the ε(I)/ε(II) ratio is -0.53 instead of the theoretical -0.33 value. In the case of $GdFe_2$ there is also a strong overlap of the two contributions, but the ε(I)/ε(II) ratio (-0.76) is clearly different from the theoretical value (-0.33). This result very likely reflects the existence of a canting of the Fe magnetic moments in $GdFe_2$, as proposed by K. N. Martin[170]. The presence of a canting in the $LuFe_2$ seems unlikely because this would imply the existence of a significant (localized $4f$) magnetic moment at the Lu site. Even if we assume the existence of an induced 5d moment in Lu, this moment will be very small to give rise to magnetocrystalline anisotropy.

R = Dy and Ho (EMD = [001])

According to the scheme above (see Table 6.7), in these two cases the experimental spectrum should be easily fitted with just one sextet. The fitting is very good in the case of $HoFe_2$, as it can be seen in the figure 6.12, and in the hyperfine values given in Table 6.8.

The fit of the $DyFe_2$, however, is not so good, having a wide linewidth. For this reason, we have also tried to fit the spectrum to two sextets with relative intensities 3:1 (EMD = [111]) and to two sextets with relative intensities 1:1 (EMD = [101]). However, no marked improvement has been found with the last two options neither in the value of χ^2 (χ^2 are 1672, 1332 and 1319 respectively), nor in the linewidths. Moreover, the values of the ε(I)/ε(II) ratio are very different from the theoretical value.

Previous works have also found the same problem in the fit of the $DyFe_2$

Compound	T(K)	m	Prob.	δ(mm/s) $\pm$0.02	ε, ΔE_Q (mm/s) $\pm$0.05	B_{hf} (T) $\pm$0.3
YFe_2	15	0	75	-0.042	0.066	21.32
		0	25	-0.042	-0.169	20.61
		Total aver.		-0.042	0.001	21.14
YFe_2	295	0	75	-0.086	0.065	18.86
		0	25	-0.086	-0.180	18.30
		Total aver.		-0.086	0.004	18.72
$LuFe_2$	15	0	75	-0.002	0.036	21.05
		0	25	-0.002	-0.047	20.27
		Total aver.		-0.002	0.015	20.85
$LuFe_2$	295	0	75	-0.120	0.042	19.0
		0	25	-0.120	-0.079	18.4
		Total aver.		-0.120	0.012	18.85
$GdFe_2$	15	0	75	0.057	0.114	23.30
		0	25	0.057	-0.136	21.18
		Total aver.		0.057	0.050	22.77
$GdFe_2$	295	0	75	-0.077	0.088	22.08
		0	25	-0.077	-0.023	21.34
		Total aver.		-0.077	0.060	21.89
$TbFe_2$	295	0	75	-0.089	0.105	21.77
		0	25	-0.089	-0.268	19.29
		Total aver.		-0.089	0.012	21.25
$DyFe_2$	295	0	100	-0.100	0.029	20.87
$HoFe_2$	15	0	100	0.021	0.032	22.15
$HoFe_2$	295	0	100	-0.100	0.018	20.20
$ErFe_2$	295	0	75	-0.107	0.089	20.05
		0	25	-0.107	-0.254	18.33
		Total aver.		-0.107	0.003	19.63

Table 6.8: Hyperfine parameters of the RFe_2 compounds. In all cases the isomer shift is taken relative to α-iron at 295 K.

spectrum [162]. In these works, the experimental Mössbauer spectra have been fitted with just one sextet and the observed asymmetry is associated to the magnetic moments being slightly canted. Including this canting effect in the fitting model would probably give rise to a better fit. Unfortunately, the canting angle is not known, so we will consider our first fit to one sextet (shown in Fig. 6.12) is the best suited one. With this fit, part of the information about the compound is missing. Nevertheless, this shortage will not affect (at least drastically) to the average values of the hyperfine parameters.

Analysis of the hyperfine parameters

In Fig. 6.13 we show the hyperfine parameters B_{hf}, δ and ε as a function of the atomic number of R.

In agreement with previous results for other R-Fe series,[41] there is an

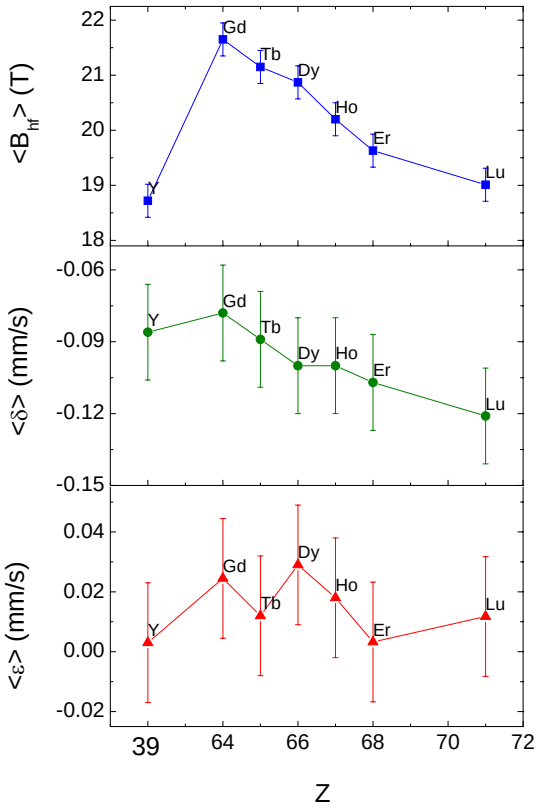

Figure 6.13: Mössbauer hyperfine parameters of the RFe_2 compounds obtained at room temperature as a function of the atomic number, Z, of the rare-earth.

evident dependence of B_{hf} on the rare-earth: B_{hf} is maximum for R=Gd and decreases from Gd to Lu. By contrast to the isomer shift (see Fig. 6.15), the hyperfine field does not present a linear dependence with the volume. This indicate that the modification of B_{hf} is not due to the lanthanide contraction but to the magnetism of the rare-earth. More precisely, this dependence is due to the rare-earth sublattice transferred field, B_{tR}, which is the field due to the 4s spin density polarized by the magnetic moments of the R atoms in the first neighbour shell.

In the case of binary RFe_2 compounds there is just one crystallographic site and just one value for μ_{Fe}. In this case, the iron transferred field can be written as:

$$B_{tFe} = \sum_l \zeta_{Fe}(l,k)\mu_{Fe}(l) = \zeta_{Fe} Z_{Fe} \mu_{Fe} = 6\zeta_{Fe}\mu_{Fe} \qquad (6.2)$$

where Z_{Fe} is the number of iron nn. Therefore, neglecting the B_{anis} term:

$$B_{hf} \approx (\alpha + \beta + 6\zeta_{Fe})\mu_{Fe} + B_{tR} \approx f\mu_{Fe} + B_{tR} \tag{6.3}$$

Besides, to a first approximation, the rare earth contribution to B_{hf} may be analyzed in terms of a two sublattice model. Accordingly, the total hyperfine field can be written as:

$$B_{hf} = B_{Fe} + B_{tR} = B_{Fe} + \langle\tilde{\zeta}_R\rangle Z_R\gamma_R\mu_R \tag{6.4}$$

where B_{Fe} represents the contribution coming from the iron sublattice, and B_{tR} represents the contribution coming from the rare earth sublattice. For μ_R the ion-free value is assumed.

In Fig. 6.14 the experimental relationship between B_{hf} and $\gamma_R\mu_R$ is shown. As it can be seen, it shows a good agreement with the proposed model in Eq. (6.4). The small differences might be due to the fact that our measurements were done at room temperature and, consequently, the ion-free approximation for μ_R is not completely valid. Also the small cantings, previously suggested for $DyFe_2$ and $GdFe_2$ compounds, may explain the divergence from the linear dependence. Differences may also be explained in terms of a significant orbital contribution, B_{orb}, as we are dealing with compounds of high symmetry. Anyway, the observed linear dependence reflects that the B_{Fe} term is nearly the same for all the members of the series and it can be approximately taken as the value of B_{hf} for $LuFe_2$. That is, the Fe sublattice behaves in a similar way in all the compounds and the differences in B_{hf} found in the RFe_2 compounds are due to the B_{tR} term. This result agrees with similar results found for other R-Fe compounds.[41].

According to Eq. (1.20), the isomer shift, δ, is proportional to the difference of the density of s electrons between the nucleus and the absorber. As δ is negative, this indicates that the electronic density in the absorber is higher than in the source. Moreover, the decrease of the isomer shift with atomic number indicates an increase of the density of s electrons in the nucleus of the absorber. Provided that the number of s electron is the same through the RFe_2 series, the observed variation is likely due to a volume effect. As the atomic number increases, the cell parameter decreases. This decrease implies a reduction of the Wigner-Seitz volume of the absorbing Fe atom, i.e. a reduction of the "available volume" around the Fe atom; so that the electronic density at the Fe nucleus increases giving rise to the observed decrease of the isomer shift. The volume dependence is clearly observed in Fig.6.15 where δ presents a linear dependence with the cell volume.

The average values of the quadrupole shift are very small, close to zero,

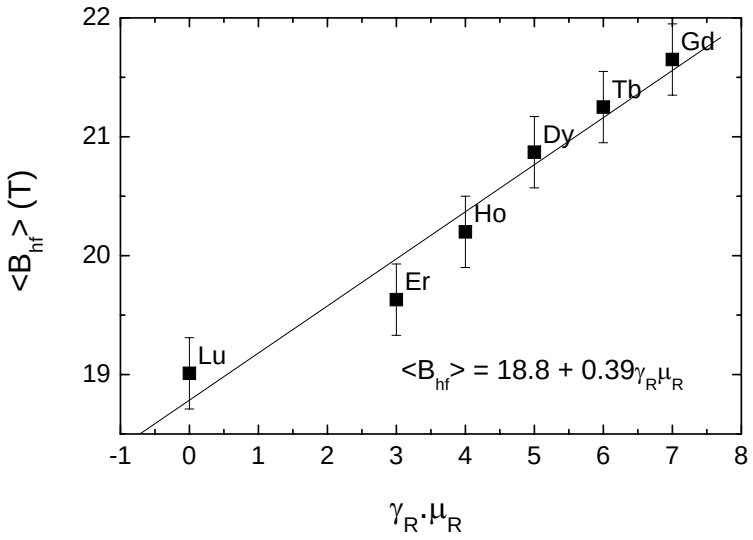

Figure 6.14: Hyperfine field at room temperature of the RFe_2 compounds.

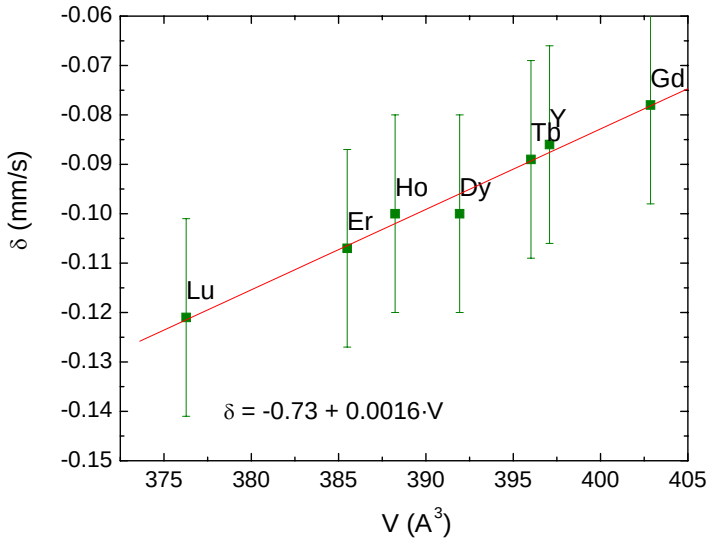

Figure 6.15: Isomer shift at room temperature of the RFe_2 compounds.

and almost constant independent on the atomic number (constant within the error). This is a reasonable result if one takes into account that we are dealing with cubic compounds, which have a high symmetry.

6.5.2 Diluted $R(Al_{1-x}Fe_x)_2$ compounds

Mössbauer spectral measurements and analysis

In these compounds, the aluminum atoms are randomly distributed over the 16 d sites (the "iron sites") only. As a consequence, the iron atoms have a random distribution of near-neighbour (nn) environments, which is treated as a binomial one:[174]

$$P(n, m, \xi) = \frac{n!}{m!(n-m)!}\xi^m(1-\xi)^{n-m}, \tag{6.5}$$

where n is the number of possible sites that the Al atom can occupy (n = 6), m = 0, 1, ...n, is the number of Al atoms in a given environment and ξ is the probability of finding Al atoms at the iron sites, which in this case coincides with the concentration of Al atoms.

In the case of $R(Al_{1-x}Fe_x)_2$, seven different nn environments are possible for the iron site as described in Table 6.9. The iron atoms surrounded by a given environment will contribute to the total Mössbauer spectrum with a relative intensity given by the probability associated to this environment. The probability of each environment depends on the Al concentration; if the compound has a low Al concentration (25%), the most probable environments will be those with few Al atoms, whereas as Al concentration increases, the environments with many Al atoms become more probable.

Site	m	x = 0.75	x = 0.50	x = 0.25
16d	0 (6 Fe)	17.8	1.6	0.02
	1 (5 Fe, 1 Al)	35.6	9.4	0.4
	2 (4 Fe, 2 Al)	29.7	23.4	3.3
	3 (3 Fe, 3 Al)	13.2	31.2	13.2
	4 (2 Fe, 4 Al)	3.3	23.4	29.7
	5 (1 Fe, 5 Al)	0.4	9.4	35.6
	6 (6 Al)	0.02	1.6	17.8

Table 6.9: Probability (%) of the different environments for the Fe atoms in $R(Al_{1-x}Fe_x)_2$ compounds with x = 0.25, 0.50 and 0.75 assuming statistical occupancy of Al-Fe atoms. A cubic C15 structure has been also assumed for the $R(Al_{0.5}Fe_{0.5})_2$ compounds. m is the number of Al atoms in each environment.

In compounds with 75% of Fe one should consider, in principle, 7 contributions to the total Mössbauer spectrum. Nevertheless, due to the small contribution coming from the iron atoms with environments containing 3 or more nn aluminum atoms, only 4 contributions for each site, labeled as $16d_m$ with m = 0, 1, 2 and 3, will be considered (see table 6.9). The $16d_m$ sextet (m = 0, 1, 2) represents the contribution coming from the iron sites with m aluminum nn, and the $16d_3$ sextet represents the average contribution coming from the iron sites with 3 or more aluminum nn, though it is mainly contributed by those iron sites with only 3 nn aluminum atoms. Hence, 4 different sextets will be used to fit the Mössbauer spectra of $R(Al_{0.25}Fe_{0.75})_2$. In the same way, we will only consider five contributions to the Mössbauer spectra corresponding to compounds with 50% of Fe (m = 1, which actually include m = 0 and 1, m = 2, m = 3, m = 4 and m = 5, which include m = 5 and 6) and four contributions for compounds with 25% Fe (m = 3, which actually include m = 0, 1, 2 and 3, m = 4, m = 5 and m = 6). This kind of simplification is a common practice when fitting diluted compounds.[41] It should be noticed that the $R(Al_{0.5}Fe_{0.5})_2$ compounds actually crystallize in the C14 hexagonal structure, having two different sites for Fe. Therefore, we should considered two different sites to calculate the binomial distribution of possible environments around Fe atoms. Nevertheless, the analysis of such a situation becomes very intricate. Taking into account that, from the local point of view, both C14 and C15 structures are very similar, having the same distribution of nearest-neighbours, we have carried out the analysis of these spectra assuming a C14 structure. The goodness of the fit (see below) validates the application of this approximation.

Additional subdivision will be required when multiple relative orientations of B_{hf} and V_{zz} are present. The EMD of the diluted compounds is not known, but some authors have reported that the EMD of the $R(Al_{1-x}Fe_x)_2$ is very sentitive to the Al content. For example, it has been found a change of EMD from [100] in $DyFe_2$ to [111] in $Dy(Al_{0.10}Fe_{0.90})_2$.[135] Therefore, for diluted compounds we have tested the different fitting models corresponding to the different possible EMD. The best fit will give us information about the EMD in the compound.

Therefore, for compounds in the paramagnetic state, several different models will be checked depending on the Fe concentration: for compounds with x = 0.75 and x = 0.25, the easiest model consist on assuming that the EMD lies along the [100] direction. In such a case only 4 contributions are considered. Otherwise, if EMD lies along the [111] direction, each of these four sextets give rise to two different contribution with relative intensities 3:1, so that a total of eight sextets have been included in the fit. For compounds with 50% of Fe (x = 0.50), the corresponding Mössbauer spectra will be fitted either to a 5

sextets model (assuming a EMD in the [100] direction) or to a 10 sextets model (EMD in the [111] direction).

For compounds in the paramagnetic state the fitting has been done with the minimum number of doublets (one or two) required to fit each experimental spectrum. In analogy to the fitting procedure followed in the ferromagnetic range, seven different doublets should be used to fit our spectra according to the binomial model. However, due the poorly structured profile of these spectra, this results in an excess of adjustable parameters and the physical reliability is missing. The use of just one (or two) contribution prevents from obtaining detailed information dependent on the environment, but it will permit us to estimate the value of the averaged hyperfine parameters. It is worth noticing that in the case of paramagnetic compounds there is not magnetic hyperfine interaction and that the parameter accounting for the quadrupolar interaction is not the quadrupolar shift, ε, anymore, but the quadrupolar splitting, ΔE_Q.

The validity of the different tested models will be checked from the goodness of the fit and by the requirement of physically reasonable hyperfine parameters. In some cases, the choice of the best suited model to fit a spectrum was not straightforward. In these cases, the same criteria used for binary compounds, i.e., the values of the linewidth and the χ^2 parameter, have been regarded. For the diluted compounds, however, owing to the fact that we are in some cases gathering the contributions coming from different environments in just one contribution, a widening of the linewidths can be expected. In fact, the observed linewidths were typically of 0.38 ± 0.02 mm/s for all the compounds, a value slightly larger than the experimental calibration linewitdh, 0.27 mm/s. This broadening has also been observed in other R-Fe substituted compounds such us $RFe_{11}Ti$, $RFe_{11}TiH$, and $RFe_{11.5}Ta_{0.5}$ [41, 173] and, very probably is due to a non-negligible contribution of the second neighbour shell, and also to slight deviations from the nominal stoichiometry or to any possible aluminum spatial inhomogeneity. This high value could also be due to small deviations of the magnetic moments from the magnetic axis, i.e. due to the existence of cantings or non-collinearity of the magnetic moments.

In the fitting procedure of compounds in the ferromagnetic state, the relative intensities of the different spectra were kept fixed according to the theoretical value and the same value of LW was assumed for all the contributions. In the fitting of paramagnetic compounds, the relative intensities of the different spectra were let to vary. In addition, it has been considered that since the magnetically inequivalent pairs are crystallographically equivalent, their isomer shifts should be identical, $\delta(\mathrm{I}) = \delta(\mathrm{II})$.

In the following, we present and discuss the spectra of some selected compounds. Further work is in progress in order to obtain a complete Mössbauer

study of all the $R(Al_{1-x}Fe_x)_2$ series. Nevertheless, the results presented below already give us some interesting information.

$R(Al_{1-x}Fe_x)_2$ compounds (R = Y and Lu)

$Y(Al_{0.25}Fe_{0.75})_2$ and $Lu(Al_{0.25}Fe_{0.75})_2$ are both paramagnetic at room temperature. In both cases the spectrum has been fitted with two symmetric doublets, whose relative intensities were allowed to vary. The relative intensities of each doublet are 59 and 41 for $Y(Al_{0.25}Fe_{0.75})_2$ and 61 and 39 for $Lu(Al_{0.25}Fe_{0.75})_2$.

In $R(Al_{0.25}Fe_{0.75})_2$ the total probability of the m = 1 and m = 2 environments is 53 % and the probability of the environments with $m \geq 2$ is 47% (see table 6.9). Moreover, the larger the volume around the absorbing Fe atom, the larger its isomeric shift. Consequently, we can associate the doublet with the lower isomeric shift to Fe-rich environments (m = 0, 1) and the doublet with the higher isomeric shift to Al-rich environments ($m \geq 2$).

At T = 15 K, both spectra show the typical profile of a diluted compound.[41, 173] The 4 sextets model is clearly insufficient to fit the spectra, while it improves markedly when the [111] EMD splitting, i.e. 8 different sextets, is taking into account. The linewidths are between 0.38 and 0.40 mm/s, quite larger than the calibration one, 0.27 mm/s. Despite the large value of the linewidths, the goodness of the fits and the physical reliability of the values obtained for the hyperfine parameters indicate that taking 8 sextets according to a EMD = [111] (the same as in the binary compounds) is the best suited model. Moreover, the adequacy of the proposed model confirms that the Al atoms are randomly distributed over the Fe sublattice. To this respect, some authors have proposed an inhomogeneous distribution of Al giving rise to the existence of Fe clusters that may affect to the relative intensities of the different contributions.[149] According to our results, the Al is statistically distributed on $R(Al_{0.25}Fe_{0.75})_2$ (R = Y, Lu) compounds as the binomial distribution gives the correct intensities required to fit the recorded spectra. Moreover, those previous works did not include the EMD splitting due to the relative orientation between V_{zz} and B_{hf} in the fit of the Mössbauer spectra. Although the possible existence of a small amount of Fe clusters cannot be completely refused, its amount would be very small. Otherwise the proposed model stemming from a binomial distribution would not work.

The $Lu(Al_{0.50}Fe_{0.50})_2$ spectra recorded at both T = 15 K and T = 295 K are both a narrow paramagnetic doublet. This implies that there is not long range order. From these spectra we cannot discern if the compound is in the paramagnetic phase with a disordered Fe moment or if the magnetic

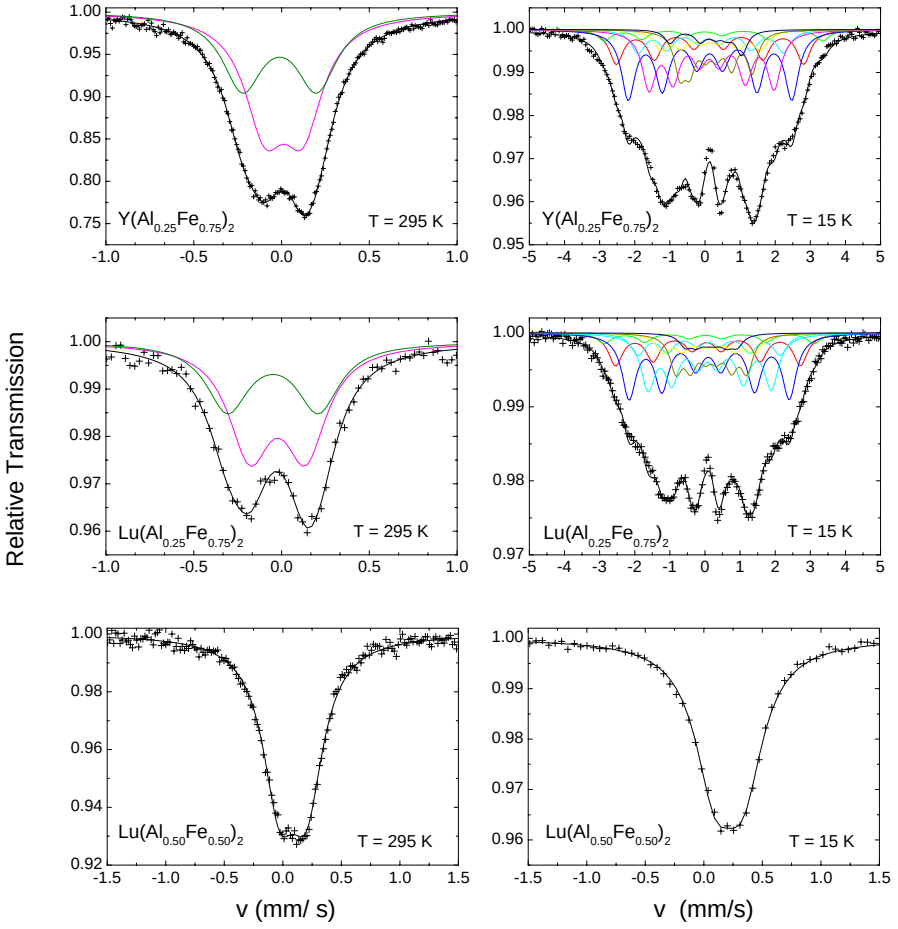

Figure 6.16: The Mössbauer spectra of $Y(Al_{0.25}Fe_{0.75})_2$, $Lu(Al_{0.25}Fe_{0.75})_2$ and $Lu(Al_{0.50}Fe_{0.50})_2$ recorded at T = 295 K (left) and T = 15 K (right).

moment of Fe has become zero. In this case, due to the poorly structured profile of the Mössbauer spectra, they have been fitted with just one doublet. The corresponding hyperfine parameters are listed in table 6.11.

Compound	T(K)	m	Prob.	δ(mm/s) $\pm$0.02	ε, ΔE_Q (mm/s) $\pm$0.05	B_{hf} (T) $\pm$0.3
YFe_2	15	0	75	-0.042	0.066	21.32
		0	25	-0.042	-0.169	20.61
		Total aver.		-0.042	0.001	21.14
YFe_2	295	0	75	-0.086	0.065	18.86
		0	25	-0.086	-0.180	18.30
		Total aver.		-0.086	0.004	18.72
$Y(Al_{0.25}Fe_{0.75})_2$	15	0	13.35	0.118	0.020	16.64
		0	4.45	0.118	0.030	19.40
		1	26.70	0.134	0.006	14.53
		1	8.90	0.134	0.033	12.92
		2	22.29	0.155	0.025	11.11
		2	7.41	0.155	0.018	8.82
		3	12.69	0.222	0.026	6.42
		3	4.21	0.222	-0.025	6.36
		Aver. m = 0		0.118	0.022	17.29
		Aver. m = 1		0.134	0.011	14.10
		Aver. m = 2		0.155	0.024	10.52
		Aver. m $\geq$ 3		0.220	0.025	6.45
		Total aver.		0.152	0.019	12.31
$Y(Al_{0.25}Fe_{0.75})_2$	295	m = 0, 1	58	0.013	0.215	–
		m > 1	42	-0.011	0.422	–
		Total aver.		0.003	0.302	–

Table 6.10: Hyperfine parameters of the $Y(Al_{1-x}Fe_x)_2$ compounds. In all cases the isomer shift is taken relative to α-iron at 295 K.

Compound	T(K)	m	Prob.	δ(mm/s) ±0.02	ε, ΔE_Q (mm/s) ±0.05	B_{hf} (T) ±0.3
$LuFe_2$	15	0	75	-0.002	0.036	21.05
		0	25	-0.002	-0.047	20.27
		Total aver.		-0.002	0.015	20.85
$LuFe_2$	295	0	75	-0.120	0.042	19.0
		0	25	-0.120	-0.079	18.4
		Total aver.		-0.120	0.012	18.85
$Lu(Al_{0.25}Fe_{0.75})_2$	15	0	13.35	0.067	0.019	16.42
		0	4.45	0.067	0.005	18.62
		1	26.70	0.107	0.014	14.22
		1	8.90	0.107	0.009	12.62
		2	22.29	0.104	0.005	10.96
		2	7.41	0.104	-0.002	8.11
		3	12.69	0.179	0.005	6.29
		3	4.21	0.179	-0.004	4.61
		Aver. m = 0		0.067	0.011	16.97
		Aver. m = 1		0.107	0.013	13.82
		Aver. m = 2		0.104	0.003	10.25
		Aver. m $\geq$ 3		0.179	0.003	5.87
		Total aver.		0.111	0.008	11.98
$Lu(Al_{0.25}Fe_{0.75})_2$	295	m = 0, 1	60	-0.022	0.319	–
		m > 1	40	-0.049	0.517	–
		Total Aver.		-0.033	0.398	–
$Lu(Al_{0.50}Fe_{0.50})_2$	15		100	0.216	0.240	–
$Lu(Al_{0.50}Fe_{0.50})_2$	295		100	0.087	0.233	–

Table 6.11: Hyperfine parameters of the $Lu(Al_{1-x}Fe_x)_2$ compounds. In all cases the isomer shift is taken relative to α-iron at 295 K.

$Gd(Al_{1-x}Fe_x)_2$ compounds

The spectra of the $Gd(Al_{0.25}Fe_{0.75})_2$ compound measured at T = 15 K and T = 295 K are shown in the top panels of figure 6.17. As it can be seen, the spectra at both temperatures are very similar. In both cases the simplest model, that includes four different sextets with the relative intensities obtained from the binomial distribution, is not enough to obtain a good fit of the spectra. It is necessary to include the effect of the relative orientation between V_{zz} and B_{hf}. In fact, good fits are only obtained when assuming that the EMD lies along the [111] direction. In such a case, each of these four sextets give rise to two different contribution with relative intensities 3:1, so that a total of eight sextets have been included in the fit. It is worth noticing that the quadrupolar shifts were let free in the fitting procedure and the obtained $\varepsilon(I)/\varepsilon(II)$ ratio is very close to the theoretical value -0.33.

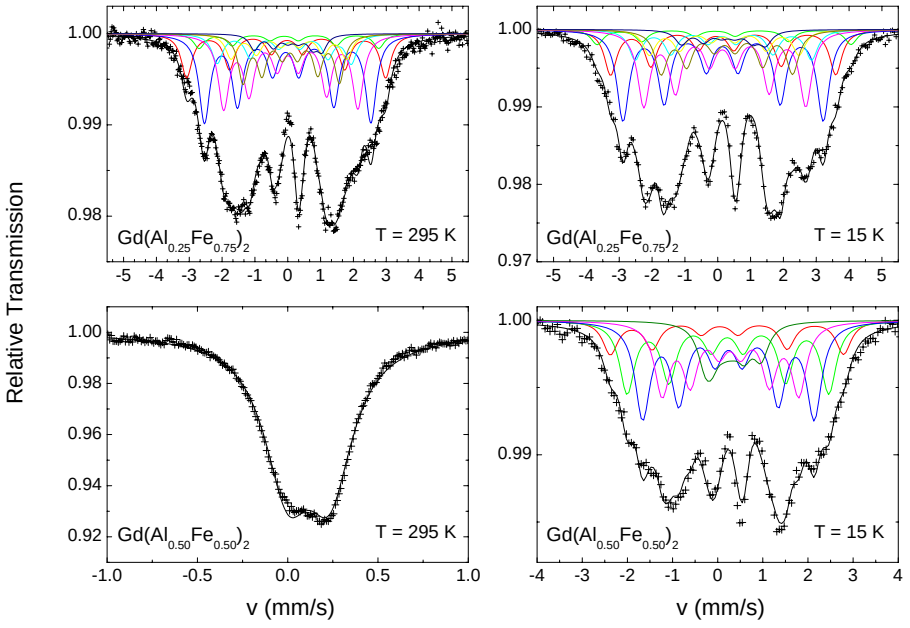

Figure 6.17: The Mössbauer spectra of $Gd(Al_{1-x}Fe_x)_2$ (x = 0.75 and 0.50) for T = 295 K (left) and 15 K (right).

$Gd(Al_{0.50}Fe_{0.50})_2$ is paramagnetic at room temperature, in agreement with the previously shown M(T) curve. One symmetric doublet has been used to fit this spectrum. In principle, seven different doublets according to the binomial model should be used. However, due to its poorly structured profile, this results in an excess of adjustable parameters and the physical reliability is missing. The use of just one contribution will permit us to estimate the value of the

averaged hyperfine parameters. On the other hand, at T = 15 K it presents the typical profile of a diluted compound. To fit this profile we have assumed a cubic C15 structure and a binomial distribution of environment as described above. As in the case of Y and Lu compounds, the goodness of the fit reflects a random distribution of the Al atoms. As it can be seen in Fig. 6.17, using 5 sextets is enough to obtain a good fit. This result reflects that, in this case, the simplest model is good enough, that is, it is not necessary to take into account the relative orientation of V_{zz} and B_{hf}. It is also probable that in this compound (for a 50% of Al) the EMD has changed form [111] to [100]. This is not a very surprising result if one takes into account that it is probably the Fe sublattice that makes the EMD to be [111]. As the Fe content is reduced, the EDM may change. The obtained hyperfine parameters are given in Table 6.12

Compound	T(K)	m	Prob.	δ(mm/s) ±0.02	ε, ΔE_Q(mm/s) ±0.05	B_{hf} (T) ±0.3
$GdFe_2$	15	0	75	0.057	0.114	23.30
		0	25	0.057	-0.136	21.18
		Total aver.		0.057	0.050	22.77
$GdFe_2$	295	0	75	-0.077	0.088	22.08
		0	25	-0.077	-0.023	21.34
		Total aver.		-0.077	0.060	21.89
$Gd(Al_{0.25}Fe_{0.75})_2$	15	0	13.35	0.120	0.083	21.40
		0	4.45	0.120	0.126	24.20
		1	26.70	0.130	0.050	19.11
		1	8.90	0.130	0.045	16.61
		2	22.29	0.198	0.016	16.15
		2	7.41	0.198	0.060	14.86
		3	12.69	0.301	0.092	11.65
		3	4.21	0.301	-0.101	7.63
		Aver. m = 0		0.120	0.094	22.10
		Aver. m = 1		0.130	0.049	18.48
		Aver. m = 2		0.198	0.027	15.83
		Aver. m ≥ 3		0.301	0.052	10.65
		Total aver.		0.177	0.051	17.01
$Gd(Al_{0.25}Fe_{0.75})_2$	295	0	13.35	-0.033	-0.014	18.89
		0	4.45	-0.033	0.071	17.06
		1	26.70	-0.031	0.031	15.81
		1	8.90	-0.031	-0.074	12.75
		2	22.29	0.049	0.045	10.96
		2	7.41	0.049	-0.015	9.17
		3	12.69	0.087	0.021	8.48
		3	4.21	0.087	-0.075	7.99
		Aver. m = 0		-0.033	0.007	18.43
		Aver. m = 1		-0.031	0.005	15.04
		Aver. m = 2		0.049	0.030	12.30
		Aver. m ≥ 3		0.087	-0.003	8.49
		Total aver.		0.012	0.011	13.72
$Gd(Al_{0.50}Fe_{0.50})_2$	15	0, 1	11.0	0.125	0.080	16.11
		2	23.4	0.219	0.008	13.93
		3	31.2	0.239	-0.002	11.85
		4	23.4	0.279	0.007	9.44
		5,6	11.0	0.285	0.055	3.86
		Total aver.		0.236	0.018	11.36
$Gd(Al_{0.5}Fe_{0.5})_2$	295		100	0.116	0.234	–
$Gd(Al_{0.75}Fe_{0.25})_2$	295		100	0.190	0.205	–

Table 6.12: Hyperfine parameters of the $Gd(Al_{1-x}Fe_x)_2$ compounds. In all cases the isomer shift is taken relative to α-iron at 295 K.

$Tb(Al_{1-x}Fe_x)_2$ compounds

The spectra corresponding to the $Tb(Al_{1-x}Fe_x)_2$ compounds measured at room temperature are shown in figure 6.18.

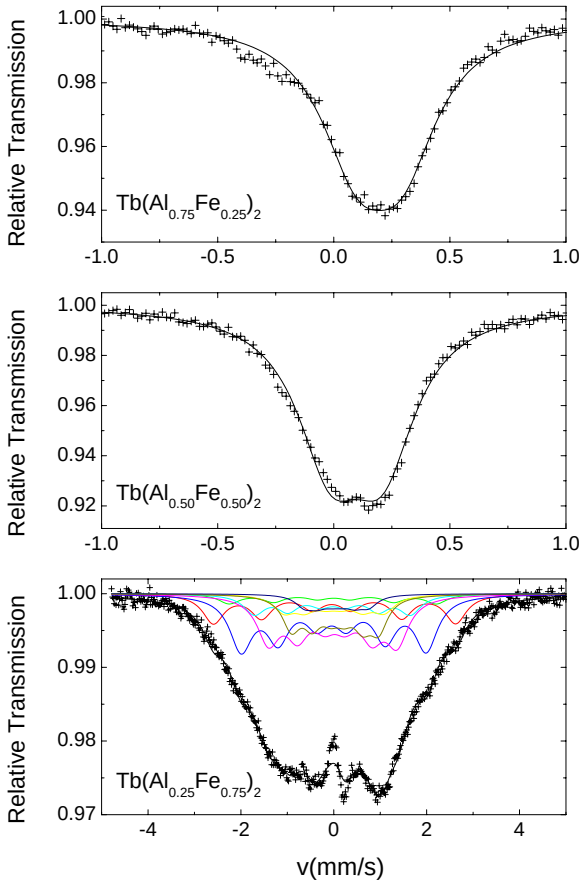

Figure 6.18: The Mössbauer spectra of $Tb(Al_{1-x}Fe_x)_2$ for x = 0.25 (top), x = 0.50 (middle) and x = 0.75 (bottom) measured at T = 295 K.

As in the case of $Gd(Al_{0.25}Fe_{0.75})_2$, the spectrum recorded for $Tb(Al_{0.25}Fe_{0.75})_2$ cannot be well fitted unless an eight sextets model, i.e. a EMD along [111], are used. In addition, in the case of $Tb(Al_{0.25}Fe_{0.75})_2$ the spectrum is similar to that of $Gd(Al_{0.25}Fe_{0.75})_2$, but with less structure. This difference may well be due to the fact that the corresponding T_C for $Tb(Al_{0.25}Fe_{0.75})_2$ is 354 K, i.e. very close to room temperature. This may affect considerably the Mössbauer spectra. In fact, as it can be seen in the M(T) measurements (see Fig. 6.10) the transition to the ordered state is very broad and at 300 K the compounds is not completely ordered. The fact that we do not have, as in the $Gd(Al_{0.25}Fe_{0.75})_2$ case, a well defined structure indicates that a temperature of 300 K is not cold enough for the Fe sublattice to completely establish a long-range order. To fit

Compound	T(K)	m	Prob.	δ(mm/s) $\pm$0.02	ε, ΔE_Q(mm/s) $\pm$0.05	B_{hf} (T) $\pm$0.3
$TbFe_2$	295	0	75	-0.089	0.105	21.77
		0	25	-0.089	-0.268	19.29
		Total aver.		-0.089	0.012	21.25
$Tb(Al_{0.25}Fe_{0.75})_2$	295	0	13.35	-0.014	0.031	16.27
		0	4.45	-0.014	0.010	13.91
		1	26.70	-0.020	0.022	12.43
		1	8.90	-0.020	-0.007	10.47
		2	22.29	0.000	-0.021	8.64
		2	7.41	0.000	0.007	6.74
		3	12.69	0.052	-0.02 5	5.86
		3	4.21	0.052	0.00 8	4.31
		Aver. m = 0		-0.014	0.021	15.68
		Aver. m = 1		-0.020	0.015	11.94
		Aver. m = 2		0.000	-0.014	8.17
		Aver. m $\geq$ 3		0.052	-0.017	5.47
		Total aver.		-0.001	0.002	10.39
$Tb(Al_{0.50}Fe_{0.50})_2$	295		100	0.098	0.226	–
$Tb(Al_{0.75}Fe_{0.25})_2$	295		100	-0.021	0.369	–

Table 6.13: Hyperfine parameters at $T = 295$ K of the $Tb(Al_{0.25}Fe_{0.75})_2$ compounds. In all cases the isomer shift is taken relative to α-iron at 295 K.

this spectrum a fixed value of $\varepsilon(I)/\varepsilon(II)$ equal to -0.33 has been considered for all the magnetically split pairs of sextets. The hyperfine parameters are shown in Table 6.13. The hyperfine fields are smaller than those of $Gd(Al_{0.25}Fe_{0.75})_2$. This is a reasonable result as the compound is not totally ordered. And the same fact explains the obtained wide linewidths, which, in this case, are 0.47 mm/s.

The spectra corresponding to x = 0.50 and x = 0.25, are both asymmetric doublets as expected for compounds with a T_C lower than RT. As in the Gd case, the spectra have been fitted by using the simplest model: just one doublet, which gives us an estimation of the average value of the hyperfine parameters.

Ho(Al$_{1-x}$Fe$_x$)$_2$ compounds

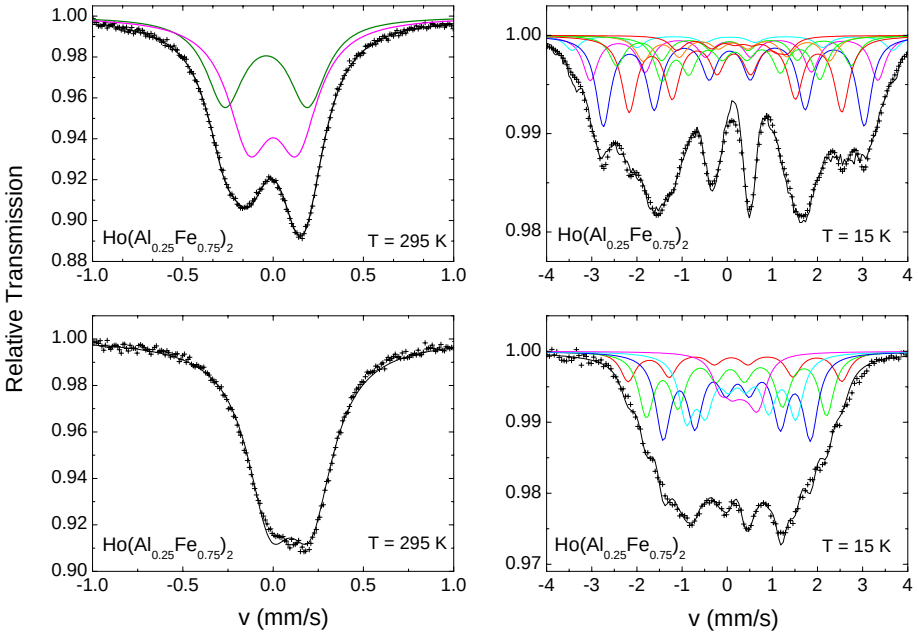

Figure 6.19: The Mössbauer spectra of Ho(Al$_{1-x}$Fe$_x$)$_2$ for T = 295 K (left) and T = 15 K (Right).

The Ho(Al$_{0.25}$Fe$_{0.75}$)$_2$ has been measured at 15 and 295 K. The low temperature spectrum is very similar to that found for Gd and Tb with the same Fe content. Also in this case the best fit is obtained if we consider eight sextets according to a EMD in the [111] direction. This indicates that the EMD changes with the Al substitution in a similar manner to that reported by Grössinger *et al.* for the Dy(Al$_{1-x}$Fe$_x$)$_2$ series.[135] At room temperature the spectrum consists of an asymmetric doublet, in agreement with the observed M(T) behaviour.

The low temperature spectrum of the Ho(Al$_{0.50}$Fe$_{0.50}$)$_2$ compound can be fitted by using the same model as in the Gd(Al$_{0.50}$Fe$_{0.50}$)$_2$ compound. Also in this case 5 sextets have been used to obtain the best fit of the experimental spectrum. At room temperature the spectrum consists in an asymmetric doublet, in agreement with the observed M(T) behaviour. The values of the different hyperfine parameters is shown in table 6.14

Compound	T(K)	m	Prob.	δ(mm/s) ±0.02	ε, ΔE_Q(mm/s) ±0.05	B_{hf} (T) ±0.3
$HoFe_2$	15	0	100	0.021	0.032	22.15
$HoFe_2$	295	0	100	-0.100	0.018	20.20
$Ho(Al_{0.25}Fe_{0.75})_2$	15	0	13.35	0.087	0.066	18.86
		0	4.45	0.087	0.029	22.13
		1	26.70	0.101	0.045	18.02
		1	8.90	0.101	0.048	16.19
		2	22.29	0.166	0.018	14.69
		2	7.41	0.166	0.035	12.87
		3	12.69	0.234	0.070	10.91
		3	4.21	0.234	-0.126	7.60
		Aver. m = 0		0.087	0.057	20.42
		Aver. m = 1		0.101	0.046	17.56
		Aver. m = 2		0.166	0.022	14.23
		Aver. m $\geq$ 3		0.234	0.021	10.09
		Total aver.		0.140	0.037	15.82
$Ho(Al_{0.25}Fe_{0.75})_2$	295	m = 0, 1	60	0.000	0.266	–
		m > 1	40	-0.038	0.458	–
		Total aver.		-0.015	0.342	–
$Ho(Al_{0.5}Fe_{0.5})_2$	15	0, 1	11.0	0.190	0.040	14.71
		2	23.4	0.180	0.079	12.43
		3	31.2	0.231	-0.010	10.20
		4	23.4	0.270	0.041	7.47
		5,6	11.0	0.328	-0.035	2.77
		Total aver.		0.234	0.025	9.76
$Ho(Al_{0.5}Fe_{0.5})_2$	295		100	0.095	0.224	–
$Ho(Al_{0.75}Fe_{0.25})_2$	295		100	0.182	0.205	–

Table 6.14: Hyperfine parameters of the $Ho(Al_{1-x}Fe_x)_2$ compounds. In all cases the isomer shift is taken relative to α-iron at 295 K.

Analysis of the hyperfine parameters

Firstly, from the general equation 1.47 we will derive some expressions that will be useful in the analysis of the hyperfine field. As we saw in section 1.4.3 the most general expression for the hyperfine field at a given iron site, k, is:

$$\begin{aligned} B_{hf}(k) &= (\alpha+\beta)\mu_{Fe}(k) + \sum_l \zeta_{Fe}(l,k)\mu_{Fe}(l) \\ &\quad + \tilde{\zeta}_R(k) Z_R(k)\gamma_R\mu_R + B_{anis}(k). \end{aligned}$$

where $(\alpha + \beta)\mu_{Fe}(k)$ is the autopolarization field, $\sum_l \zeta_{Fe}(l,k)\mu_{Fe}(l)$ and $\tilde{\zeta}_R(k)Z_R(k)\gamma_R\mu_R$ are the iron sublattice and rare-earth sublattice transferred field, respectively, and $B_{anis}(k)$ is the anisotrope contribution, which is usually neglected.

In the case of $R(Al_{1-x}Fe_x)_2$ diluted compounds, there is only one iron site, but several environments are possible depending on the number of Al nearest-neighbours, m. For each environment:

$$B_{hf}(m) = (\alpha+\beta)\mu_{Fe}(m) + \sum_l \zeta_{Fe}(l,m)\mu_{Fe}(l) + B_{tR}(m) + B_{anis}(m)$$

In principle, all the terms may depend on m. However, we will consider some approximations. The contribution coming from B_{anis} will be neglected and α, β and B_{tR} will be considered independent on m. Besides, in a mean field approximation, the iron sublattice transferred field can be taken as proportional to the average magnetic moment of the iron atoms in the first neighbour shell:

$$B_{tFe}(m) = \sum_l \zeta_{Fe}(l,m)\mu_{Fe}(l) = (6-m)\zeta_{Fe}(m)\langle\mu_{Fe}\rangle_{1nn} \tag{6.6}$$

where (6 - m) is the number of Fe atoms in the first nn shell. Hence:

$$B_{hf}(m) \approx (\alpha+\beta)\mu_{Fe}(m) + (6-m)\zeta_{Fe}(m)\langle\mu_{Fe}\rangle_{1nn} + B_{tR} \tag{6.7}$$

From this expression it can be easily inferred that even if $\mu_{Fe}(m)$ and $\zeta_{Fe}(m)$ were constant, $B_{hf}(m)$ will decrease with increasing the number of Al nearest-neighbours due to the (6-m) term. For m = 0, i.e., for environments without Al atoms nearest-neigbours,

$$B_{hf}(0) \approx (\alpha+\beta)\mu_{Fe}(0) + 6\zeta_{Fe}(0)\langle\mu_{Fe}\rangle_{1nn} + B_{tR} \tag{6.8}$$

which is very similar to the expression of B_{hf} in the parent RFe_2 compounds (see Eq. (6.3)).

Eq. (6.7) yields to the following expression for the average hyperfine field:

$$\begin{aligned} \langle B_{hf}\rangle(x_{Fe}) &\approx \Big(\alpha+\beta+\Big\langle(6-m)\zeta_{Fe}(m)\Big\rangle(x_{Fe})\Big)\langle\mu_{Fe}\rangle(x_{Fe})+B_{tR} \\ &\approx f(x_{Fe})\Delta\langle\mu_{Fe}\rangle(x_{Fe})+B_{tR} \end{aligned} \tag{6.9}$$

where the dependence on x_{Fe} indicates that both $\langle\zeta_{Fe}\rangle$ and $\langle\mu_{Fe}\rangle$ may depend on the Al content in the compound. It should be noted that $f(x_{Fe})$ depends on the (6 - m) term, which decreases as the Al content is increased.

Taking into account these expressions for $\langle B_{hf}\rangle$ and $B_{hf}(0)$ we will try to derive as much information as possible about the magnetic behaviour of Fe in our systems.

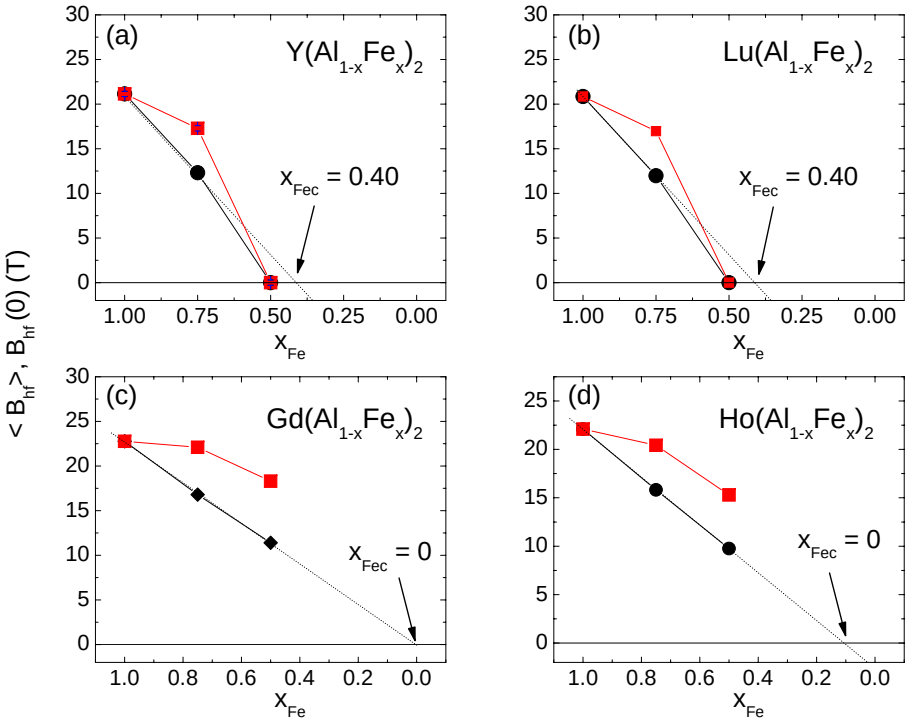

Figure 6.20: Modification of the average hyperfine magnetic field,$\langle B_{hf}\rangle$ (●), and the hyperfine magnetic field for m = 0, $B_{hf}(0)$ (■), with Fe concentration, x_{Fe}, for different $R(Al_{1-x}Fe_x)_2$ compounds (T = 15 K). Dotted black line is the linear fit obtained from x = 1 and 0.75.

Fig. 6.20 shows the dependence of $\langle B_{hf}\rangle$ at T = 15 K with the Fe content, x_{Fe}. In all the studied cases $\langle B_{hf}\rangle$ decreases almost linearly when decreasing the Fe content. This reduction of the average hyperfine magnetic field may be due to either a simple dilution effect when substituting Fe atoms by Al (the (6-m)$\zeta_{Fe}(m)$ term will decrease) or a reduction of the Fe magnetic moment.

Trying to disentangle these two effects, we have also analyzed the dependence on x_{Fe} of the hyperfine field corresponding to an environment without Al atoms, $B_{hf}(0)$, which is also displayed in Fig. 6.20.

As it can be seen in Fig. 6.20, $B_{hf}(0)$ also decreases as the Fe content decreases, but much slowly than $\langle B_{hf} \rangle$ does. The differences in $B_{hf}(0)$ between $LuFe_2$ (20.85 T) and $Lu(Al_{0.25}Fe_{0.75})_2$ (16.97 T) can be due to differences in $\mu_{Fe}(0)$, $\langle \mu_{Fe} \rangle$ and $\zeta_{Fe}(0)$ (see Eq. (6.8)). In principle, there is no reason to think that only one of them will decrease. Therefore, our results suggest that **there is a slight reduction of both ζ_{Fe} and $\langle \mu_{Fe} \rangle$ with increasing Al**.

There is another important conclusion that can be derived from the analysis of $B_{hf}(0)$. In $LuFe_2$, B_{hf} = 20.85 T and $\mu_{Fe} \sim 1.5\ \mu_B$. These values give a ratio $f = B_{hf}/\mu_{Fe}$ = 13.9 T/ μ_B (see Eq. (6.9)), very close to that observed in other Y-Fe binary compounds.[36, 37] Using the same value of f for $Lu(Al_{0.25}Fe_{0.75})_2$, the experimentally obtained value of $\langle B_{hf} \rangle$ gives $\langle \mu_{Fe} \rangle$ ($Lu(Al_{0.25}Fe_{0.75})_2$)= 1.2 μ_B. Moreover, very likely, f is smaller in compounds with just 75% of Fe due to a dilution effect (see Eq. (6.9)). In fact, a reduction of f as the Fe content decreases has been reported for other diluted series.[41, 173]. Therefore, our results indicate that **the average magnetic moment of Fe for $Lu(Al_{0.25}Fe_{0.75})_2$ and $Y(Al_{0.25}Fe_{0.75})_2$ compounds is at least 1.2 μ_B.**

It is worth noticing that the reduction of μ_{Fe} derived from M(H, T) data is much more abrupt than the observed B_{hf} diminution. This can be seen in Fig. 6.21, where both magnitudes have been compared. Indeed, the small magnetic moment obtained for $Y(Al_{0.25}Fe_{0.75})_2$ and $Lu(Al_{0.25}Fe_{0.75})_2$ is no compatible with the measured hyperfine field. Thus, for instance, in $Y(Al_{0.25}Fe_{0.75})_2$, $B_{hf}(0)$ is 17.29 T. If μ_{Fe} were the value obtained from M(50 kOe, 5 K), i.e., $\mu_{Fe} = 0.5\ \mu_B$ ($\mu_{Fe} \approx 0.3\ \mu_B$ is the spontaneous value derived from M(H, 5 K)), the f factor would be at least 34.6 T/μ_B (86.4 T/μ_B if the spontaneous value is considered), which, as discussed above, make no sense due to the dilution effect. The discrepancy between magnetization and Mössbauer measurements has been already reported by other authors for Y-Fe-Al[148] and Y-Fe-Mo compounds.[175, 176] Although no completely satisfactory answer has been done so far, this result points out the existence of localized magnetic moments of Fe even if we cannot observe this moment in the M(H, T) measurements. This result supports the idea that in these compounds there is a partially non-collinear magnetic structure as discussed in section 6.4.

Once we have gained some information about the behaviour of $\langle \mu_{Fe} \rangle$ we can take up again the analysis of $\langle B_{hf} \rangle$ displayed in Fig. 6.20. In the Y and Lu based compounds it is clear that the observed reduction of $\langle B_{hf} \rangle$ between $x_{Fe} = 1$ and $x_{Fe} = 0.75$ is due to both, a slight reduction of $\langle \mu_{Fe} \rangle$ and a

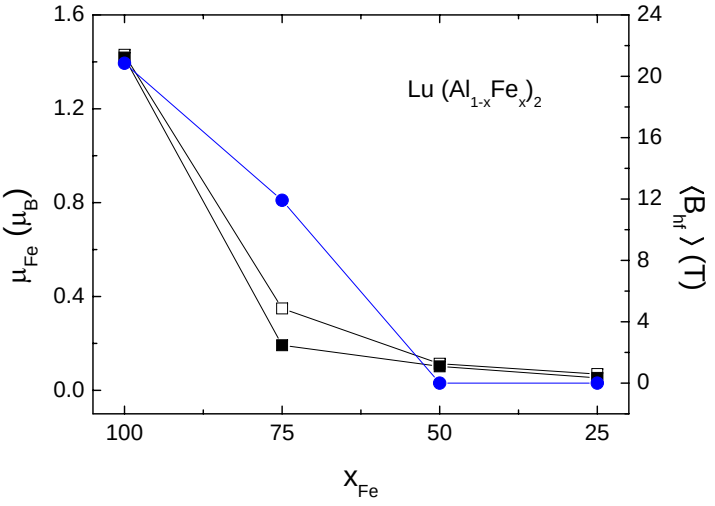

Figure 6.21: Comparison of the variation of the average hyperfine field (•), the magnetic moment of Fe derived from M(50 kOe, 5 K)(□) and the spontaneous magnetic moment derived from M(H,5K) (■) as a function of Fe content in $Lu(Al_{0.25}Fe_{0.75})_2$.

dilution effect (through the (6-m)$\zeta_{Fe}(m)$ term). Interpolating this behaviour down to $x_{Fe} = 0$ (dotted black line in Fig. 6.20), the data of the $x_{Fe} = 1$ and $x_{Fe} = 0.75$ compounds predict that the long-range order of the Fe sublattice should disappear at $x_{Fe} = 0.4$, very near to the value $x_{Fe} = 0.5$, for which is experimentally found that the compound is not magnetic. That is, our results indicate that the Y and Lu series essentially behaves as a typical diluted compound. However, it is worth nothing that the reduction of $\langle B_{hf} \rangle$ is more abrupt from $x_{Fe} = 0.75$ to $x_{Fe} = 0.50$ than from $x_{Fe} = 1$ to and $x_{Fe} = 0.75$ (see Fig. 6.20), which may indicate that the influence of Al in the magnetic properties of the Fe sublattice is more pronounced for high Al contents.

As commented in section 6.4, some authors have indicated that in these compounds μ_{Fe} becomes zero from a given Al concentration due to electron transfer from Al to Fe. Our data, however, seem to indicate that the long-range order disappears owing mainly to a dilution effect ($\langle B_{hf} \rangle$ shows a nearly linear dependence on x_{Fe}). This conclusion is in agreement with susceptibility results, where only a very slight reduction of the effective magnetic moment of iron is reported along the $Y(Al_{1-x}Fe_x)_2$ series.[149]

Regarding the compounds with magnetic rare earth (cases (c) and (d) of Fig. 6.20), we can observe that the behavior of $\langle B_{hf} \rangle$ as a function of x_{Fe} is slightly different to that found for the Y and Lu series. First, the long-range order of the Fe sublattice persists for higher Al contents. Second, the decrease of $\langle B_{hf} \rangle$ is completely linear with x_{Fe}; the extrapolation of the $x_{Fe} = 1, 0.75,$

and 0.50 data (dotted line in Fig. 6.20) suggest that at this temperature the $R(Al_{1-x}Fe_x)_2$ compounds will keep a magnetic order up to $x_{Fe} \approx 0$. Provided that the dilution effect is the same in magnetic and non-magnetic rare earths compounds, the slower diminution of both $\langle B_{hf} \rangle$ and $\langle B_{hf} \rangle(0)$ observed when R is magnetic suggests a smaller decrease of $\langle \mu_{Fe} \rangle$. Moreover, the gradual reduction of $B_{hf}(0)$ (see Fig. 6.20) is in agreement with the slow reduction of μ_{Fe} derived from magnetization measurements in $Gd(Al_{1-x}Fe_x)_2$. Since neither the behaviour of $\langle B_{hf} \rangle$ nor that of $B_{hf}(0)$ depends on the specific magnetic rare-earth, this result seems to indicate that the modification of μ_{Fe} is the same for all the $R(Al_{1-x}Fe_x)_2$ series with magnetic R. Therefore, this would imply that the anomalous behaviour of M(H) and M(T) curves should be explained in terms of RAM or Spin Glass behaviour.

All these results indicates that when Fe is replaced by Al in $R(Al_{1-x}Fe_x)_2$ compounds the Fe sublattice behaves differently for magnetic and non-magnetic R compounds. When R is a magnetic rare earth the long-range order of the Fe sublattice persists at higher Al contents, and the decrease of $\langle \mu_{Fe} \rangle$ as a function of the Al content is smaller. This behaviour suggest that, **very likely due to the R-Fe interaction, the presence of a magnetic R reinforces the Fe sublattice magnetism in the $R(Al_{1-x}Fe_x)_2$ compounds.**

Further information about the evolution of μ_{Fe} with Fe substitution by Al can be obtained by comparing the influence of the rare-earth on $\langle B_{hf} \rangle$. More precisely, we can explore how differently μ_{Fe} behaves for magnetic R *vs.* non magnetic R. This is shown in Fig. 6.22, where $\langle B_{hf} \rangle$ is plotted *vs.* B_{tR}.

Within the $\langle B_{hf} \rangle = \langle B_{Fe} \rangle + \langle B_{tR} \rangle = \langle B_{Fe} \rangle + \langle \tilde{\zeta}_R \rangle Z_R \gamma_R \mu_R$ two-sublattice approach, if μ_{Fe} is independent on R, $\langle B_{hf} \rangle$ will display a linear relationship with $\langle B_{tR} \rangle$ and the value of $\langle B_{Fe} \rangle$ derived from the linear dependence should coincide with $\langle B_{hf} \rangle$(Lu).

In the case of pure binary RFe_2, $\langle B_{hf} \rangle$ is linear with $\langle B_{tR} \rangle$ (both at T = 15 and 295 K) and $\langle B_{Fe} \rangle$ is very similar to $\langle B_{hf} \rangle(LuFe_2)$. In particular, ($\langle B_{Fe} \rangle$ = 18.8 T, and 20.9 T, and $\langle B_{hf} \rangle(LuFe_2)$ = 19.0 T, and 20.8 T at T = 295 and 15 K, respectively. An analogous analysis of $\langle B_{hf} \rangle$ has been performed in compounds with 75% and 50% of Fe. For the diluted compounds, our results are in agreement with a constant $\langle \mu_{Fe} \rangle$ for compounds with magnetic R, but a clearly smaller $\langle \mu_{Fe} \rangle$ in Lu and Y compounds. This difference enhances with Al content. Although this is a preliminary result (only two compounds with magnetic R have been analyzed so far), this result indicates that, while in binary Laves phases the magnetic moment of iron in $LuFe_2$ is very similar to that of compounds with magnetic rare-earth, in pseudobinary series μ_{Fe} is markedly smaller for Lu and Y compounds. In addition, the B_{Fe} component to B_{hf} obtained from the linear fit of the $R(Al_{0.25}Fe_{0.75})_2$ data gives $\langle B_{Fe} \rangle$ = 15 T

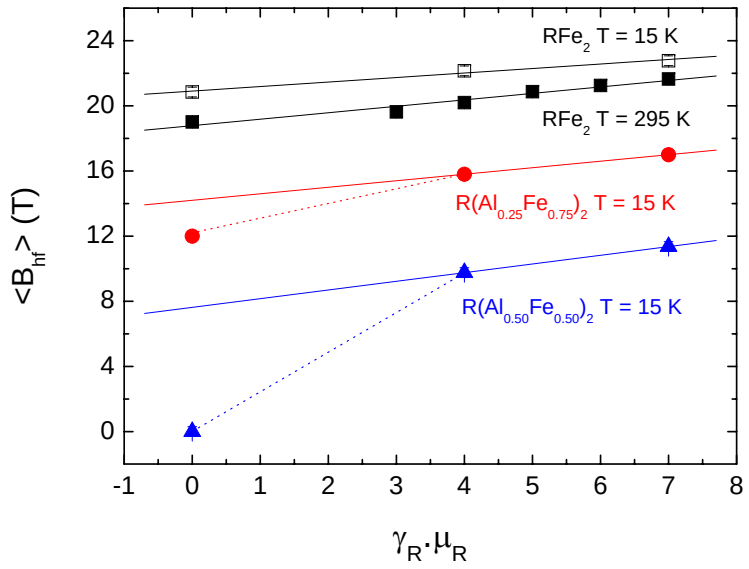

Figure 6.22: The total average hyperfine field $\langle B_{Fe} \rangle$ as a function of the product $\gamma_R \mu_R$ for RFe_2 at room temperature (□), RFe_2 at T = 15 K (■), $R(Al_{0.25}Fe_{0.75})_2$ at T = 15 K (●) and $R(Al_{0.50}Fe_{0.50})_2$ at T = 15 K (▲).

,significantly smaller than $\langle B_{hf} \rangle (LuFe_2) = 21$ T. That is, $\langle \mu_{Fe} \rangle$ in $R(Al_{1-x}Fe_x)_2$ compounds (with magnetic R) is smaller than in LuFe2. Consequently, we can conclude that:

1.2 $\mu_B < \langle \mu_{Fe} \rangle$ **(Lu$(Al_{0.25}Fe_{0.75})_2$)** $< \langle \mu_{Fe} \rangle$ **(R$(Al_{0.25}Fe_{0.75})_2$)**$< \langle \mu_{Fe} \rangle$ **(LuFe$_2$).**

That is, only slight decrease of $\langle \mu_{Fe} \rangle$ takes place in the R$(Al_{0.25}Fe_{0.75})_2$ compounds, being this decrease less pronounced when R is a magnetic rare earth.

In order to investigate further the influence of Al into the Fe magnetic moment we have analyzed the variation of B_{hf} with the number of Al atoms nn, showed in Fig.6.23. We can observe that in $R(Al_{0.25}Fe_{0.75})_2$ compounds, the effect of substituting one Fe atom by one Al atom is the same for all the rare-earths (they all have the same slope). Moreover, in the case of $R(Al_{0.25}Fe_{0.75})_2$, the linear dependence holds for all the possible environments. On the other hand, $R(Al_{0.5}Fe_{0.5})_2$ compounds show a linear dependence up to m = 4, whereas the reduction is more abrupt in the case of m = 5 (Al rich environments).

This dependence can be explained if we assume a linear decrease of μ_{Fe} in the form: μ_{Fe} (m) = μ_{Fe} (0) - m Δ μ_{Fe}. In this case, we obtain the following

expression for the dependence of B_{hf} with m:

$$\begin{aligned} B_{hf}(m) &\approx (\alpha+\beta)\mu_{Fe}(0) + 6\zeta_{Fe}(0)\langle\mu_{Fe}\rangle_{1nn} \\ &- m\Big((\alpha+\beta)\Delta\mu_{Fe} + 6\zeta_{Fe}(m)\langle\mu_{Fe}\rangle_{1nn}\Big) + B_{tR} \\ &\approx B_{hf}(0) - m\Big((\alpha+\beta)\Delta\mu_{Fe} + 6\zeta_{Fe}(m)\langle\mu_{Fe}\rangle_{1nn}\Big) \\ &= A - mB \end{aligned} \tag{6.10}$$

Therefore, our results seems to indicate that the product $\zeta_{Fe}(m)\langle\mu_{Fe}\rangle$ and $\Delta\mu_{Fe}$ bear little dependence on the environment. That is, **the behaviour of our compounds is the typical of diluted compounds** at least when the concentrations of Al are not very high. The results also indicate that for higher Al contents (i.e. environments with 1 or 0 Fe atoms), the systems stops behaving as a typical dilution. **This behaviour of B_{hf} may well be associated to the fact that the decrease of μ_{Fe} (and so ζ_{Fe}) with increasing m is likely very slow for Fe-rich environments, but decreases more abruptly as m increases.** Consequently, $\mu_{Fe}(x_{Fe})$ can be approximated to a linear dependence for Fe-rich environments, but as Al increases, the linear approximation is not valid anymore.

Furthermore, it should be noted that the effect of replacing one Fe atom by Al is stronger in x = 0.75 than in x = 0.50 compounds. Thus, in the case of 75% of Fe, it corresponds to a reduction of 3.6 T while it is only 2.4 T for x = 0.50. This is a quite reasonable result since both μ_{Fe} and ζ_{Fe} are smaller for low Fe concentrations. (see. Eq. (6.10)).

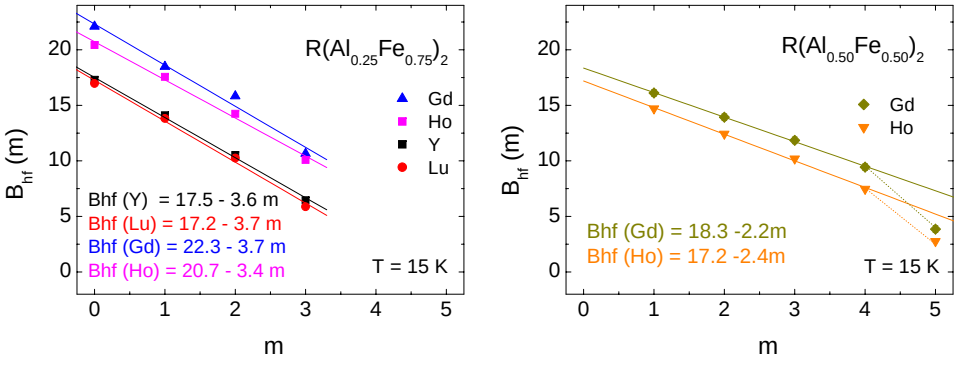

Figure 6.23: Dependence of the hyperfine field on the number of Al atoms nearest-neighbours, B_{hf}(m) for a given Fe concentration.

In Figure 6.24 it can be seen that the average isomeric shift, $\langle\delta\rangle$, decreases as Al content increases. There is also a nearly linear dependence of δ on the

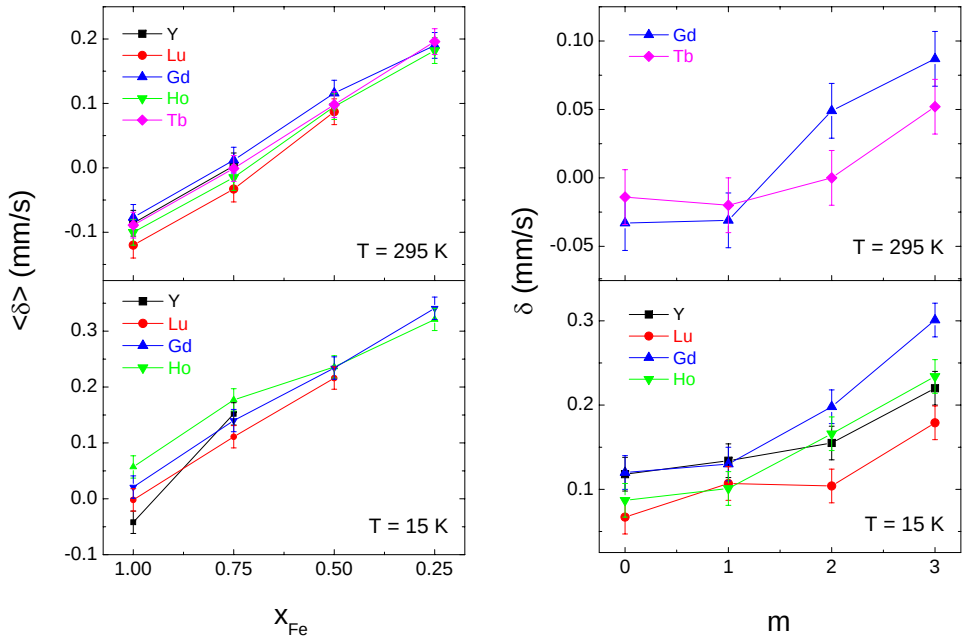

Figure 6.24: Left: Dependence of the isomeric shift on the Fe concentration, x_{Fe}. Right: Dependence of the isomeric shift on the number of Al atoms nearest-neighbours, m.

number of nearest-neighbours Al atoms, m. This dependence is the expected one as the isomeric shift is proportional to the Weigher-Seitz volume (i.e. the free volume around the absorbing atom). This result gives reliability to the values obtained for the hyperfine fields, B_{hf}, presented above.

6.6 XAS at the Fe and Co K-edges

The comparison of the absorption spectra at the Fe K-edge throughout the $R(Al_{1-x}Fe_x)_2$ series is reported in Fig. 6.25.

In the case of pure RFe_2 compounds, the XAS profile is kept constant independently on the R counterpart. On the one hand, this results points out that the differences of the lattice parameter has little influence into the XAS spectra. Moreover, the appearance of a shoulder-like feature at the raising edge, similar to that of bcc iron, and the fact that its intensity is kept constant through the RFe_2 series indicate that the electronic state of Fe atoms is mostly retained when the rare-earth is changed.

This scenario strongly changes as the transition metal is substituted by

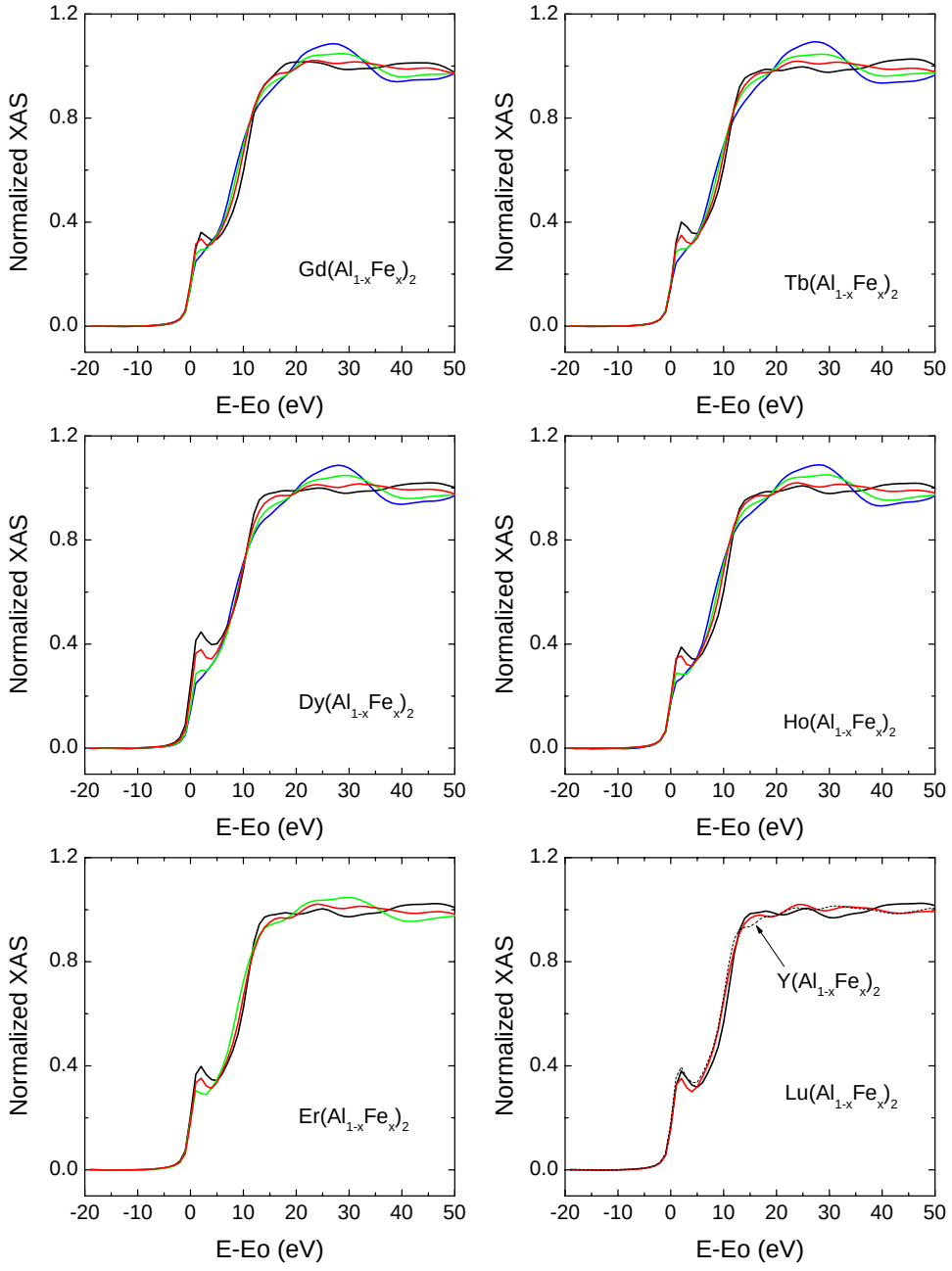

Figure 6.25: XAS spectra at the Fe K-edge in $R(Al_{1-x}Fe_x)_2$ compounds for x = 0.25 (blue line), x = 0.50 (green), x = 0.75 (red), x = 1 (black).

Al. First, the amplitude of the XANES or EXAFS oscillations is significantly

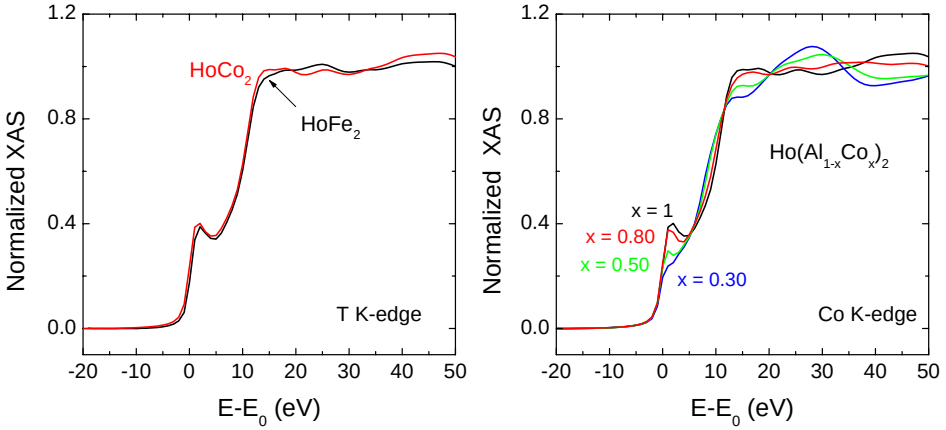

Figure 6.26: Left panel: XAS spectra at the T K-edge in HoT_2 compounds for T = Fe (black line) and Co (red line). Right panel: XAS spectra at the Co K-edge in $Ho(Al_{1-x}Co_x)_2$ compounds for x = 0.30 (blue line), x = 0.50 (green), x = 0.80 (red), x = 1 (black).

modified as the Al content in the compound increases. This is expected as, despite the crystal structure is retained, the scattering properties of Al strongly differs from those of Fe and Co. However, while this effect accounts for the modification of the high energy region of the XAS spectra, containing the local structure information, a different explanation has to be given regarding the near edge.

Differences at the threshold are related to the electronic state of T. In particular, the step-like feature at the edge is well known[19] to be the result of the hybridization of the 4p states with the d states of metal character. Therefore, the decrease of this spectral feature as the Al concentration increases indicates that the Al atoms produce a modification of the electronic structure.

As shown in Fig. 6.26, the same behaviour is observed when one measures the XAS spectra at the Co K-edge in the $R(Al_{1-x}Co_x)_2$ compounds.

6.7 XMCD at the Fe and Co K-edges

The comparison of the different measured XMCD spectra is expected to contribute to both the interpretation of the XMCD spectra at the Fe K-edge and the description of the magnetism of the iron sublattice through the $R(Al_{1-x}Fe_x)_2$ series.

Binary Laves phases: Effect of the rare-earth

The normalized Fe K-edge XMCD signals of RFe_2 for R= Y, Gd, Tb, Dy, Ho and Er are compared in Fig. 6.27. For the samples in which the rare-earth is non-magnetic, i.e. Y and Lu, the shape of the XMCD signal is similar to that of Fe metal[**?**], as previously observed for other intermetallic compounds [84, 85, 86]. This spectrum is characterized by a prominent peak (A, $\sim$ 3 eV wide) at the absorption edge followed by a broad twofold dip ($\sim$ 10 eV wide). Notice that, for the sake of clarity, the signal of Lu and Y compounds has been reversed in Figure 6.27 (top).

However, in the case of magnetic R compounds, the Fe K-edge XMCD profile is markedly different in several aspects. Firstly, the signals are reversed in relation to those of Lu and Y. This is due to that, contrary to the $RFe_{11}Ti$ series case, the R magnetic sublattice dominates the overall magnetization of the compound. Besides, although the first narrow feature at $\sim$ 0 eV is still present, its size is strongly modified. Indeed, for $HoFe_2$ and $ErFe_2$ compounds it has almost disappeared. This behaviour contrasts with that observed through the 2:14 and 1:11 series (with respect to R:Fe ratio). In these cases the intensity and the shape of this spectral feature at $\sim$ 0 eV (typically considered of Fe origin) remains unaltered through the series. In addition, in the case of compounds with magnetic R, the XMCD spectra present a more structured profile. The negative double dip (positive for magnetic R) expands, (from $\sim$ 1 eV to $\sim$ 13 eV for Gd and to 18 eV in the case of Er) and its intensity increases. In addition, there is an extra peak (C) appearing in the middle of the "negative" dip, at $\sim$ 7 eV above the absorption threshold. The appearance of this additional spectral feature is in accord with that observed in other R-T intermetallics. Both the width and the amplitude (intensity) of the emerging feature (C) strongly depends on the specific rare-earth. It is noticeable, however, that the shape of feature C in the case of RT_2 compounds is quite different to that found in the previously studied 2:14 and 1:11 series. Indeed, in RT_2 the emerging feature C is not a single peak but a twofold structure (C1 and C2).

These findings are not limited to the RFe_2 compounds, but they are also observed for the RCo_2 ones. As shown in Figure 6.28 a similar behaviour is found at the Co K-edge XMCD spectra recorded through the RCo_2 series.

The direct comparison Fe *vs.* Co is presented in Fig.6.29. Surprisingly, while the K-edge XMCD of both bcc-Fe and hcp-Co present strong differences, specially regarding the appearance of the narrow positive peak in the case of Fe, the XMCD recorded for both RFe_2 and RCo_2 at the Fe K-edge and Co K-edge are markedly similar when R is a magnetic rare-earth. This similarity

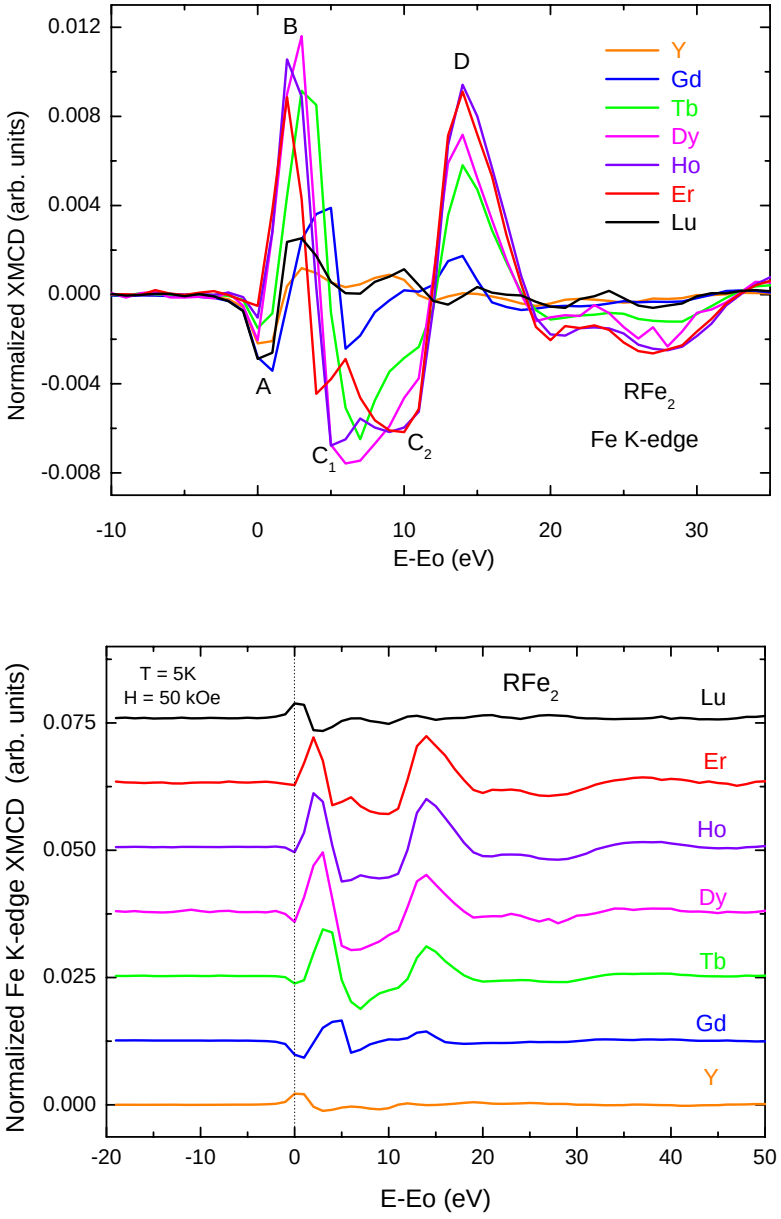

Figure 6.27: XMCD spectra at the Fe K-edges in RFe_2 compounds for R = Y (orange), Gd (blue), Tb (green), Dy (magenta), Ho (violet), Er (red) and Lu (black). YFe_2 and $LuFe_2$ have been multiplied by -1 for the sake of clarity in the top panel. In the bottom panel the same spectra are plotted but they have been vertically shifted. The XMCD spectra were recorded at 5 K and under the action of an applied magnetic field of 50 kOe.

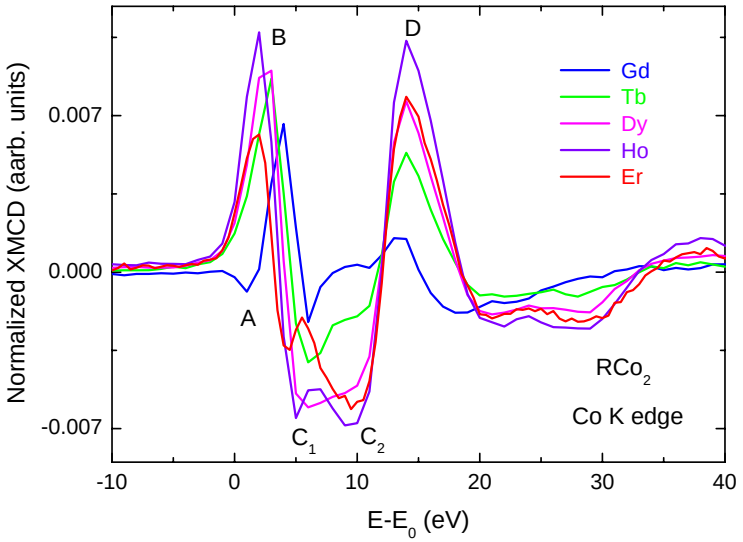

Figure 6.28: XMCD spectra at the Co K-edges in RCo_2 compounds for R = Gd (blue), Tb (green), Dy (magenta), Ho (violet) and Er (red). The XMCD spectra were recorded at 5 K and under the action of an applied magnetic field of 50 kOe.

is a first fingerprint of the influence of the rare-earth sublattice that, as will be discussed later, dominates the XMCD signal even when this is recorded at the transition metal K-edge.

Pseudobinary Laves phases: Effect of Al.

Fig. 6.30 illustrates the modification of the Fe K-edge XMCD spectra as a function of the Fe-Al substitution through the $R(Al_{1-x}Fe_x)_2$ series. In the case of compounds with a magnetic R, the intensity of features B, C and D undergoes a reduction as the Fe concentration decreases while the spectral shape remains unaltered. Indeed, these features are clearly observable even for the lowest Fe content compound, $R(Al_{0.75}Fe_{0.25})_2$. By contrast, the first part of the spectrum is strongly modified upon increasing the Al content. Indeed, the intensity of peak A is strongly reduced in such a way that for x = 0.75 no negative peak can be observed.

Excluding the reduction of peak A, which is not present for Co compounds, the same evolution is observed at the Co K -edge when Al atoms substitute the Co ones. This is shown in Figure 6.31, where the Co K-edge XMCD signal has been recorded for different $Ho(Al_{1-x}Co_x)_2$ compounds.

Previous results reported on the $R_2Fe_{14}B$ and $RFe_{11}Ti$ series have suggested

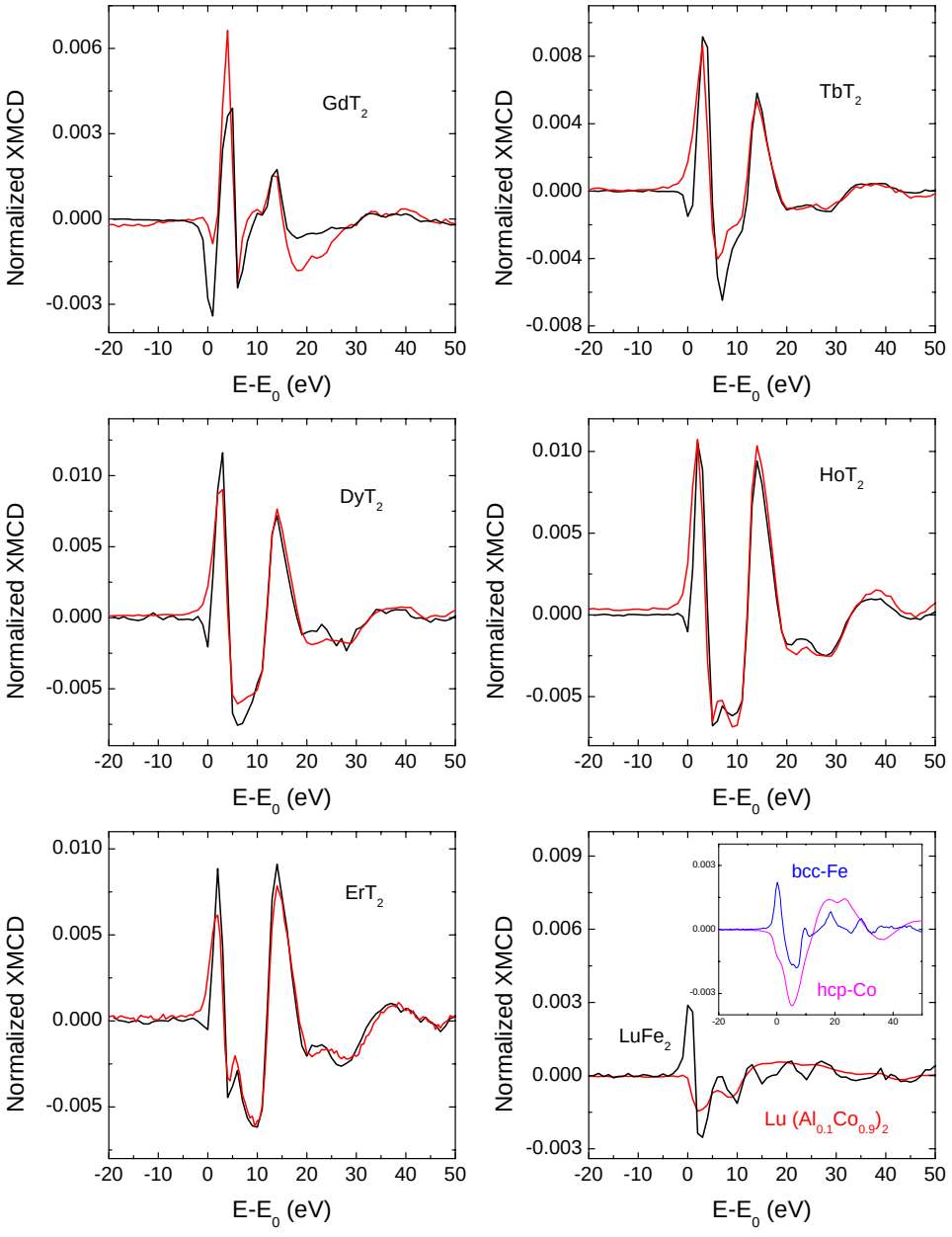

Figure 6.29: Comparison of the XMCD spectra of RFe_2 and RCo_2 recorded at the K-edge of the transition metal. The spectra were recorded at 5 K and under the action of an applied magnetic field of 50 kOe. Inset: comparison of the T K-edge XMCD spectra of bcc-Fe and hcp-Co.

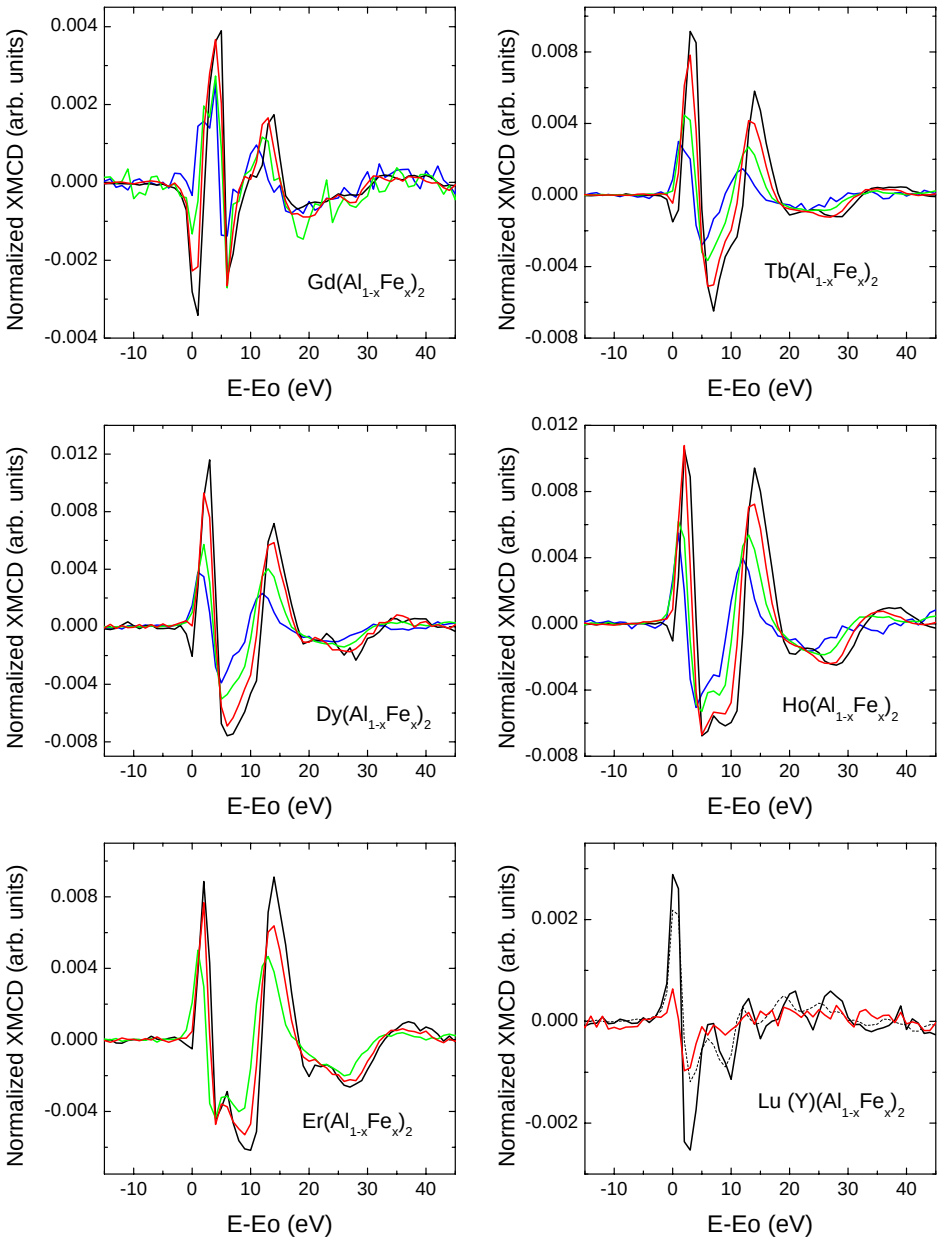

Figure 6.30: XMCD spectra at the Fe K edge for $R(Al_{1-x}Fe_x)_2$ compounds. x = 0.25 (blue line), x = 0.50 (green), x = 0.75 (red), x = 1 (black).

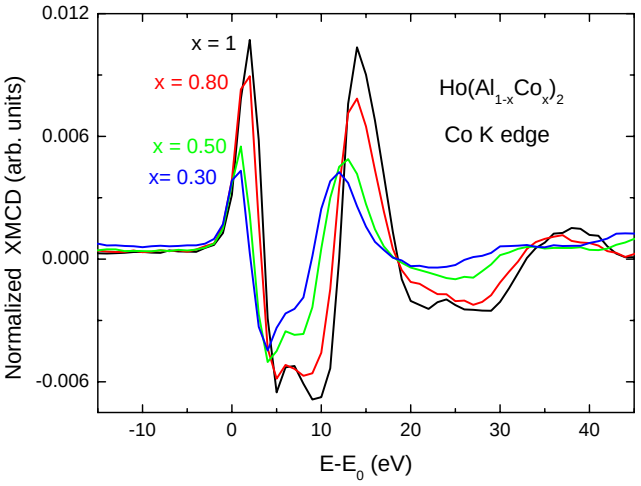

Figure 6.31: XMCD spectra at the Co K edge for $Ho(Al_{1-x}Co_x)_2$ compounds. x=0.3 (blue line), x=0.5 (green), x=0.8 (red), x= 1 (black).

that the A-feature of the Fe K-edge XMCD spectrum is mainly due to Fe. In addition, the features at higher energies are associated to the R contribution through the hybridization of the outermost states of the absorbing Fe with the 5d states of the rare-earth neighbours [84, 128]. Within this framework, the reduction of the intensity of the high energy peaks can be addressed to the weakening of the Fe(3d)-R(5d) hybridization induced by Al and, consequently, to the weakening of the influence of the rare-earth. However, no clear explanation can be given to account for the depletion of the first spectral feature (A) as Al content increases.

Previous studies on Fe-P amorphous alloys [**?**] reported a similar behaviour showing the reduction of the A peak as the metalloid content increases. This peculiar behaviour was interpreted, by comparing the K-edge XMCD spectral shape of bcc-Fe and hcp-Co, in terms of the change in the nature of the ferromagnetism from weak to strong. According to the authors, in Fe-P, the change from a weak to strong ferromagnetism is likely due to the displacement of the Fermi level to higher energies as a consequence of the increase of the electronic charge transfer. In our case, one could assume an electron transfer from Al to Fe. However, the same scheme does not seem to be valid in our case to establish a straightforward relation between the drastic depletion of the peak at lower energy and the magnetic behaviour of μ_{Fe}. The results on the $Lu(Al_{1-x}Fe_x)_2$ Laves compounds, i.e. where there is not magnetic R contribution, show that the intensity of the dichroic signal changes accordingly with the variation of μ_{Fe} derived from the M(H) curves, whereas no change

of the shape is observed. That is, the same reduction is observed for all the features on the spectrum (see last panel of Fig. 6.30). Within the framework proposed by Fdez-Gubieda *et al.* the disappearance of peak A would be due to the modification (enhancement) of the ferromagnetic character of Fe as the Al content increases. Consequently, if the disappearance of peak A in the $R(Al_{1-x}Fe_x)_2$ series had its origin purely in the magnetic behaviour of Fe, it should also undergo a stronger diminution in the case of Lu.

Moreover, Mössbauer results (section 6.5.2) indicate that the decrease of μ_{Fe} derived from the M(H) curves is mainly due to a partially randomized magnetic structure, the effect of electron transfer being, if existing, negligible in a first approximation. Indeed, μ_{Fe} has been estimated to be at least 1.2 μ_B in $Lu(Al_{0.25}Fe_{0.75})_2$. In the same way, the observed reduction of the XMCD signal in this compound can be explained as due to the partially disordered magnetic structure but not due to electron transfer.

On the other hand, our results indicate that the depletion of peak A in compounds containing a magnetic R can be most likely related to the presence of the contribution coming from R and to its modification as Al substitutes Fe. Thus, in the case of binary RFe_2 compounds, the electronic and magnetic state of iron can be considered constant (at least in a first approximation) through the whole RFe_2 series [143, 144]. In RFe_2 with R = heavy rare-earth, the magnetic moment of Fe is $\sim 1.6\ \mu_B$, ferrimagnetically coupled to the magnetic moment of R.[143, 144] Bearing in mind the previuos results one would expect a negative A peak, whose intensity is independent on R and slightly smaller than that found for pure Fe ($\mu_{Fe} \sim 2.2\ \mu_B$). On the contrary, we found that the intensity of peak A depends on R and almost disappears for Ho and Er. Therefore, the large modification of peak A observed in Figure 6.27 in the RFe_2 compounds is an indication of the strong influence of R on the Fe K-edge XMCD spectrum even at low energy.

Comparison with other R:Fe series, shown in Figure 6.32, reinforces the hypothesis stating that the R contribution hides the peak at ~ 0 eV. In all the cases studied so far the positive peak A, associated to Fe, does not significantly vary as the rare-earth ion is changed. However, in the case of the Laves phases the R contribution is so large that it seems to affect the XMCD spectra along the whole energy range. In chapter 4 we have obtained that the R contribution to the Fe K-edge XMCD spectrum resembles the magnetic state of the rare-earth, μ_R. Experimental data shown in Figure 6.32 indicate that, in addition, **the rare-earth contribution is proportional to the R concentration or more likely to the number of R atoms nearest-neighbours.** In Laves phases, the Fe atoms have 6 rare-earth nn, in the case of Ho_6Fe_{23} the number of R nn varies from 3 to 6 depending on the specific Fe site and this number

reduces to 1 or 2 in $RFe_{11}Ti$ compounds. Laves phases have a much higher R content (R nn) than the compounds chosen on previous studies such us 2:14, 1:11 and 6:23 series. As a consequence, **the influence of the R sublattice in the Fe K-edge signal is much stronger, affecting also to peak A, which had been typically considered purely of Fe origin.**

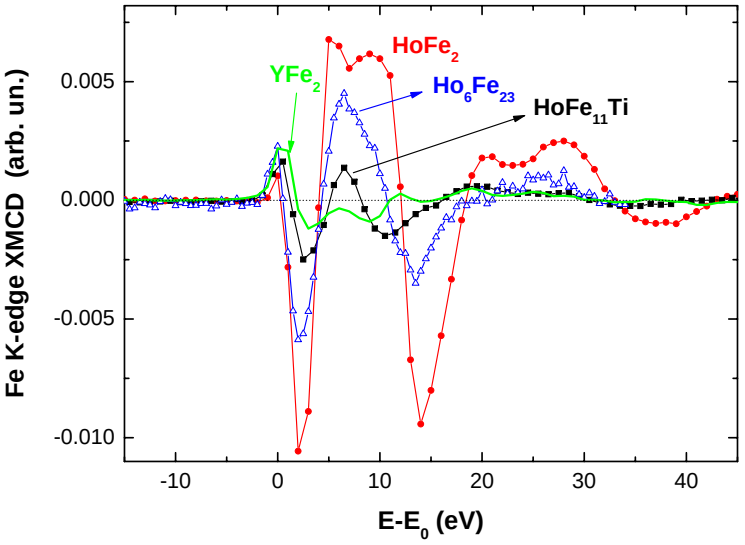

Figure 6.32: Comparison of the Fe K-edge XMCD spectrum recorded for different Ho-Fe intermetallic compounds. All the XMCD spectra were recorded at conditions giving rise to nearly saturated moments.

As a result of the large R contribution, the iron contribution is somehow hidden and their disentanglement becomes very intricate. In the case of pure Laves phases their magnetism is well described and we know that the Fe contribution to the XMCD signal will be very similar to that of $LuFe_2$. Consequently, one could apply a two-sublattice method as previously made for other R-T series to separate $XMCD_R$ and $XMCD_T$ contributions. However, the situation becomes intricate in the case of Fe-Al diluted compounds. As previously commented, no clear determination of μ_{Fe} has been obtained from other experimental methods up to now. In addition, the large R contribution makes difficult to obtain information about both μ_{Fe} and the contribution of Fe to the XMCD signal, which remains as an open question.

Nevertheless, in some cases the $XMCD_R$ contribution does not completely hide the $XMCD_{Fe}$ contribution, so that some hints can be found about the behaviour of Fe in the pseudobinary compounds. In particular, Gd compounds have a relatively small R contribution and the A feature can be clearly seen.

Lu *vs.* Gd comparison (see Fig. 6.33) shows that not only the first peak is similar for binary compounds but also in the case of $Gd(Al_{0.25}Fe_{0.75})_2$ it is much larger than for $Lu(Al_{0.25}Fe_{0.75})_2$. These results are in agreement with the information obtained from M(H) and Mössbauer experiments. They point out that the abrupt reduction of peak A is not due to the magnetic moment of Fe undergoing a transition from weak (WFM) to strong ferromagnetism (SFM), but it can be explained by assuming a disordered magnetic structure for Lu diluted compounds, whereas in Gd compounds the magnetic moments are collinearly aligned. The reduction of the intensity of peak A from ∼0.0034 in $GdFe_2$ to ∼0.0023 in $Gd(Al_{0.25}Fe_{0.75})_2$ shows that μ_{Fe} slightly reduces according to M(H) and Mössbauer results.

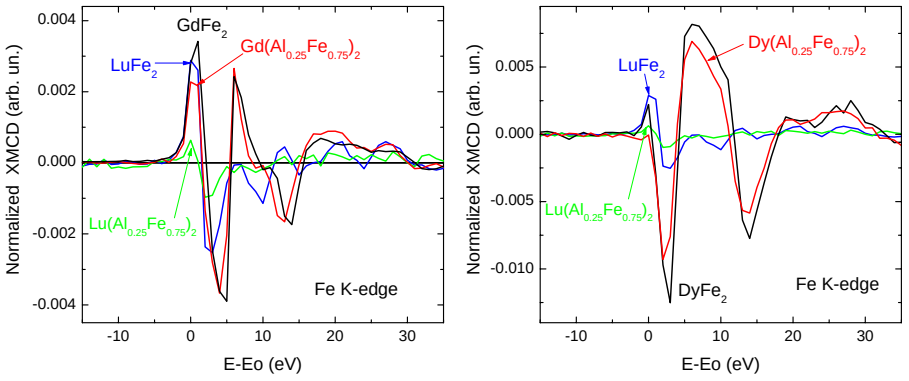

Figure 6.33: Comparison of the Fe K-edge XMCD spectra measured on different RFe_2 and $R(Al_{0.25}Fe_{0.75})_2$ compounds: Gd *vs.* Lu (left) and Dy *vs.* Lu (right). The XMCD spectra were recorded at 5 K and under the action of an applied magnetic field of 50 kOe.

When a pseudobinary Laves phase compound with a heavy rare-earth different from Gd is studied, the analysis of the spectra becomes more difficult. When R is Tb, Dy, Ho or Er, the R contribution to the XMCD spectrum is very large and completely hides the Fe contribution. Moreover, the experimental spectra in Fig. 6.30 suggest not only a reduction of the R features with increasing Al content (which would allows us to see the Fe contribution) but also the narrowing and the shift of the R features to lower energies.[3] Consequently, our results seems to indicate that the shift of the R contribution features towards lower energy results in an overlapping of A and B peaks so this effect can also be responsible for the apparent depletion of the first spectral feature (A peak). As a consequence, we cannot deduce from the XMCD

[3]This energy shift can be tentatively addressed to the modification of the DOS due to volume expansion of the lattice as Al increases. Unfortunately we cannot easily verify this hypothesis.

spectra if, in these compounds, the Fe moments have an ordered or disordered magnetic structure. Taking into account the M(H) results one could expect the Fe moments to be nearly collinear and so a $XMCD_{Fe}$ contribution similar to that found for Gd but, unfortunately, this cannot be clarified based on these XMCD data, thus remaining as an open question.

Temperature dependence.

Initially, the XMCD spectra corresponding to $R(Al_{1-x}Fe_x)_2$ samples were recorded at T = 5 K. With the purpose of further verify our results, we have extended this study including the modification of the signal with temperature. The thermal dependence of the XMCD signal recorded at H = 50 kOe for different compounds is shown in Figure 6.34.

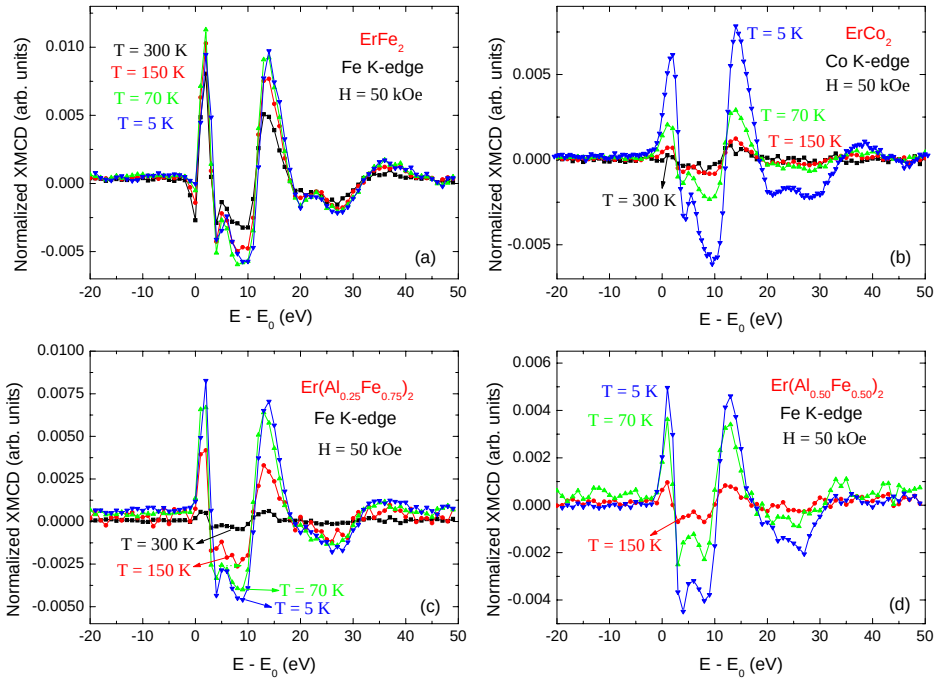

Figure 6.34: Thermal dependence of the XMCD spectra at the T K edge of $ErFe_2$ (a), $ErCo_2$ (b), $Er(Al_{0.25}Fe_{0.75})_2$ (c) and $Er(Al_{0.50}Fe_{0.50})_2$ (d) compounds.

In the case of $ErFe_2$ XMCD spectra, the intensity of the feature at E - $E_0 \sim 0$ eV enhances with increasing temperature, while the rest of the features undergo a reduction. This result is easily understood if one considers that B, C_1, C_2 and D features are mainly due to R, while peak A has also a sig-

nificative contribution from Fe. The observed behaviour resembles the fact that the magnetization of the rare earth sublattice decreases faster that the magnetization of the Fe sublattice as the temperature increases. On the other hand, the magnetic moment of Co in Laves phases is strongly dependent on the R magnetism (μ_{Co} is induced by the molecular field of R) so that one can expect a reduction of M_{Co} proportional to that of M_R, in agreement with the observed gradual reduction of all the features in the XMCD signal. In the case of $Er(Al_{1-x}Fe_x)_2$ diluted compounds, the thermal evolution is similar to that found for Co compounds. This result may be tentatively explained in terms of a decrease of the strength of the Fe-Fe interaction caused by Al substitution. The R-Fe would then become the main interaction into determining the Fe K-edge XMCD signal so that the Fe contribution to the signal, $XMCD_{Fe}$, seems to be related to the magnetic moment of the rare-earth sublattice in analogy to the Co behaviour of RCo_2 compounds.

6.8 XMCD at the R-L_2 edge

The R L_2-edge XMCD spectra measured on the binary Laves phases RAl_2, RFe_2 and RCo_2, at 5 K and under an applied magnetic field of 50 kOe are displayed in Fig. 6.35. The L_2 spectral profile of RAl_2 consists on a main negative peak centered at E - $E_0 \sim 2$ eV above the edge (E) and a smaller positive peak at higher energy, E - $E_0 \sim 7$ eV (F). An additional feature at E - $E_0 \sim$ -5 eV (C) appears for R = Tb, Dy, Ho and Er. This feature is a negative shoulder in Dy, Ho and Er, while in the case of Tb, it is an small positive peak. When the rare-earth in the compound is a light one, the opposite sign is found in the XMCD spectrum.

The amplitude of the RAl_2 spectra decreases as the rare-earth atomic number, Z, increases in accordance with the R(4f) spin. However, contrary to the 4f spin case, this decrease is not linear with Z, so it cannot be directly related with the R(4f) spin. In the same way, the evolution of the signal does not resemble the R(4f) orbital, L, or total, J, magnetic moments.

Bearing in mind that the magnetism of the 5d band, and consequently the R $L_{2,3}$-edges XMCD spectra of RAl_2, is thought to be originated from the 4f-5d polarization, it is not unreasonable to assign this modification through RAl_2 in terms of the lanthanide contraction.[18] The reduction of the atomic radius of the R ion with increasing Z is much weaker (about 10 times) than the decrease of the 4f shell, leading to a smaller overlap of the 4f and 5d shells with increasing Z. In addition, trying to get a deeper insight into the origin of these spectra and, in view of the indirect 4f-4f interaction mediated by the conduction band, we have compared the intensity of these XMCD signals with the n_{RR} molecular

field coefficient. In Figure 6.36 we have displayed the comparison between the intensity of the XMCD signals (peak E) and n_{RR} calculated from T_C (ecs. 1.3 - 1.5). **As it can be seen the XMCD dependence of the RAl_2 compounds remarkably mimics the modification of the molecular field coefficient n_{RR} within this series. This result points out the common origin of these two magnitudes, which on the one hand would indicate the important role of the R(5d) states in the magnetism of the RAl_2 compounds and, in addition, it would supply an alternative method to experimentally study the R-R interaction.** Such a relationship has not been reported previously. Since our results are based on the study performed through just one R-Al series, we cannot conclude if this is a general result or a particularity of the RAl_2 series.

Different arguments have to be considered to explain the spectral modification induced by substitution of Al by Fe or Co. When the 3d metal is placed in the lattice, the spectrum amplitude undergoes a decrease. This reduction does not occur equally through the whole energy range. For compounds with heavy R, the low energy part of the main negative peak, E_1 at E - $E_0 \sim 0$ eV, undergoes an abrupt decrease, while the diminution in the higher energy part, E_2, is much slighter. This is clearly observed in the case of $DyFe_2$, $HoFe_2$ and $ErFe_2$ compounds. Indeed, $ErFe_2$ not only presents a reduction of E_1, but a positive peak at energies ~ 0 eV.[4] On the other hand, the effect of the magnetic transition metal is not observable at first sight in Gd compounds. However, a closer inspection (see inset in Fig. 6.35.a) shows that for $GdFe_2$ the position of the minimum is shifted (1 eV) towards higher energy, the negative peak becomes asymmetric and its intensity decreases. This result suggests that although the E_1 and E_2 structures cannot be energy resolved the reduction of the low-energy component of the E peak due to Al substitution is also present in the Gd case.

In addition, the above described change of the L_2-edge signal holds for both Co and Fe Laves phases. The reduction of E_2 is similar for Fe and Co compounds, while the modification of the profile at E_1 is clearly more obvious in the case of Fe compounds.

The different behaviour observed for RAl_2, RFe_2 and RCo_2 cannot be explained in terms of the different magnetic properties of the rare-earth through the three series. Indeed, it is commonly assumed that the magnetic 4f moments are close to the free-ion values in these compounds. Consequently, no significant variation of the intra-atomic 4f-5d polarization effect is expected, (at least to account for the experimental XMCD behaviour). The fact that the magnetic properties of the R counterpart (Al, Fe and Co) are clearly differ-

[4] notice that E_1 feature has been called D in chapter 5

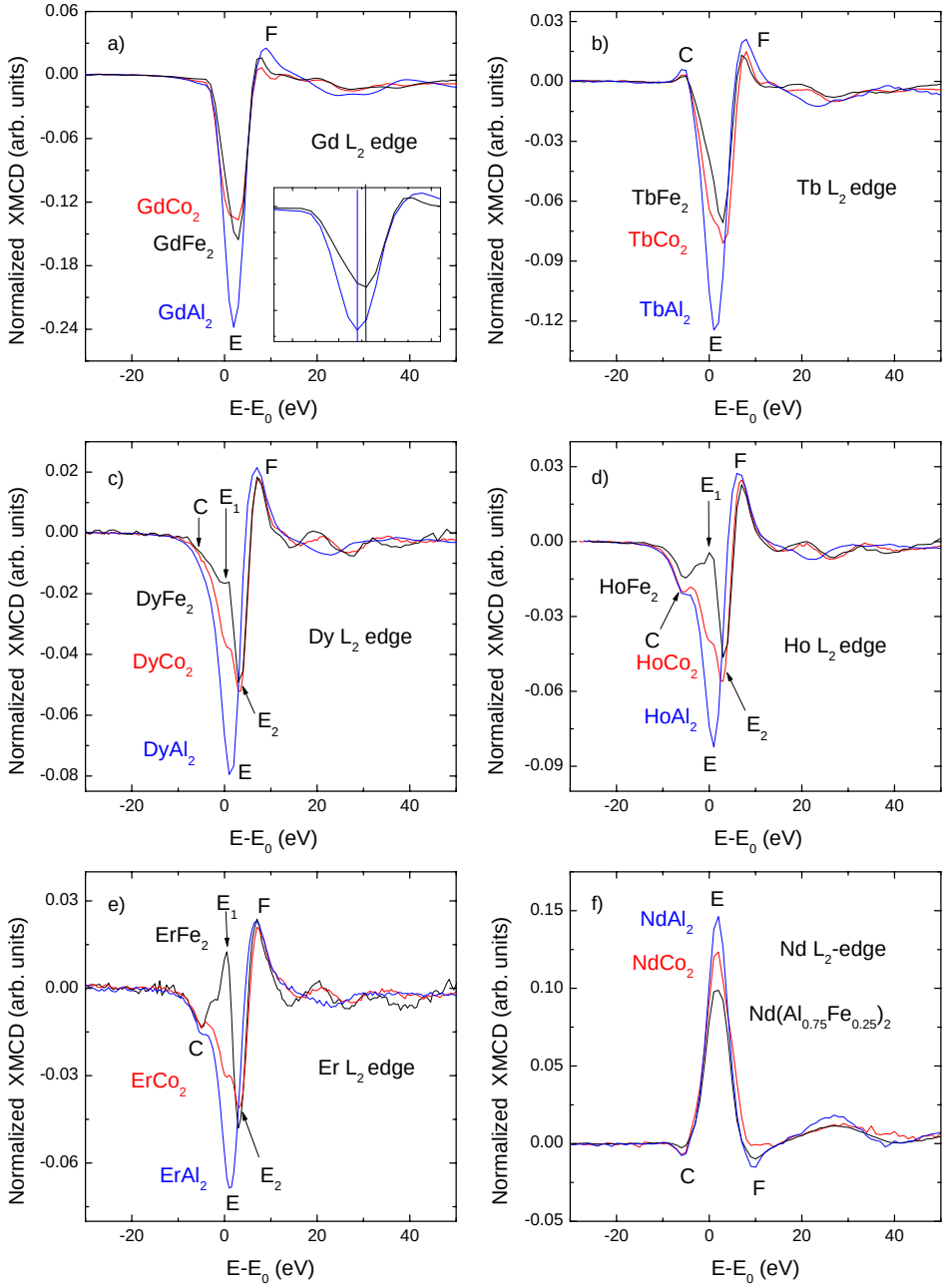

Figure 6.35: XMCD spectra recorded at T = 5 K and H = 50 kOe at the R L_2-edge in RT_2.

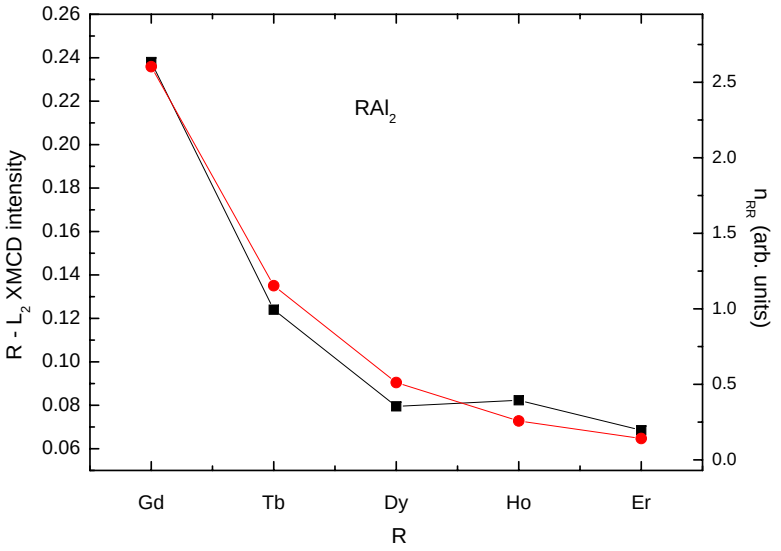

Figure 6.36: Comparison of the intensity of the XMCD spectra at the R $L_{2,3}$-edges in RAl_2 and the n_{RR} coefficients obtained from M(T) curves

ent through the studied series suggests that **the origin of such an unusual behaviour stems from an unexpected magnetic contribution arising from the T sublattice even if the R are proven.**

In order to get a deeper insight into this possibility we have extended this study to the $R(Al_{1-x}Fe_x)_2$ and $R(Al_{1-x}Co_x)_2$ pseudobinary Laves phases. In all the studied series a gradual evolution of the L_2 spectrum is observed as Fe (Co) substitutes Al. This gradual reduction of the signal is more evident in the low energy part of the negative peak E. This is illustrated in Fig. 6.37, where the XMCD spectra recorded at the rare-earth L_2-edge for different R(Al, $T)_2$ series are shown. Despite the reduction of the intensity at E - $E_0 \sim 0$ eV is more noticeable as the atomic number of R increases, it should be noticed that the general trend is the same no matter the specific R in the compound. Indeed, also in the $Gd(Al_{1-x}Fe_x)_2$ series a gradual evolution is observed even if no unambiguous discrimination E_1 *vs.* E_2 can be done.

In the same way, a similar behaviour is found independently on the transition metal placed on the lattice (Co or Fe). In Fig. 6.38 we have compared the evolution of $Ho(Al_{1-x}Fe_x)_2$ and $Ho(Al_{1-x}Co_x)_2$ Ho L_2-edge XMCD spectra with the Al content. It can be observed that the modification of the XMCD spectral profile is the same for both series (the signal at E - $E_0 \sim 0$ eV is markedly reduced). The only difference between them concerns the intensity of this reduction. Thus, the intensity of the XMCD spectrum of RCo_2 at E -

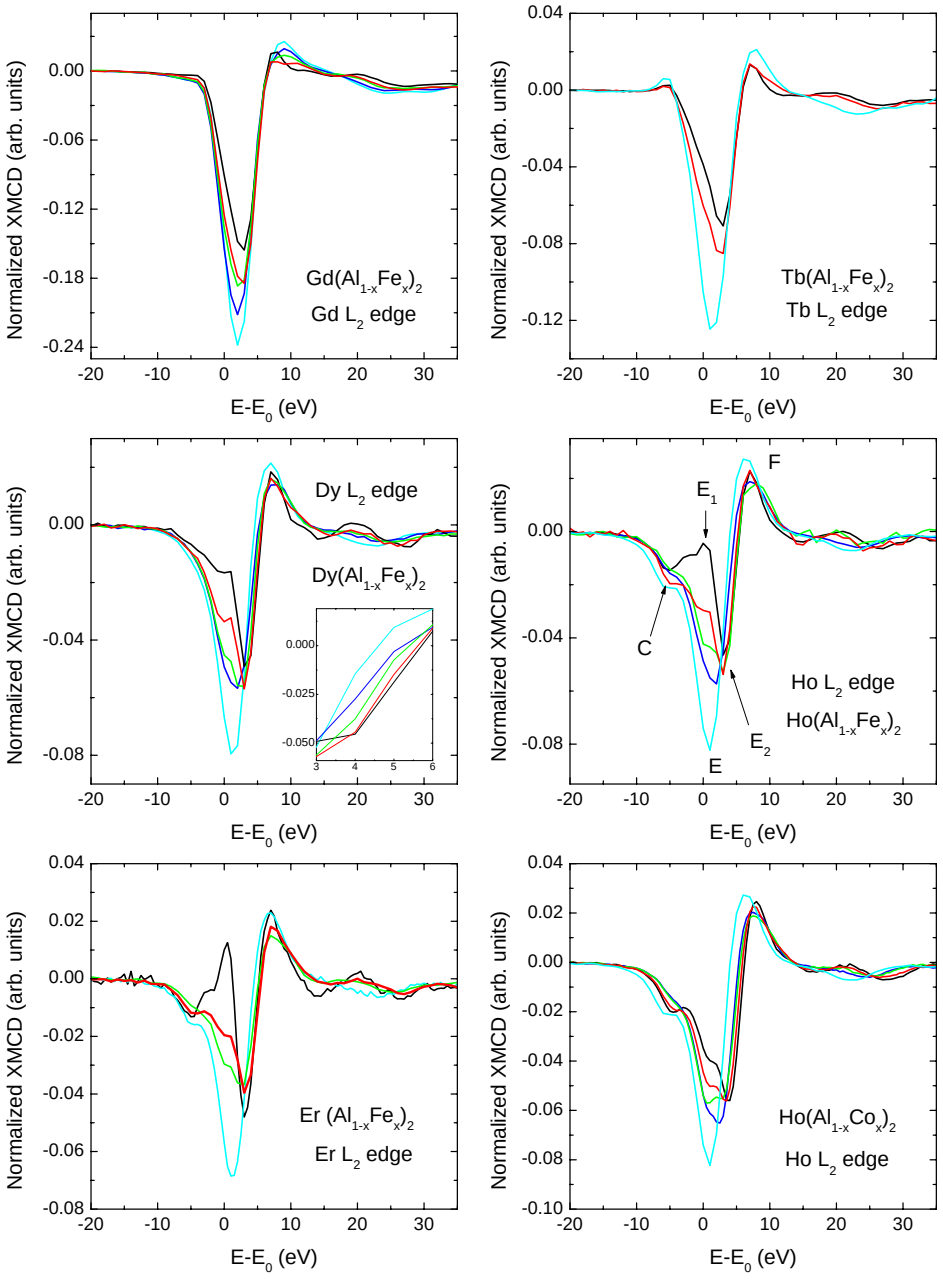

Figure 6.37: XMCD spectra at the R L_2-edges in R$(Al_{1-x}Fe_x)_2$ compounds with x = 1 (black line), x = 0.75 (red), x = 0.50 (green), x = 0.25 (blue), and x = 0 (cyan) and Ho$(Al_{1-x}Co_x)_2$ compounds with x = 1 (black line), x = 0.80 (red), x = 0.50 (green), x = 0.30 (blue), and x = 0 (cyan). All the spectra have been recorded at T = 5 K and H = 50 kOe.

$E_0 \sim 0$ eV is clearly smaller than that of RFe_2 compounds, while is very alike to that found in the compounds with 75% of Fe content. A direct comparison including the "pure" binary Laves phases for a given R and those with 75% Fe is plotted in Fig. 6.39.

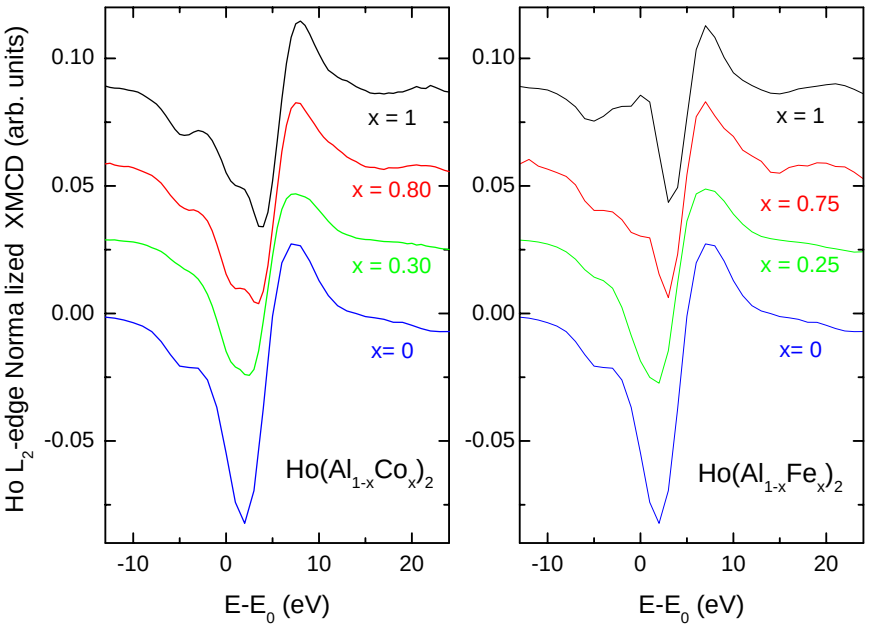

Figure 6.38: XMCD spectra at the R L_2-edges in $Ho(Al_{1-x}Fe_x)_2$ compounds with x = 1 (black line), x = 0.75 (red), x = 0.25 (green), and x = 0 (blue) and $Ho(Al_{1-x}Co_x)_2$ compounds with x = 1 (black line), x = 0.80 (red), x = 0.30 (green), and x = 0 (blue).

How can we account for such a behaviour? What is the origin of the described XMCD evolution? In chapter 5 we assumed that the measured signal at the L_2 edge on Ho_6Fe_{23} was made up of two contributions of Ho and Fe origin. Is this scheme consistent with the present results? In the following discussion we will show that the presence of a transition metal contribution agrees with our results. Additionally, the effect of other possible important factors such as crystal structure and magnetostriction effects, quadrupolar transition influence, etc, will be discussed.

All the samples employed in this work (except those with x = 0.5) present the same $MgCu_2$-type (C15) crystal structure. Therefore, the described changes on XMCD cannot be associated to structural modifications. Of course, differences in the lattice parameter involve differences in the density of states (DOS) and will have an effect on the XMCD spectrum. However, this effect is expected to affect all the features, but not to change the intensity of a particular one while the others remain unaltered. The experimental results do not hold

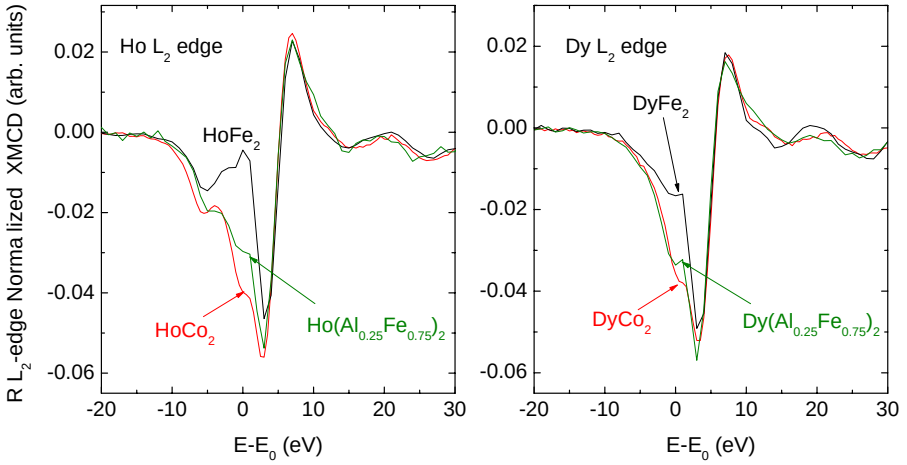

Figure 6.39: Comparison of the XMCD spectra measured at the R L_2-edge in $R(Al_{0.25}Fe_{0.75})_2$, RFe_2 and RCo_2 compounds with R = Dy and Ho.

such an assumption. Indeed, the width of the signal does not seems to vary, at least in a first sight, even for the largest lattice parameter difference, i.e. that between RAl_2 and RCo_2 compounds where a relative change of $\sim 9\%$ is observed in the lattice parameter. On the contrary, differences occur only in a specific region of the spectra (-2 eV < E - E_0 < 2 eV). In the same way, also the possible role of magnetostriction and lattice distortion can be discarded. Although magnetostriction is expected to be more important in RFe_2 than in RAl_2 and, subsequently, it could alter in a different manner the different absorption spectra, the volume modifications due to magnetostriction are very small. Among alloys, $Tb_xDy_{1-x}Fe_2$ exhibit the highest known room temperature magnetostriction, about 2600 x 10^{-6}, in a field of 2 kOe.[140] That is, a relative modification of $\sim 0.2\%$, which can be neglected if we take into account that the effect of the $\sim 9\%$ volume modification between RAl_2 and RCo_2 cannot be clearly observed in the measured XMCD spectra. In fact, some years ago, Chaboy *et al.* tried to study the effect of magnetostriction on XAS signal by using the $TbFe_2$ compound, but this experience was not successful as they could not appreciate any clear modification on the XAS signal.[5]

Moreover, this strong reduction of the signal at the low energy region cannot be either explained in terms of easy direction of magnetization, EMD, and magnetocrystalline anisotropy properties. As one can see in Table 6.15, RFe_2, RCo_2 and RAl_2 present the same EMD for a given R so that the evolution of the L_2 spectrum with the 3d content cannot be explained in terms of a change of

[5] J. Chaboy and A. Marcelli, private communication.

the magnetocrystalline anisotropy. In addition, EMD in Laves phases depends on the specific R in the compound. Thus, for example, the EMD is [111] for Er compounds, while in Laves phases with Dy is the [100] direction. If magnetocrystalline anisotropy were at the origin of the changes in the spectral profile, it should be reflected on the dichroic signals by affecting in a different manner to compounds with diverse EMD. On the contrary, we observe the same evolution independently on the EMD in the series.

Compound	EMD	Compound	EMD	Compound	EMD
$GdFe_2$	[111]	$GdCo_2$	[001]	$GdAl_2$	-
$TbFe_2$	[111]	$TbCo_2$	[111]	$TbAl_2$	[111]
$DyFe_2$	[001]	$DyCo_2$	[001]	$DyAl_2$	[001]
$HoFe_2$	[001]	$HoCo_2$	[011] [001]*	$HoAl_2$	[011] [001]**
$ErFe_2$	[111]	$ErCo_2$	[111]	$ErAl_2$	[111]

Table 6.15: EMD at 4.2 K [169, 177, 178] (*above spin reorientation 17 K, **above 20 K)

As discussed in section 6.4, the analysis of the magnetization measurements does not show any indication suggesting a modification of the electronic, nor of the magnetic state of the rare-earth atoms upon substitution of Fe by Al through the whole $R(Al_{1-x}Fe_x)_2$ series that can explain the XMCD behaviour.

Finally, being the quadrupolar transitions of a well defined atomic character, it appears rather improbable to connect the observed behaviour as a function of the Fe:Al (Co:Al) concentration to the modification on these quadrupolar transitions. In addition, the energy in which this modification appears is incompatible (too high) with a quadrupolar origin as the R(4f) states must be located at lower energies.

The gradual evolution through the $R(Al_{1-x}Fe_x)_2$ and $R(Al_{1-x}Co_x)_2$ series points out that the presence of a magnetic transition metal in the compound is at the origin of an *extra* contribution at the rare-earth L_2-edge XMCD spectra. Thus, the large decrease at E - $E_0 \sim$ 0 eV can be regarded as the result of a positive peak appearing at this energy as the T content increases. If the intensity of the emerging positive feature is smaller than the negative dip on RAl_2, just a reduction of the dip is observed. However, a total positive peak may appear in some cases if the new peak is large enough. As shown in Fig. 6.35, $ErFe_2$ exemplifies this case.

Moreover, the progressive substitution of Al by Fe (Co) increases the number of Fe (Co) ions surrounding the absorbing lanthanide, so that the progressive increase can be related to the number of magnetic Fe (Co) atoms in the neighbourhood of the rare-earth one. Furthermore, the comparison of Fe *vs.* Co series (Figures 6.38 and 6.39) indicates that the new feature is not only con-

nected to the number of T neighbours, but also to the magnetic moment of the transition metal in the crystal lattice. This might explain why RCo_2 presents a weaker reduction of the intensity at E - $E_0 \sim 0$ eV than RFe_2, whereas it is quite similar to that of $R(Al_{0.25}Fe_{0.75})_2$: The value of the magnetic moment of Fe atoms in RFe_2 compounds is: $\sim 1.6\ \mu_B$ whereas that of Co in RCo_2 compounds is: ~ 0.8 - $1\ \mu_B$. According to M(H) and Mössbauer data, the magnetic moment of iron in $R(Al_{0.25}Fe_{0.75})_2$ is thought to range between 1.2 μ_B and 1.6 μ_B. Taking into account both the number of T atoms and their magnetic moment, one can easily explain the differences in the XMCD profiles shown in Fig. 6.39. **These results, i.e., the modification of the XMCD intensity at ~ 0 eV with both T concentration and moment of the T component, are a clear evidence of the influence of the magnetic 3d at this edge.**

Assuming that there is an extra feature originated by the presence of the transition metal, this T contribution can be isolated by subtracting from each recorded dichroic spectrum that of RAl_2 with the same R. That is: $XMCD_T = XMCD_{RT_2} - XMCD_{RAl_2}$.

Before discussing the subtracted signals, several comments must be given in relation to the substraction procedure: The RAl_2 (R = Dy, Ho, Er) signals have been slightly ($\Delta E \leq 1$ eV) shifted in energy before the substraction procedure. If the XMCD(RT_2) - XMCD(RAl_2) subtraction is made directly, a quite intense negative peak appears at ~ 5 eV. This is illustrated in Fig. 6.40 where the extracted signal for both situations has been plotted in the case of XMCD($DyFe_2$) - XMCD($DyAl_2$). As it can be seen, the shape of the XMCD signal remains almost invariable along the measured energy range but at ~ 5 eV, where the profile is very sensitive to the relative shift between RAl_2 and RFe_2 (RCo_2) spectra. This feature stems from a derivative effect due to the progressive shift of the XMCD signal at ~ 5 eV as T atoms substitute the Al ones, which is "clearly" observed for R = Dy, Ho and Er (see inset if Fig. 6.37). This progressive shift can be thought to be originated from DOS expansion due to the lattice contraction. Unfortunately, this "volume effect" hypothesis cannot be verified in an easy manner. An alternative explanation for this small shift can be found in the different backscattering amplitude and phase of Al, Fe and Co neighbouring atoms. Furthermore, the fact that this energy shift is not discriminated in Gd and Tb series indicates that the negative peak at $\sim$ 5 eV in the subtracted signal is likely due to a derivative-like effect due to the crystal cell variation. Therefore, the signals RAl_2 (R = Dy, Ho, Er) have been shifted so that this feature has been minimized.

The result of applying this substraction procedure, is shown in Fig. 6.41. **The subtracted signal is mainly made of a very intense positive peak,**

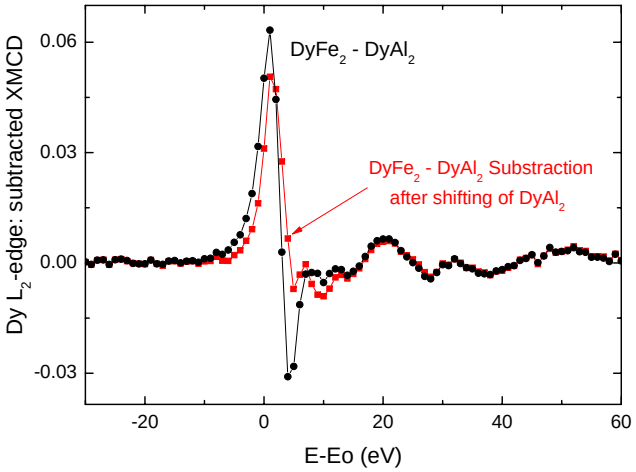

Figure 6.40: Dy L_2-edge XMCD (T = 5 K, H = 50 kOe) spectrum corresponding to the $DyAl_2$-$DyFe_2$ subtraction without shifting any signal (•), and after shifting of the $DyAl_2$ signal (■)(see text for details).

at $\sim$ 1 eV, followed by an small structured negative peak at higher energies. As it can be seen, the profile is basically the same no matter the rare-earth, nor the transition metal alloying component. Besides, the size of the Fe contribution is 1.4 - 2 times the obtained for the Co Laves phases (see Fig. 6.44). As the Fe magnetic moment, $\sim$ 1.6 μ_B, is about twice larger than the Co magnetic moment, $\sim$ 0.8 μ_B, in RT_2 Laves phases, this result agrees with the fact that the emerging peak is related with a magnetic contribution stemming from the 3d metal.

Fig. 6.42 presents the result of applying the same process to pseudobinary $Gd(Al_{1-x}Fe_x)_2$ compounds. **The shape is kept invariable with Fe content while the size of the features enhances with the number of Fe atoms.** The relative intensity of this subtracted signal as a function of the Fe concentration, x, is 0.28 : 0.53 : 0.65 : 1.

Taking into account the coupling scheme presented in 1.1, the origin of this new emerging feature should be searched in the T(3d)-R(5d) hybridization. Trying to go further into the nature of the emerging component, the R-L_2-edge XMCD spectra have been also recorded in Laves phases containing a non-magnetic rare-earth: $LuFe_2$ and $Lu(Al_{0.1}Co_{0.9})_2$. In principle, none of these two compounds should exhibit XMCD signal at the Lu L_2 edge as Lu is a non-magnetic ion. On the other hand, non zero $L_{2,3}$-edges XMCD spectra have been observed in $LuFe_2$.[179, 180] The appearance of a non-zero Lu XMCD

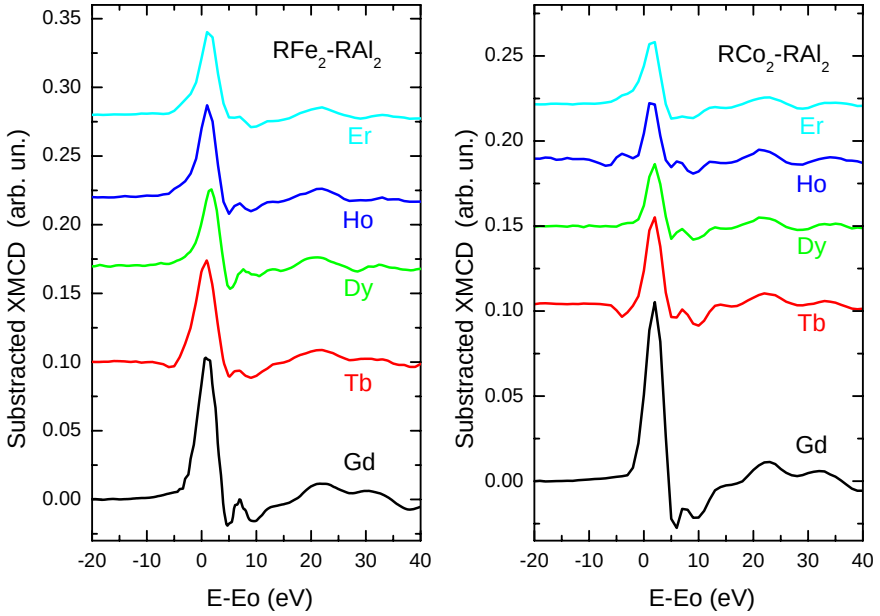

Figure 6.41: Comparison of the XMCD spectra obtained after XMCD(RT_2) - XMCD(RAl_2) subtraction.

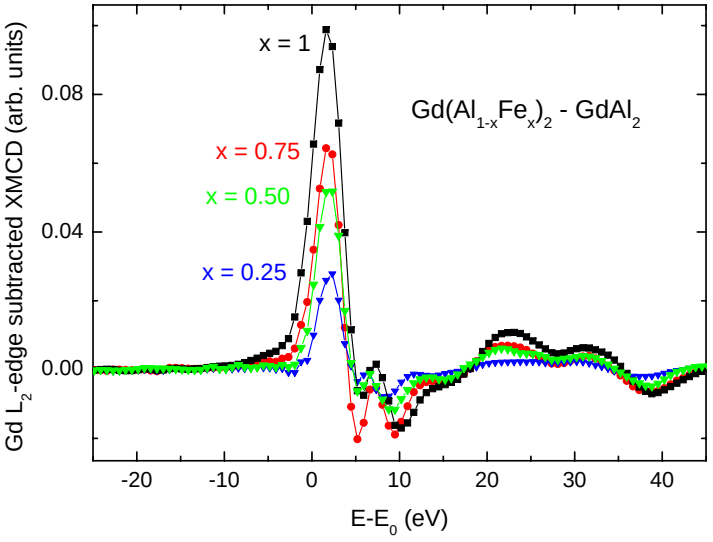

Figure 6.42: Comparison of the XMCD spectra obtained after $Gd(Al_{1-x}T_x)_2$ - $GdAl_2$ subtraction.

signal is thought to be due to the 5d - 3d exchange. If our hypothesis is correct, the T(3d)-R(5d) hybridization should give rise to a Lu-L_2 XMCD signal proportional to μ_{Fe}.

The corresponding spectra are shown in Fig. 6.43. Despite Lu is "non magnetic", an intense dichroic signal is found in both cases. Additionally, the intensity of the $LuFe_2$ signal (-0.053) is about twice that of the Co compound ($\sim$ -0.024) in agreement with the different values of μ_{Fe} and μ_{Co}. Macroscopic magnetic data give a magnetic moment of 2.86 μ_B for $LuFe_2$ while that of $Lu(Al_{0.1}Co_{0.9})_2$ is 1.16μ_B (both measured at H = 50 kOe). In addition, the sign of the Lu $L_{2,3}$ edges gives the correct sign for the orbital and spin magnetic moments of the R(5d) states, contrary with the wrong signs found for other R-T intermetallics with magnetic R.

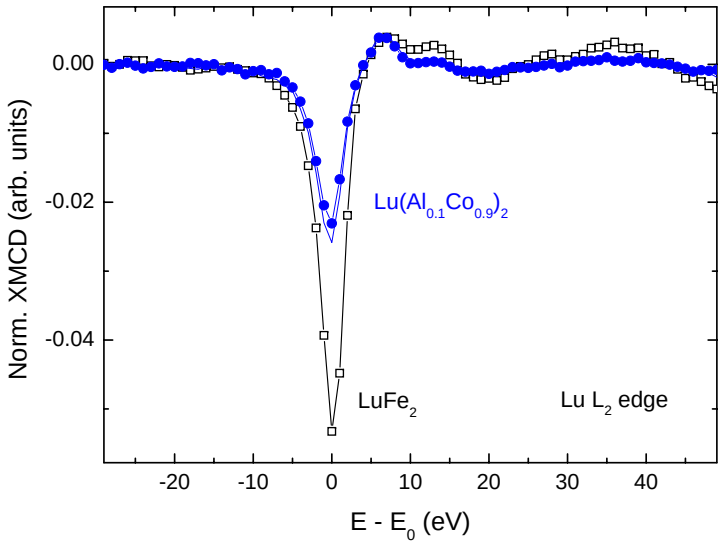

Figure 6.43: Lu L_2-edge XMCD (T = 5 K, H = 50 kOe) spectrum recorded on $LuFe_2$ (□, T = 5 K, H =50 kOe) and $Lu(Al_{0.1}Co_{0.9})_2$ (•, T = 5 K, H = 30 kOe) and (blue line, T = 5 K, H = 100 kOe)

Moreover, the comparison of the subtracted signals to the Lu L_2-edge spectra of $LuFe_2$ and $Lu(Al_{0.1}Co_{0.9})_2$ compounds reports some other important results:

- We have found that the maximum of the Lu XMCD spectrum appears at the same E - E_0 energy where the "T contribution" is located in the RFe_2 cases.
- In the case of Lu samples the L_2 XMCD spectrum is negative, while

the subtracted signal is positive. This is in agreement with the opposite direction of $\mu_{Fe(Co)}$ relative to the total magnetization of the sample for Lu and heavy magnetic rare-earth samples.

- Also, the profile of the subtracted signals closely resembles the corresponding Lu signal. This provides further support to the applied substraction procedure.

Taking into account that the Lu L_2-edge XMCD signal cannot arise from the R(4f)-R(5d) hybridization, as Lu has its 4f band complete filled, it has to be explained in terms of the T(3d)-R(5d) hybridization. There is no reason for the disappearance of the influence of the Fe(3d) moments into the polarization of the R(5d) states when R carries a 4f magnetic moment. **Consequently, the magnetism of the R(5d) states results from the interplay of both R(4f)- R(5d) and T(3d) - R(5d) spin polarization. As a result, the XMCD at these edges probes both the R and T magnetism.**

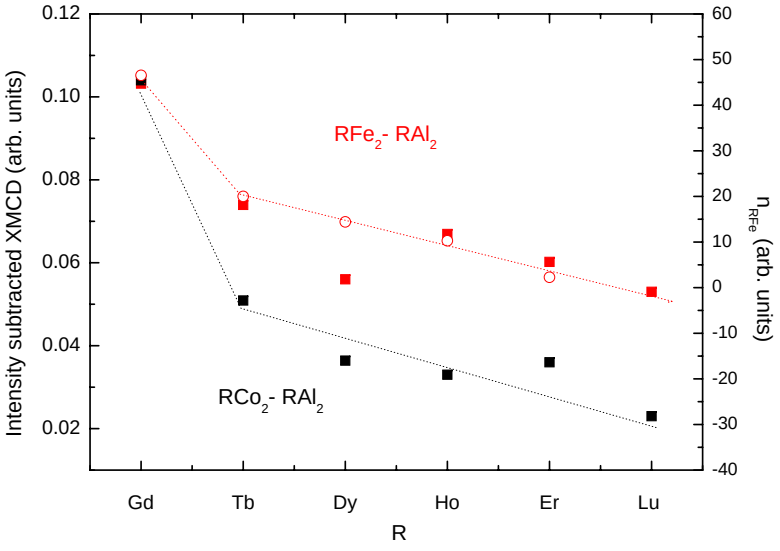

Figure 6.44: Comparison of the intensity of the XMCD(RT_2) - XMCD(RAl_2) subtracted XMCD spectra and the intensity of the XMCD spectra measured in Lu Laves phase compounds (Fe series: ■ and Co series:■). In a different scale the modification of the n_{RFe} coefficient calculated from M(T) curves is also included (◯). Dotted lines are guides for the eyes.

Furthermore, in Fig. 6.44, the intensity of the subtracted signals is compared with that of the Lu reference compounds. In the case of Dy, Ho and Er Laves phases, the subtracted signal has almost the same intensity as the Lu one. However, the difference between the values of the intensity of the

$XMCD_T$ signal increases towards Gd. Indeed, it can be observed in figure 6.44 that, as a general trend, the subtracted XMCD signal presents a reduction as the atomic number increases. To explain this behaviour we have taken into consideration several remarks:

Band-structure calculations show that the decreasing lattice constant with the atomic number, Z, leads to an enhancement of the T(3d)-R(5d) hybridization. [181] Therefore, this volume effect alone would not explain the decrease of the T contribution.

The magnetic moment of Fe can be regarded as constant through the binary RFe_2 series including $LuFe_2$. Therefore, the evolution of the subtracted $XMCD_{Fe}$ signal presented in Fig. 6.44 can hardly been explained in terms of a modification of μ_{Fe}. Even is we assume that μ_{Fe} varies from $LuFe_2$ (1.45 μ_B) to $GdFe_2$($\sim$ 1.60 μ_B) as reported by Burzo,[143, 144] this increase is too small to account for the clear difference observed in the intensity of the subtracted signal.

A further point to be considered is the fact that the strength of the T(3d)-R(5d) hybridization will also depend on the polarization of the R(5d) states due to the R(4f) shell. Indeed, we have shown in figure 6.36 that both the L_2 XMCD signal of RAl_2 and the R(4f)-R(5d) exchange decreases with increasing atomic number so that this effect may counteract the volume effect. In relation to the R(4f)-R(5d) exchange, it is interesting to notice that also the T-R interaction is considered to be strongly affected by the intratomic R(4f)-R(5d) exchange. In fact, in view of the indirect nature of the R-T interaction, Belorizki *et al.* explained the decrease of the molecular field coefficient across the lanthanide series, n_{RT}, in terms of the reduction of the R(4f)-R(5d) hybridization. They conclude that the variation of the Fe(3d)-R(5d) hybridization through the series is negligible in a first approximation. Following this argument, we show in Fig. 6.44 the comparison between the intensity of the subtracted signal and n_{RT} obtained from T_C values (see. Eq. (1.5)). Both, the intensity of the subtracted signal and n_{RT} show the same trend, which suggests the common origin of both $XMCD_T$ and n_{RT}.

Regarding the Co magnetic moment, neutron diffraction experiments have determined μ_{Co} to vary from 1.00 μ_B in $GdCo_2$ to 0.72 μ_B in $ErCo_2$.[133] From magnetization measurements we have obtained $\mu_{Co} = 0.7\,\mu_B$ for $Lu(Al_{0.1}Co_{0.9})_2$. Therefore, this modification of μ_{Co} with R is in agreement with the observed results in $XMCD_{Co}$. For these compounds we cannot make a comparison between the intensity of the subtracted signal and n_{RT} obtained from T_C values due to the particular behaviour of Co in this series. Indeed, $Lu(Al_{0.1}Co_{0.9})_2$ shows a higher T_C than $HoCo_2$ and $ErCo_2$. However, estimates of n_{RCo} obtained from other methods indicate also a diminution with increasing atomic

number across the RCo_2 series.[133]

Concluding, in the light of the above results, the XMCD signal measured at the R L_2-edge in compounds with two magnetic sublattices, R and T, can be regarded as consisting on the addition two different contributions. The main magnetic signal is basically a negative peak and emerges as a consequence of the polarization of the 5d states by the 4f ones through an interatomic exchange. It seems rather reasonable to suppose that the magnetic state of the rare earth is not influenced by the Al substitution, and hence this contribution can be considered T independent and equal to the total signal of RAl_2. In addition, an extra magnetic contribution (a positive peak), coming from the T(3d)-R(5d) hybridization, has to be taken into account to explain the XMCD spectrum. T(3d) states will produce an extra polarization of the R(5d) states in the case of intermetallics with a magnetic T transition metal. Our results point out that this additional contribution is related to both the magnetic moment of the transition metal and to the number of T neighbours around the absorbing R. Furthermore, the fact that the intensity of $XMCD_T$ varies for the different rare-earths, decreasing with atomic number, suggests that the specific rare-earth plays also a role into this contribution. Our results suggest that $XMCD_T$ it is related not only to the value of μ_T itself, but also to the R(4f)-R(5d) exchange.

To illustrate to what extent this schematic two sublattice picture is suitable for describing the XMCD spectra at the L_2 edge in the case of R-T intermetallics, we have "re-built" the spectrum of RAl_2 by the addition of RT_2+ LuT_2 signals. In Fig. 6.45, the result of such a procedure has been plotted for binary compounds. As it can be seen, the experimental RAl_2 spectra matches with the profile obtained by applying a two sublattice model. A similar result is obtained for all the RT_2 compounds.

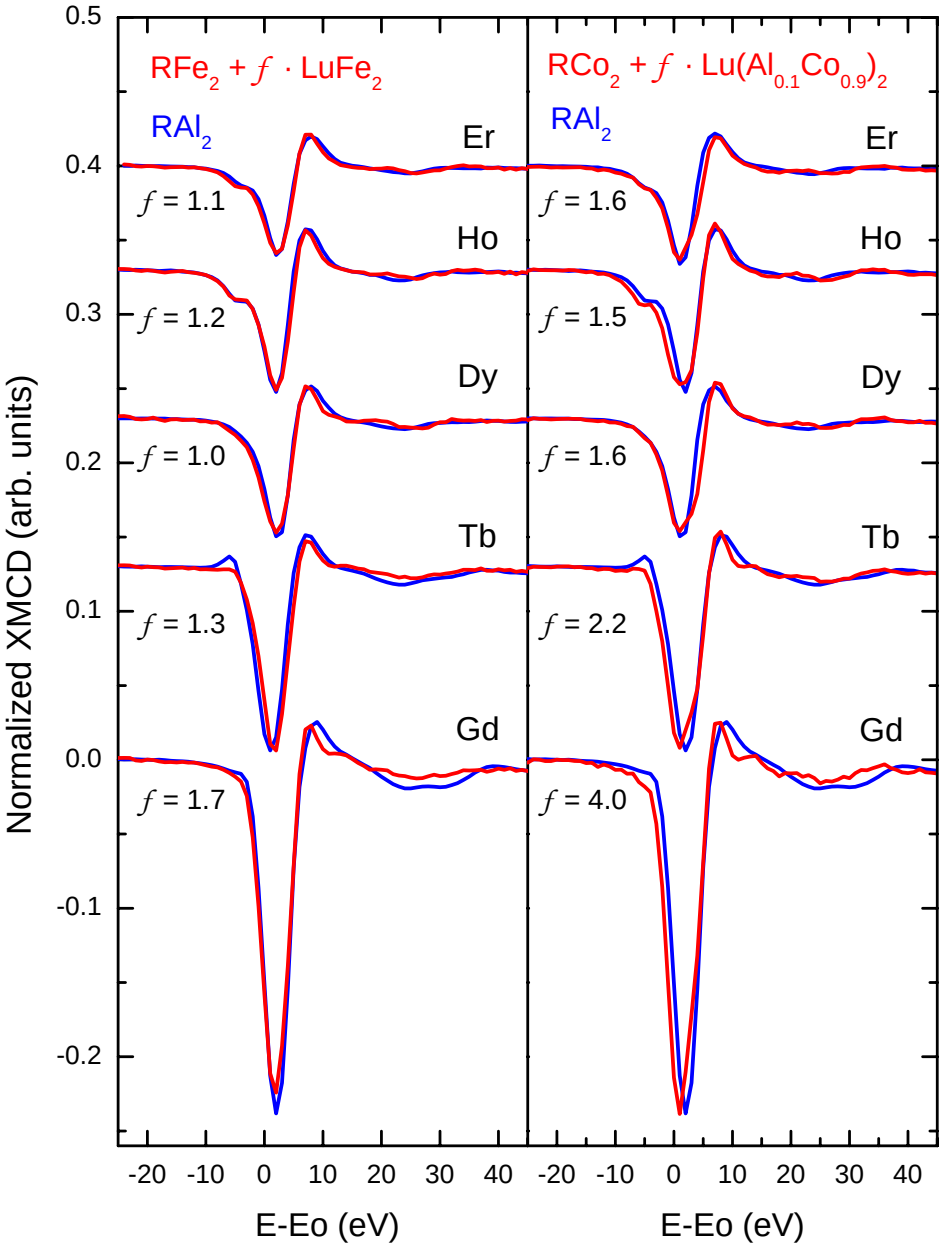

Figure 6.45: R L_2-edge XMCD spectrum recorded on RAl_2 (blue line) and XMCD spectrum obtained as the RT_2 + $LuFe_2$ (or $Lu(Al_{0.1}Co_{0.9})_2$) addition. As shown, the f factor necessary to meet both profiles depends on the specific compound. The spectra have been plotted in the same scale and vertically shifted for the sake of clarity

Temperature and pressure effect

In order to further verify the above interpretation of the L_2 dichroic spectra, this study has been extended by determining the dependence of the XMCD spectra with the modification of both temperature and pressure conditions.

Figure 6.46 shows the R L_2 spectrum at H = 50 kOe for different $R(Al_{1-x}T_x)_2$ compounds as a function of temperature. In the case of $HoFe_2$ and $ErFe_2$ XMCD spectra, the intensity of the feature at E - $E_0 \sim 0$ eV (E_1) enhances with increasing temperature, while the rest of the features undergo a reduction. This result is in agreement with the thermal behaviour observed in Ho_6Fe_{23} (section 5.3) and resembles the fact that the magnetization of the rare earth sublattice decreases faster that the magnetization of Fe sublattice as the temperature decreases. On the other hand, the magnetic moment of Co in Laves phases is strongly dependent on the R magnetism (induced by the molecular field of R) so that one can expect a reduction of M_{Co} proportional to M_R, in agreement with the observed gradual reduction of all the features in the XMCD signal.

In the case of $Er(Al_{1-x}Fe_x)_2$ diluted compounds, the thermal evolution is similar to that found for Co compounds. This result is consistent with the decrease of the strength of the Fe-Fe interaction as the Al content increases, as observed and discussed for the thermal evolution of the Fe K-edge XMCD of the same compounds.

XMCD measurements as a function of pressure have been performed in the case of $ErCo_2$. Previous works [182, 183]report that magnetic moment of Co in $ErCo_2$ vanishes with increasing temperature. Therefore, according to our hypothesis, a progressive modification of the XMCD profile towards the profile of $ErAl_2$ has to be found as pressure increases. Our results, shown in Fig.6.47, completely matches the expected modification.

Comparisons with other R:Fe series.

Finally, as the R(5d)-T(3d) hybridization is not specific of the Laves phases, but it is considered to play an essential role in the magnetism of every R-T intermetallic compound, the influence of Fe on the R L_2-edge XMCD can be expected to be present independently on the particular R:T stoichiometry.

Thus, in Fig. 6.48 we present a comparison of the Er L_2 XMCD spectra for RT_2, $R_2Fe_{14}B$ and R_2Fe_{17} series. Er_2Fe_{17} and $Er_2Fe_{14}B$ spectra correspond to earlier measurements recorded under different temperature and applied magnetic field conditions.[53, 65] Despite the intensity of the spectral features cannot be directly compared, the relative intensities of the main features for a

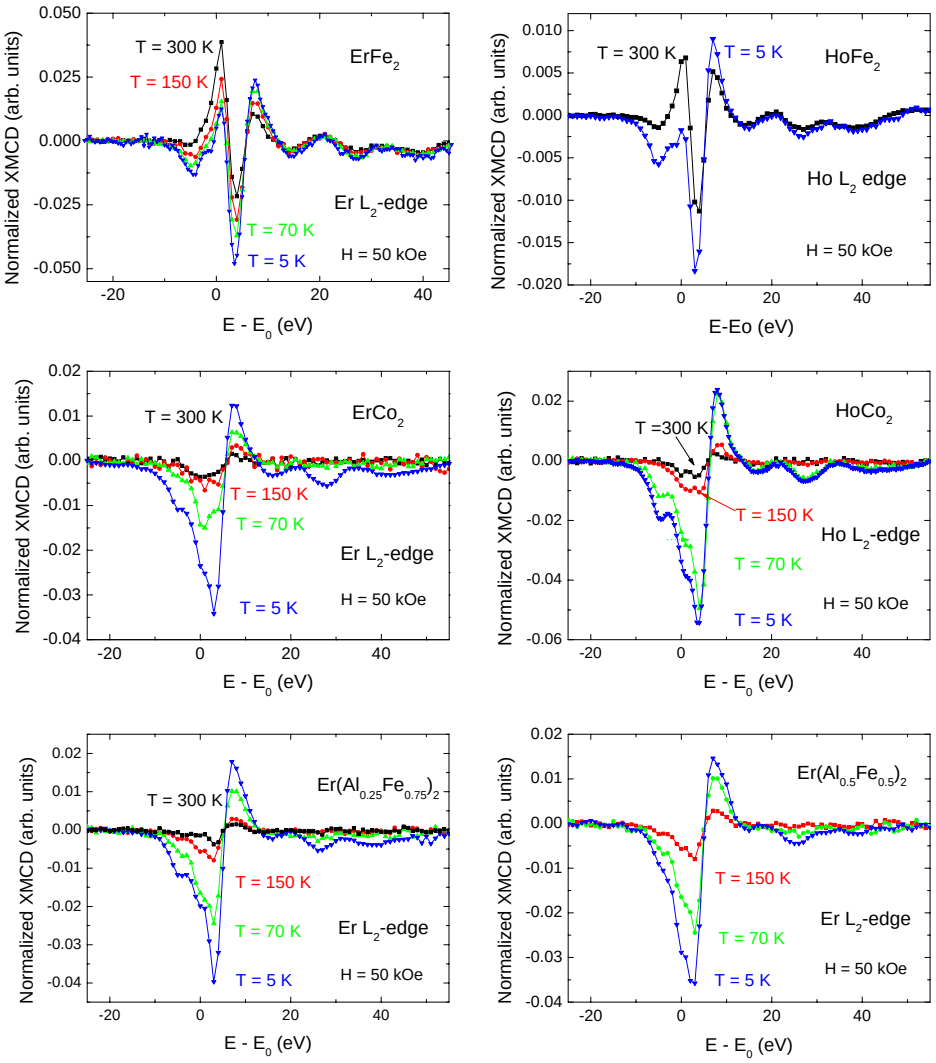

Figure 6.46: Comparison of the thermal dependence of the R L_2-edge XMCD spectra recorded for different $R(Al_{1-x}T_x)_2$ compounds.

given spectrum provide a clear confirmation of the presence of a contribution of Fe origin. It should be noted that in order to perform a correct comparison Er_2Fe_{17} and $Er_2Fe_{14}B$ spectra have been multiplied by -1. This is due to the fact that the magnetization in the Laves phases is dominated by the R-sublattice, M_R, while the contrary holds for Er_2Fe_{17} and $Er_2Fe_{14}B$, being the Fe-magnetization, M_{Fe}, larger than M_R. The effect of the Fe sublattice is reflected not only in the sign of the XMCD spectra but also in the relative magnitude of the features. Thus, when Er is the only magnetic element, as

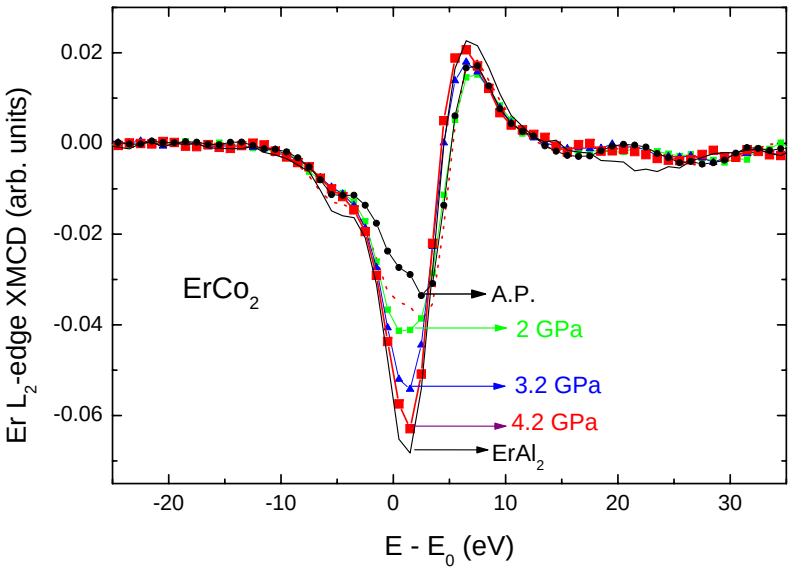

Figure 6.47: Modification of the Er L_2-edge XMCD spectrum of $ErCo_2$ with increasing applied pressure. Measurements were performed at T = 5 K and H = 5 T. $ErAl_2$ (black line) has been also included for the sake of comparison.

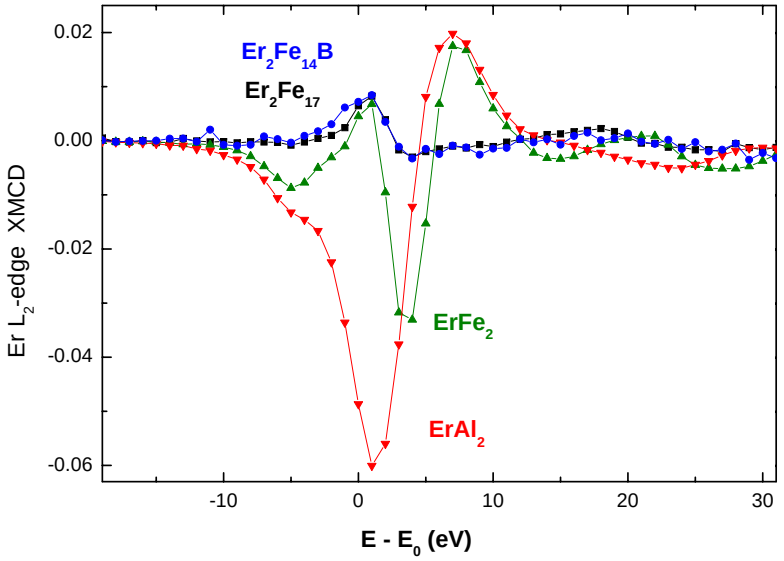

Figure 6.48: XMCD spectra at the Er $L_{2,3}$-edges in $ErAl_2$, $ErFe_2$, Er_2Fe_{17} and $Er_2Fe_{14}B$.

in $ErAl_2$, the spectrum has a main negative peak at E - $E_0 \sim 2$ eV whereas in Er_2Fe_{17} and $Er_2Fe_{14}B$ this peak at E - $E_0 \sim 2$ eV has almost disappeared. For these two compounds the main feature is a positive peak at E - $E_0 \sim 0$ eV. $ErFe_2$ presents an intermediate behaviour with both a positive peak at E - $E_0 \sim 0$ eV and a negative peak at E - $E_0 \sim 4$ eV. According to our hypothesis, the magnitude of the feature at ~ 0 eV is related to M_{Fe}. This explains why the spectra of Er_2Fe_{17} and $Er_2Fe_{14}B$ present a profile with a main peak at E - $E_0 \sim 0$ eV. Due to the large M_{Fe}, the Fe contribution at E - $E_0 \sim 0$ eV is the largest feature and almost hides the R contribution. In addition, Er_2Fe_{17} and $Er_2Fe_{14}B$ present a very similar profile, in agreement with a similar M_{Fe} : M_R ratio. On the other hand, $ErFe_2$ has a relatively smaller Fe contribution to the XMCD signal so that both the negative and the positive peaks are similarly noticeable. **Therefore, our results indicate that the existence of a magnetic T contribution to the R-L_2 XMCD spectrum is a general result for R-T alloys.**

6.9 XMCD at the R-L_3 edge

XMCD spectra have been also recorded at the R L_3-edge. For all the measured samples, the same profile has been obtained, consisting on a negative dip at E - $E_0 \sim$ -3 eV followed by a main positive peak at ~ 3 eV above the edge. The latter feature is of dipolar origin while the former spectral feature has been associated to a quadrupolar transition that should be present at the L_3 edge spectra of heavy rare earths.[62] To date, experimental evidences for the occurrence of these quadrupolar channels have been provided in the case of Dy and Er[48, 45] but it has never been clearly observed in the case of Gd. As shown in Fig. 6.49, this transition is also present in the case of Gd although its intensity is significantly reduced when compared to that of heavier rare-earths. Upon Al substitution by a 3d metal, the shape of the L_3 XMCD spectra is mostly retained through the whole $R(Al_{1-x}T_x)_2$ series. No uniform variation in the intensity of the positive dipolar feature as a function of the transition metal content has been observed. Indeed, the modification of the intensity of the main XMCD spectral feature (B) as a function of the Fe content strongly depends on the specific rare earth. On the contrary, in all the cases peak A is enhanced by increasing the Fe content (excluding RAl_2 spectra). This is a quite unexpected result as, in principle, the quadrupolar contribution should not be affected by the number of Al(Fe) atoms. This behaviour would indicate that the feature is not purely of quadrupolar origin as typically assumed.

Trying to confirm this hypothesis a two sublattice procedure has been applied at the R L_3 edge, in analogy with the analysis previously performed at the

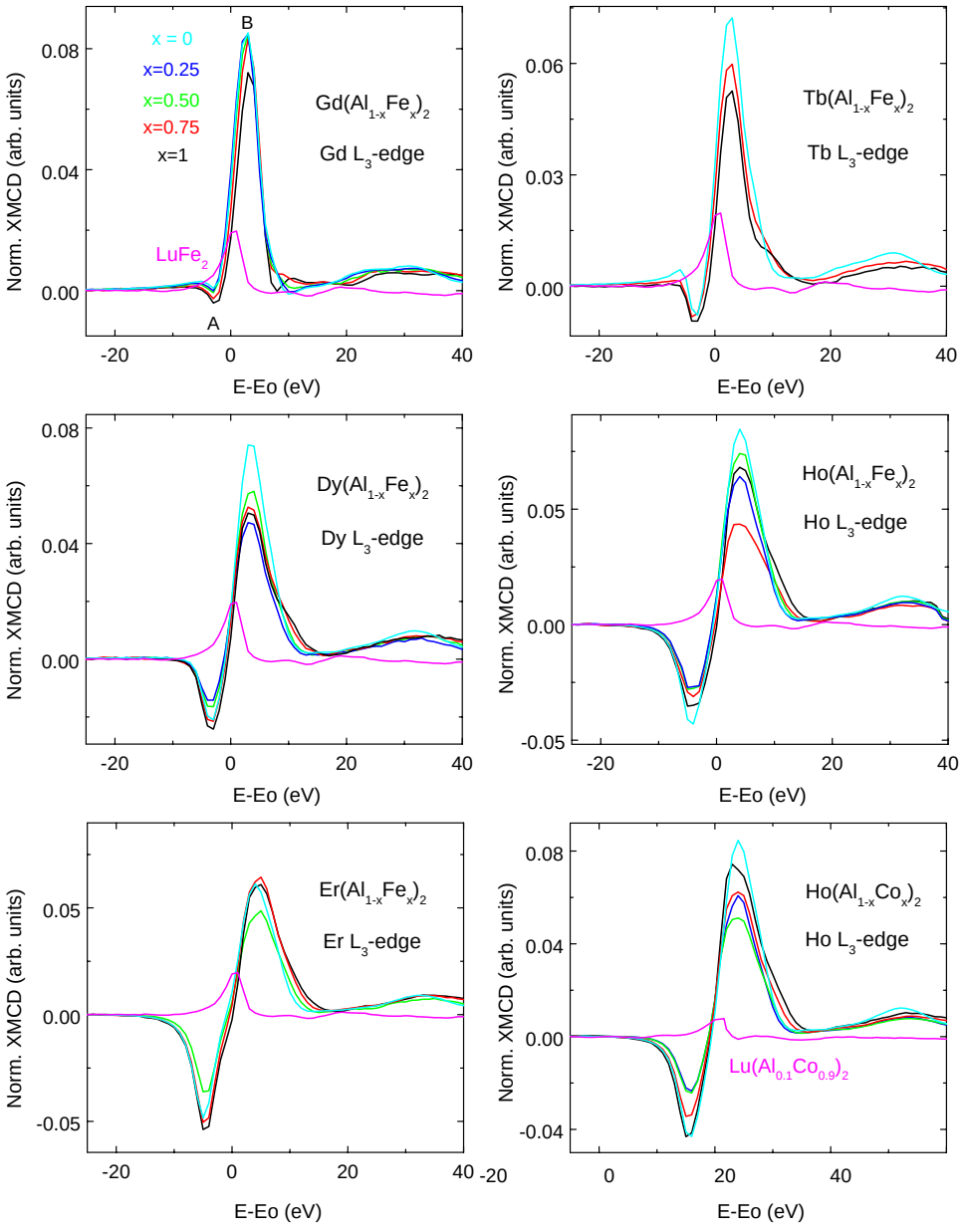

Figure 6.49: XMCD spectra at the R L_3-edge in $R(Al_{1-x}T_x)_2$ compounds recorded at T = 5 K and H = 50 kOe.

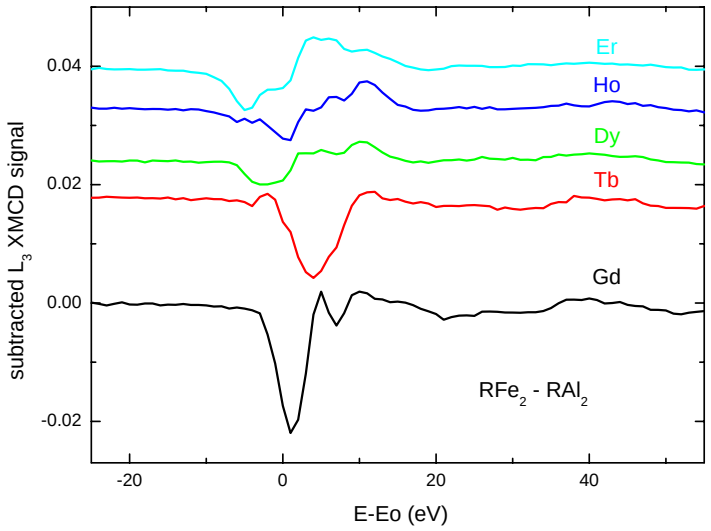

Figure 6.50: Comparison of the R L_3-edge XMCD spectra obtained after RFe_2 - RAl_2 subtraction

R L_2 edge. The subtracted signal has been compared to the Lu L_3 spectrum measured on $LuFe_2$ and $Lu(Al_{0.1}Co_{0.9})_2$.

As it can be seen in Figure 6.50 in some cases (Gd and Ho subtractions) a negative peak can be very roughly identified at 1 eV. This would indicate that a similar Fe contribution is also present at the L_3 edge. However, the details of the profile depend strongly on the specific RFe_2-RAl_2 substraction. Therefore, a similar conclusion to that found at the R-L_2 edge, i.e. the existence of a T contribution that resembles the profile obtained in Lu compounds, is not so straightforward for the L_3 edge. Nevertheless, this idea should not be completely discarded either. The peculiar position of the "possible" T contribution might prevent from an easy disentanglement of R and T contributions. Another possible explanation for the anomalous modification of peak-A intensity, can be found in the influence of the K-edge EXAFS affecting the signal at the R L_3 edge. Thus, for example, the energy difference between Fe K-edge and Gd L_3edge is just 131 eV. The influence of the Fe K-edge EXAFS makes more difficult a proper XAS and XMCD spectra normalization at this L_3 edge. In turn, this effect would also obstruct the isolation of the T contribution, if any, to the L_3 edge XMCD spectra.

6.10 Conclusions

1. Our results in the $R(Al_{1-x}Fe_x)_2$ series confirm that the Fe K-edge XMCD signal in R-Fe intermetallic compounds is due to the addition of magnetic contributions from both the iron and the rare-earth sublattices. In addition, the XMCD spectra recorded at the Co K-edge on RCo_2 show that this conclusion can be also applied to intermetallic compounds with a transition metal different from Fe.

2. We have also found that the R contribution to the T K-edge signal is not only proportional to the magnetic moment of R but also to the R:Fe ratio or more likely to the number of R neighbours. Indeed, in RFe_2 and RCo_2 Laves phases series the R contribution is so large that even affects the first peak (A), which in the studies performed in 2:14 and 1:11 series had been considered as purely of Fe origin. The huge influence of R in RFe_2 and RCo_2 is clearly made evident by the almost identical profile of both Co-K edge and Fe K-edge XMCD spectra.

3. The R contribution to the T K-edge XMCD does not significantly modify its shape when sweeping through the series from RFe_2 (or RCo_2) to RAl_2. Indeed, the effect of the Al atoms on the R contribution merely consists in an decrease of the magnitude of the signal.

4. Regarding the modification of the Fe contribution to the Fe K-edge XMCD, $XMCD_{Fe}$, our results cast doubts on previous assignments on the relationship between the Fe K-edge XMCD spectral features and the magnetic character of Fe. Indeed, while the XMCD peak at the edge has been typically considered as purely of Fe sublattice origin, the present results show that this picture does not hold for compounds with a high R:Fe ratio. In the case of Laves phases the R contribution is very large and affects to the whole energy range. As a consequence, monitoring the modification of the XMCD spectrum as Al substitutes Fe is not a valid tool to study the magnetic character of Fe in a straightforward way, mainly when an additional contribution is present on the XMCD spectrum.

5. In relation to the magnetic characterization of Fe through the $R(Al_{1-x}Fe_x)_2$ series, the combined analysis of the magnetization, Mössbauer spectra and Fe K-edge XMCD spectra indicates that the μ_{Fe} does not undergo and abrupt decrease but just an small reduction as the Al content increases. In the case of Lu compounds, the results are in agreement with a disordered magnetic structure giving rise to very small values of M_{Fe}, whereas Gd series are not affected by this effect. When R is a heavy rare

earth, other than Gd, none of the techniques used in this thesis is able to give us the required detailed information about the magnetism of the Fe sublattice in diluted compounds.

Concerning the R $L_{2,3}$-edges XMCD spectra:

1. We have found that in the case of the RAl_2 series, i.e. where R is the only magnetic atom, the intensity of the R L_2 XMCD signal clearly resembles the modification of n_{RR} with the atomic number. This provides a direct method to study the strength of the 4f-5d interaction.

2. The modifications observed in the R L_2-edge XMCD spectra when changing any of the parameters, namely specific T in the compound, T concentration, temperature or pressure, indicate the presence of an additional magnetic contribution of T origin.

3. Our results point out that this additional T contribution, a positive peak which appears always at $\sim$ 1 eV, is related to both the number of Fe (Co) neighbouring atoms around the absorbing R atom and the magnetic moment of the 3d metal.

4. The existence of a L_2-edge XMCD spectrum for Lu Laves phases indicates that the origin of this extra contribution has to be searched into the hybridization of the R(5d) states with the 3d states of the neighbouring transition metal atoms. This result can be considered as the counterpart of the R contribution found at the the K-Fe edge [84] in R-T systems.

5. The R dependence of the subtracted XMCD(RT_2) - XMCD(RAl_2) signal seems to show a relation with the n_{RT} molecular field coefficient. If we could corroborate (and quantify) a relation between the subtracted XMCD signal and the strength of the R(5d)-Fe(3d) hybridization, this result would give rise to a direct method to study the 4f-5d-3d interactions in R-T intermetallics.

6. Therefore, our results indicate the need of including a transition metal contribution prior to account for the XMCD at the rare-earth $L_{2,3}$-edges in R-T intermetallic materials.

7. Unfortunately, the same conclusion cannot be straightforwardly obtained in the case of the R L_3-edge XMCD signal since an analogue result could not be systematically obtained. In the case of this edge, further work is still needed to account for the evolution of the different features with Fe content.

It is important to notice that, in all the cases, namely studies as a function of specific R and T in the alloy, T concentration, temperature and pressure, the behaviour of the XMCD spectra can be consistently explained by assuming an extra contribution appearing always at the same energy.

Chapter 7

Application of the XMCD technique to specific problems

7.1 Introduction

As we have seen in the previous chapters, the interpretation of the XMCD signals at both T K-edge and R $L_{2,3}$-edges is a complex subject. However, despite the open questions regarding this interpretation, the XMCD technique can be a suited tool to study different problems in R-T intermetallic compounds. In this chapter we present two specific examples of the usefulness of XMCD to study specific questions in R-T intermetallic compounds: *"The study of the decoupling of the magnetic ordering of the Er and Co sublattices in* $Er_{1-x}Y_xCo_2$ *systems"* and *"The relationship between the Lu magnetic moment and the magnetic behavior of* $(Y_tLu_{1-t})(Co_{1-x}Al_x)_2$ *systems"*. Both subjects are at the present a matter of controversy. What we present in this chapter is the XMCD investigations we have carried out trying to get a deeper insight into each of them.

Thus, in the first part, we present an X-ray magnetic circular dichroism (XMCD) study performed at Co K-edge and at the Er $L_{2,3}$-edges in the $Er_{1-x}Y_xCo_2$ series. Our results indicate that both Er and the Co magnetic sublattices order at the same temperature for all the investigated compounds. In the case of the $Er_{0.6}Y_{0.4}Co_2$ compounds, the XMCD data do not show the decoupling of the magnetic ordering for both Er and Co sublattices. In addition, no experimental evidence of the occurrence of an inverse itinerant electron metamagnetic (IEM) transition has been found for applied magnetic fields of up to H = 100 kOe. Moreover, a non-zero magnetic moment is found at the Co sites in the case of the $Er_{0.5}Y_{0.5}Co_2$ compound.

Regarding the relationship between the Lu magnetic moment and the mag-

netic behavior of $(Y_tLu_{1-t})(Co_{1-x}Al_x)_2$ systems, we present an X-ray magnetic circular dichroism (XMCD) study performed at both the Co K-edge and the Lu $L_{2,3}$-edges on these compounds. The XMCD spectra reflect the different magnetic character of the systems allowing to monitor the transition from weak to strong ferromagnetism. The XMCD at the Lu $L_{2,3}$-edges indicates the existence of an ordered 5d moment at the lutetium sites that is coupled antiparallel to the Co moment. Estimates of the Lu magnetic moment have been obtained by applying the XMCD sum-rules. Our results show that in the $(Y_tLu_{1-t})(Co_{1-x}Al_x)_2$ compounds there is a correlation between the Lu 5d induced magnetic moment and the magnetic character of the system, suggesting that in these compounds the developing of a 5d magnetic moment at the Lu sites may play an important role into reinforcing the magnetic interactions and favoring the ferromagnetism character of the Lu rich compounds.

7.2 XMCD study of the decoupling of the magnetic ordering of the Er and Co sublattices in $Er_{1-x}Y_xCo_2$ systems.

7.2.1 Introduction

The intermetallic RCo_2 compounds are of particular interest among the intermetallic rare-earth compounds with 3d transition metals. In the case of the isostructural RNi_2 and RFe_2 compounds the 3d subsystem is, respectively, non magnetic or bearing a stable magnetic moment. By contrast, it shows an intermediate behavior in the RCo_2 case. The RCo_2 compounds are characterized by both the dependence of the Co magnetic moment upon the R alloying component and by the occurrence of a metamagnetic transition in the Co 3d itinerant subsystem. For compounds in which R is non magnetic (YCo_2, $LuCo_2$) the Co susceptibility is of the Pauli type, while a $\sim 1\ \mu_B$ Co moment is induced in the case of compounds with magnetic R metals. In the latter case, the magnetic order of the d subsystem is due to the effect of the molecular field created by the R moments acting on the Co sites.

The RCo_2 compounds have been widely studied as they can be regarded as model materials for a large variety of magnetic phenomena related with the itinerant electron metamagnetism (IEM) [4, 184, 185, 133]. This long-standing interest is still open as new magnetic properties have been discovered during this research. This is the case of the magnetic characterization of the $Er_{1-x}Y_xCo_2$ systems. These systems were tailored to study the modification of the IEM behavior associated to the reduction of the molecular field acting on the Co atoms by substituting Er by a non-magnetic rare-earth as Y. The electronic and magnetic properties of the $Er_{1-x}Y_xCo_2$ systems were early studied by Duc *et al.* [186], who found that the magnetic moment of Co atoms decreases with decreasing the Er content, as it does the Curie temperature. These authors concluded the induced character of the Co magnetic moment and, in addition, that the character of the magnetic transition changes from first to second order around x = 0.3 [186]. Later, neutron diffraction experiments performed by Baranov *et al.* [187] shown that an increase of the yttrium concentration will cause a sharp drop in μ_{Co} and μ_{Er}. These studies also emphasize the coexistence of both long-range and short-range order for yttrium concentrations close to the critical one where the long-range magnetic order disappears. According to the results by Baranov *et al.* the sharp drop in μ_{Co} starts for $x > 0.4$ and there is no short range ordering for $x > 0.6$ down to T = 4.2 K [187].

More recently, Hauser *et al.* have proposed that for a certain yttrium con-

centration, x = 0.4, the magnetic ordering of the Er and Co sublattices takes place at different temperatures [188, 189, 190, 191]. This result is mainly based on specific heat capacity measurements of $Er_{0.6}Y_{0.4}Co_2$ showing two anomalies with maxima at T 11 K and 14.5 K [188, 190]. According to these authors the Er sublattice magnetically orders at T = 14.5 K but, as the molecular field acting on the Co atoms is smaller than the critical one, the Co sublattice remains magnetically disordered. The critical condition for the onset of magnetic order in the Co subsystem is fulfilled on cooling, thus resulting in a second transition when a magnetic moment is induced at the Co sites at T = 11 K. However, the showy result that the itinerant Co sublattice orders at a lower temperature than the Er sublattice has not been confirmed by recent neutron studies. In particular, single crystal neutron diffraction experiments on $ErCo_2$ and $Er_{0.6}Y_{0.4}Co_2$ showed that both Er and the Co magnetic sublattices order at the same temperature (35.9 and 17.0 K, respectively) [192, 193]. Moreover, macroscopic data on single crystal specimens do not show two separate peaks neither for the specific heat nor for the magnetic susceptibility, in disagreement with the experiments on polycrystalline materials reported by Hauser *et al.* [188, 190]. This controversy extends also to other results as the so called inverse IEM transition. This transition is induced by increasing the external field, as the effective field acting upon the Co subsystem decreases and the Co moment abruptly collapses. In the case of $Er_{0.6}Y_{0.4}Co_2$ the inverse IEM transition occurs at 85 kOe [133, 191]. However, Markosyan *et al.* have reported this value to be 70 kOe, being reduced with pressure so as to vanish above a critical value of 2 kbar [194]. By contrast, results by Podlesnyak *et al.* indicate that no inverse IEM is observed under pressures of up to 6 kbar [192]. Finally, contradictory results are also reported for the magnetic behavior of the $Er_{1-x}Y_xCo_2$ compounds near the critical yttrium concentration for the occurrence of long-range magnetic order. While several authors suggest the coexistence of both long-range and short-range order[187, 195, 192], other works indicate that for $Er_{0.5}Y_{0.5}Co_2$ only the Er sublattice is magnetically ordered although the Co subsystem is still affected by the molecular field and a 0.22 μ_B moment at the Co sites is reported [190].

Aimed to clarify this debate we have performed an X-ray magnetic circular dichroism (XMCD) study at the Co K-edge and at the Er $L_{2,3}$-edges in the $Er_{1-x}Y_xCo_2$ series. This XMCD approach is expected to furnish a disentangled magnetic characterization of both Er and Co sublattices by studying the variation of the XMCD as a function of the yttrium concentration, the applied magnetic field and the temperature.

7.2.2 Synthesis and structural characterization.

$Er_{1-x}Y_xCo_2$ (x = 0, 0.2, 0.3, 0.4, 0.5 and 0.6) samples were prepared by arc-melting the pure elements under Ar protective atmosphere. In order to have single-phase samples, a 3 % wt. excess was added to the stoichiometric amounts of Er and Y. The ingots were annealed in quartz tubes with Ar atmosphere at 850 ^{o}C for one week.

Structural characterization was performed at room temperature by means of powder x-ray diffraction. The diffraction patterns, Rietveld-refined using the FULLPROF code [89], showed that all the samples present a single C15 Laves phase, being the presence of secondary phases (R_2O_3) less than $< 2\%$ overall. The cell parameters, determined from the XRD patterns are summarized in Table 7.1.

Table 7.1: Structural (lattice constant, a) parameters of the $Er_{1-x}Y_xCo_2$ compounds:

Compound	a(Å)	Compound	a(Å)
x = 0	7.157	x = 0.4	7.177
x = 0.2	7.166	x = 0.5	7.190
x = 0.3	7.173	x = 0.6	7.192

7.2.3 Macroscopic Magnetic Measurements

The temperature dependence of the magnetization of the $Er_{1-x}Y_xCo_2$ series is shown in Fig. 7.1. For both $ErCo_2$ and $Er_{0.8}Y_{0.2}Co_2$ compounds, the variation

Table 7.2: Magnetic parameters of the $Er_{1-x}Y_xCo_2$ compounds: Curie temperature (T_C); magnetization measured at 50 kOe (M_{50kOe}) and the Co moment derived from the magnetization data at H = 50 kOe.

Compound	T_C (K)	M_{50kOe} (μ_B/f.u.)	μ_{Co} (μ_B/f.u.)
x= 0	32	7.2	0.9
x= 0.2	23.5	5.8	0.7
x= 0.3	18.5	4.9	0.7
x= 0.4	15	4.3	0.55
x= 0.5	12	3.7	0.4
x= 0.6	8.5	3.0	0.3

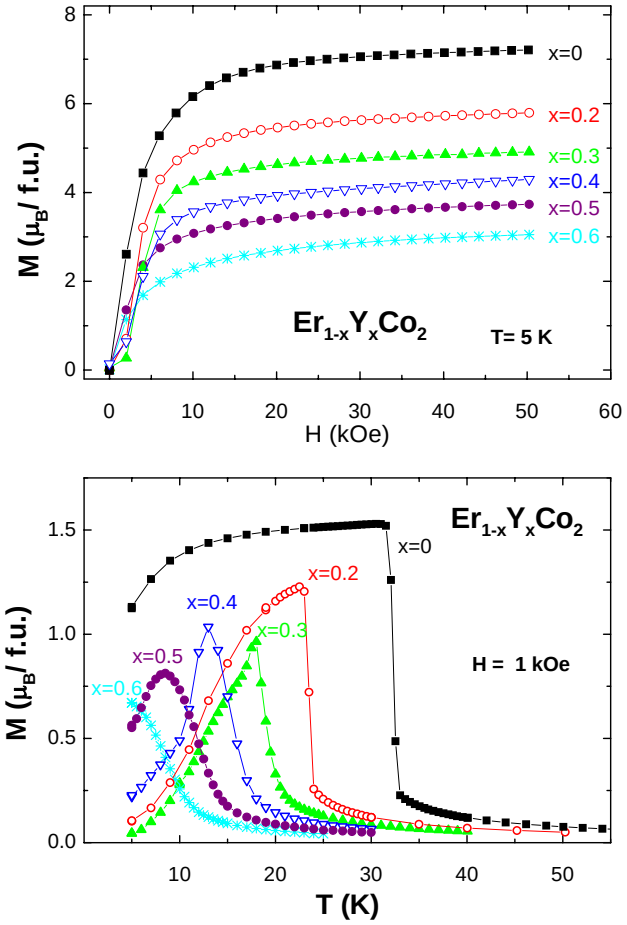

Figure 7.1: In the top panel, magnetization *vs.* applied magnetic field curves recorded at T = 5 K are shown. Bottom panel: thermal dependence of the magnetization (zero field cooled) of the $Er_{1-x}Y_xCo_2$ compounds: x = 0 (■), 0.2 (○, red), 0.3 (▲, green), 0.4 (▽, blue), 0.5 (●, purple) and 0.6 (⋆, cyan).

of the magnetization at the onset of the magnetic ordering temperature, T_C, proceeds step-like, as corresponding to the first-order character of the transition. However, for higher yttrium contents the change of the magnetization proceeds smoothly, indicating that the transition becomes second order [186]. Magnetization *vs.* applied magnetic field curves recorded at T = 5 K (see Fig. 7.1) show the progressive reduction of the magnetization as the Y content increases, although ferrimagnetic behavior is retained. Assuming the free-ion value (9 μ_B) to the erbium moment and that μ_{Er} is not affected by the yttrium substitution [186, 196], μ_{Co} in the $Er_{1-x}Y_xCo_2$ series is determined to decrease from $\sim$ 0.9 μ_B in $ErCo_2$ to 0.3 in $Er_{0.4}Y_{0.6}Co_2$.

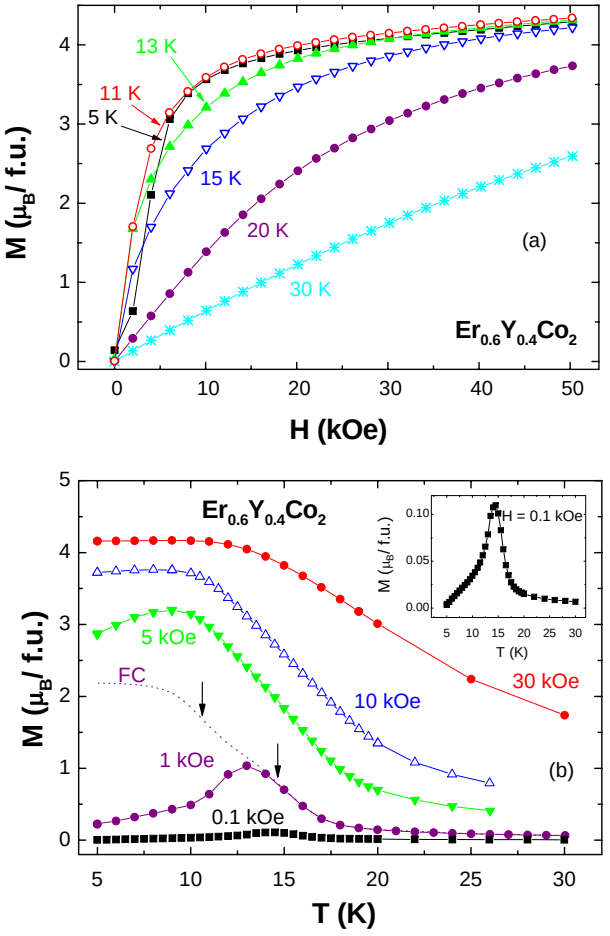

Figure 7.2: a) Magnetization *vs.* applied magnetic field curves of $Er_{0.6}Y_{0.4}Co_2$ recorded at different temperatures: T = 5 K (■), 11 K (○, red), 13 K (▲, green), 15 K (▽, blue), 20 K (●, purple) and 30 K (⋆, cyan). b) Zero-field cooled magnetization *vs.* temperature curves of $Er_{0.6}Y_{0.4}Co_2$ recorded at different applied magnetic fields: H = 30 kOe (●, red), 10 kOe (△, blue), 5 kOe (▼), 1 kOe (●, purple) and 0.1 kOe (■). In the case of H = 1 kOe the field-cooled curve is also reported (dotted line) and the arrows mark the step-like features discussed in the text. The inset reports a detailed view of M(T) at H = 0.1 kOe.

The magnetic behavior of the $Er_{0.6}Y_{0.4}Co_2$ compound deserves a special discussion. Hauser *et al.* have proposed that the magnetic ordering of both the Er and Co magnetic sublattices take place at different temperatures [188, 190]. This result is mainly based in the appearance of two anomalies in C_p measurements of polycrystalline samples. The thermal dependence of C_p is similar to that early reported by Duc at al. *et al.*, although the above referred anoma-

lies were not detected [186]. Indeed, recent measurements on a $Er_{0.6}Y_{0.4}Co_2$ single crystal do not show separate peaks neither for the specific heat nor for the magnetic susceptibility [193]. In addition to the C_p anomalies, Hauser *et al.* argue that evidence of different ordering temperatures for the Er and Co subsystems in $Er_{0.6}Y_{0.4}Co_2$ can be found in the behavior of the magnetization [190]. In this way, M *vs.* T curves of $Er_{0.6}Y_{0.4}Co_2$ cooled under an applied 10 Oe field shows two smooth steps that are interpreted as due to two separate magnetic transitions. However, this interpretation of the magnetization data for such a small external field (10 Oe) is not free of controversy as the effect of the microstructure, coercivity and the domain structure of the polycrystalline samples is not considered. Indeed, the double-step feature of the FC magnetization can be observed for higher applied fields of up to 0 kOe (see Fig. 7.2). However, as the external magnetic field is increased the anomalies disappear, which is difficult to reconcile with the expected behavior of the IEM transitions with the external field. According to the mean-field approach, the cobalt moment in RCo_2 systems is induced by the molecular field on the Co atoms, B_{mol}^{Co}, exerted by the localized 4f moments. The direction of B_{mol}^{Co} is antiparallel to that of the Er moment and, hence, to that of the applied magnetic field. Consequently, the effective field acting upon the Co subsystem decreases with increasing the external field: $B_{eff}^{Co} = B_{mol}^{Co} - B_{ext}$. Moreover, if B_{ext} exceeds a critical field B_{cr}, the Co sublattice magnetization is destabilized and the Co moment abruptly collapses in the so called inverse IEM transition. Consequently, contrary to the observed results, the effect of increasing the magnetic field in the presence of two separate transitions would enhance the different temperature ordering of both the Er and Co sublattices. It can be argued to account for such a disagreement that upon increasing the field the Er magnetization increases in such a way that the second transition is favored and coupled to that of the Er sublattice. However, it is difficult to reconcile this picture with the M *vs.* H behavior. As shown in Fig. 7.2, the magnetization at low and moderate applied fields ($H \leq 20$ kOe) is always smaller at 13 K than at T= 11 K. By contrast, if the Co sublattice orders ferrimagnetically coupled to that of Er at T = 11 K, one expects a decrease of the magnetization that is not observed.

Consequently, the magnetic characterization of $Er_xY_{1-x}Co_2$ compounds shows contradictory results even when the same experimental techniques are used. This controversy specially regards the decoupling of the magnetic ordering of the Er and Co sublattices near the critical yttrium concentration for the onset of long-range magnetic ordering [188, 189, 190, 191, 192, 193, 187, 195]. Trying to get a deeper insight on this debate we have extended our study by using X-ray magnetic circular dichroism (XMCD) at the Co K-edge and at the Er $L_{2,3}$-edges. In this way, the element-selectivity properties of XMCD

can provide a magnetic characterization of the systems in which the magnetic behavior of both the Co and Er sublattices are disentangled.

7.2.4 XMCD results and discussion

Er L_3-edge XMCD

The Er L_3-edge XMCD spectra of several $Er_{1-x}Y_xCo_2$ compounds are shown in Fig. 7.3. These spectra are characterized by a negative peak (A) below the edge ($\sim$ -5 eV) and a main positive peak (B) at $\sim$ 3 eV above the edge. These structures have been interpreted as due to both a quadrupolar and dipolar transition, respectively [48]. Consequently, the low-energy feature is influenced by the localized Er 4f states while the high energy feature is linked to the magnetic behavior of the conduction 5d states. For all the investigated $Er_{1-x}Y_xCo_2$ compounds the amplitude of the Er L_3 XMCD signal is smaller than that obtained for $ErAl_2$. This result can be interpreted in terms of a reduction of the Er magnetic moment in the case of the Co-containing samples with respect the Er free-ion value that is assigned to the $ErAl_2$ compound [197]. However, the intensity of the main XMCD features (A and B) presents a different dependence on the Y content through the $Er_{1-x}Y_xCo_2$ series. In particular, the intensity of feature B is similar for both $Er_{0.6}Y_{0.4}Co_2$ and $Er_{0.5}Y_{0.5}Co_2$ compounds, being significantly smaller ($\sim$ 20 %) for $ErCo_2$. By contrast, peak A intensity is near the same for the three cobalt compounds.

In a first approach, one can consider that the intensity of the quadrupolar peak is, to some extent, reflecting the Er(4f) magnetic moment being the same for three investigated compounds. The modification of the dipolar contribution, peak B, can be addressed to two different effects. On the one hand, it can be simply interpreted in terms of the reduction of the Er(5d) moment in $ErCo_2$ with respect to that in the Y-doped compounds. However, this interpretation is in conflict with the expected behavior for the $Er_{1-x}Y_xCo_2$ compounds, as the Er-Y substitution leads to the relaxation of the magnetic ordering within the rare-earth magnetic sublattice. On the other hand, recent results obtained in Al-doped RFe_2 series indicates that the transition metal contributes, with contrary sign, to the XMCD signals recorded at the rare-earth $L_{2,3}$-edges [198]. Accordingly, if the dipolar contribution of the Er L_3 XMCD signal is considered as made up by the addition of both the Er and Co contributions (with contrary sign), the reduction of the intensity of peak B in $ErCo_2$ as compared to both $Er_{0.6}Y_{0.4}Co_2$ and $Er_{0.5}Y_{0.5}Co_2$ indicate that the Co contribution is more important in the pure compound than in the Y-doped ones. This contribution being related to the Co magnetic moment, this result indicates that μ_{Co} decreases in the Y substituted samples, in agreement with the behavior derived

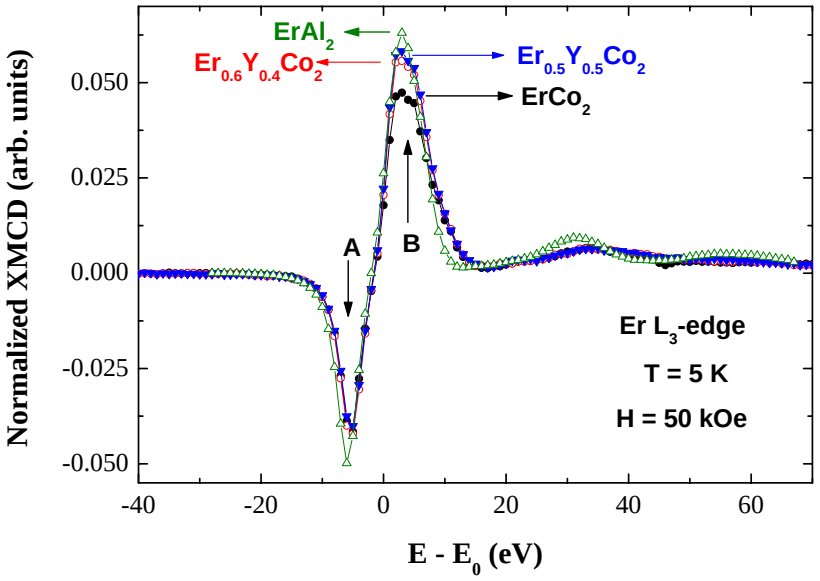

Figure 7.3: Comparison of the Er L_3-edge XMCD spectra recorded at T = 5 K and H = 50 kOe in the case of: $ErAl_2$ (green, △), $ErCo_2$ (black, •), $Er_{0.6}Y_{0.4}Co_2$ (red, ○) and $Er_{0.5}Y_{0.5}Co_2$ (blue, ▼).

from the magnetization data. Within the experimental resolution, the XMCD signal of $Er_{0.5}Y_{0.5}Co_2$ is slightly larger than the $Er_{0.6}Y_{0.4}Co_2$ one, in agreement also with the observed variation of μ_{Co} as a function of the Y content.

Fig. 7.4a reports the comparison of the Er L_3-edge XMCD spectra of $Er_{0.6}Y_{0.4}Co_2$ recorded at different applied magnetic fields and at two different temperatures: T = 13 K and T = 5 K. According to Hauser *et al.*, the Er sublattice magnetically orders at T_{Er}= 14.5 K, while the onset of magnetic order in the d subsystem takes place for a lower T_{Co} = 11 K temperature [188, 189, 190]. Based on the above results, one expects that Er L_3-edge XMCD recorded at temperatures $T_{Co} < T < T_{Er}$ and $T < T_{Co}$ reflects the different magnetic ordering of the Co sublattice. However, the shape of the XMCD is similar for both temperatures. Indeed, as shown in Fig. 7.4 b, the signals obtained at T = 5 K can be reconstructed by using a scaling factor from those recorded at T = 13 K by applying the same magnetic field. The scaling factor needed to match both signals is ∼ 1.4 for low applied fields, while it is ∼ 1.1 for H = 50 kOe. This behavior is similar to that exhibited by the M(H) curves at the same temperatures. At the maximum applied field, H = 50 kOe, the magnetization of $Er_{0.6}Y_{0.4}Co_2$ is near the same for both temperatures. By contrast, for applied fields of H = 5 kOe and 10 kOe it is necessary to apply a constant enhancing factor (∼ 1.1) to the M(H) values recorded at T = 13 K

to match those found at T = 5 K.

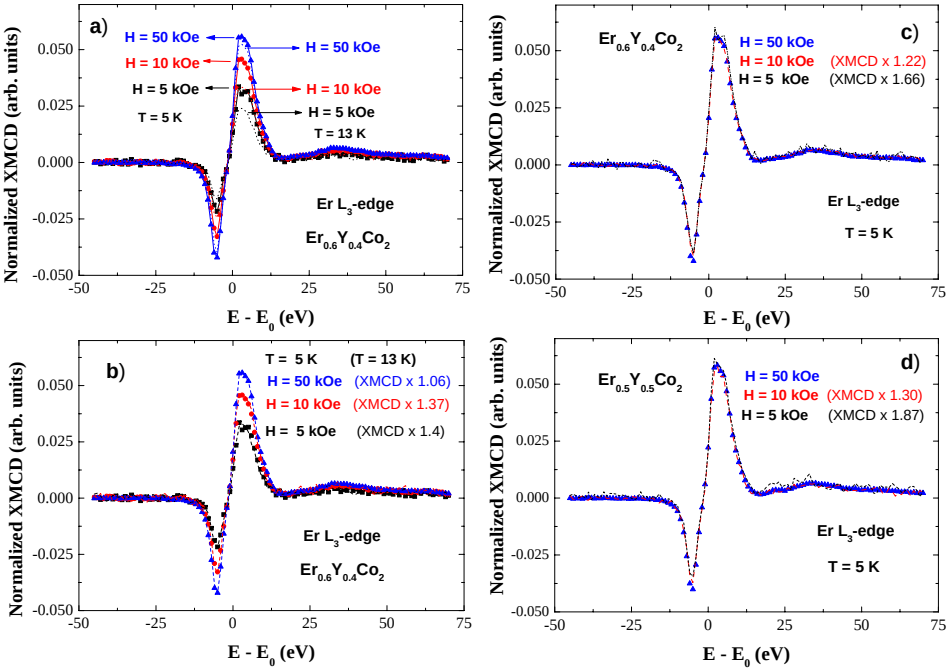

Figure 7.4: a) Comparison of the Er L_3-edge XMCD spectra of $Er_{0.6}Y_{0.4}Co_2$ recorded at T = 5 K at different applied magnetic fields: H = 5 kOe (■), 10 kOe (red, •) and 50 kOe (blue, △). The dotted lines show the same comparison for the spectra recorded at T = 13 K. b) Comparison of the Er L_3-edge XMCD spectra of $Er_{0.6}Y_{0.4}Co_2$ recorded at T = 5 K and different H (symbols) and those obtained (see text for details) scaling the XMCD recorded at the same fields at T = 13 K (dotted lines). c) and d) panels show the comparison of the Er L_3-edge XMCD spectrum recorded at T = 5 K and H = 50 kOe (blue, △) and those obtained by scaling the spectra recorded at H = 10 kOe (red, dashed) and 5 kOe (black, dotted) in the case of $Er_{0.6}Y_{0.4}Co_2$ (c panel) and $Er_{0.5}Y_{0.5}Co_2$ (d panel)

As shown in Fig. 7.4 b the agreement between the XMCD spectra recorded at T = 5 K and those scaled from the T = 13 K ones concerns both the low-energy (A) and the edge (B) main spectral features. Being peak A addressed to Er and peak B reflecting the contribution of both Er and Co sublattices, these results seem to indicate that the magnetic state of the cobalt sublattice in $Er_{0.6}Y_{0.4}Co_2$ is the same at both temperatures, i.e., the Co sublattice orders at the same temperature as the Er one does. This behavior does not depend on the applied magnetic field. Indeed, the effect of the field only affects the amplitude of the spectra being the shape unaltered by varying the applied field. As shown in Fig. 7.4 c the XMCD spectrum recorded at H = 50 kOe is reproduced by those recorded at H = 5 kOe and 10 kOe by using a scaling factor

of 1.7 and 1.2, respectively. These scaling factors coincide with those needed to match the macroscopic M(H) values at the same applied fields. Interestingly, the same behavior is observed for the $Er_{0.5}Y_{0.5}Co_2$ compound (Fig. 7.4 d). According to Hauser *et al.* only the Er sublattice is magnetically ordered in this compound. However, the XMCD results indicate that the behavior of both $Er_{0.5}Y_{0.5}Co_2$ and $Er_{0.6}Y_{0.4}Co_2$ is similar, thus supporting than in the x = 0.5 compound Co atoms also carry a magnetic moment and that both Er and Co sublattices are magnetically ordered.

Er L_2-edge XMCD

The results obtained from the Er L_3-XMCD can be corroborated by studying the evolution of the Er L_2-edge XMCD spectra throughout the $Er_{1-x}Y_xCo_2$ series. In this way, we present in Fig. 7.5 the comparison of the XMCD spectra recorded for the Co-containing samples and for the reference $ErAl_2$. As shown in the figure, the spectral profile of the Er L_2-edge spectrum of $ErAl_2$ consists of a main negative peak centered at $\sim$ 2 eV above the edge and a positive peak of lower intensity at E = 7 eV. In the case of the Co containing samples, the shape of the positive structure remains unaltered and all the samples show a similar intensity. However, the main negative feature is strongly modified, both in shape and intensity, with respect to that of $ErAl_2$. For the $ErCo_2$ XMCD spectrum the negative peak splits, the position of the minimum is shifted towards higher energy and its intensity decreases. As a result one finds that the amplitude of the Er L_2-edge XMCD signal of $ErCo_2$ is about half of that of $ErAl_2$. According to macroscopic data, such a strong difference cannot be accounted in terms of the reduction of the Er magnetic moment. It is therefore necessary to appeal to the existence of additional contributions, other than the Er magnetization itself, to account for the observed behavior of the XMCD signals. To this respect, recent results obtained on R-Fe intermetallic compounds have demonstrated the existence of an extra contribution at the rare-earth L_2-edge XMCD spectra that is connected to the presence of the transition metal [198, 199]. Consequently, the XMCD results reported in Fig. 7.5 indicate that Co is contributing to the Er L_2 dichroism even when Er is probed. This cobalt contribution can be extracted by subtracting both $ErAl_2$ and $ErCo_2$ spectra yielding, as in the case of R-Fe systems [198, 199], a positive contribution.

This finding allow us to understand the evolution of the Er L_2-edge XMCD spectra as Y content increases through the $Er_{1-x}Y_xCo_2$ series. As shown in Fig. 7.5, the intensity of the negative peak of the XMCD spectra increases as Y does. In this way, the shape of the signal for $Er_{0.5}Y_{0.5}Co_2$ looks closer to that of $ErAl_2$, while that of $Er_{0.6}Y_{0.4}Co_2$ lies in between the $ErCo_2$ and $ErAl_2$ ones.

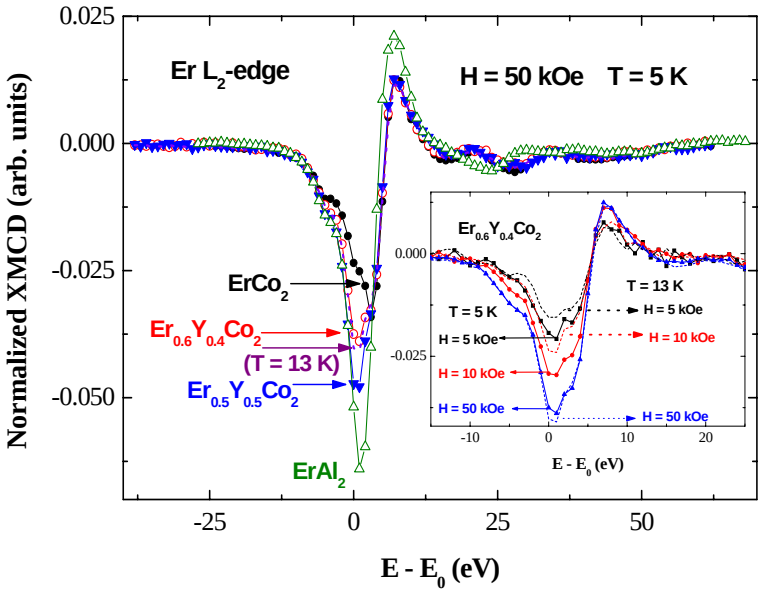

Figure 7.5: Comparison of the Er L_2-edge XMCD spectra in the case of $ErAl_2$ (green, △), $ErCo_2$ (black, •), $Er_{0.6}Y_{0.4}Co_2$ (red, ○) and $Er_{0.5}Y_{0.5}Co_2$ (blue, ▽) recorded at T= 5 K and H = 50 kOe. The XMCD spectrum of $Er_{0.6}Y_{0.4}Co_2$ recorded at T = 13 K is also shown (purple, dotted line). The inset shows the comparison of the Er L_2-edge XMCD spectra of $Er_{0.6}Y_{0.4}Co_2$ recorded at T = 5 K at different applied magnetic fields: H = 5 kOe (■), 10 kOe (red, •) and 50 kOe (blue, △). The dotted lines show the same comparison for the spectra recorded at T = 13 K.

According to the hypothesis above, Co is contributing with positive sign to the region of the spectrum where the main negative peak lies. As a result, the peak is strongly depressed for $ErCo_2$. As Co magnetic moment decreases, its contribution to the spectrum does too and consequently the negative intensity of this spectral feature is enhanced. Then, this behavior indicates that i) as Y content increases the Co moment decreases, and ii) a Co moment is present in the case of both $Er_{0.6}Y_{0.4}Co_2$ and $Er_{0.5}Y_{0.5}Co_2$ compounds. The reduction of μ_{Co} has been estimated in the following way: we have assigned that the difference of the XMCD at E = 1 eV between $ErCo_2$ and $ErAl_2$ is proportional to μ_{Co}, that according to magnetization data is $\sim 0.9\ \mu_B$ at T = 5 K and H = 50 kOe. In the case of $Er_{0.6}Y_{0.4}Co_2$ and $Er_{0.5}Y_{0.5}Co_2$ the difference is only the 64% and 41%, respectively, of that of $ErCo_2$. Accordingly, the Co magnetic moment derived from the Er L_2 XMCD are 0.58 μ_B and 0.37 μ_B for $Er_{0.6}Y_{0.4}Co_2$ and $Er_{0.5}Y_{0.5}Co_2$, respectively, being in good agreement with the values, 0.55 and 0.4 μ_B, derived from the magnetization data reported in Table. 7.2.

A final study is deserved to the thermal dependence of μ_{Co} in $Er_{0.6}Y_{0.4}Co_2$. Accordingly to the analysis above, the comparison between the XMCD signals recorded at T = 13 K and T = 5 K, shown in Fig. 7.5, indicates that an ordered magnetic moment on Co sites exists at both temperatures. This result is in agreement with that obtained at the Er L_3-edge. However, because several works suggest that the onset of magnetic order in the Co sublattice is decoupled from the Er one and it takes place at T_{Co} = 11 K [188, 189, 190], we have further verified this finding by recording the XMCD at different magnetic applied fields. As shown in Fig. 7.5 (inset), the XMCD spectra recorded at T = 13 K, i.e., at temperatures above the proposed one for the onset of Co magnetic ordering, are similar to those obtained at T = 5 K, i.e., when both sublattices are ordered. The dependence of the XMCD intensity on the applied magnetic field resembles, for both temperatures, the behavior of the M(H) curves. Consequently, these results indicate that the Co sublattice orders at the same temperature as the Er one does.

Co K-edge XMCD

Being our main aim to determine if the magnetic ordering or the Er and Co sublattices of $Er_{0.6}Y_{0.4}Co_2$ are decoupled [188, 189, 190, 191] or not [192, 193] one may think that the study of Co K-edge XMCD can offer a direct answer to this debate. In this way, the analysis of the temperature dependence of the Co K-edge XMCD would be preferable than using an indirect way, i.e. studying the Co contribution to the Er $L_{2,3}$-edges XMCD spectra, to solve the problem. However, the analysis of the Co K-edge in R-Co intermetallic compounds is nowadays an open task.

Previous works performed on R-Fe intermetallic compounds have unambiguously determined that there is a rare-earth contribution to the Fe K-edge XMCD reflecting the magnetic state of the R atoms [84, 85, 86, 128, 199]. Similar result has been obtained at the Co K-edge XMCD spectra of $TbCo_5$, $Dy(Ni_{0.2}Co_{0.8})_5$ and $TbCo_2$ compounds [200]. The systematic research performed on the R-Fe compounds has determined that this rare-earth contribution depends on the R:Fe ratio in such a way that by increasing the number of rare-earth neighbors around the absorbing Fe atom its influence on the Fe K-edge XMCD spectrum is enhanced. Throughout all the studied series ($RFe_{11}Ti$ [128], $R_2Fe_{14}B$ [84, 85, 86], R_6Fe_{23} [199] and RFe_2 [201]) the maximum contribution is found for the RFe_2 Laves compounds.

The presence of such additional R-contribution makes difficult the analysis of the Fe K-edge XMCD spectra in the R-Fe intermetallics. However, it is possible to disentangle both the Fe and R components to the spectrum by

performing a two-sublattices analysis assuming the additivity of the Fe and R magnetic contributions to the XMCD. In the case of R-Fe intermetallics, this disentangling is favored because the iron contribution to the Fe K-edge XMCD spectrum closely resembles that of Fe metal. It shows a narrow positive peak at the absorption threshold and a broad negative dip (∼12 eV wide) at high energies, where the rare-contribution is mainly located. This peak at ∼ 0 eV can be used in most cases as a fingerprint to determine the Fe contribution [?]. By contrast, such a feature is absent in the Co K-edge XMCD of R-Co compounds and both Co and R contributions are mixed throughout the whole energy range. Moreover, in the case of the RCo_2 Laves compounds the rare-earth contribution is so intense as to completely hide the Co one.

This is illustrated in Fig. 7.6, where the Co K-edge dichroism of $ErCo_2$ is compared to that of $Y(Co_{0.85}Al_{0.15})_2$ and $Lu(Co_{0.9}Al_{0.1})_2$. In the latter case the rare-earth contribution to the XMCD is absent as the rare-earth is non magnetic. In a first approach, one can consider that the Co K-edge XMCD of these compounds reveals the contribution of the cobalt sublattice to the Co K-edge spectrum XMCD of the RCo_2 compounds in which R is magnetic. As shown in the figure, the amplitude of the XMCD is one order of magnitude larger in $ErCo_2$ than in $Lu(Co_{0.9}Al_{0.1})_2$ for an applied field of H = 100 kOe. Moreover, even for a low 5 kOe applied field, the amplitude of the $ErCo_2$ signal is twice of that of the Lu compound recorded at 100 kOe. These differences cannot be ascribed to the magnitude of μ_{Co}, being of the same order (∼ 0.7 - 0.9 μ_B) in both compounds. As discussed previously, the XMCD signal is mainly due to the Er magnetic contribution even when Co is probed by tuning its K-edge absorption edge.

A similar behavior is observed for the Y-doped $ErCo_2$ samples. Fig. 7.7 shows the magnetic field dependence of the Co K-edge XMCD in the case of $Er_{0.6}Y_{0.4}Co_2$ recorded at low temperature. The spectral shape is the same as for $ErCo_2$ and only its amplitude is concerned, being the observed modification of the intensity in agreement with the magnetization data. In addition, the XMCD amplitude of $Er_{0.6}Y_{0.4}Co_2$ is similar for applied magnetic fields of H = 50 kOe and 100 kOe. This result indicates that, contrary to previous claims [133, 191, 194], no inverse IEM transition occurs up to applied magnetic fields of H = 100 kOe. Indeed, if the Co moment collapsed by increasing the external field no Co contribution would be present in the XMCD spectrum recorded at 100 kOe. Consequently, the substraction of the XMCD signals recorded at H = 50 kOe and 100 kOe, shown in Fig. 7.7, would be not zero but corresponding to the Co contribution at H = 50 kOe. This signal would be similar to that of the $Y(Co_{0.85}Al_{0.15})_2$ and $Lu(Co_{0.9}Al_{0.1})_2$ compounds shown in Fig. 7.6. By contrast, the Co K-edge XMCD data indicate that the Co magnetic state is similar at both applied fields without an inverse IEM being detected.

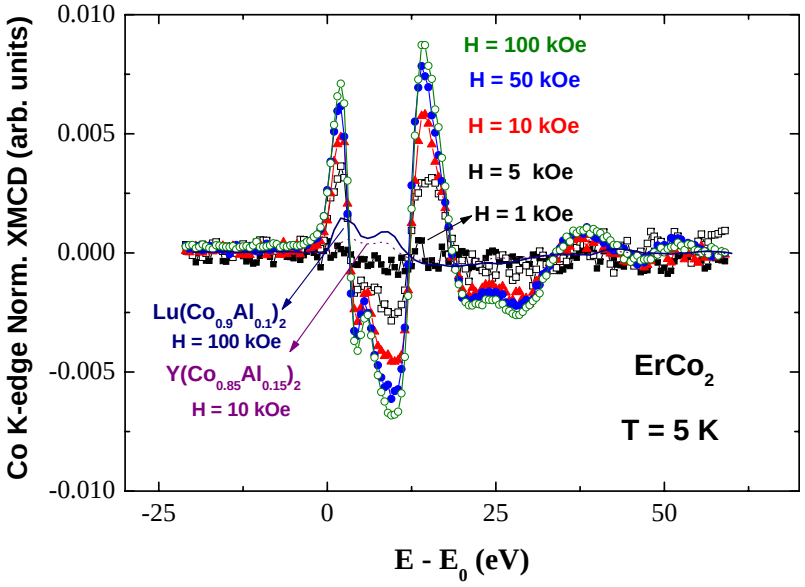

Figure 7.6: Comparison of the Co K-edge XMCD spectra of $ErCo_2$ recorded at T = 5 K and different applied magnetic fields: H = 1 kOe (■), 5 kOe (black, □), 10 kOe (red, △), 50 kOe (blue, •) and 100 kOe (green, ○). For the sake of comparison the XMCD spectra of $Y(Co_{0.85}Al_{0.15})_2$ (purple, dotted line) and $Lu(Co_{0.9}Al_{0.1})_2$ (navy, solid line) recorded at H = 10 kOe and T = 5 K are also shown.

More important to our aim is the comparison of the XMCD signals of $Er_{0.6}Y_{0.4}Co_2$ recorded at different temperatures shown in the bottom panel of Fig. 7.7. According to magnetization data (Fig. 7.2), the amplitude of the spectrum recorded at T = 13 K has been factorized by 1.06 to account for the different magnetization of the Er sublattice at both temperatures. No appreciable difference between both signals is found, which points out that the Co sublattice orders at the same temperature as the Er one does in this compound. Indeed, magnetization data indicate that $\mu_{Co} \sim 0.55\ \mu_B$ in $Er_{0.6}Y_{0.4}Co_2$ at T = 5 K. If the Co sublattice is not magnetically ordered at T = 13 K, the difference reported in Fig. 7.7 would correspond to the XMCD signal of a RCo_2 compound without magnetic rare-earth, as the Er contribution is canceled by the substraction, and showing a $\mu_{Co} \sim 0.5\ \mu_B$. Consequently, the difference would exhibit a similar shape and an intermediate amplitude between those of $Y(Co_{0.85}Al_{0.15})_2$ ($\mu_{Co} \sim 0.2\ \mu_B$) and $Lu(Co_{0.9}Al_{0.1})_2$ ($\mu_{Co} \sim 0.7\ \mu_B$) depicted in Fig. 7.6. Such a signal would be easily detectable. However, it is not observed in the present experimental spectra, which indicates that the Co sublattice is magnetically ordered at both temperatures.

Finally, we have faced the problem of confirming the existence of an average

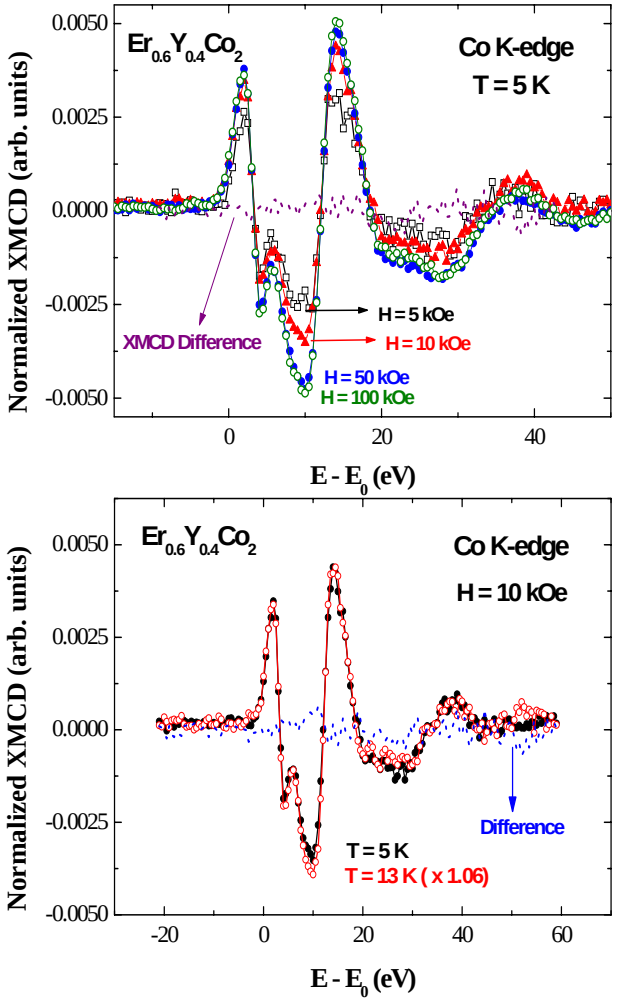

Figure 7.7: Comparison of the Co K-edge XMCD spectra of $Er_{0.6}Y_{0.4}Co_2$ recorded at T = 5 K and different applied magnetic fields: H = 5 kOe (black, □), 10 kOe (red, ▲), 50 kOe (blue, •) and 100 kOe (green, ○). The dotted line (purple) corresponds to the difference of the XMCD spectra recorded at 100 kOe and 50 kOe. In the bottom panel the XMCD spectra of $Er_{0.6}Y_{0.4}Co_2$ recorded with a H = 10 kOe applied at T = 5 K (black, •) and T = 13 K (red, ○) are compared.

Co moment in the case of $Er_{0.5}Y_{0.5}Co_2$ for which different and contradictory results are given in literature. To this aim we have applied a two-sublattice model to account for the Co K-edge XMCD spectrum, as previously applied to the R-Fe case[84, 85, 86, 128, 199]. According to this model, it is assumed that the XMCD corresponds to the addition of the contribution of the magnetic Co sublattice and of the Er one, being the latter proportional to the

number of neighboring Er atoms around absorbing Co. In order to verify this hypothesis, we have compared the Co K-edge XMCD spectra of compounds with a different Er-Y content. If our hypothesis is right, the amplitude of the Er contribution in $Er_{0.6}Y_{0.4}Co_2$ and $Er_{0.5}Y_{0.5}Co_2$ would be reduced by a factor 0.6 and 0.5, respectively, with respect to that of $ErCo_2$. Consequently, we have scaled by a 0.6 (0.5) factor the XMCD signals of $Er_{0.6}Y_{0.4}Co_2$ ($Er_{0.5}Y_{0.5}Co_2$), to re-normalize their Er contribution to that of the $ErCo_2$ XMCD. As shown in Fig. 7.8, after applying this procedure the three signals perfectly match in the high energy region, i. e., where the Er contribution is maximum. Differences are only found in the low-energy region, i. e., where the Co contribution is expected to be according to the XMCD of both Y and Lu compounds. Hence, the signal obtained after subtracting the above re-normalized XMCD of $Er_{0.6}Y_{0.4}Co_2$ and $Er_{0.5}Y_{0.5}Co_2$ to the XMCD of $ErCo_2$ would correspond to the different Co magnetism in the three samples. The difference signals obtained in this way are shown in the bottom panel of Fig. 7.8. They exhibit the characteristic two-peaks spectral feature of the Co K-edge XMCD of both $Y(Co_{0.85}Al_{0.15})_2$ and $Lu(Co_{0.9}Al_{0.1})_2$, supporting that the signal extracted according the method above is related exclusively with the Co contribution to the XMCD. Then, we have applied the same method to the case of $Er_{0.6}Y_{0.4}Co_2$ and $Er_{0.5}Y_{0.5}Co_2$ compounds. In this way, the XMCD signal of $Er_{0.5}Y_{0.5}Co_2$ has been multiplied by 1.2 (0.6/0.5) to recover the same Er contribution as for $Er_{0.6}Y_{0.4}Co_2$. As shown in Fig. 7.9, there is a perfect coincidence of both signals for energies higher than 12 eV, and their difference shows at low energy the Co-like two-peaks spectral profile. The extracted difference is related to that of the Co magnetic moment in both compounds in the form $\mu_{Co}|_{0.6}$ - 1.2 x $\mu_{Co}|_{0.5}$, where $\mu_{Co}|_{0.6}$ and $\mu_{Co}|_{0.5}$ are the μ_{Co} in $Er_{0.6}Y_{0.4}Co_2$ and $Er_{0.5}Y_{0.5}Co_2$, respectively. The amplitude of the difference signal is the same as for the Co K-edge XMCD spectrum of $Y(Co_{0.85}Al_{0.15})_2$ recorded at $\mu_0 H$ = 50 kOe. For the latter compound M(H) data yields a Co magnetic moment value of $\mu_{Co} = 0.22\ \mu_B$. Then, by using this value and by considering that from magnetization data $\mu_{Co}|_{0.6} = 0.55\ \mu_B$, this analysis yields $\mu_{Co}|_{0.5} = 0.28\ \mu_B$. Consequently, the Co K-edge XMCD data indicate, in agreement with the Er $L_{2,3}$ study, that there is also a non-negligible magnetic moment at the Co sites in $Er_{0.5}Y_{0.5}Co_2$.

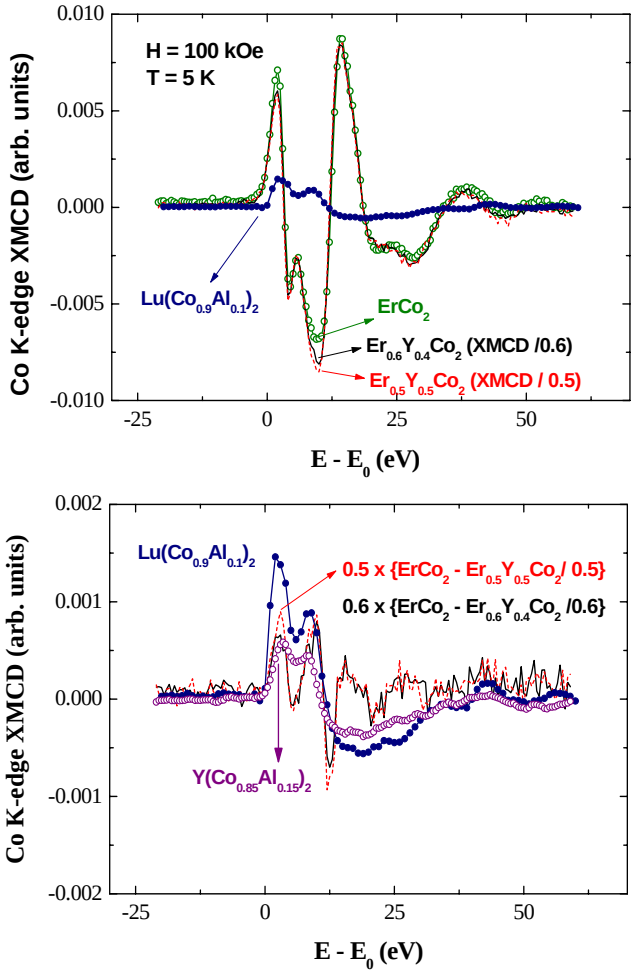

Figure 7.8: Top panel: Comparison of Co K-edge XMCD spectra recorded at T = 5 K and H = 100 kOe of $Lu(Co_{0.9}Al_{0.1})_2$ (navy, •) and $ErCo_2$(green, ○) to those of $Er_{0.6}Y_{0.4}Co_2$ (black, solid line) and $Er_{0.5}Y_{0.5}Co_2$ (red, dotted line) renormalized to the Er contribution (see text for details). Bottom panel: Comparison of Co K-edge XMCD spectra of $Lu(Co_{0.9}Al_{0.1})_2$ (navy,•) and $Y(Co_{0.85}Al_{0.15})_2$ (purple, ○) to the difference between the $ErCo_2$ XMCD and the renormalized signals of $Er_{0.6}Y_{0.4}Co_2$ (black, solid line) and $Er_{0.5}Y_{0.5}Co_2$ (red, dotted line) (see text for details).

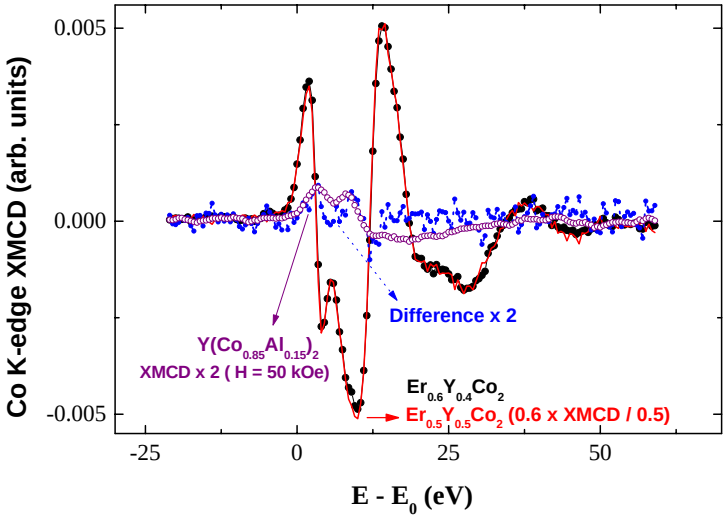

Figure 7.9: Comparison of Co K-edge XMCD spectra of $Er_{0.6}Y_{0.4}Co_2$ recorded at T = 5 K and H = 100 kOe (black, •) and that of $Er_{0.5}Y_{0.5}Co_2$ (red, dotted line) renormalized to the Er contribution (see text for details). Its difference (blue, dots) is compared to the XMCD of $Y(Co_{0.85}Al_{0.15})_2$ (purple, ○) recorded at the same temperature and H = 50 kOe.

7.2.5 Summary and Conclusions

We have reported here a systematic XMCD study performed at Co K-edge and at the Er $L_{2,3}$-edges in the $Er_{1-x}Y_xCo_2$ series as a function of the yttrium concentration, the applied magnetic field and the temperature.

In the case of the $Er_{0.6}Y_{0.4}Co_2$ compounds, XMCD data do not show the decoupling of the magnetic ordering for both Er and Co sublattices. In addition, no experimental evidence of the occurrence of an inverse IEM has been found for applied magnetic fields of up to H = 100 kOe. In addition, a non-zero magnetic moment is found at the Co sites in the case of the $Er_{0.5}Y_{0.5}Co_2$ compound.

Our results shed light on the current debate existing on the magnetic behavior of the $Er_{1-x}Y_xCo_2$ systems for yttrium concentrations close to the critical one for the existence of long-range magnetic order [188, 189, 190, 191, 192, 193, 187, 195]. This XMCD study will contribute to a better understanding of the nature of both IEM and inverse IEM metamagnetic transitions in itinerant-electron R-Co systems and in the modification of the effective field acting on the Co subsystem by diluting the magnetic rare-earth.

7.3 Relationship between μ_{Lu} and the magnetic behavior of $(Y_tLu_{1-t})(Co_{1-x}Al_x)_2$ systems

7.3.1 Introduction

The intermetallic RCo_2 compounds (R stands for rare-earth elements) are particularly interesting to study the magnetism of 3d and 4f metals as the Co moment strongly depends upon the R alloying component [202, 133]. These intermetallic compounds are characterized by the occurrence of a metamagnetic transition in the Co 3d itinerant subsystem and by the dependence of the Co magnetic moment on the R alloying component. For compounds in which R is non magnetic (YCo_2, $LuCo_2$) the Co susceptibility is of the Pauli type, while in the case of compounds with magnetic R metals a Co moment $\sim 1\ \mu_B$ is induced . The magnetic order of the d subsystem in the RCo_2 compounds with magnetic R is referred to the effect of the molecular field acting on the Co sites (H_{fd}).

Another peculiarity of this family comes from the fact that substitution of Co by a non-magnetic atom as Al induces ferromagnetic order. YCo_2 is a typical exchange-enhanced Pauli paramagnet and the occurrence of a ferromagnetic state takes place upon applying a critical field B_c= 69 T at T = 10 K [203, 202]. The critical field of the metamagnetic transition, B_c, decreases in $Y(Co_{1-x}Al_x)_2$ alloys as Co is replaced by non-magnetic Al. Weak-ferromagnetism occurs for $0.12 < x < 0.20$ compounds being the spontaneous Co magnetic moment $\mu_{Co} \sim 0.1\ \mu_B$. Within the series both the maximum spontaneous moment, $\sim 0.14\ \mu_B$/Co, and the maximum Curie temperature, $T_C \sim$ 25 K, corresponds to the $x \simeq 0.15$ compound [204, 205, 206, 207, 208, 209].

The magnetic behavior of these systems has been addressed to the modification of the 3d density of states (DOS) whose shape near the Fermi level, E_F, is rather peculiar [146, 12]. In this way, different hypothesis have been formulated to account for the impact of Al into the magnetic properties of YCo_2. On the one hand, several authors argue that the increase of the lattice parameter due to Al leads to both the narrowing of the bandwidth and the increase of the density of states at Fermi level, $N(E_F)$ [204]. By contrast, it has been also postulated that the increase of $N(E_F)$ comes from the decrease in the density of 3d-electrons produced by the substitution of Co ($3d^7$) configuration by Al ($3d^0$) [210]. However, none of the above interpretations take into account the change of the DOS near the Fermi level produced by Al substitution. Theoretical band calculations suggest that the strong hybridization between the Co(3d) and Al(3p) bands modifies the shape of the characteristic peak of the YCo_2 DOS in such a way that upon increasing Al content $N(E_F)$ increases and weak

ferromagnetism is favoured [211, 212]. Additional support to this hypothesis is given by x-ray photoelectron spectroscopy (XPS) measurements that are interpreted in terms of the lowering of E_F with Al substitution, [213] and by the modification of magnetic behavior of YCo_2 upon doping with Fe and Ni [214]. More recently, band calculations reported by Khmelevskyi *et al.* have shown that the increase of the DOS at the Fermi energy in the $Y(Co_{1-x}Al_x)_2$ systems is a direct consequence of the smoothing of the DOS peaks due to the substitution of Co by Al [215].

Research was extended to the case of $Lu(Co_{1-x}Al_x)_2$, in which Lu bears no 4f magnetic moment [210, 216, 217], and $(Y_{1-t}Lu_t)(Co_{0.88}Al_{0.12})_2$, in which the crystal cell parameter is kept constant and similar to that of YCo_2 [210, 216], systems. These studies reveal that the influence of Al substitution on the magnetic properties of Y and Lu compounds is rather different. The $Lu(Co_{1-x}Al_x)_2$ compounds show SFM behavior for the same concentration at which the $Y(Co_{1-x}Al_x)_2$ compounds become WFM ferromagnets [210, 216, 218]. Moreover, by contrast to the Y case, the $Lu(Co_{1-x}Al_x)_2$ systems show a sharp metamagnetic transition without a remarkable change in magnitude of the field-induced moment.[219, 217]. In the case of the $(Y_{1-t}Lu_t)(Co_{0.88}Al_{0.12})_2$ compounds it was found that the magnetic ground state changes from WFM (in Y-rich compounds) to SFM (in Lu-rich compounds) within a narrow concentration range in the vicinity of t = 0.4 [220]. Moreover, no metamagnetic transitions are observed for the Lu-rich compounds. [217] These differences cannot be explained in terms of a rigid band model and have been qualitatively interpreted in terms of the different hybridization between Co(3d)-Y(4d) and Co(3d)-Lu(5d) [219, 217, 221].

Aimed to furnish direct information about the modification of the electronic structure induced by Al in both Y and Lu compounds we have performed a combined X-ray absorption spectroscopy (XAS) and X-ray magnetic circular dichroism (XMCD) study of the $Y(Co_{1-x}Al_x)_2$, $Lu(Co_{1-x}Al_x)_2$ and $(Y_tLu_{1-t})(Co_{0.88}Al_{0.12})_2$ series. In this way, both the Co K-edge and the Lu $L_{2,3}$-edges XAS and XMCD spectra have been measured through the PM - WFM - SFM transitions in the $(Y_tLu_{1-t})(Co_{1-x}Al_x)_2$ series. In addition, XMCD sum-rules [26, 27] have been applied to the Lu $L_{2,3}$-edges spectra to determine the existence of a magnetic moment at the Lu sites and its relationship with the different, WFM *vs.* SFM, magnetic behavior of Y and Lu based compounds.

Table 7.3: Structural parameter (lattice constant, a) of the $(Y_{1-t}Lu_t)(Co_{1-x}Al_x)_2$ compounds:

Compound	a(Å)	Compound	a(Å)
$Y(Co_{1-x}Al_x)_2$		$(Y_{1-t}Lu_t)(Co_{0.88}Al_{0.12})_2$	
x= 0.06	7.2541(4)	t= 0.2	7.2617(3)
x= 0.10	7.2759(4)	t= 0.4	7.2375(3)
x= 0.11	7.2849(3)	t= 0.6	7.2218(3)
x= 0.13	7.2982(3)	$Lu(Co_{0.9}Al_0.1)_2$	7.1680(2)
x= 0.15	7.3014(3)		
x= 0.20	7.3247(5)		

7.3.2 Synthesis and structural characterization

$Y(Co_{1-x}Al_x)_2$ (with x = 0.06, 0.10, 0.11, 0.13, 0.15 and 0.20), $Lu(Co_{0.9}Al_{0.1})_2$ and $(Y_{1-t}Lu_t)(Co_{0.88}Al_{0.12})_2$ (t = 0.2 0.4 y 0.6) samples were prepared by arc-melting the pure elements under Ar protective atmosphere following standard procedures [204, 216, 210]. In order to have single-phase samples, a 3 % wt. excess was added to the stoichiometric amounts of Lu and Y. The ingots were annealed at 850 ^{o}C for one week. Structural characterization was performed at room temperature by means of powder x-ray diffraction. The diffraction patterns, analyzed by using the FULLPROF code [**?**], showed that all the samples show the $MgCu_2$-type (C15) Laves structure (Fd3m space group). In all the compounds, the presence of secondary phases (Y_2O_3 or Lu_2O_3) is less than $< 3.5\%$ overall.

7.3.3 Macroscopic Magnetic Measurements

The thermal dependence of the magnetization of $Y(Co_{1-x}Al_x)_2$, $Lu(Co_{0.9}Al_{0.1})_2$ and $(Y_{1-t}Lu_t)(Co_{0.88}Al_{0.12})_2$ compounds is shown in Fig. 7.10. In the case of $Y(Co_{1-x}Al_x)_2$, magnetic ordering transitions are clearly observed for compounds with x $\geq$ 0.13 while for compounds which Al concentrations below x $\leq$ 0.11 no magnetic order is found. Magnetization *vs.* applied magnetic field curves, M(H), and Arrott plots (M^2 *vs.* H/M) indicate that ferromagnetism is stabilized only for x $\geq$ 0.13. In agreement to previous works the Co magnetic moment, derived from the value of the magnetization at H = 50 kOe, reaches its maximum value for x = 0.15 and a progressive decrease takes place upon further Al substitution (see Table 7.4). In the case of $Lu(Co_{1-x}Al_x)_2$ the critical Al concentration for the onset of ferromagnetism has been previously

Table 7.4: Magnetic parameters of the $(Y_{1-t}Lu_t)(Co_{1-x}Al_x)_2$ compounds: magnetization measured at 50 kOe (M_{5T}) and the Co moment derived from the magnetization data at H = 50 kOe and T = 5 K.

Compound	M_{50kOe} (μ_B/f.u.)	μ_{Co} (μ_B/f.u.)
$Y(Co_{1-x}Al_x)_2$		
x= 0.06	0.055	0.029
x= 0.10	0.134	0.074
x= 0.11	0.210	0.118
x= 0.13	0.340	0.195
x= 0.15	0.378	0.222
x= 0.20	0.228	0.143
$Lu(Co_{1-x}Al_x)_2$		
x= 0.10	1.156	0.642
$(Y_{1-t}Lu_t)(Co_{0.88}Al_{0.12})_2$		
t= 0.2	0.485	0.276
t= 0.4	0.845	0.480
t= 0.6	1.047	0.595

reported to be within the range $0.06 \leq x \leq 0.1$ [206, 218]. However, recent studies have shown that the onset of ferromagnetism strongly depends on annealing due to the coexistence of paramagnetic and ferromagnetic states of Co atoms for $x \lesssim 0.08$ [222, 217]. Therefore, here we have concentrated our study in the compound with x = 0.1 for which the maximum μ_{Co} occurs within this series [216]. In this case, the M(H) curve shows a magnetic state approaching to saturation being the magnetization per Co atom 0.6 μ_B at H = 50 kOe. Finally, $(Y_{1-t}Lu_t)(Co_{0.88}Al_{0.12})_2$ compounds with t = 0.2 0.4 and 0.6 exhibit ferromagnetic behavior. While the T_C temperature linearly increases with Lu content a different behavior is found regarding the μ_{Co} values [210, 216]. For low Lu content (t = 0.2) the system exhibits the hallmarks of a WFM ferromagnet and the Co moment increases linearly with the applied magnetic field. The magnetization per Co atom, μ_{Co}, is ~ 0.3 μ_B at 5 T. By contrast the richest Lu compound (t = 0.6) shows a saturated magnetic state with $\mu_{Co} \sim 0.6$ μ_B. In the case of the intermediate Lu content, t = 0.4, the system evolves under the action of an applied magnetic field from WFM to SFM behavior [133].

The complex magnetic behavior induced in the three classes of compounds by the aluminium substitution is usually discussed in terms of the electronic modification of the systems. The inspection of the cell parameters of the

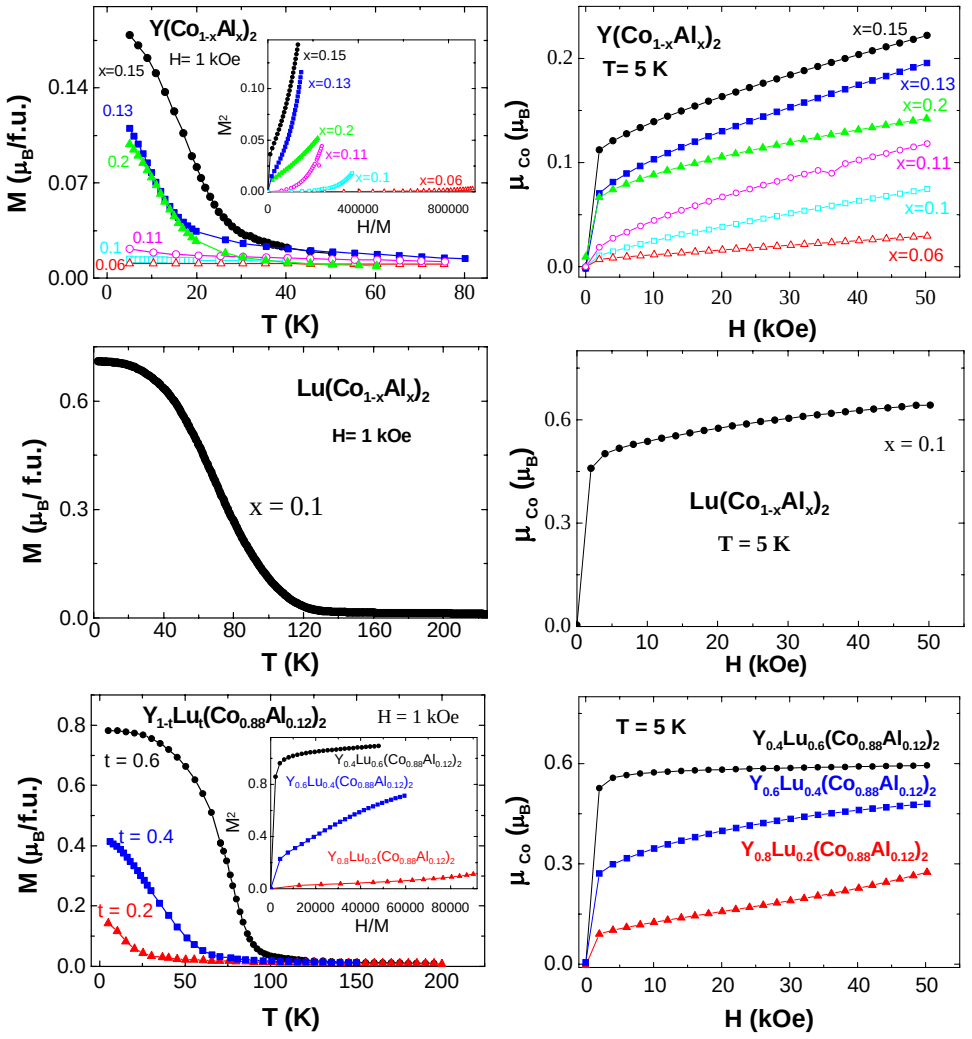

Figure 7.10: Left: Dependence of the magnetization *vs.* temperature in the case of: $Y(Co_{1-x}Al_x)_2$ (top panel), $Lu(Co_{1-x}Al_x)_2$ (middle) and $(Y_{1-t}Lu_t)(Co_{0.88}Al_{0.12})_2$ systems (bottom). In all the cases, samples were zero field cooled down to 4.2 K and the magnetization *vs.* temperature curves were recorded on heating. In the case of the systems containing Y, Arrot plots (recorded at T = 5 K) are shown in the insets. Right: Dependence of the magnetization, per Co atom, with the applied magnetic field.

$(Y_{1-t}Lu_t)(Co_{1-x}Al_x)_2$ compounds, summarized in Table 7.3, indicates that the effect of Al substitution is not simply linked to the narrowing of the DOS. Indeed, while magnetic WFM and SFM ordering is stabilized in $Y(Co_{1-x}Al_x)_2$ and $Lu(Co_{1-x}Al_x)_2$, respectively, as the cell parameter increases, the opposite

behavior occurs for the $(Y_{1-t}Lu_t)(Co_{0.88}Al_{0.12})_2$ series. Consequently, the complexity of this magnetic behavior cannot be simply addressed to the increase of the density of states at Fermi level due to the narrowing of the DOS. On the contrary, it suggests that there is an interplay between this structural effect and the Al-induced modification of the DOS through the Co-Al hybridization.

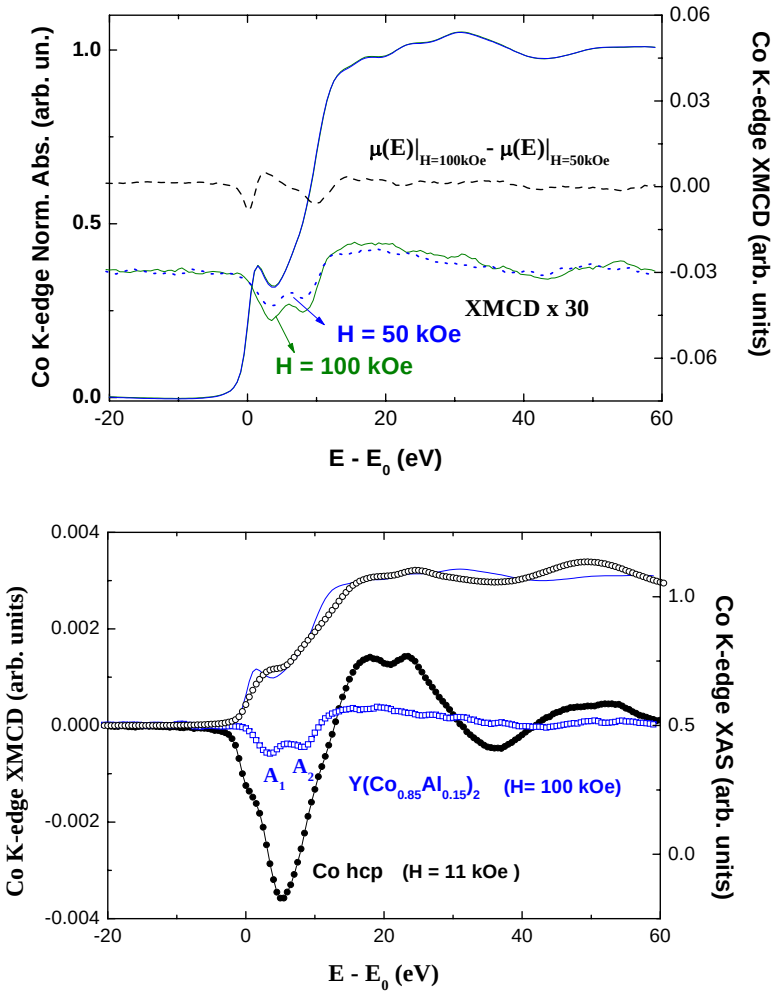

Figure 7.11: Top panel: Comparison of the Co K-edge XMCD spectra of $Y(Co_{0.85}Al_{0.15})_2$ recorded at H = 50 (blue, dots) and 100 kOe (green, solid line) and the difference of the XAS spectra recorded with the same applied magnetic fields (black, dashed line). For sake of comparison the normalized Co K-edge XAS spectrum recorded at H = 50 kOe (blue, solid line) is also shown. Bottom panel: Comparison of the normalized Co K-edge XMCD spectra of $Y(Co_{0.85}Al_{0.15})_2$ (□, blue) and hcp cobalt (•,black). For sake of clarity, the normalized Co K-edge XAS spectra are also shown: $Y(Co_{0.85}Al_{0.15})_2$ (solid line, blue); hcp cobalt (open circles, black).

This scenario poses the need of obtaining a further knowledge on this interplay. X-ray absorption spectroscopy suits well to this purpose as it is a simple and sensitive probe of the local unoccupied states of a given symmetry around the selected absorbing atomic species [129]. Consequently, we performed an analysis of the XAS and XMCD spectra at the Co K-edge and Lu $L_{2,3}$-edges in the $(Y_tLu_{1-t})(Co_{1-x}Al_x)_2$ systems.

7.3.4 XMCD results and discussion

Co K-edge XAS and XMCD

The near-edge region of the absorption spectrum is extremely sensitive to the modification of the DOS, while the high energy region of the spectrum is related to the local structure around the absorbing atom. In order to discern the origin, structural *vs.* electronic, of the differences in the absorption spectra it is instructive to compare the XAS spectra recorded on the same compound at different applied fields. In this way, Fig. 7.11 reports the comparison between the Co K-edge spectra recorded at H = 50 kOe and 100 kOe in the case of $Y(Co_{0.85}Al_{0.15})_2$. As the crystal structure is retained, the difference between both absorption spectra shows the energy region that is mainly affected by the modification of the DOS. As shown in Fig. 7.11 these differences lie in the first 15 eV's of the spectrum, i.e., at the raising edge region. For the sake of completeness, we have compared this difference to the XMCD spectra recorded at the same applied fields. As shown in the figure, the main features of the XMCD spectra lie at the same region as above where, in addition, their intensity also shows the maximum modification on the applied magnetic field. Consequently, it is possible to address that differences in this energy region reflect the different magnetic state, as determined from a different DOS, while differences in the high energy region are related to structural effects.

Once we have determined the extension of the absorption spectrum in which electronic effects are expected to dominate over the structural ones, we have focused our study to monitor the proposed change of the Co magnetic ground state from weak (WFM) to strong (SFM) in the $(Y_tLu_{1-t})(Co_{1-x}Al_x)_2$ compounds as a function of the Y, Lu and Al concentration. To this end, we have compared the normalized Co K-edge XMCD spectra of $Y(Co_{0.85}Al_{0.15})_2$ and hcp cobalt, as shown in Fig. 7.11. The difference in the magnitude of the XMCD signals indicates the different magnetic ground state of Co in both systems. Indeed, μ_{Co} in hcp cobalt is $\sim 1.7\ \mu_B$ while it is only about $0.2\ \mu_B$ in the case of $Y(Co_{0.85}Al_{0.15})_2$. It should be noted that the spectrum in the Y compound has been recorded at 5 K and under the application of a 100 kOe magnetic field, while the reference was measured at room temperature and by

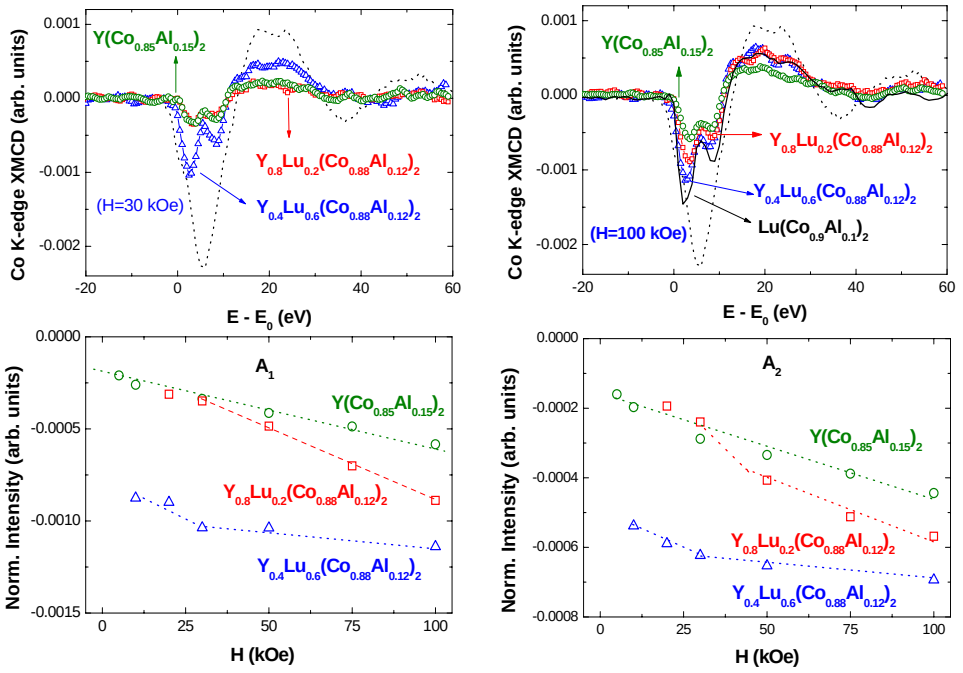

Figure 7.12: Upper panel: Comparison for different applied magnetic fields of the normalized Co K-edge XMCD spectra of $Y(Co_{0.85}Al_{0.15})_2$ (green, ○), $(Y_{0.8}Lu_{0.2})(Co_{0.88}Al_{0.12})_2$ (red,□) and $(Y_{0.4}Lu_{0.6})(Co_{0.88}Al_{0.12})_2$ (blue, △). For sake of clarity, the normalized Co K-edge XMCD spectra of both hcp Co recorded at H = 10 kOe (black, dotted line) and $Lu(Co_{0.9}Al_{0.1})_2$ recorded at H = 100 kOe (black, solid line) are also shown. Lower panel: Dependence of the main XMCD features A_1 and A_2 with the magnetic applied field: $Y(Co_{0.85}Al_{0.15})_2$ (green, ○), $(Y_{0.8}Lu_{0.2})(Co_{0.88}Al_{0.12})_2$ (red,□) and $(Y_{0.4}Lu_{0.6})(Co_{0.88}Al_{0.12})_2$ (blue, △). The dotted lines are guide for the eyes.

applying a magnetic field of 10 kOe. The XMCD spectral shape is markedly different in both cases. Hcp Co shows a main broad negative peak extending over the first 17 eV's with a shoulder-like feature at E = 0 eV that coincides with the inflection point of the XAS spectrum. By contrast, the XMCD of the Y-based compounds exhibits two well resolved negative peaks (A_1 and A_2) in the same energy region.

In a first approach, one can expect that the shape of the Co K-edge XMCD spectra evolves from that of $Y(Co_{0.85}Al_{0.15})_2$ to that of hcp cobalt as the magnetic ground state of Co changes from weak (Y-rich) to strong ferromagnetism character (Lu-rich) throughout the $(Y_tLu_{1-t})(Co_{1-x}Al_x)_2$ series. Such a class of modification has been previously reported in the case of Fe-P amorphous alloys [**?**]. As the P concentration increases the system change from WFM to

SFM character and the shape of the Fe K-edge XMCD evolves from that of bcc Fe up to resemble that of hcp Co. However, this is not the case here. Fig. 7.12 shows the dependence of the Co K-edge XMCD as a function of the applied field in $Y(Co_{0.85}Al_{0.15})_2$, $(Y_{0.8}Lu_{0.2})(Co_{0.88}Al_{0.12})_2$ and $(Y_{0.4}Lu_{0.6})(Co_{0.88}Al_{0.12})_2$. As shown in the figure, the shape of the XMCD signals is the same for both Y-rich and Lu-rich compounds, i.e., for compounds showing WFM and SFM magnetic behavior, respectively. Moreover, in all the cases the XMCD spectrum is clearly different to that of hcp cobalt. Therefore, it is concluded that the particular shape of the XMCD spectra cannot be straightforwardly inferred from the magnetic character of the Co atoms, but is mainly determined by the details of the DOS.

Despite all the signals show similar XMCD shape, their intensities clearly reflects the different magnetic (WFM *vs* SFM) regime. The Y-rich compounds show a small XMCD signal whose intensity linearly grows as the magnetic field is increased. This behavior reflects its weak itinerant ferromagnetic nature. By contrast, the XMCD of the richest Lu compound, $(Y_{0.4}Lu_{0.6})(Co_{0.88}Al_{0.12})_2$, is: i) significantly greater than for the Y-rich compounds, and ii) its magnitude remains nearly constant when varying the applied magnetic field. This is shown in Fig. 7.12 where the dependence of the intensity of the characteristic XMCD spectral features A_1 and A_2 are plotted as a function of the magnetic field for all the compounds. The behavior of $Y(Co_{0.85}Al_{0.15})_2$ can be assigned as corresponding to a weak itinerant ferromagnet while that of $(Y_{0.4}Lu_{0.6})(Co_{0.88}Al_{0.12})_2$ corresponds to a SFM material. By contrast, the behavior of $(Y_{0.8}Lu_{0.2})(Co_{0.88}Al_{0.12})_2$ shows the hallmarks of a WFM-SFM transition. Indeed, at low applied fields its XMCD intensity matches with that of the WFM $Y(Co_{0.85}Al_{0.15})_2$, while for $H > 30$ kOe it departs from the WFM behavior and tends to the SFM one.

This is clearly observed when the normalized XMCD intensities are compared to the macroscopic magnetization data. As shown in Fig. 7.13 both XMCD and M(H) data perfectly scale for the three compounds for applied fields $H \geq 30$ kOe. In the case of $(Y_{0.4}Lu_{0.6})(Co_{0.88}Al_{0.12})_2$ the values of the XMCD intensity obtained for low applied fields, $H = 10$ and 20 kOe, are below the magnetization curve. We think this is related to the different signal to noise ratio that improves as the applied magnetic field, and consequently the XMCD intensity, increases. Indeed, the dependence of the XMCD intensity of both A_1 and A_2 features is different for these two points (see lower panels in Fig. 7.12). For the sake of completeness we have also included the data for $Lu(Co_{0.9}Al_{0.1})_2$ compound although their XMCD has been recorded only at $H = 100$ kOe. The values of μ_{Co} derived from the magnetization data at 90 kOe are 0.30, 0.47 and 0.61 μ_B for $Y(Co_{0.85}Al_{0.15})_2$, $(Y_{0.8}Lu_{0.2})(Co_{0.88}Al_{0.12})_2$ and $(Y_{0.4}Lu_{0.6})(Co_{0.88}Al_{0.12})_2$, respectively. For $Lu(Co_{0.9}Al_{0.1})_2$ the same pro-

cedure yields $\mu_{Co} = 0.7\ \mu_B$. Therefore, μ_{Co} appears to be "saturated" in the Y-Lu compound with maximum Lu content, $(Y_{0.4}Lu_{0.6})(Co_{0.88}Al_{0.12})_2$, while that with low Lu content, $(Y_{0.8}Lu_{0.2})(Co_{0.88}Al_{0.12})_2$, evolves from the Y-rich WFM state towards the SFM as the applied magnetic field increases.

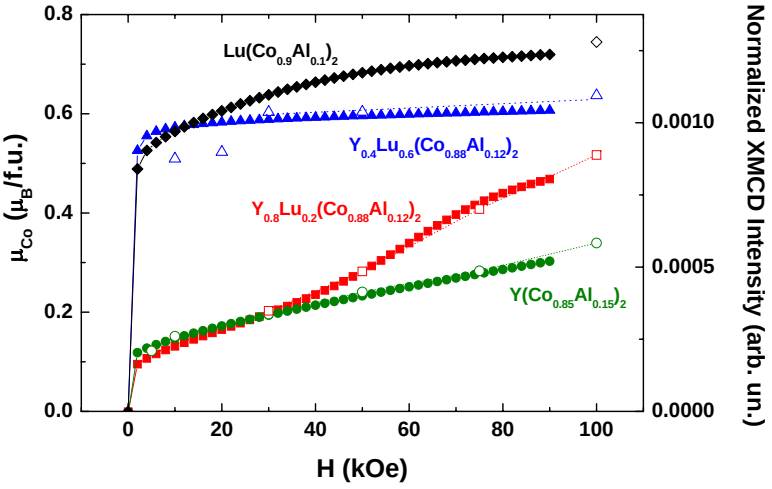

Figure 7.13: Comparison of the dependence with the magnetic applied field of the magnetization per cobalt atom (solid symbols) and the intensity of the A_1 feature in the Co K-edge XMCD (open symbols) in the case of $Y(Co_{0.85}Al_{0.15})_2$ (green, ○), $(Y_{0.8}Lu_{0.2})(Co_{0.88}Al_{0.12})_2$ (red,□), $(Y_{0.4}Lu_{0.6})(Co_{0.88}Al_{0.12})_2$ (blue, △), $Lu(Co_{0.93}Al_{0.07})_2$ (purple, ▽)and $Lu(Co_{0.9}Al_{0.1})_2$ (black, ◇). The dotted lines are guide for the eyes.

Lu $L_{2,3}$-edges XMCD

The XMCD results evidence that there is no direct relationship between the different behavior of μ_{Co} in both WFM and SFM compounds and the cell parameters. The occurrence of the SFM state seems to be favored by the increasing of Lu concentration. As commented in the introduction, this behavior has been tentatively addressed to the different hybridization between Co(3d)-Y(4d) and Co(3d)-Lu(5d) [220, 219, 217, 221]. Also, it has been suggested that the Co(3d)-Al(p) hybridization modifies the shape of the characteristic peak of the YCo_2 DOS in such a way that upon increasing Al content $N(E_F)$ increase and weak ferromagnetism is favored. [211, 212]. However, despite the near-edge region is extremely sensitive to the modification of the DOS, no drastic difference of both the XAS and XMCD signals is found at the Co K-edge throughout the $(Y_tLu_{1-t})(Co_{1-x}Al_x)_2$ series.

Trying to get a deeper insight on the origin of this puzzle, we have explored

the possibility of this magnetic behavior being due to the development of a magnetic moment at the Lu sites. To this aim we have extended our study to the case of the Lu $L_{2,3}$ absorption edges.

As shown in Fig. 7.14 strong XMCD signals are found in the case of the SFM compounds $Lu(Co_{0.9}Al_{0.1})_2$ and $(Y_{0.4}Lu_{0.6})(Co_{0.88}Al_{0.12})_2$, whose intensity does not vary as increasing the applied magnetic field. On the contrary, the XMCD intensity shows a linear variation with the field in the case of the WFM $(Y_{0.8}Lu_{0.2})(Co_{0.88}Al_{0.12})_2$. On the one hand, the presence of a non-negligible Lu L_2-edge XMCD signal points out that Lu bears a magnetic moment, μ_{Lu}, in all the studied compounds. As previously commented in chapter 6, this XMCD signal is thought to be originated from the polarization of the Lu (5d) states by the Co(3d) and so the Lu magnetic moment is induced by the Co one. Moreover, Fig. 7.14 shows that the behavior of the Lu XMCD signals, and thus of μ_{Lu}, is different in both WFM and SFM systems. This is shown in Fig. 7.15 where the Lu L_2 XMCD signals for the investigated compounds are compared at low (30 kOe) and high (100 kOe) magnetic fields. The Lu magnetic moment appears to be saturated in both $Lu(Co_{0.9}Al_{0.1})_2$ and $(Y_{0.4}Lu_{0.6})(Co_{0.88}Al_{0.12})_2$ compounds that are considered as strong ferromagnetic materials. By contrast, small XMCD signals are obtained at low magnetic fields for $(Y_{0.8}Lu_{0.2})(Co_{0.88}Al_{0.12})_2$. However, as the applied magnetic field increases the XMCD intensity of $(Y_{0.4}Lu_{0.6})(Co_{0.88}Al_{0.12})_2$ tends to the values shown by the SFM materials, in agreement with the existence of the WFM to SFM transition induced by the external field inferred also from the analysis of the Co K-edge XMCD.

This can be clearly observed in Fig. 7.16 where the maximum of the L_2 XMCD signals (E = 0 eV) is plotted *vs.* the applied magnetic field for all the investigated compounds. The XMCD intensity remains nearly constant for the SFM compounds $(Y_{0.4}Lu_{0.6})(Co_{0.88}Al_{0.12})_2$ and $Lu(Co_{0.9}Al_{0.1})_2$, while it markedly increases ($\sim$ 150 %) with the field for the WFM compound. This behavior is in agreement with that obtained at the Co K-edge showing a relative increase of $\sim$ 10 % and 150 % for the SFM and WFM compounds, respectively. It is interesting to note that in the case of compounds without Lu, as $Y(Co_{0.85}Al_{0.15})_2$, the increase of the magnetization per Co atom is only the 73 %. This result suggests that despite Lu moment is induced by the Co one, its presence feeds the enhancement of the Co one by reinforcing the strong ferromagnetic character of the system.

Finally, aimed to get a relationship between μ_{Lu} and μ_{Co} we have performed a sum-rule analysis. These sum-rules have been derived connecting the integrated XMCD spectra at the $L_{2,3}$-edges of Lu with the ground-state expectation value of both $\langle$ Lz $\rangle$ and $\langle$ Sz $\rangle$ of the 5d states [26, **?**]:

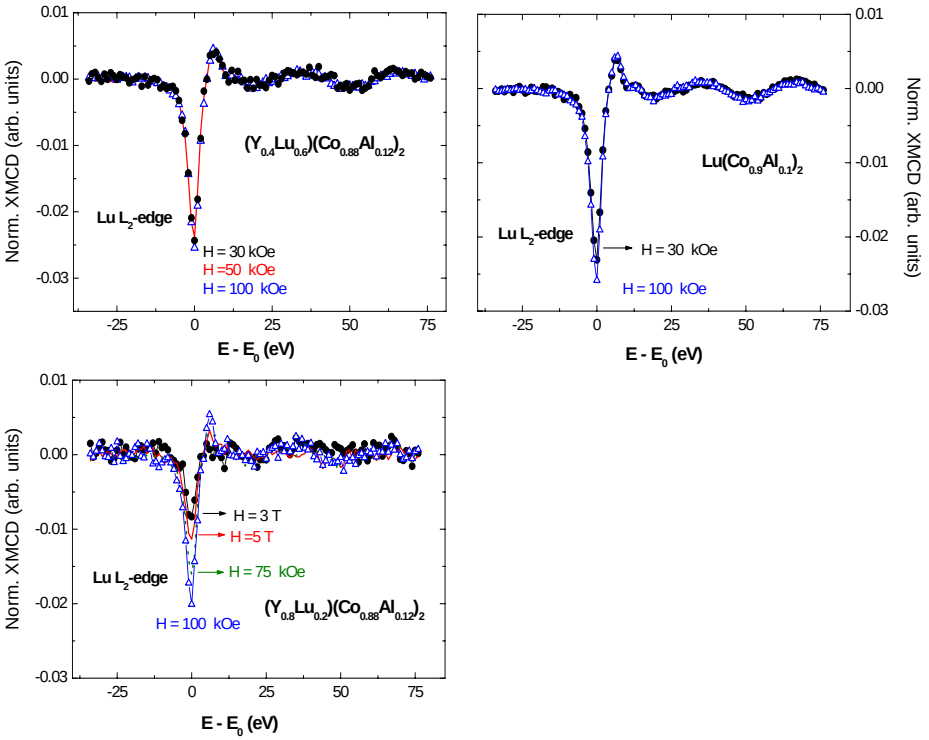

Figure 7.14: Dependence of the Lu L_2-edge XMCD signals with the applied magnetic field in the case of $Lu(Co_{0.9}Al_{0.1})_2$, $(Y_{0.4}Lu_{0.6})(Co_{0.88}Al_{0.12})_2$ and $(Y_{0.8}Lu_{0.2})(Co_{0.88}Al_{0.12})_2$. XMCD spectra were recorded at T = 5 K and with a fixed applied field of: 30 kOe(back, •), 50 kOe (red, solid line), 75 kOe (green, dotted line) and 100 kOe ((blue, △).

$$\langle L_z \rangle = 2 \times (A_{L_3} + A_{L_2}) \times \frac{n_h}{\mu} \tag{7.1a}$$

$$\langle S_z \rangle + \frac{7}{2}\langle T_z \rangle = \frac{3}{2} \times (A_{L_3} - 2 \times A_{L_2}) \times \frac{n_h}{\mu}, \tag{7.1b}$$

where A_{L_3} and A_{L_2} are the integrals over the dichroic signal at the L_3 and L_2 edges, respectively. n_h is the number of holes in the Lu $5d$ band and μ is the unpolarized $L_{2,3}$-edge cross-section after subtraction of a double step function that ideally models the contribution of the continuum states (see Fig. 7.17). No normalization to the absorption jumps has been done neither in the L_3-edge, nor in the L_2-edge spectra in order to preserve the direct applicability of the sum rules. The analysis of the XMCD signals have been performed under the following assumptions: i) μ is approximated by $\frac{3}{2}(\mu^+ + \mu^-)$; ii) $\langle T_z \rangle$

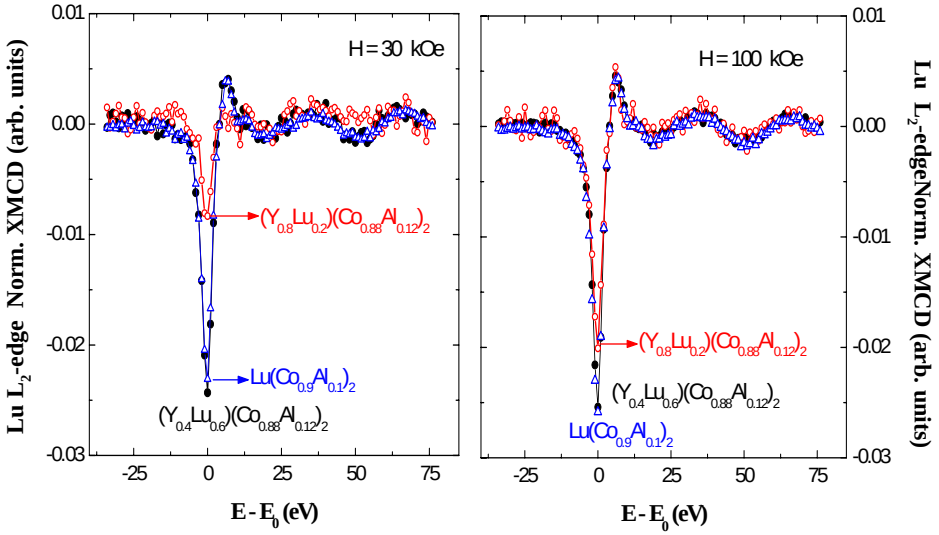

Figure 7.15: Comparison of the Lu L_2-edge XMCD signals recorded at H = 30 kOe (left panel) and 100 kOe(right panel): $Lu(Co_{0.9}Al_{0.1})_2$ (blue, △), $(Y_{0.4}Lu_{0.6})(Co_{0.88}Al_{0.12})_2$ (black, •) and $(Y_{0.8}Lu_{0.2})(Co_{0.88}Al_{0.12})_2$ (red, ○).

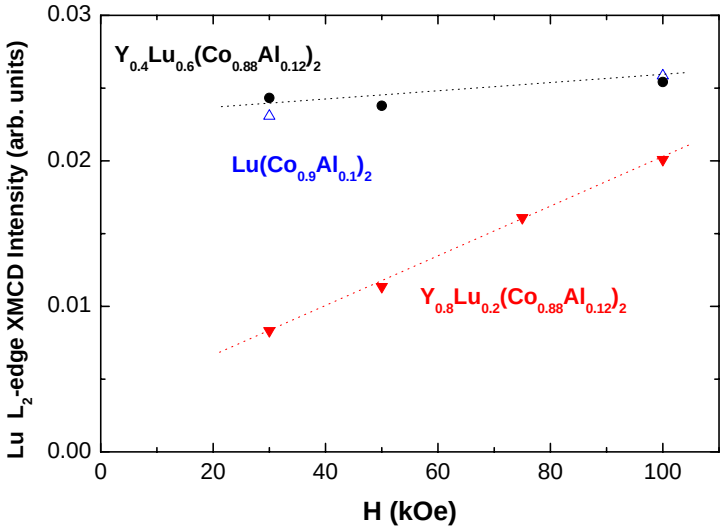

Figure 7.16: Modification of the maximum of the Lu L_2-edge XMCD signals as a function of the applied magnetic field: $Lu(Co_{0.9}Al_{0.1})_2$ (blue, △), $(Y_{0.4}Lu_{0.6})(Co_{0.88}Al_{0.12})_2$ (black, •) and $(Y_{0.8}Lu_{0.2})(Co_{0.88}Al_{0.12})_2$ (red, ▼).

is assumed to be negligible in the spin sum rule; iii) estimates of both the orbital, $\langle L_z \rangle$, and spin, $\langle S_z \rangle$, moments have been derived from the sum-rule by

considering $n_h = 9$. These approximations can be rather crude in order to get a correct estimate of the magnetic moment. Despite the absolute value of the 5d Lu magnetic moment derived from the XMCD spectra has to be considered with some caution, the trend of its modification, obtained by using the same parameters, through the whole series of compounds studied is not seriously concerned.

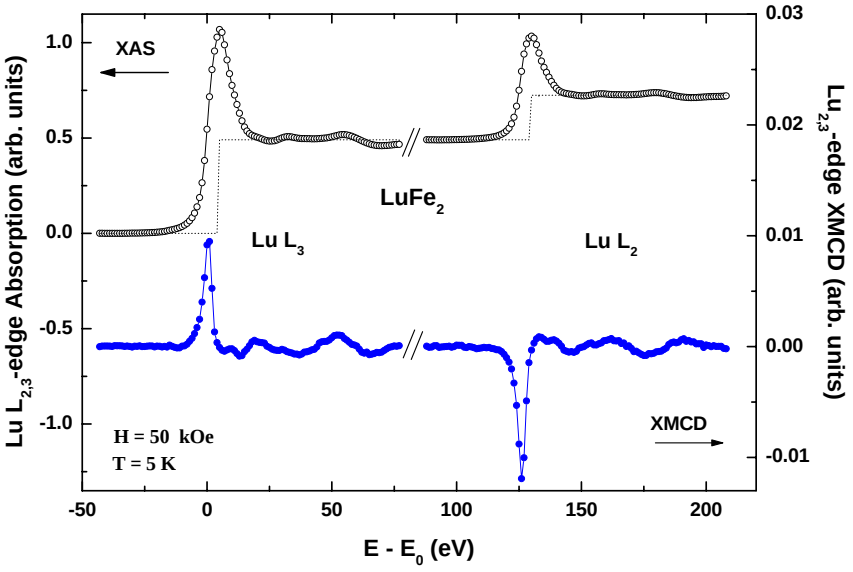

Figure 7.17: Lu $L_{2,3}$-edge XMCD (blue, •) and XAS (black, ○) spectra of $LuFe_2$ as used for the sum-rules application. No normalization has been applied and the L_2 XAS spectrum has been vertically shifted to match to the L_3 one. The dotted line shows the two-step-like function used to obtain the d-state isolated spectra.

The values of both the orbital and spin moments of the Lu 5d states are summarized in Table 7.5. For the sake of comparison the data of $LuFe_2$ are also shown. In all the cases the induced moment at the Lu sites is of opposite sign to that of Co, in agreement with band-structure calculations [12, 10, 14]. In the case of $LuFe_2$, theoretical calculations by Yamada and Shimizu have predicted a 5d μ_{Lu} moment of -0.33 μ_B [10] while calculations by Brooks *et al.* yields a -0.41 μ_B moment at the Lu sites from which -0.27 $\mu_B$is of partial 5d character [14]. The existence of an ordered moment at the lutetium sites was early confirmed by XMCD [43] although no estimates of its value were reported. For this compound, our data yields $\mu_{Lu} \sim 0.13\ \mu_B$, a value significantly smaller than the theoretically predicted. The different magnitude of the Lu moment estimates derived from both XMCD and band calculations are probably due to the strong approximations included in the sum-rules analysis and to the fact

that band calculations are deserved for ideal systems. Notwithstanding the different magnitude both band-calculations and XMCD data yields the same coupling scheme for the 3d magnetic moment of Co and the Lu 5d one. Indeed, similar ferrimagnetic coupling is found between the Co and Lu moments in the studied $Lu(Co_{0.9}Al_{0.1})_2$ and $(Y_{1-t}Lu_t)(Co_{0.88}Al_{0.12})_2$ compounds. However, the maximum μ_{Lu} found, $\sim 0.05\ \mu_B$, is half of that of $LuFe_2$ case. This result agrees with the fact that the Lu magnetic moment is induced by that of the transition metal in both Fe and Co compounds, being $\mu_{Co} < \mu_{Fe}$. Moreover, the XMCD data show that this induced μ_{Lu} is near saturated, between $\sim$ 0.05-0.06 μ_B, in those compounds showing strong ferromagnetic behavior as $Lu(Co_{0.9}Al_{0.1})_2$ and $(Y_{0.4}Lu_{0.6})(Co_{0.88}Al_{0.12})_2$. By contrast, the WFM systems $(Y_{0.8}Lu_{0.2})(Co_{0.88}Al_{0.12})_2$ and $Lu(Co_{0.93}Al_{0.07})_2$ shows a reduced ($\sim 0.01\ \mu_B$) μ_{Lu} at low applied magnetic field that increases approaching ($\sim 0.04\ \mu_B$) the "saturated" value at H = 100 kOe.

Table 7.5: Estimates (in μ_B) of the ground-state expectation value of the orbital, $\langle$ Lz $\rangle$, and spin, $\langle$ Sz $\rangle$, moment of the Lu 5d states derived from the XMCD sum-rules analysis at T = 5 K. The uncertainty of these values is estimated to be of 15 %.

Compound	30 kOe	50 kOe	75 kOe	100 kOe
$(Y_{0.8}Lu_{0.2})(Co_{0.88}Al_{0.12})_2$				
$<L_z>$	-0.004	-0.003	-0.007	-0.010
$<S_z>$	0.008	0.015	0.022	0.025
$\mu_{Lu}\|_{5d}$	-0.012	-0.027	-0.037	-0.040
$(Y_{0.4}Lu_{0.6})(Co_{0.88}Al_{0.12})_2$				
$<L_z>$	-0.009	-0.010	-	-0.010
$<S_z>$	0.031	0.032	-	0.034
$\mu_{Lu}\|_{5d}$	-0.053	-0.054	-	-0.058
$Lu(Co_{0.9}Al_{0.1})_2$				
$<L_z>$	-	-	-	-0.003
$<S_z>$	-	-	-	0.028
$\mu_{Lu}\|_{5d}$	-	-	-	-0.053
$LuFe_2$ (300 K)				
$<L_z>$	-	-0.002	-	-
$<S_z>$	-	0.049	-	-
$\mu_{Lu}\|_{5d}$	-	-0.096	-	-
$LuFe_2$ (5 K)				
$<L_z>$	-	-0.004		-
$<S_z>$	-	0.065		-
$\mu_{Lu}\|_{5d}$	-	-0.126		-

A final comment is deserved to the relationship between the existence of a magnetic moment at the Lu sites and the *Lu paradox* [221, 223]. This refers to the unusual magnetic behavior of the $Lu(Co_{1-x}Al_x)_2$ systems showing magnetic ordering temperatures, $\sim$ 150 K [216], higher than that of isostructural $R(Co_{1-x}Al_x)_2$ compounds for x $>$ 0.12, where R is a magnetic heavy rare-earth. By contrast, T_C does not exceed 30 K for $Y(Co_{1-x}Al_x)_2$ [204]. These results have been tentatively addressed to differences of the d-states in both Y and Lu compounds [147]. However, no theoretical computation confirms this fact and, consequently, its detailed explanation is missed to date. The XMCD results indicate that the highest T_C occurs for those compounds showing an enhanced Lu moment, while μ_{Lu} is strongly reduced in those compounds showing low T_C. As discussed above, no clear relation exists among volume effects, differences of the d-states in both Y and Lu compounds and the high magnetic ordering temperature exhibited by the Lu-rich compounds. The results presented here point out that the developing of an ordered moment at the Lu sites is critical into favoring ferromagnetism through the reinforcement of the magnetic interactions in the system. Further work is needed to determine the role, if present, of an induced moment at the Y sites.

7.3.5 Summary and Conclusions

The peculiar magnetic behavior of the $(Y_tLu_{1-t})(Co_{1-x}Al_x)_2$ systems has been studied by means of X-ray absorption spectroscopy (XAS) and X-ray magnetic circular dichroism (XMCD) techniques.

The Co K-edge XMCD spectra of all the $(Y_tLu_{1-t})(Co_{1-x}Al_x)_2$ compounds studied is similar, independently of the magnetic character of the systems (WFM *vs.* SFM), and markedly different to that of Co hcp. Despite the XMCD spectral shape is retained, its intensity reflects the different magnetic character of the systems and monitors the WFM-SFM transitions. In particular, the Co magnetic moment seems saturated in $(Y_{0.4}Lu_{0.6})(Co_{0.88}Al_{0.12})_2$ while it evolves from the Y-rich WFM state towards the SFM as the applied magnetic field increases in the case of the low Lu content $(Y_{0.8}Lu_{0.2})(Co_{0.88}Al_{0.12})_2$ compound.

The XMCD at the Lu $L_{2,3}$-edges indicates the existence of an ordered 5d moment at the lutetium sites (induced by the Co one), ferrimagnetically coupled to the Co moment. Estimates of the Lu magnetic moment have been obtained by applying the XMCD sum-rules. As in the case of the Co edge, the behavior of the Lu XMCD signals is clearly different in both WFM and SFM systems. For SFM compounds $\mu_{Lu} \sim 0.06\ \mu_B$ seems to be saturated. By contrast, μ_{Lu} increases from $\sim 0.01\ \mu_B$ to $\sim 0.04\ \mu_B$ as the applied magnetic

field is increased in WFM systems. The present results indicate that the highest T_C occurs for those compounds showing an enhanced Lu moment, while μ_{Lu} is strongly reduced in those compounds showing low T_C. These results suggest that the existence of a Lu moment is critical into favoring ferromagnetism through the reinforcement of the magnetic interactions in the system.

To date, the peculiar magnetic behavior of the $(Y_tLu_{1-t})(Co_{1-x}Al_x)_2$ systems has been addressed to the modification of the DOS induced by Al, by qualitative considering volume effects, a rigid-band mechanism or the change of the DOS shape due to the hybridization between the Co(3d) and Al(3p) states. By contrast, little attention has been given to the role played by both Y and Lu into contributing to the magnetic behavior. The present results show the different electronic impact of Al in both Y and Lu compounds; the induction of a 5d magnetic moment at the Lu sites and the way in which it varies through the WFM-SFM transitions and as the function of different external parameters. This suggests the need of explicitly including both the Co(3d)-Y(4d) and Co(3d)-Lu(5d) hybridization into the theoretical description of the magnetic properties of these compounds. We think that these results can stimulate further theoretical work in order to get a proper understanding of the itinerant magnetic systems.

Concluding Remarks

In this thesis we have performed a systematic XMCD study in different R-T intermetallic series aimed to get as much insight as possible into the interpretation of the XMCD spectra at both the T K edge and the R $L_{2,3}$ edges.

Regarding the T K-edge XMCD spectra:

1. Our results confirm that the T K-edge XMCD signal in R-T intermetallic compounds is due to the addition of magnetic contributions from both the transition metal and the rare-earth sublattices.

2. The comparison of the isolated R-sublattice magnetic contribution to the T K-edge XMCD and magnetization data indicates that these signals resemble the magnetic state of the rare-earth. That is, this technique allows to monitor the rare-earth moment even when one is looking at the T K-edge absorption!!

3. Moreover, the R contribution to the T K-edge signal is also related to the R:Fe ratio or more likely to the number of R neighbors.

4. Regarding the modification of the Fe contribution, $XMCD_{Fe}$, to the Fe K-edge XMCD signal our results cast doubts on previous assignments on the relationship between the Fe K-edge XMCD spectral features and the magnetic character of Fe. When the T K-edge XMCD spectrum of R-T intermetallics is analyzed, the R contribution may be very large and affect to the whole energy range. The strong R contribution may partially or even totally hide the Fe contribution to the XMCD spectrum. Therefore, the model proposed by Fdez-Gubieda *et al.* relating the evolution of peak A with a transition in the nature of the Fe ions from weak to strong ferromagnetism, although valid in some cases, is not an general rule to study the magnetic character of Fe, mainly when an additional contribution is present on the XMCD spectrum.

Concerning the R $L_{2,3}$-edges XMCD spectra:

1. We have found that in the case of the RAl_2 series, i.e. where R is the only magnetic atom, the intensity of the R L_2 XMCD signal clearly resembles the modification of n_{RR} with the atomic number. This provides a experimetnal method to study the strength of the R(4f) - R(5d) interaction.

2. Our results show that the R L_2-edge XMCD spectra in R-T intermetallic compounds is due to the addition of magnetic contributions from both the transition metal and the rare-earth sublattices.

3. In addition, we have found that the T contribution, a positive peak which appears always at ~ 1 eV, is related to both the number of Fe (or Co) neighbouring atoms around the absorbing R atom and the magnetic moment of the 3d metal. Furthermore, we have proposed a method to disentangle the two contributions. We have found that the T contribution can be identified, at least in a first approximation, as the L_2-edge XMCD spectrum of the Lu compound corresponding to same R-T series. In addition, the intensity of this $XMCD_T$ signal seems to show a relation with the n_{RT} molecular field coefficient. If we could corroborate (and quantify) a relation between the subtracted XMCD signal and the strength of the R(5d)-Fe(3d) hybridization, this result would give rise to a direct method to study the R(4f)-R(5d)-T(3d) interactions in R-T intermetallics.

   In the relation to the subtracted signals, it is worth mentioning that, although the data analysis method do not allow us to go beyond the qualitative analysis, the large differences observed in the XMCD signals validate, without doubt, the derived conclusions.

Comparison of the XMCD spectra for different R-T series shows that the presence of an *extra* T contribution to the R L_2-edge XMCD spectra and, conversely, an *extra* R contribution to the T K-edge XMCD spectra is a general result of the R-T intermetallics. These results indicate the need of including the two contributions in both XMCD spectra prior to account for the XMCD at the rare-earth $L_{2,3}$-edges in R-Fe intermetallic materials and, consequently, of getting the characterization of the lanthanides 5d states by means of XMCD. To this respect, we have shown that the influence of these contributions on the values of the orbital and spin moments derived by using sum rules analysis is not negligible.

In relation to this, is important to be aware that one of the most important properties of XMCD has typically been its atomic and shell selectivity (as commented in chapter 1), which completely disagree with the results presented in this thesis. We are probing the conduction band where the outer-

most states from the different atomic species are strongly hybridized. Within this framework, the origin of the extra contribution (T on the R absorbtion edge and, conversely, R on T absorption edge) can be easily understood in terms of the R(5d)-R(3d) hybridization. Our results indicate that the atomic and shell selectivity is not a general property of XMCD. On the contrary, by correctly accounting these mixed effects it is possible to reveal the transition-metal magnetism by tuning the rare-earth absorption edges and, conversely, the rare-earth magnetism by looking at the transition metal!

Finally, despite their difficult interpretation, these XMCD signals have been also used to shed light on some current debates existing on the magnetic behavior of some particular R-T systems:

i) The comparison of the XMCD signals between the pure $RFe_{11}Ti$ compounds and their hydrides shows that hydrogen effects are more important for the rare-earth sublattice than for the iron one. The contribution of the R-sublattice to the XMCD signal, related to the rare-earth magnetic moment, is determined to decrease upon hydrogen absorption.

ii) In the case of the $Er_{0.6}Y_{0.4}Co_2$ compounds, XMCD data do not show the decoupling of the magnetic ordering for both Er and Co sublattices. In addition, no experimental evidence of the occurrence of an inverse IEM has been found for applied magnetic fields of up to H = 100 kOe.

iii) Regarding the peculiar magnetic behavior of the $(Y_tLu_{1-t})(Co_{1-x}Al_x)_2$ systems, the XMCD at the Lu $L_{2,3}$-edges indicates the existence of an ordered 5d moment at the lutetium sites, ferrimagnetically coupled to the Co moment. Our results indicate that the highest T_C occurs for those compounds showing an enhanced Lu moment, while μ_{Lu} is strongly reduced in those compounds showing low T_C. These results suggest that the existence of a Lu moment is critical into favoring ferromagnetism through the reinforcement of the magnetic interactions in the system.

Bibliography

[1] K.H.J. Buschow, in *Handbook of Magnetic Materials*, edited by E.P. Wohlfarth, Vol. 4, (North-Holland, Amsterdam, 1988) and references therein.

[2] E. Burzo and H.R. Kirchmayr, in *Handbook on the Physics and Chemistry of Rare Earths*, edited by K.A. Gschneidner Jr. and L. Eyring, Vol. 12, (North-Holland, Amsterdam, 1989) and references therein.

[3] H.R. Kirchmayr and C.A. Poldy, in *Handbook on the Physics and Chemistry of Rare Earths*, edited by K.A. Gschneidner Jr. and L. Eyring, Vol. 2, (North-Holland, Amsterdam, 1979) and references therein.

[4] J.J.M. Franse and R.J. Radwanski, in *Handbook of Magnetic Materials*, edited by K.H.J. Buschow, Vol. 7, (North-Holland, Amsterdam, 1993) and references therein.

[5] See for example K. N. R. Taylor and M. I. Darby, *Physics of Rare Earth Solids*, (Chapman and Hall, London, 1972).

[6] E. C. Stoner, Rep. Progr. Phys. **9**, 43 (1946).

[7] See for example K. H. J. Buschow and F. R. de Boer, *Physics of Magnetism and Magnetic Materials*, (Kluwer, New York, 2003).

[8] I.A. Campbell, J. Phys. F **2**, L47 (1972).

[9] N. H. Duc, in *Handbook on the Physics and Chemistry of Rare Earths*, edited by K.A. Gschneidner Jr. and L. Eyring, Vol. 24, (North-Holland, Amsterdam, 1997) and references therein.

[10] H. Yamada and M. Shimizu, J. Phys. F: Metal Phys. **16**, 1039 (1986).

[11] H. Yamada and M. Shimizu, J. Phys. F: Metal Phys. **15**, L175 (1985).

[12] H. Yamada, J. Inoue, K. Terao, K. Kanda and M. Shimizu, J. Phys. F: Metal Phys. **14**, 1943 (1984).

[13] H. Yamada, J. Inoue and M. Shimizu, J. Phys. F: Metal Phys. **15**, 169 (1985).

[14] M. S. S. Brooks, O. Eriksson and B. Johansson, J. Phys.: Condens. Matter **1**, 5861 (1989).

[15] M. S. S. Brooks, L. Nordström and B. Johansson, J. Phys.: Condens. Matter **3**, 2357 (1991).

[16] M. S. S. Brooks, L. Nordström and B. Johansson, J. Phys.: Condens. Matter **3**, 3393 (1991).

[17] M.S.S. Brooks and B. Johansson, *Handbook of Magnetic Materials*, edited by K.H.J. Buschow, Vol.7, (Elsevier, Amsterdam, 1993).

[18] E. Belorizky, M. A. Fremy, J. P. Gavigan, D. Givord and H. S. Li, *J. Appl. Phys.* **61(8)**, 3971 (1987).

[19] For more detailed information about XAS see, for example, *X-Ray Absorption: Principles,Applications, Techniques of EXAFS, SEXAFS, XANES*, edited by R. Prins and D. Koningsberger (J. Wiley & Sons, New York, 1988) and references therein; *X-Ray Absorption Fine Structure for Catalysts and Surfaces*, edited by Y. Iwasawa (World Scientific, Singapore, 1996).

[20] G. Schütz, M. Knülle, R. Wienke, W. Wilhelm, W. Wagner, P. Kienle, R. Frahm, Z. Phys. B **73**, 67 (1988).

[21] G. Schütz, R. Wienke, W. Wilhelm, W. Wagner, P. Kienle and R. Frahm, Z. Phys. B **75**, 495 (1989).

[22] U. Fano, Phys. Rev. B **178**, 131 (1969).

[23] If the photoelectron originates from a spin-orbit split level, e.g., the $p_{3/2}$ level (L_3 edge), its angular momentum can be transferred in part to the spin through the spin-orbit coupling. Right-circularly-polarized photons transfer to the electron a momentum opposite to that from left-circularly-polarized photons; hence, photoelectrons with opposite spins are created in the two cases. Since the $p_{3/2}$ (L_3) and $p_{1/2}$ (L_2) levels have opposite spin-orbit coupling (l + s and l - s, respectively) the spin polarization will be opposite at the two edges.

[24] The Fano parameter can be calculated under certain assumptions: P_e= 0.01 K and L_1-edge; P_e = -0.5 L_2; P_e = 0.25 L_3.

[25] J. Stöhr and Y. Wu, *Proceedings NATO Advanced Study Intitute "New Directions in Research with Third Generration Soft X-Ray Synchrotron Radiation Sources"*, (Kluwer Academic Publishers, Netherlands, 1995).

[26] B.T. Thole, P. Carra, F. Sette and G. van der Laan, Phys. Rev. Lett. **68**, 1943 (1992).

[27] P. Carra, B. T. Thole, M. Altarelli and X. Wang, Phys. Rev. Lett. **70**, 694 (1993).

[28] M. Altarelli, Phys. Rev. B **47**, 597 (1993).

[29] A. Ankudinov and J.J. Rehr, Phys. Rev. B **51**, 1282 (1995).

[30] F. Grandjean and G. J. Long in *Mössbauer spectroscopic studies of interstitial intermetallic compounds*, edited by F. Grandjean, G. J. Long and K. H. J. Buschow, NATO ASI Series, Series E: Applied Sciences. Vol. 281, Kluwer Academic Publishers, Netherlands (1995).

[31] N. N. Greenwood and T. C. Gibb in "*Mössbauer spectroscopy*", (Chapman and Hall Ltd., London, 1971).

[32] D.E. Dickson, *Mössbauer spectroscopy*, edited by D.E. Dickson and F. J. Berry. (Cambridge University press, 1986).

[33] M. Kawakami, T. Hihara, Y. Koi and T. Wakiyama, J. Phys. Soc. Japan **33**, 1591-1598 (1972).

[34] M. T. Averbuch-Pouchot, R. Chevalier, J. Deportes, B. Kebe and R. Lemarie, J. Magn. Mag. Mat. **68**, 190-196 (1987).

[35] The quadrupole shift is sometimes defined as $\varepsilon = e^2qQ(3\cos^2\theta\text{-}1)/2$, the difference in the splitting between line 1 and 2, and the splitting between line 5 and 6 of the magnetic spectra.

[36] R. Coehoorn, C. J. M. Denissen and R. Eppenga, J. Appl. Phys. **69**, 6222 (1991).

[37] T. Beuerle and M. Fähnle, J. Magn. Mag. Mat. **110**, L29 (1992).

[38] V. A. Niculescu, T. J. Burch and J. I. Budnick, J. Magn. Magn. Mat. **39**, 223 (1983).

[39] S. Blügel, H. Akai, R. Zeller and P. H. Dederichs, Phys. Rev. B **35**, 7 (1987).

[40] Z. W. Li, X. Z. Zhou and A. H. Morrish, J. Phys.: Condens. Matter **4**, 10409 (1992).

[41] C. Piquer, J. Rubín, J. Bartolomé, V. Kuncser and G. Filoti, Phys. Rev. B **73**, 174433 (2006).

[42] R. Coehoorn, J. Magn. Magn. Mat. **159**, 55 (1996).

[43] F. Baudelet, C. Brouder, E. Dartyge, A. Fontaine, J.P. Kappler, and G. Krill, Europhys. Lett. **13**, 751 (1990).

[44] J. Chaboy, A. Marcelli, L.M. García, J. Bartolomé, M. Kuzmin, H. Maruyama, K. Kobayashi, H. Kawata, and T. Iwazumi, Europhys. Lett. **28**, 135 (1994)

[45] J. C. Lang, S. W. Kycia, X. D. Wang, B. N. Harmon, A. I. Goldman, D. J. Branagan, R. W. McCallum, and K. D. Finkelstein, Phys. Rev. B **46**, 5298 (1992).

[46] J. C. Lang, X. Wang, B. N. Harmon, A. I Goldman, K. W. Dennis, R. W. McCallum, and K. D. Finkelstein, Phys. Rev. B **50**, 13805 (1994).

[47] J. C. Lang, X. Wang, V. P. Antropov, B. N. Harmon, A. I. Goldman, H. Wan, G. C. Hadjipanayis, and K. D. Finkelstein, Phys. Rev. B **49**, 5993 (1994).

[48] J. C. Lang, G. Srajer, C. Detlefs, A. I. Goldman, H. König, X. Wang, B. N. Harmon, and R. W. McCallum, Phys. Rev. Lett. **74**, 4935 (1995).

[49] J. Chaboy, H.Maruyama, L.M. García, J. Bartolomé, K. Kobayashi,N. Kawamura, A. Marcelli, and L. Bozukov, J. Phys. (France) IV **7**, C2-449 (1997).

[50] J. Chaboy , L.M. García, F. Bartolomé, A. Marcelli, G. Cibin, H.Maruyama, S. Pizzini, A. Rogalev, J.B. Goedkoop, and J. Goulon, Phys. Rev. B **57**, 8424 (1998).

[51] T. Nakamura, M. Mizumaki, Y. Watanabe, and S. Nanao, J. Phys. Soc. Jpn. **67**, 3964 (1998).

[52] J. Chaboy, F. Bartolomé, L.M. García, and G. Cibin, Phys. Rev. B. **57**, 5598 (1998).

[53] J. Chaboy, H. Maruyama, N. Kawamura, and M. Suzuki Phys. Rev. B **69**, 014427 (2004).

[54] C. Giorgetti, E. Dartyge, F. Baudelet, and R.-M. Galéra, Phys. Rev. B **70**, 035105 (2004).

[55] X. Wang, T.C. Leung, B.N. Harmon and P. Carra, Phys. Rev. B **47**, 9087 (1993).

[56] H R. Wienke, G.Schütz and H. Ebert, J. Appl. Phys. **69**, 6147 (1991).

[57] B.N. Harmon and A.J. Freeman, Phys. Rev. B **10**, 1979 (1974).

[58] See for example, R. M. Galera, S. Pizzini, J. A. Blanco, J. P. Rueff, A. Fontaine, Ch. Giorgetti, F. Baudelet, E. Dartyge, and M. F. López, Phys. Rev. B **51**, 15957 (1995).

[59] P. Carra, B. N. Harmon, B. T. Thole, M. Altarelli and G. A. Sawatzky, Phys. Rev. Lett. **66**, 2495 (1991).

[60] M. H. Krisch, C. C. Kao, F. Sette, W. A. Caliebe, K. Hämäläinen, and J. B. Hastings, Phys. Rev. Lett. **74**, 4931 (1995).

[61] M. H. Krisch, F. Sette, U. Bergmann, C. Masciovecchio, R. Verbeni, J. Goulon, W. Caliebe, and C. C. Kao, Phys. Rev. B **54**, R12673 (1996).

[62] F. Bartolomé, J.M. Tonnerre, L. Seve, D. Raoux, J. Chaboy, L.M. García, M. Krisch and C.C. Kao, Phys. Rev. Lett. **79**, 3775 (1997).

[63] Ch. Brouder and M. Hikam, Phys. Rev. B **43**, 3809 (1991).

[64] F. Baudelet, Ch. Giorgetti, S. Pizzini, Ch. Brouder, E. Dartyge, A. Fontaine, J.P. Kappler and G. Krill, J. Electron Spectr. **62**, 153 (1993).

[65] J. Miguel-Soriano, J. Chaboy, L.M. García and F. Bartolomé, J. Appl. Phys. **87**, 5884 (2000).

[66] T. Jo and S. Imada, J. Phys. Soc. Jpn. **62**, 3721 (1993).

[67] H. Matsuyama, I. Harada and A. Kotani, J. Phys. Soc. Jpn. **66**, 337 (1997).

[68] I. Harada, K. Asakura, A. Fujiwara and A. Kotani, J. Electron Spectr. **136**, 125 (2004).

[69] M. van Veenendaal, J.B. Goedkoop and B.T. Thole, Phys. Rev. Lett. **78**, 1162 (1997).

[70] C. Neumann, B. W. Hoogenboom, A. Rogalev and J. B. Goedkoop, Solid State Commun. **110**, 375 (1999).

[71] K. Fukui, H. Ogasawara, A. Kotani, I. Harada, H. Maruyama, N. Kawamura, K. Kobayashi, J. Chaboy and A. Marcelli, Phys. Rev. B **64**, 104405 (2001).

[72] K. Asakura, J. Nakahara, I. Harada, H. Ogasawara, K. Fukui and A. Kotani, J. Phys. Soc. Jpn. **71**, 2771 (2002).

[73] J. Igarashi and K. Hirai, Phys. Rev. B **50**, 17820 (1994).

[74] J. Igarashi and K. Hirai, Phys. Rev. B **53**, 6442 (1996)

[75] G.Y. Guo, Phys. Rev. B **57**, 10295 (1998).

[76] G.Y. Guo, Phys. Rev. B **55**, 11619 (1997).

[77] G.Y. Guo, J. Phys.: Condens. Matter **8**, L747 (1996).

[78] S. Pizzini, A. Fontaine, E. Dartyge, C. Giorgetti, F. Baudelet, J.P. Kappler, P. Boher, and F. Giron, Phys. Rev. B **50**, 3779 (1994).

[79] K.J. Gofron, C.W. Kimball, P.L. Lee, G. Jennings, and P.A. Montano, in *Proceedings of the 9th International Conference on X-ray Absorption Fine Structure, Grenoble, 1996* [J. Phys. IV **7**, C2-421 (1997)].

[80] M. L. Fdez-Gubieda, A. García-Arribas, J. M. Barandiarán, R. López Antón, I. Orue, P. Gorria, S. Pizzini and A. Fontaine, Phys. Rev. B **62**, 5746 (2000).

[81] G. Schütz, W. Wagner, W. Wilhelm, P. Kienle, R. Zeller, R. Frahm and G. Materlik, Phys. Rev. Lett. **58**, 737 (1987).

[82] S. Stähler, G. Schütz, and H. Ebert, Phys. Rev. B **47**, 818 (1993).

[83] Ch. Brouder, M. Alouani and K.H. Bennemann, Phys. Rev. B **54**, 7334 (1996).

[84] J. Chaboy, H.Maruyama,L.M. García, J. Bartolomé, K. Kobayashi, N. Kawamura, A. Marcelli and L. Bozukov, Phys. Rev. B **54**, R15637 (1996).

[85] J. Chaboy, L. M. García, F. Bartolomé, H. Maruyama, A. Marcelli and L. Bozukov, Phys. Rev. B **57,** 13386 (1998).

[86] J. Chaboy, C. Piquer, N. Plugaru, M. Artigas, H. Maruyama, N. Kawamura and M. Suzuki, J. Appl. Phys. **93**, 475 (2003).

[87] L. Bozukov, A. Apostolov and T. Mydlarz, J. Magn. Magn. Mater. **83**, 555 (1990).

[88] L. Bozukov, A. Apostolov and M. Stoytchev, J. Magn. Magn. Mater. **101**, 355 (1991).

[89] J. Rodriguez-Carvajal, Physica B. **55**, 192 (1993).

[90] Herman Winick (Ed.), "Synchrotron Radiation Sources. A primer"(World Scientific, Singapore, 1994) and references therein.

[91] H. Maruyama, M. Suzuki, N. Kawamura, M. Ito, E. Arakawa, J. Kokubun, K. Hirano, K. Horie, S. Uemura, K. Hagiwara, M. Mizumaki, S. Goto, H. Kitamura, K. Namikawa, and T. Ishikawa, J. Synchrotron Rad. **6**, 1133 (1999).

[92] More information about both SPring-8 and BL39XU can be found at *http://www.spring8.or.jp/en/*

[93] K. Hirano, K. Izumi, T. Ishikawa, S. Annaka and S. Kikuta, Jpn. J. Appl. Phys. **30**, L407 (1991).

[94] N. Ishimatsu, Y. Ohishi, M. Suzuki, N. Kawamura, M. Ito, H. Maruyama, S. Nasu, T. Kawakami and O. Shimomura, Nuclear Instruments and Methods in Physics Research A **467**, 1061 - 1064 (2001).

[95] M. Suzuki, N. Kawamura, M. Mizumaki, A. Urata, H. Maruyama, S. Goto and T. Ishikawa, Jpn. J. Appl. Phys. **37**, L1488 (1998).

[96] J. M. Friedt, A. Vasquez, J. P. Sanchez, Ph. L'Heritier and R. Fruchart, J. Phys. F: Met. Phys. **16**, 651 (1986).

[97] J. M. D. Coey, A. Yaouanc and D. Fruchart, Solid State Comm. **58**, 413 (1986).

[98] A. V. Andreev, A. V. Deryagin, N. V. Kudrevatykh, N. V. Mushnikov, V. A. Reïmer and S. V. Terent'ev, Sov. Phys. JETP **63**, 608 (1986).

[99] L.Y. Zhang and W.E. Wallace, J. Less-Common Met. **149**, 371 (1989).

[100] L.Y. Zhang, S.G. Sankar, W.E. Wallace and S.K. Malik, *Proceedings of the 6th International Symposium on Magnetic Anisotropy and Coercivity in Rare Earth-Transition Metal Alloys*, (Carnegie Mellon University, Pittsburgh) 493 (1990).

[101] A. Apostolov, R. Bezdushnyi, R. Damianova, N. Stanev and I. Naumova, J. Magn. Magn. Mater. **150**, 393 (1995).

[102] L. Y. Zhang, F. Pourarian and W. E. Wallace, J. Magn. Magn. Mat. **71**, 203 (1988).

[103] L. Pareti, O. Moze, D. Fruchart, Ph. L'Heritier and A. Yaouanc, J. Less Com. Met. **142**, 187 (1988).

[104] C. Piquer, J. Bartolomé, M. Artigas and D. Fruchart, Phys. Rev. B **62**, 1004 (2000).

[105] J. Chaboy, A. Marcelli and L. Bozukov, J. Phys.: Condens. Matter **7**, 8197 (1995).

[106] S.A. Nikitin, I.S. Tereshina, V.N. Verbetsky and A.A. Salamova, J. Alloys Comp. **316**, 46 (2001).

[107] J. Chaboy, A. Marcelli, L. Bozukov, F. Baudelet, S. Pizzini, E. Dartyge and A. Fontaine, Phys. Rev. B **51**, 9005 (1995).

[108] O. Isnard and M. Guillot, J. Appl. Phys. **83**, 6730 (1998).

[109] I.S. Tereshina, P. Gaczynski, V.S.Rusakov, H. Drulis, S.A. Nikitin, W. Suski, N.V. Tristan and T. Palewski, J. Phys.: Condens. Matter **13**, 8161 (2001).

[110] S.A. Nikitin, I.S. Tereshina, V.N. Verbetsky, A.A. Salamova, K.P. Skolov, N.Yu Pankratov, Yu.V. Skourski, N.V. Tristan, V.V. Zubenko and I.V. Telegina, J. Alloys Comp. **322**, 42 (2001).

[111] S.A. Nikitin, I.S. Tereshina, N. Yu Pankratov, Yu. V. Skourski, Phys. Rev. B **63**, 134420 (2001).

[112] I.S. Tereshina, S.A. Nikitin, N.V. Pankratov, G.A. Bezkorovajnaya, A.A. Salamova, V.N. Verbetsky, T. Mydlarz and Yu.V. Skourski, J. Magn. Magn. Mater. **231**, 213 (2001).

[113] S.A. Nikitin, I.S. Tereshina, Yu.V. Skourski, N.V. Pankratov, K.P. Skolov, V.V. Zubenko and I.V. Telegina, Phys. Solid State **43**, 290 (2001).

[114] Bo-Ping Hu, Hong-Shuo Li, J.P. Gavigan and J.M.D. Coey, J. Phys.: Condens. Matter **1**, 755 (1989).

[115] C. Piquer, Ph. D. Thesis. University of Zaragoza, (2001).

[116] T. H. Jacobs, Ph. D. Thesis. University of Leiden, (1992).

[117] J. Rodriguez-Carvajal and T. Roisnel, *http://www−llb.cea.fr/fullweb/fp2k/fp2k.htm.*

[118] C.G. Shull and H.A. Mook, Phys. Rev. Let. **16**, 184 (1966).

[119] S. Wakoh and Y. Kubo, J. Magn. Magn. Matter. **66**, 202 (1977).

[120] J. Chaboy and C. Piquer, Phys. Rev. B **66**, 104433 (2002).

[121] J. F. Herbst and J. J. Croat, J. Appl. Phys. **55**, 3023 (1984).

[122] For detailed infomation see, for example, H. R. Kirchmayr and E. Burzo, in *Compounds Between Rare Earth Elements and 3d, 4d, or 5d Elements*, edited by H. P. J. Wijn (Springer-Verlag, Berlin) Landolt-Börnstein New Series, Group III, **19, d2** (1990).

[123] J. J. Rhyne, K. Hardmann-Rhyne, H. Kevin Smith and W.E. Wallace, J. Less Common Met. **94**, 95 (1983).

[124] K. Hardmann, W. J. James and W. Yelon, *The Rare Earth in Modern Science and Technology* (Plenem Press, New York) **.2**, 403 (1980).

[125] P. C. M. Gubbens, A. M. Van der Kraan and K. H. J. Buschow, Solid State Commun., **26**, 107 (1978).

[126] K. H. J. Buschow, Rep. Prog. Phys., **40**, 1179 (1977).

[127] J.P. Rueff, R. M. Galera, S. Pizzini, A. Fontaine, L. M.García, C. Giorgetti, E. Dartyge and F. Baudelet, Phys. Rev. B **55 (5)**, 3063-3070 (1997).

[128] J. Chaboy, M. A. Laguna-Marco, M. C. Sánchez, H. Maruyama, N. Kawamura, and M. Suzuki, Phys. Rev. B **69**, 134421 (2004).

[129] J.E. Müller and J.W. Wilkins, Phys. Rev. B **29**, 4331 (1984).

[130] See for example J. F. Cannon, D. L. Rpbertson and H. T. Hall, Mat. Res. Bull. **7**, 5 (1972).

[131] J. H. Wernick, *Topologically Close-Packed Structures* in Intermetallic Compounds, J. H. Westbrook Ed., Wiley, New York (1967).

[132] A. K. Sinha, *Topologically Close-Packed Structures of Transition Metal Alloys* in Progress in Materials Science, Pergamon Press Ldt., New York (1972).

[133] E. Gratz and A. Markosyan, J. Phys.: Condens. Matter **13**, R385 (2001).

[134] H. Oesterreicher, Inorganic Chemistry **13**, 2807 (1974).

[135] R. Grössinger and W. Steiner, Phys. Stat. Sol. (a) **28**, K135 (1975).

[136] H. Oesterreicher, Phys. Stat. Sol. (a) **40**, K139 (1977).

[137] R. L. Berry and G. V. Raynor, Acta Crystallogr. **6**, 178 (1953).

[138] R. Y. Kitano, Y. Komure, H.K. Kajiwara and K. Watanabe, Acta Crystallogr. A, **36**, 16 (1980).

[139] See for example: K.H.J. Buschow and A.S. Van der Goot, J. Less Common Met. **22**, 419 (1977); E. Burzo, Z. Angew. Phys **32**, 127 (1971); H. Oesterreicher, J. Less Common Met. **25**, 341 (1971).

[140] A. E. Clark, *Handbook on the Physics and Chemistry of Rare-Earths*, Chapter 15: Magnetostrictive RFe_2 intermetrallic compounds. Edited by K.A. Gschneider and L. Eying, North-Holland Publishing Company (1979).

[141] B. Barbara, J.P. Giraud, J. Laforest, R. Lemaire, E.Siaud and J. Schweizer, Physica **86-88 B**, 155-157 (1977).

[142] A.E. Dwight and C. W. Kimball, Acta Crystallogr. B, **30**, 2791 (1974).

[143] E. Burzo, Solid State. Commun. **14**, 1295 (1974).

[144] E. Burzo, Solid State. Commun. **20**, 569 (1976).

[145] A. A. Sorokin, B.A. Komissarova, G. K. Ryasny, L.G. Shpinkova, Z.Z. Akselrod, A. V. Tsvyashchenko, E. N. Shirani and L.N. Fomicheva, JEPT **84**, 599 (1997).

[146] Cyrot and M. Lavagna, J. Physique **40**, 763 (1979).

[147] I.S. Dubenko, R.Z. Levitin, A.S. Markosyan and H. Yamada, J. Magn. Magn. Mater. **136**, 93 (1994) and references therein.

[148] M.J. Besnus, P. Bauer and J.M. Génin, J. Phys. F: Metal Phys. **8**, 191-204 (1978).

[149] M. Reissner, W. Steiner, J. P. Kappler, P Bauer and M.J. Besnus, J. Phys. F: Metal Phys., **14**, 1249 (1984).

[150] M.J. Besnus, A. Herr and G. Fisher, J. Phys. F: Metal Phys., **9**, 745 (1979).

[151] E. Burzo, J. Phys. F: Metal Phys. **10**, 2025 (1980).

[152] H. Oesterreicher, J. Appl. Phys. **42**, 5137 (1971).

[153] H. Oesterreicher and R. Pitts, J. Appl. Phys. **43**, 5174 (1972).

[154] V. Sima, R. Grössinger, V. Sechovsky, Z. Smetana and H. Sassik, J. Phys. F: Met. Phys. **14**, 981 (1984).

[155] H. Oesterreicher, J. Phys. Chem. Solids **43**, 1267 (1973).

[156] W. Steiner, J. Magn. Magn. Mater. **14**, 47 (1979).

[157] H. Oesterreicher and W. E. Wallace, J. Less-Common Metals **13**, 91 (1967).

[158] E. Gratz, R. Grössinger, H. Oesterreicher and F. T. Parker, Phys. Rev. B **23**, 2542 (1981).

[159] D. Konopka and W. Zarek, J. Less-Common Metals, **81**, 5 (1981).

[160] A. Szajek, A. Kowalczyk, J. Baszynski, A. Jezierski and T. Mylardz, J. Magn. Magn. Mater. **157-158**, 723 (1996).

[161] A. Kowalczyk, A. Szajek, J. Baszynski, J. Kovac and G. Chelkowska, J. Magn. Magn. Mater. **166**, 237-242 (1997).

[162] J.J. Bara, A. T. Pedziwiatr, W. Zarek, D. Konopka and U. Gacek, J. Magn. Magn. Mater. **27**, 159 (1982).

[163] A. Pösinger, H. Winkler, W. Steiner, A. X. Trautwein and M. Reissner, J. Phys.: Condens. Matter **3**, 2713 (1991).

[164] W.M. Swift and W. E. Wallace, J. Phys. Chem. Solids, **29**, 2053 (1968).

[165] E. Joven, Ph. D. Thesis. University of Zaragoza (1991).

[166] A. del Moral, J. I. Arnaudas and P. M. Gehring, J. Phys.: Condens. Matter **6**, 4779 (1994).

[167] P. M. Gehring, M. B. Salamon, A. del Moral and J. I. Arnaudas, Phys. Rev. B **41**, 9134 (1990).

[168] A. Slebarski and W. Zahorowski, J. Phys. F: Metal Phys., **14**, 1553 (1984).

[169] G. J. Bowden, D. St. P. Bukbury, A. P. Guimaraess and R. E. Snyder, J. Phys. C. (Proc. Phys. Soc.) **1**, 1376 (1968).

[170] K. N. Martin, P. A. J. de Groot, B. D. Rainford, K. Wang, G. J. Bowden, J. P. Zimmermann and H Fangohr, J. Phys.: Condens. Matter **18**, 459 (2006).

[171] F. Grandjean and G. J. Long, in *Interstitial Intermetallic Alloys. NATO ASI Series, Series E: Applied Sciences, Vol. 281* edited by F. Grandjean, G. J. Long and K. H. J. Buschow, p. 463 (Kluwer Academic Publishers, 1995).

[172] chapter §15 (p. 650) of *Modeling of Data* de *Numerical Recipes in Fortran 77: The art of scientific computing*, (Cambridge University Press, Cambridge 1986-1992).

[173] C. Piquer, F. Grandjean, O. Isnard and G. J. Long, J. Phys.: Condens. Matter **18**, 221 (2006); C. Piquer, F. Grandjean, O. Isnard and G. J. Long, J. Phys.: Condens. Matter **18**, 205 (2006).

[174] Th. Sinnemann, M. U. Wisniewski, M. Rosenberg and K. H. J. Buschow, J. Magn. Magn. Mat. **83**, 259 (1990).

[175] I. A. Al-Omari, S. S. Jaswal, A. S. Fernando, D. J. Sellmyer and H. H. Hamdeh, Phys. Rev. B **50**, 12665 (1994).

[176] C. Christides, A. Kostikas, G. Zouganelis, V. Psyharis, X. C. Kou and R. Grossinger, Phys. Rev. B **47**, 11220 (1993).

[177] G. Dublon and U. Atzmony, J. Phys. F **7**, 1069 (1977).

[178] H. G. Purwins and A. Leson, Advances in Physics **39**, 309 (1990).

[179] J. C. Lang, G. Srajer, C. S. Nelson, C. T. Venkataramen, A. I. Goldman, C. Detlets, Z. Islam, B. N. Harmon, K. W. Dennis, and R. W. McCallum (unpublished).

[180] C. Giorgetti, Ph. D. Tesis, University of Paris-Sud (Centre d'Orsay), (1994).

[181] J. P. Liu, F. R. de Boer, P. F. de Chatel, R. Coehoorn and K.H.J. Buschow, J. Magn. Magn. Mater. **132**, 159-179 (1994).

[182] R. Hauser, E. Bauer and E. Gratz, Phys. Rev. B **57**, 054433 (1998).

[183] O. Syshchenko, T. Fujita, V. Sechovsky, M. Divis and H. Fujii, Phys. Rev. B **63**, 054433 (2001).

[184] N. H. Duc and P. E. Brommer, in *Handbook on Magnetic Materials* Vol. 12, edited by K. H. J. Buschow (Elsevier Science, Amsterdam, 1999), chap.3.

[185] N. H. Duc and T. Goto, in *Handbook on the Physics and Chemistry of Rare Earths* Vol. 26, edited by K. A. Gschneidner Jr. and L. Eyring, (Elsevier Science, Amsterdam, 1999), chap. 171.

[186] N. H. Duc, T. D. Hien, P. E. Brommer and J. J. M. Franse, J. Phys. F: Met. Phys. **18**, 275 (1988).

[187] N. V. Baranov, A. I. Kozlov, A. N. Pigorov and E. V. Sinitsyn, Sov. Phys. JETP **69**, 382 (1989).

[188] R. Hauser, E. Bauer, E. Gratz, M. Rotter, G. Hilscher, H. Michor and A. S. Markosyan, Physica B **237-238**, 577 (1997).

[189] R. Hauser, E. Bauer, E. Gratz, M. Rotter, H. Müller, G. Hilscher, H. Michor and A. S. Markosyan, Physica B **239**, 83 (1997).

[190] R. Hauser, E. Bauer, E. Gratz, H. Müller, M. Rotter, H. Michor, G. Hilscher, A. S. Markosyan, K. Kamishima and T. Goto, Phys. Rev. B **61**, 1198 (2000).

[191] R. Hauser, C. Kussbach, R. Grössinger, G. Hilscher, Z. Arnold, J. Kamarad, A. S. Markosyan, E. Chappel and G. Chouteau, Physica B **294-295**, 182 (2001).

[192] A. Podlesnyak, T. Strässle, A. Mirmelstein, A. Pirogov and R. Sadykov, Eur. Phys. J. B **29**, 547 (2002).

[193] A. Podlesnyak, T. Strässle, J. Schefer, A. Furrer, A. Mirmelstein, A. Pirogov, P. Markin and N. Baranov, Phys. Rev. B **66**, 012409 (2002).

[194] A. S. Markosyan, R. Hauser, M. Galli, E. Bauer, E. Gratz, G. Hilscher, K. Kamishima and T. Goto, J. Magn. Magn. Mater. **185**, 235 (1998).

[195] N. V. Baranov and A. N. Pigorov, J. Alloys Compd. **217**, 31 (1995).

[196] R. M. Moon, W. C. Koehler and J. Farrel, J. Appl. Phys. **36**, 978 (1965).

[197] H. G. Purwins, E. Walker, B. Barbara, M. F. Rossignol and A. Furrer, J. Phys. C: Solid State Phys. **9**, 1025 (1976).

[198] M. A. Laguna-Marco, J. Chaboy, C. Piquer, H. Maruyama, N. Ishimatsu, N. Kawamura, M. Takagaki and M. Suzuki, Phys. Rev. B **72**, 052412 (2005).

[199] M. A. Laguna-Marco, J. Chaboy and H. Maruyama, Phys. Rev. B **72**, 094408 (2005).

[200] J. P. Rueff, R. M. Galéra, C. Giorgetti, E. Dartyge, C. Brouder and M. Alouani, Phys. Rev. B **58**, 12271 (1998).

[201] M. A. Laguna-Marco, J. Chaboy, C. Piquer, H. Maruyama, N. Kawamura and M. Takagaki, J. Magn. Magn. Mater., in press (2006).

[202] T. Goto, H. A. Katori, T. Sakakibara, H. Mitamura, K. Fukamichi and K. Murata, J. Appl. Phys. **76**, 6682 (1994).

[203] T. Goto, K. Fukamichi, T. Sakakibara and H. Komatsu, Solid State Commun. **72**, 945 (1989).

[204] K. Yoshimura and Y. Nakamura, Solid State Commun. **15**, 767 (1985).

[205] T. Sakakibara, T. Goto, K. Yoshimura, M. Shiga and Y. Nakamura, Phys. Lett. A **117**, 243 (1986).

[206] T. Sakakibara, T. Goto, K. Yoshimura, M. Shiga, Y. Nakamura and K. Fukamichi, J. Magn. Magn. Mater. **70**, 126 (1987).

[207] H. Wada, K. Yoshimura, G. Kido, M. Shiga, M. Mekata and Y. Nakamura, Solid State Commun. **65**, 23 (198).

[208] T. Sakakibara, T. Goto, K. Yoshimura and K. Fukamichi, J. Phys.: Condens. Matter **2**, 3381 (1990).

[209] V. V. Aleksandryan, A. S. Lagutin, R. Z. Levitin and A. S. Markosyan, Sov. Phys. JETP **62**, 153 (1985).

[210] I. L. Gabelko, R. Z. Levitin, A. S. Markosyan, V. I. Silant'ev and V. V. Snegirev, J. Magn. Magn. Mater. **94**, 287 (1991).

[211] M. Aoki and Y. Yamada, Physica B **177**, 259 (1992).

[212] M. Aoki and Y. Yamada, J. Magn. Magn. Mater. **78**, 377 (1989).

[213] J. Y. Son, T. Konishi, T. Mizokawa, A. Fujimori, K. Koui and T. Goto, Physica B **237-238**, 400 (1997).

[214] T. Sakakibara, H. Mitamura and T. Goto, Physica B **201**, 127 (1994).

[215] S. Khmelevskyi, I. Turek and P. Mohn, J. Phys.: Condens. Matter **13**, 8405 (2001).

[216] I. L. Gabelko, R. Z. Levitin, A. S. Markosyan and V. V. Snegirev, JETP Lett. **45**, 458 (1987).

[217] T. Yokohama, H. Saito, K. F. K. Manishima, T. Goto and H. Yamada, J. Phys.: Condens. Matter **13**, 9281 (2001).

[218] M. Iijima, K. Endo, T. Sakakibara and T. Goto, J. Phys.: Condens. Matter **2**, 10069 (1990).

[219] K. Fukamichi, T. Yokohama, H. Saito, T. Goto and H. Yamada, Phys. Rev. B **64**, 134401 (2001).

[220] I. S. Dubenko, R. Z. Levitin, A. S. Markosyan, V. V. Snegirev and A. Y. Sokolov, J. Magn. Magn. Mater. **135**, 326 (1994).

[221] I. S. Dubenko, R. Z. Levitin and A. S. Markosyan, J. Magn. Magn. Mater. **111**, 146 (1992).

[222] T. Yokohama, H. Nakajima, H. Saito, K. Fukamichi, H. Mitamura and T. Goto, J. Alloys Comp. **266**, 13 (1998).

[223] I. S. Dubenko, R. Z. Levitin, A. S. Markosyan, V. V. Snegirev, A. Y. Sokolov, and H. Yamada, J. Magn. Magn. Mater. **140-144**, 827 (1995).

ISBN 978-84-7733-952-6

Prensas Universitarias de Zaragoza